MECHANOSENSATION OF TIGHT JUNCTIONS DEPENDS ON ZO-1 PHASE SEPARATION AND FLOW

by

Cornelia Schwayer

December, 2019

A thesis presented to the
Graduate School
of the
Institute of Science and Technology Austria, Klosterneuburg, Austria
in partial fulfillment of the requirements
for the degree of
Doctor of Philosophy

The dissertation of Cornelia Schwayer, titled *Mechanosensation of tight junctions depends on ZO-1 phase separation and flow*, is approved by:

Supervisor: Carl-Philipp Heisenberg, IST Austria, Klosterneuburg, Austria

Signature: _____

Committee Member: Daria Siekhaus, IST Austria, Klosterneuburg, Austria

Signature: _____

Committee Member: Antonio Jacinto, Chronic Diseases Research Center, Portugal

Signature: _____

Exam Chair: Edouard Hannezo, IST Austria, Klosterneuburg, Austria

Signature: _____

signed page is on file

IST Austria Thesis, ISSN: 2663-337X

I hereby declare that this dissertation is my own work and that it does not contain other people's work without this being so stated; this thesis does not contain my previous work without this being stated, and the bibliography contains all the literature that I used in writing the dissertation.

I declare that this is a true copy of my thesis, including any final revisions, as approved by my thesis committee, and that this thesis has not been submitted for a higher degree to any other university or institution.

I certify that any republication of materials presented in this thesis has been approved by the relevant publishers and co-authors.

Signature: _____

Cornelia Schwayer

December 16, 2019

signed page is on file

Abstract

Tissue morphogenesis in developmental or physiological processes is regulated by molecular and mechanical signals. While the molecular signaling cascades are increasingly well described, the mechanical signals affecting tissue shape changes have only recently been studied in greater detail. To gain more insight into the mechanochemical and biophysical basis of an epithelial spreading process (epiboly) in early zebrafish development, we studied cell-cell junction formation and actomyosin network dynamics at the boundary between surface layer epithelial cells (EVL) and the yolk syncytial layer (YSL). During zebrafish epiboly, the cell mass sitting on top of the yolk cell spreads to engulf the yolk cell by the end of gastrulation. It has been previously shown that an actomyosin ring residing within the YSL pulls on the EVL tissue through a cable-constriction and a flow-friction motor, thereby dragging the tissue vegetal wards. Pulling forces are likely transmitted from the YSL actomyosin ring to EVL cells; however, the nature and formation of the junctional structure mediating this process has not been well described so far. Therefore, our main aim was to determine the nature, dynamics and potential function of the EVL-YSL junction during this epithelial tissue spreading. Specifically, we show that the EVL-YSL junction is a mechanosensitive structure, predominantly made of tight junction (TJ) proteins. The process of TJ mechanosensation depends on the retrograde flow of non-junctional, phase-separated Zonula Occludens-1 (ZO-1) protein clusters towards the EVL-YSL boundary. Interestingly, we could demonstrate that ZO-1 is present in a non-junctional pool on the surface of the yolk cell, and ZO-1 undergoes a phase separation process that likely renders the protein responsive to flows. These flows are directed towards the junction and mediate proper tension-dependent recruitment of ZO-1. Upon reaching the EVL-YSL junction ZO-1 gets incorporated into the junctional pool mediated through its direct actin-binding domain. When the non-junctional pool and/or ZO-1 direct actin binding is absent, TJs fail in their proper mechanosensitive responses resulting in slower tissue spreading. We could further demonstrate that depletion of ZO proteins within the YSL results in diminished actomyosin ring formation. This suggests that a mechanochemical feedback loop is at work during zebrafish epiboly: ZO proteins help in proper actomyosin ring formation and actomyosin contractility and flows positively influence ZO-1 junctional recruitment. Finally, such a mesoscale polarization process mediated through the flow of phase-separated protein clusters might have implications for other processes such as immunological synapse formation, C. elegans zygote polarization and wound healing.

Acknowledgments

A lot of people supported me during my journey of PhD and I am very grateful to all of them. I will start acknowledging people in a more or less chronological order. First, I would like to thank my supervisor Carl-Philipp Heisenberg for giving me the opportunity to work on this project in his lab. I very much appreciate the freedom that I had in order to develop my own ideas of how to tackle problems and also for his continuous support during my project. When I initially started working with zebrafish as model system, Hitoshi Morita and Martin Behrndt thought me the basic steps and principles of zebrafish handling and for this I would like to thank both of them. Further, I would like to thank Philipp Schmalhorst and Daniel Capek for their help with establishing the CRISPR/Cas9 system in the Heisenberg lab and for their support in the troubleshooting associated with it. Kornelija Pranjic-Ferscha, Deborah Kurtzemann and Verena Mayer supported me big time in fin clipping and genotyping of the many generated zebrafish mutants – thank you so much for that. Furthermore, Kornelija Pranjic-Ferscha also supported me in executing the qRT-PCRs and in cloning constructs such as Occludin-A-mNeonGreen. I am grateful to Shayan Shamipour, Robert Hauschild and Christoph Sommer for their continuous support in data analysis aspects. In addition, Shayan Shamipour and Alexandra Schauer helped me with some experiments in the revision period, which I am very grateful for (Shayan supported me with imaging retrograde flow in caMypt and caRhoA samples and with quantification of the junctional integration efficiency; Alexandra was doing in situs of papc and supported me in imaging of Phalloidin staining of ΔC, ΔABR constructs). I would like to thank Nicoletta Petridou and Diana Pinheiro for their invaluable critical feedback and fruitful discussions throughout my PhD studies – the continuous exchange of scientific questions and ideas was integral for my progress. Before I started my PhD at IST, Daria Siekhaus and Aparna Ratheesh initially introduced me into the scientific field; this included invaluable skill sets such as how to think critically and how to address scientific questions. Besides helping me in building up such skills, their mentorship was also critical for my scientific development, which I am tremendously grateful for. I would like to further thank Daria Siekhaus, my internal committee member, for the frequent meetings we had to discuss the progress of my project. Thanks also to my external committee member Antonio Jacinto for his input at certain milestones along my PhD and to our collaborators at UCL, Karl Matter, Masazumi Tada and Maria Balda, for their valuable input and feedback on the topic of tight junctions. I would like to thank Oliver Beutel and Alf Honigmann from MPI-CBG Dresden for the exchange on unpublished data and fruitful discussions about the phase separation of Zonula Occludens proteins. Along with all the previously mentioned people, I am grateful to the current and former members of the Heisenberg group, not only for the countless discussion on various scientific and non-scientific topics, but also for the supportive atmosphere: Silvia Caballero Mancebo, Feyza Nur Arslan, Ste Tavano, Karla Huljev, Peng Xia, Suyash Naik, Roland Kardos, Ehsan Ghasemian, David Labrousse Arias, Daniel Capek, Vanessa Barone, Jana Slovakova, Matt Sikora, Keisuke Sako, Julien Compagnon, Gabby Krens and of course the neighboring Sixt lab people. Big thanks to all the facilities at IST AUSTRIA, the bioimaging facility, the fish facility and the EM facility, and all the people working there to support us on a daily basis. Special thanks to my family, to my parents and my brother, for supporting me in my decision to pursue a PhD. Finally, my boyfriend has deserved gold medal for being there for me also during tough periods and for understanding the long nights and weekends that I spent with my beloved fish – your continuous support means a lot to me. Finally, I am very grateful that I had all these inspiring and supportive people by my side during this interesting path of

PhD; all their support helped me to get me where I am right now. Having said this, I would like to end in thanking all the creative artists and songwriters, without whose artwork I could have not made it through countless nights with the same motivation and enthusiasm.

About the Author

Cornelia Schwayer completed a BSc in Molecular Biology at the University of Vienna, and joined the group of Daria Siekhaus at IST Austria in 2012. During her work as a technical assistant in the Siekhaus group, Cornelia helped characterizing mutants in order to identify new signaling pathways required for invasive migration during early development of Drosophila melanogaster. In 2013 Cornelia joined the PhD program at IST Austria and her main research focus in the Heisenberg group included how tissues spread during zebrafish gastrulation. She became particularly interested in a mechanosensitive and phase separation mediated process affecting epithelial spreading. During her PhD, Cornelia presented the progress of her work at several conferences, such as at EMBO symposia, Gordon conference and at the ASCB conference. In 2016, Cornelia together with colleagues from the Heisenberg group published a review on 'Actin Rings of Power' in Developmental Cell. Her main research work was built on genetic, cell biological, biochemical and biophysical methods. In October 2019, Cornelia together with colleagues from the Heisenberg group and collaborators from the University College London, UK, published the study 'Mechanosensation of tight junctions depends on ZO-1 phase separation and flow' on her main PhD project in the journal Cell.

List of Publications Appearing in Thesis

1. Schwayer, C., Sikora, M., Slováková, J., Kardos, R. & Heisenberg, C. P. Actin Rings of Power. *Dev. Cell* **37**, 493–506 (2016).
   DOI: https://doi.org/10.1016/j.devcel.2016.05.024

2. Schwayer C, Shamipour S, Pranjic-Ferscha K, Schauer A, Balda M, Tada M, Matter K and Heisenberg CP. Mechanosensation of tight junctions depends on ZO-1 phase separation and flow. *Cell* **179**, 937-952.e18 (2019)
   DOI: https://doi.org/10.1016/j.cell.2019.10.006

πάντα ῥεῖ

('Everything flows')

Heraclitus - Greek philosopher
Plato, Cratylus 402a

Table of Contents

List of Figures

List of Abbreviations

ABR	Actin Binding Region
AJ	Adherens Junction
aPKC	atypical Protein Kinase C
ca	constitutively active
CK2	Casein Kinase 2
DYRK3	Dual specificity tyrosine (Y)-phosphorylation-Regulated Kinase 3
ERK	Extracellular-signal-Regulated Kinase
EVL	Enveloping Layer
eYSL	external Yolk Syncytial Layer
GAP	GTPase-Activating Protein
GDP	Guanosine Diphosphate
GEF	Guanine nucleotide exchange factor
GTP	Guanosine-5'-triphosphate
GUK	Guanylate Kinase
HDMEC	Human Dermal Microvascular Endothelial Cells
hpf	hours post fertilization
IDR	Intrinsically Disordered Region
iYSL	internal Yolk Syncytial Layer
JAM	Junctional Adhesion Molecule
LAT	Linker for Activation of T cells
LLPS	Liquid-Liquid Phase Separation
MAGUK	Membrane-Associated GUanylate Kinase
MAPK	Mitogen Activated Protein Kinase
MAPKAPK2	Mitogen Activated Protein Kinase Activated Protein Kinase 2
MDCK	Madin-Darby Canine Kidney cells
mTORC1	mechanistic/mammalian Target Of Rapamycin Complex 1
MZT	Maternal-Zygotic Transition

N-WASP	Neural Wiskott-Aldrich syndrome protein
NMDA	N-Methyl-D-Aspartate
Par3	Partitioning-defective protein 3
Par6	Partitioning-defective protein 6
PDZ	First letter of each: PSD-95 (Post Synaptic Density Protein 95), Drosophila disc large tumor suppressor (Dlg1), and Zonula Occludens 1 (ZO-1)
PML	Promyelocytic Leukaemia protein
pMLC	Phospho-Myosin Light Chain 2
PP1	Protein Phosphatase 1
PRM	Proline-Rich Region
PSD	Post Synaptic Density
PSG	PDZ-SH3-GUK
PTM	Posttranslational Modification
RBP	RNA-Binding Proteins
RNA	Ribonucleic Acid
RNP	Ribonucleoproteins
ROCK	Rho-associated protein kinase
SH3	SRC Homology 3
TCR	T Cell Receptor
TJ	Tight Junction
TOR	Target Of Rapamycin
VE-cadherin	Vascular Endothelial cadherin
YCL	Yolk Cytoplasmic Layer
YSL	Yolk Syncytial Layer
ZO	Zonula Occludens

1 Introduction

1.1 Morphogenesis in development

Morphogenesis literally means the creation of shape (from Greek γεννητση- gennisi meaning '*creation or emergence'* and μορφη- morphi, meaning '*shape'*)[1]. During early developmental stages, an organism needs to grow in its cell mass (proliferation), these cells need to get specified from an initially pluripotent mass of cells into cells with specific functions (differentiation) and the organism also needs to take its destined shape (morphogenesis)[2]. Organisms manage to reach their final shape through processes such as oriented cell division, changes in cell shapes and cell migration[2]. In general, these processes are regulated through molecular and mechanical information[3]. While the regulation via molecular information has been heavily studied in the past, the influential and pioneering work 'On Growth and Form' by D'Arcy W. Thompson opened new doors for the field of biology in a way to introduce mathematical and physical views on biological shape and pattern formation[4]. One sentence from this seminal work captures the overarching concept – that not only non-living matter but also biological and living matter are subject to physical laws - very well: *'The search for differences or fundamental contrasts between the phenomena of organic and inorganic, of animate and inanimate things, has occupied many men's minds, while the search for community of principles or essential similitudes has been pursued by few; and the contrasts are apt to loom too large, great though they may be.'*[4] Within the last decades, a multitude of concepts from physics and other disciplines (mathematics, chemistry) have been applied successfully to explain the emergence of pattern formation and morphogenesis in biological systems[2,3,5–7]. In the course of this PhD thesis we will discuss biochemical as well as biophysical concepts involved in tissue morphogenetic processes, which have been previously proven to greatly influence such systems[2,3,5–7].

The goal of this PhD thesis was to shed more light on the tissue mechanics of a spreading epithelium during early zebrafish development, and specifically the contribution of mechanosensitive tight junctions therein. To prepare the reader for the results section, we will cover several chapters on (1) tissue morphogenesis including actin ring formation, maturation and the contribution of cell-cell junctions during tissue morphogenetic processes. Importantly, while working on the mechanistic description of this tissue spreading process, we encountered an interesting behavior of one junctional protein, best described through the physical concept of *phase transition* or specifically *phase separation*. This physical concept has been recently applied to describe various other biological processes[8,9], and we will therefore introduce it in a bit more detail during the introductory chapter (2). At the end of the introduction we will converge to the actual process investigated during this PhD thesis - zebrafish epiboly (3). The results chapter will contain the published paper on the main PhD project and some additional information addressing the mechanosensitivity of other tight junction proteins. In the final discussion chapter, we will briefly go through some remaining open questions and then end with the broader implications of the described mechanosensation process for other tissue morphogenetic and polarization processes.

1.2 Tissue morphogenesis

For a tissue to undergo changes in its shape, it relies on processes such as (1) force generation for instance mediated via actomyosin structures, (2) force transmission at cell-cell junctions and (3) force integration at a tissue level[2,10]. These concepts will accompany us throughout the thesis and we will start the first subchapter emphasizing the force generation of actin ring structures during various morphogenetic and physiological processes such as wound healing, *Drosophila* dorsal closure, zebrafish epiboly and epithelial cell extrusion. Force transmission and integration will also be briefly mentioned in some of these processes, however, a more detailed discussion on force transmission at cell-cell junctions and integration at tissue scale will follow in the next subchapter (1.2.2).

1.2.1 Actin rings of power[11]

Publication:

Schwayer, C., Sikora, M., Slováková, J., Kardos, R. & Heisenberg, C. P. Actin Rings of Power. *Dev. Cell* **37**, 493–506 (2016).
DOI: https://doi.org/10.1016/j.devcel.2016.05.024

Developmental Cell
Review

Actin Rings of Power

Cornelia Schwayer,[1] Mateusz Sikora,[1] Jana Slováková,[1] Roland Kardos,[1] and Carl-Philipp Heisenberg[1,*]
[1]Institute of Science and Technology Austria, Am Campus 1, 3400 Klosterneuburg, Austria
*Correspondence: heisenberg@ist.ac.at
http://dx.doi.org/10.1016/j.devcel.2016.05.024

Circular or ring-like actin structures play important roles in various developmental and physiological processes. Commonly, these rings are composed of actin filaments and myosin motors (actomyosin) that, upon activation, trigger ring constriction. Actomyosin ring constriction, in turn, has been implicated in key cellular processes ranging from cytokinesis to wound closure. Non-constricting actin ring-like structures also form at cell-cell contacts, where they exert a stabilizing function. Here, we review recent studies on the formation and function of actin ring-like structures in various morphogenetic processes, shedding light on how those different rings have been adapted to fulfill their specific roles.

Introduction

Force generation in various biological processes relies on the interaction between actin filaments and myosin motors. In the cellular environment, actin filaments (F-actin) are assembled with the assistance of actin nucleators, such as formins generating long unbranched actin filaments and Arp2/3 creating branched filaments (Firat-Karalar and Welch, 2011; reviewed in Pollard, 2007; Sept and McCammon, 2001). Depending on the available actin monomer pool the incorporation of actin monomers can occur at both ends of the filaments, but with different kinetics. Consequently, one can distinguish between a fast-growing barbed or plus end and a more slowly elongating pointed or minus end (reviewed in Bugyi and Carlier, 2010; Pollard and Borisy, 2003). Actin is a rather versatile protein, which can appear in diverse organizations. For instance in a moving cell, actin can form branched networks (lamellipodia), anti-parallel filaments (stress fibers), or parallel bundles (filopodia). The diversity in structure is also reflected in the different mechanical properties of actin networks, which can exhibit viscoelastic, contractile, or rigid behavior (Blanchoin et al., 2014).

Actin filaments themselves can generate forces during polymerization by the addition of actin monomers to their growing ends. Such a force-generating mechanism operates, for instance, in the lamellipodium of migrating cells where the incorporation of actin monomers plays a ratchet-like role in stabilizing instantaneous membrane fluctuations, effectively pushing the leading-edge membrane forward (Démoulin et al., 2014; Peskin et al., 1993). Other processes, however, require contractile forces arising from the interaction of actin and myosin motors (reviewed in Conti and Adelstein, 2008; Vicente-Manzanares et al., 2009). In this review, we primarily focus on the conventional non-muscle myosin II (hereafter referred to as myosin), although other myosins, such as myosin V (Laplante et al., 2015), myosin VI (Maddugoda et al., 2007; Engl et al., 2014; Lin et al., 2007), and myosin VII (Tuxworth et al., 2001; Küssel-Andermann et al., 2000) have also been implicated in actomyosin-based morphogenetic processes. The heavy chain of the myosin motor protein consists of a head domain and a tail domain. The head region is responsible for actin filament binding and also contains the motor domain. Two heavy chains can dimerize through the tail domain and, together with two essential light chains and two regulatory chains, form a functional hexamer unit (Weeds and Lowey, 1971). Myosin motor activity is regulated through phosphorylation/dephosphorylation of the regulatory light chain. Kinases such as Rho-associated kinase (ROCK), a downstream effector of Rho guanosine triphosphatases (GTPases), phosphorylate and thus activate myosin, while phosphatases such as myosin light-chain phosphatase (MLCP) holoenzyme deactivate it (Amano et al., 1996; Mitsui et al., 1992; Shirazi et al., 1994). ROCK also phosphorylates the myosin phosphatase-targeting subunit of MLCP, thereby blocking its phosphatase function and thus preventing it from deactivating myosin (Feng et al., 1999; Kimura et al., 1996; Murányi et al., 2005). The phosphorylation of myosin regulatory light chain, besides turning on myosin motor activity, also promotes the formation of bipolar myosin mini-filaments through tail-to-tail association, which can then further mature into thick filaments found, for example, in the sarcomere of skeletal muscles (Niederman and Pollard, 1975; Ricketson et al., 2010; Scholey et al., 1980; Turbedsky et al., 2005). In contrast, phosphorylation of the heavy chain of myosin by kinases, such as protein kinase C (PKC), reduces myosin filament assembly (Dulyaninova et al., 2005; Egelhoff et al., 1993). Bipolar myosin filaments can simultaneously bind to several cross-linked actin filaments with opposing polarity and translocate them in respect to each other, a mechanism typically observed in highly ordered actomyosin structures such as sarcomeres (Figure 1). Besides these highly ordered actomyosin structures consisting of bundled actin filaments, myosin motors can also bind to and interact with less ordered actin structures, such as meshwork-like actin networks lacking any preferential filament orientation/alignment (Figure 1) (Martin, 2010). Depending on filament cross-linking by actin-binding proteins and the abundance of myosin motors, these distinct actin networks can show different contractile properties. Actin network reorganization and/or contraction is typically associated with cell-shape changes, which when coordinated with each other can lead to tissue shape changes, such as tissue invagination or elongation (Munjal and Lecuit, 2014).

Actin filaments not only appear as linear or meshwork-like networks but frequently also assemble in ring-like arrangements. Such a ring-like arrangement has recently been shown to arise from the spontaneous assembly of actin filaments within spherical droplets (Miyazaki et al., 2015). In this reduced in vitro system, single actomyosin rings form at the equator of spherical

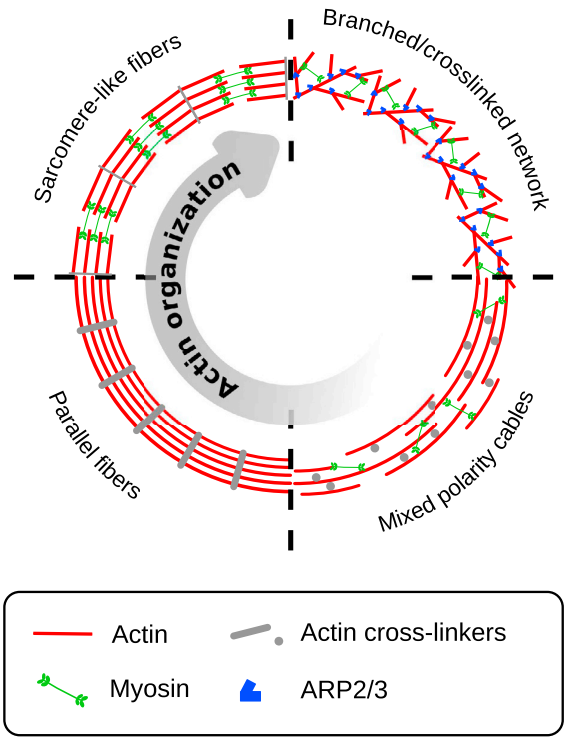

Figure 1. Actin Network Organization
Cells can form distinct actin network structures depending on their function and localization. The most prominent structures are contractile, branched actomyosin networks built of cross-linked actin fibers coupled to myosin motors. More anisotropic networks are formed when long actin fibers with mixed polarity are linked together and thus aligned with each other by different cross-linker proteins. Parallel actin fibers are generated when cross-linked actin fibers are aligned in the same direction. Regular arrays of parallel actin fibers connected by myosin motors are found in sarcomeres, representing the highest level of actin organization. Actin rings have been associated with most of these structures.

droplets in the presence of bundling factors, but in the absence of any regulatory proteins known in vivo to control the spatiotemporal pattern of actomyosin ring formation. The formation of these spontaneously assembled actomyosin rings has been proposed to be the result of minimized elastic energy of actin filaments at the equator, and only to occur when the spherical droplets have a diameter smaller than or equal to the persistence length of actin filaments (Miyazaki et al., 2015).

In this review we summarize the assembly mechanisms and functions of actin ring-like structures in various cell biological and developmental processes. In vivo, different examples of ring-like actomyosin structures have been described both on a single-cell level, such as in cell division (Maupin and Pollard, 1986) and cell-cell adhesion (Engl et al., 2014; Maitre et al., 2012), or on a multicellular level, such as in adhering epithelial cells (Burnside, 1971), wound healing (Bement et al., 1993; Danjo and Gipson, 1998; Martin and Lewis, 1992), and epithelial cell extrusion (Rosenblatt et al., 2001). The existence of single-cell actomyosin-based contractile rings triggering cytokinesis during cell division dates back to about a billion years ago across phyla, pointing at the possibility that contractile actomyosin rings represent a basic cytoskeletal apparatus that has been adapted throughout evolution to drive a diverse number of biological processes. Regardless of the specific system in which those actin rings function and apparent differences in ring architecture and size, actin rings are typically composed of actin filaments cross-linked by myosin motor proteins and/or numerous other actin-binding components. Besides these conserved structural and functional components, Rho-family GTPases (Rho, Rac, Cdc42) have generally been associated with the regulation of actin ring initiation, formation, and contraction. Finally, actin rings generate and/or maintain cortical anisotropies, a concept that seems to be universal and fully scalable.

Many morphogenetic processes in development, such as *Drosophila* dorsal closure (Jacinto et al., 2002a; Kiehart et al., 2000; Young et al., 1993) or zebrafish epiboly (Behrndt et al., 2012; Köppen et al., 2006), are thought to be dependent on the formation of actomyosin ring-like structures. In the majority of such cases, the actomyosin ring functions by constricting, such as in *Drosophila* dorsal closure and zebrafish epiboly, but there are also cases, such as cell-cell adhesion and tissue formation, where actomyosin rings function as mechanical scaffolds stabilizing cell shapes and assemblies. In the following, we summarize and discuss the core features and properties shared by actomyosin ring-like structures in various biological processes, and how these core features have been modified by different actomyosin rings to acquire their specific functions.

Cytokinesis

The formation of contractile ring-like structures composed of actin and myosin constitutes an essential step in various fundamental cell biological and developmental processes. One of the most notable and best-studied events in which contractile actomyosin rings are involved is the last step of animal or fungi cell division when the dividing cell is cleaved into two parts. This is typically achieved by the formation of an actomyosin ring (cytokinetic ring), which by constricting gives rise to the cleavage furrow separating the genetic material between the newly forming daughter cells. The spatiotemporal control of cleavage furrow formation and constriction needs to be tightly coordinated with the alignment and poleward movement of the sister chromosomes, i.e., the ring needs to be assembled between the separating chromosomes and start to constrict when the chromosomes begin to move toward the poles. Two principal non-exclusive models have been proposed by which the cleavage furrow is correctly positioned during cytokinesis: (1) localized activation of actomyosin assembly at the division plane due to stimulating signals originating from the central spindle (an anti-parallel array of MT between the separating chromosomes), and/or from astral MT anchored to the cell cortex at the prospective cleavage furrow; and (2) inhibition of actomyosin assembly at the poles of the dividing cells due to inhibitory signals originating from the astral MT anchoring to the poles. The centralspindlin complex is thought to represent the source of signals stimulating cleavage furrow formation by localizing to the central spindle and adjacent division plane and recruiting and activating the RhoGEF Ect2 (Nishimura and Yonemura, 2006; Tatsumoto et al., 1999; Yüce et al., 2005). Localized recruitment of Ect2 to the division plane in turn leads to the activation of RhoA, which ultimately triggers actomyosin ring formation by

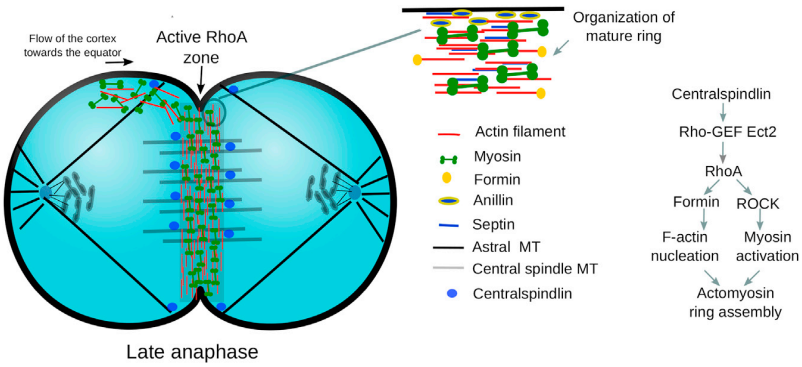

Figure 2. Cytokinesis

At the onset of anaphase the centralspindlin complex translocates toward the division plane by associating with central spindle MT and astral MT projecting toward the division plane. The centralspindlin complex then recruits and activates the RhoGEF Ect2, resulting in the generation of an active RhoA zone at the division plane. RhoA promotes actomyosin ring assembly by activating the actin nucleator formin and the myosin activator ROCK. Besides the localized assembly of actomyosin fibers, the flow of cortical actomyosin toward the division plane also contributes to cytokinetic ring formation. At late anaphase, actin and myosin (mini)filaments are preferentially aligned along the division plane (Schroeder, 1973) and start to cleave the cell into two parts by circumferential ring constriction. Notably, the degree of such filament alignment can considerably vary depending on the cell type. For the cleavage furrow to form, not only does the cytokinetic ring need to constrict, but the plasma membrane needs also to be tightly attached to the ring through the scaffolding protein anillin and the actin-bundling protein septin.

activating myosin and the actin nucleator formin (Figure 2). RhoA activation at the division plane has also been proposed to trigger a cortical actomyosin tension gradient between the division plane and the poles, giving rise to a directional flow of the actomyosin cortex toward the division plane of the dividing cell, thereby promoting ring formation (Salbreux et al., 2009).

The cytokinetic furrow in dividing cells ranging from very small cells, such as dividing yeast cells, to very large cells, such as cleaving vertebrate oocytes, is often composed of anti-parallel actin filaments (Kamasaki et al., 2007; Mabuchi et al., 1988; Sanger and Sanger, 1980) that are to a varying extent aligned along the division plane (Fishkind and Wang, 1993; Maupin and Pollard, 1986; Schroeder, 1968, 1972, 1973). How actin filaments within the cytokinetic ring become aligned is not yet fully understood, but both myosin-dependent capture and realignment of randomly nucleated actin filaments at the division plane (Vavylonis et al., 2008) and/or remodeling of an initially isotropic network through actomyosin flowing from the poles to the division plane (Salbreux et al., 2009) are thought to be involved.

Two basic mechanisms have been put forward by which the cleavage furrow constricts during cytokinesis: (1) myosin motors pulling on anti-parallel actin filaments and (2) depolymerization of cross-linked actin filaments. Electron microscopy studies analyzing the ultrastructure of cytokinetic rings have revealed actin filaments that are arranged in anti-parallel arrays between which myosin mini-filaments are intercalated (Mabuchi et al., 1988; Sanger and Sanger, 1980). Ring constriction is then triggered by the bipolar myosin mini-filaments moving toward the plus end of adjacent anti-parallel actin filaments, thereby pulling these filaments along each other and reducing the ring diameter (Figure 2). Alternatively or in addition to this myosin-mediated actin filament pulling mechanism, depolymerization of actin filaments that are cross-linked by minus-end tracking proteins has been speculated to generate tension that can drive cytokinetic ring constriction (Zumdieck et al., 2007). Interestingly, myosin is thought to function in both of these mechanisms by directly pulling on adjacent actin filaments as well as triggering actin disassembly (Mendes Pinto et al., 2012).

A key feature of cytokinetic rings is that the speed of their constriction closely scales with their size so that the time required for cytokinesis remains unchanged by alterations in cell size (Carvalho et al., 2009). This scaling effect has been attributed to the ring size being proportional to the number of "contractile units" within the ring, i.e., larger rings contain more contractile units than smaller rings and thus constrict faster, assuming that actomyosin turnover, and thus readjustment of unit number within the ring, is slow compared with the time needed for ring constriction. A key feature of the contractile unit model is that each unit has a predefined size that might be set by the mean filament length of actin (Miyazaki et al., 2015). Analogous to this contractile unit model, the concentration of stable myosin and/or the extent of actin filament overlap, and consequently the contraction force generated between these filaments has been proposed to scale with ring size, thereby coupling the speed of ring constriction to its size (Reymann et al., 2012).

Finally, for actomyosin ring constriction driving cleavage furrow formation and cytokinesis, the ring must be effectively linked to the adjacent plasma membrane. Several structural ring components have been associated with this function, such as anillins and septins. Anillins are scaffolding proteins that play a pivotal role in the recruitment of structural and signaling constituents of the contractile ring. Anillin can interact with the core ring components actin and myosin, and is also able to bind to RhoA, thereby ensuring ring integrity and contraction (Field and Alberts, 1995; Piekny and Glotzer, 2008; Straight et al., 2005). In addition, it can interact with the cell membrane, suggesting a prominent role in anchoring the ring to the membrane (Sun et al., 2015). Septins are scaffolding ring components that cross-link actin filaments into curved, tightly packed arrays (Mavrakis et al., 2014) and link the ring to the plasma membrane by either directly binding to the plasma membrane or indirectly binding to anillins, which again anchor to the plasma membrane (Bertin et al., 2010; Hickson and O'Farrell, 2008).

Notably, coupling of the cytokinetic ring to the adjacent plasma membrane and proteins located therein has also been implicated in planar divisions of epithelial cells. In the *Drosophila* epidermis, for instance, the ingression of the cleavage furrow during planar divisions is faster on the basal than on the apical side (Guillot and Lecuit, 2013). This difference in the speed of cleavage furrow ingression has further been attributed to the cell-cell adhesion molecule E-cadherin coupling the cytokinetic

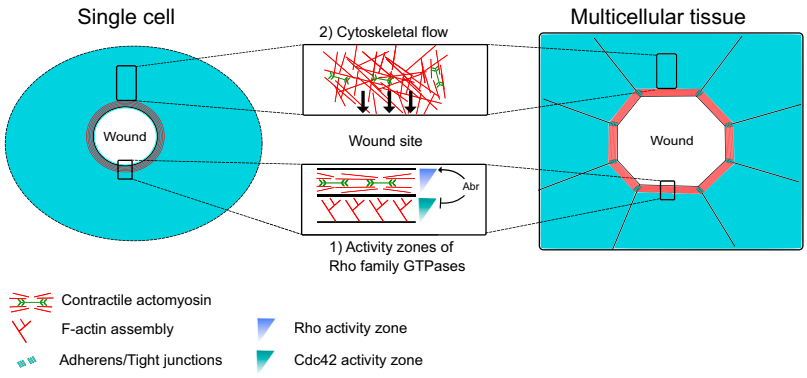

Figure 3. Wound Healing
(1) In single-cell and multicellular wound healing, Ca^{2+}-dependent Rho and Cdc42 activity zones regulate the formation and contraction of actomyosin ring-like structures at the wound site. Upon wounding, two zones of Rho-family GTPases are formed at the wound edge, which are separated from each other by Abr (dual GEF-GAP), simultaneously activating Rho and inactivating Cdc42. (2) Flow of cytoskeletal components such as F-actin and myosin promote actomyosin ring formation at the wound edge. In single-cell wound healing, the coupling of the membrane and the actomyosin ring can be mediated via E-cadherin. In multicellular wounds, formation and constriction of actomyosin rings at the wound edge requires anchoring of actomyosin ring segments to the membrane, for example, via AJs or TJs.

ring to rigid adherens junctions (AJs) at the apical side of those cells, thereby resisting furrow ingression there. Consistent with a critical function of cadherins in anchoring the cytokinetic ring to the plasma membrane, there are also reports in *Drosophila* showing that cadherins can replace anillins in cleavage furrow formation and cytokinesis during spermatocyte division (Goldbach et al., 2010).

Single-Cell and Multicellular Wound Closure

Constricting actomyosin rings are not only found in dividing cells but can also be observed in various morphogenetic processes, such as wound healing and closure of epithelial holes. In wound healing, for instance, the assembly of actomyosin ring-like structures share several features with the cleavage furrow during cell division, such as the involvement of Rho-family GTPases and actomyosin flows in their formation and constriction. Upon wound induction in either single cells or tissues, a contractile ring is assembled within seconds to minutes after damage. The exact process by which actomyosin ring assembly is initiated is still not completely understood, but the release of intracellular Ca^{2+} from mechanosensitive Ca^{2+} channels in response to mechanical stress upon wounding is likely to play an important role therein (Antunes et al., 2013; Benink and Bement, 2005; Clark et al., 2009; Cordeiro and Jacinto, 2013; Sonnemann and Bement, 2011). Ca^{2+} again might trigger actomyosin ring formation by activating Rho-family GTPases (Bement and von Dassow, 2014; Benink and Bement, 2005; Clark et al., 2009) or Ca^{2+}-dependent actin filament-severing proteins that have been implicated in actomyosin ring assembly (Antunes et al., 2013).

Single-cell wound repair has been extensively studied in *Xenopus laevis* oocytes and has been shown to reflect the basic features of wound healing (Bement and von Dassow, 2014). In frog oocytes, Ca^{2+} levels increase within seconds after laser-induced wounding, triggering concentric zones of Rho and Cdc42 activity around the wound circumference (Figure 3.1) (Benink and Bement, 2005). Initially these zones are overlapping, but soon segregate from each other, with the Rho zone being placed directly adjacent to the wound site and the Cdc42 zone further away encompassing the Rho zone. This segregation is thought to be driven by the recruitment of the RhoGEF and GAP factor Abr adjacent to the wound site, which both activates Rho and inactivates Cdc42 (Vaughan et al., 2011). Eventually, these non-overlapping zones of Rho and Cdc42 trigger F-actin polymerization and myosin activation at the wound margin, leading to actomyosin ring formation, constriction, and wound closure (Benink and Bement, 2005). Interestingly, simultaneous reduction of Rho, Rac, and Cdc42 was found to slow down but not completely abolish single-cell wound closure in *Drosophila*, suggesting that wound closure does not entirely depend on Rho-family GTPase activity (Abreu-Blanco et al., 2014). Besides Rho-family GTPases, flow of actomyosin and microtubules toward the wound site has also been associated with single-cell wound closure by promoting actomyosin ring formation through stimulation of network contraction and/or assembly (Mandato and Bement, 2001, 2003) (Figure 3.2).

Analogous to single-cell wounds, a contractile actomyosin ring-like structure has also been observed upon wounding of embryonic or adult multicellular tissues (Danjo and Gipson, 1998; Martin and Lewis, 1992). In such cases, a supracellular actomyosin ring spanning several cells is assembled around the wound site. As in single-cell wounds, the formation and constriction of such supracellular actomyosin rings is initiated by Ca^{2+}-dependent Rho and Cdc42 activity zones forming around the wound margin (Figure 3.1) (Clark et al., 2009) and mediated by the resultant activation of Rho effectors, such as ROCK (Brock et al., 1996; Russo et al., 2005). Moreover, Ca^{2+}-dependent activation of actin filament-severing proteins, such as gelsolin, is thought to promote multicellular wound closure by providing a large enough pool of actin monomers and barbed ends needed for effective actomyosin flow toward the wound (Antunes et al., 2013) (Figure 3.2). Such gelsolin-dependent flow was found to propagate across several cells toward the wound site and has been hypothesized to promote actomyosin ring formation and constriction (Antunes et al., 2013).

Interestingly, wounds can also close in a contraction-independent manner, although at a slower rate (Burkel et al., 2012). For instance, in frog oocytes where the motor activity of myosin is inhibited, the actomyosin ring still closes around the wound site by a GTPase signal "treadmill" that generates activity gradients of Rho and Cdc42 emanating from the wound site. How such activity gradients lead to wound closure is not yet entirely clear, but pushing by polarized actin polymerization within the Cdc42 domain and/or ring constriction by polarized actin depolymerization within the Rho domain have been suggested (Burkel et al., 2012; Sharif and Maddox, 2012).

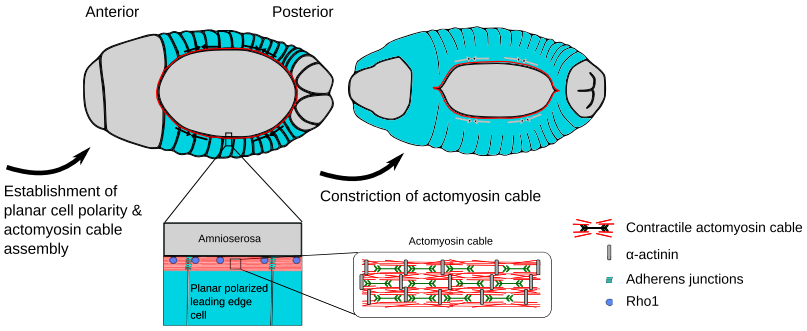

Figure 4. *Drosophila* Dorsal Closure
At the onset of dorsal closure (dorsal view), the leading edge cells of the lateral epidermis become planar polarized and assemble a supracellular actomyosin cable encompassing a dorsal hole. Constriction of the actomyosin ring promotes dorsal closure by acting in a purse-string-like manner. The ring is composed of a sarcomere-like assembly of F-actin, myosin, and α-actinin and is regulated by its upstream GTPase Rho1, an essential component of ring constriction. As in many other supracellular actomyosin rings, the intracellular ring segments are linked to AJs.

Notably, in both single cells (Mandato and Bement, 2001) and multicellular tissues (Jacinto et al., 2001), the actomyosin ring surrounding the wound site can still constrict and close even in case of being not fully continuous around the wound. This, in conjunction with the observation of spatially restricted recoil of the actomyosin ring after local UV laser cutting in single-cell wounds (Mandato and Bement, 2001), suggests that the actomyosin ring is efficiently anchored to surrounding structures at the wound site and argues against a simple "purse-string" mechanism whereby continuous circumferential constriction of the ring closes the wound. E-cadherin has been suggested to mediate the coupling of the actomyosin ring to the plasma membrane in single-cell wounds (Abreu-Blanco et al., 2011). In multicellular epithelial wound repair, the actomyosin cable can be mechanically integrated at AJs (Wood et al., 2002). AJs have further been suggested not only to serve as anchoring sites but also to function as "signaling centers" by recruiting Rho GTPases that regulate the actomyosin network during epithelial remodeling (Takeichi, 2014). Consistent with this notion, wounding in frog embryos has been found to activate Rho at both the wound site and the closest cell-cell junction, resulting in the formation of a hybrid ring consisting of junctional and non-junctional actomyosin pulling the wound edges together (Clark et al., 2009). Notably, the assembly of the actomyosin ring around the wound site is not only associated with the local accumulation of AJ proteins, such as E-cadherin and β-catenin (Danjo and Gipson, 1998), but also with proteins characteristic for tight junctions (TJs) such as zonula occludens 1 (ZO-1) (Bement et al., 1993; Tamada et al., 2007). TJs might function in wound healing by anchoring the actomyosin ring to the membrane (Tamada et al., 2007) and/or maintaining apical-basal polarity of cells surrounding the wound (Bement et al., 1993; Sonnemann and Bement, 2011).

Drosophila Dorsal Closure

Much like wound healing, dorsal closure in *Drosophila* is a morphogenetic movement during which a dorsal hole in the epithelium is closed. Multiple actomyosin-mediated processes are thought to drive this process by acting not only in the epithelial cells surrounding the hole but also in the extraembryonic tissue, the amnioserosa (AS), underlying the hole. A contractile supracellular actomyosin cable positioned at the leading edge of the surrounding epithelium has been suggested to act as a purse-string driving dorsal closure (Hutson et al., 2003; Jacinto et al., 2002b; Kiehart et al., 2000; Rodriguez-Diaz et al., 2008; Young et al., 1993). In addition, the AS cells undergo pulsatile apical constrictions (Franke et al., 2005; Solon et al., 2009) and reduce their volume (Saias et al., 2015), and a fraction of these cells also delaminate (Toyama et al., 2008), thereby contributing to dorsal closure by pulling on the margin of the surrounding epithelium. At the final stage of dorsal closure, actin- and microtubule-rich filopodia extend from the leading edge of epithelium toward the opposing epithelial edge, thereby zipping the two sheets of cells together (Jacinto et al., 2000; Jankovics and Brunner, 2006).

At the onset of dorsal closure, the leading-edge epidermal cells elongate along the dorsal-ventral axis of the embryo and establish planar cell polarity (PCP) (Kaltschmidt et al., 2002). This is accompanied by a dynamic redistribution of AJ- and PCP-associated proteins, such as Dishevelled, Frizzled, and Flamingo, eventually leading to actin accumulation in puncta at AJs and assembly into cables, which become connected across leading-edge cells to form a supracellular purse-string surrounding the dorsal hole (Jacinto et al., 2002b; Kaltschmidt et al., 2002) (Figure 4). Several signals have been involved in the formation of this actomyosin cable, including Jun amino-terminal kinase, Decapentaplegic, Wingless, and Notch (Jacinto et al., 2002b; Kaltschmidt et al., 2002; Zecchini et al., 1999). Besides these signals, Echinoid (Ed), a nectin ortholog, has been suggested to serve as an initial spatial cue for determining the future localization of the multicellular actomyosin cable (Laplante and Nilson, 2011). Ed, initially expressed in both epidermal and AS cells, disappears from AS cells at the onset of dorsal closure, generating an Ed expression boundary between non-expressing AS and expressing epidermal cells. The asymmetric expression of Ed has been speculated to trigger actomyosin ring assembly at the leading edge of epidermal cells by controlling the localization of different actin regulators to the edge (Laplante and Nilson, 2011).

Similar to actomyosin rings during cytokinesis and wound healing, the actomyosin cable in dorsal closure is composed of F-actin and myosin (Young et al., 1993) and has been suggested to constrict by myosin pulling on adjacent anti-parallel actin filaments (Martin, 2010; Rodriguez-Diaz et al., 2008) (Figure 4). The cable in the leading-edge cells shows an alternative pattern of (non-muscle) α-actinin and myosin, which is analogous to contractile units of sarcomeres that are made up of actin filaments, cross-linked by α-actinin, and pulled by myosin motors (Martin, 2010; Rodriguez-Diaz et al., 2008). Formation and maintenance of this actomyosin cable depends on the function of Rho1, a

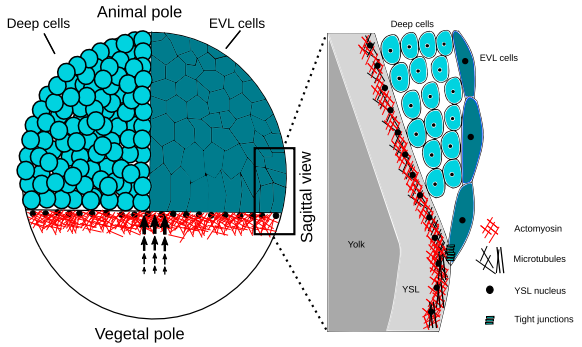

Figure 5. Zebrafish Epiboly
The spreading of the EVL over the surface of the yolk is driven by constriction of a large actomyosin ring located within the extraembryonic YSL. This actomyosin ring pulls the margin of the EVL toward the vegetal pole by constricting along the circumference of the embryo, thereby acting as a purse-string. In addition, constriction of the ring along its width generates a retrograde flow of actin and myosin within the YSL (black arrows), which, when resisted by friction with adjacent structures, generates a pulling force on the margin of the EVL, promoting EVL epiboly movements. Besides actomyosin, microtubules also flow toward the EVL margin. TJs, connecting the EVL margin to the actomyosin ring within the YSL, potentially ensure proper force transmission between the ring and the EVL.

homolog of vertebrate RhoA, controlling both actomyosin assembly and AJ formation (Jacinto et al., 2002b; Magie et al., 2002; Strutt et al., 1997). Also, the downstream effector ROCK has been shown to be involved in proper cable assembly at the leading edge (Mizuno et al., 2002).

The cable has been suggested to function in dorsal closure by both acting as a purse-string pulling the epidermal leading edges together (Hutson et al., 2003; Jacinto et al., 2002b; Kiehart et al., 2000; Mizuno et al., 2002; Rodriguez-Diaz et al., 2008; Young et al., 1993) and keeping the leading-edge cells in a taut row to ensure proper zippering and sealing of the epithelial segments upon closure (Jacinto et al., 2002a). Initial laser ablation studies identified the multicellular purse-string within the leading-edge cells and the dynamic AS cells as the main motor driving dorsal closure (Hutson et al., 2003; Kiehart et al., 2000). Interestingly, a recent study revealed that the actomyosin cable in combination with AS cells, undergoing cell volume decrease, can trigger a force imbalance that is required to initiate and propagate the closure process (Saias et al., 2015).

Although several studies utilizing laser ablations and mathematical modeling have provided evidence for the contractile property and purse-string-like behavior of the actomyosin cable during dorsal closure (Hutson et al., 2003; Kiehart et al., 2000), viewing the cable as a simple purse-string is incompatible with observations of local cable impairment having only spatially restricted effects on dorsal closure (Kiehart et al., 2000). Moreover, the actomyosin cable does not form one continuous purse-string but is rather composed of several contractile building blocks coupled by intercellular junctions (Kaltschmidt et al., 2002; Kiehart et al., 2000). The leading-edge cells are also mechanically connected to the adjacent AS cells via integrins and AJs (Kaltschmidt et al., 2002; Narasimha and Brown, 2004), which are required for proper force transmission between the epidermal edge and AS cells. Together, this suggests that the actomyosin cable in dorsal closure constitutes a contractile actomyosin cable-like structure that is mechanically integrated in the surrounding structures, thereby ensuring dorsal closure progression even in case of local cable rupture.

Zebrafish Epiboly

Epiboly in zebrafish, the spreading of the blastoderm over the spherical yolk cell during gastrulation, is dependent on the contraction of a submembranous actomyosin ring within the yolk syncytial layer (YSL), a thin multinucleated cytoplasmic layer on the surface of the yolk (Lepage and Bruce, 2010). This actomyosin ring within the YSL has further been proposed to function in epiboly by pulling on the margin of the enveloping layer (EVL), a simple squamous epithelial cell layer on the blastoderm surface, thereby pulling the EVL over the yolk cell and consequently facilitating deep cell epiboly movements (Figure 5).

Actomyosin ring formation within the YSL first becomes apparent before the onset of gastrulation by the accumulation of actin and myosin within the YSL adjacent to the EVL margin. The width of this originally broad actomyosin band decreases during epiboly, giving rise to a ring-like structure once the EVL covers around 70%–80% of the yolk cell (Behrndt et al., 2012). The formation and maturation of the YSL actomyosin ring depends critically on the activity of the actin nucleator diaphanous-related formin 2 (zDia2) and the RacGAP α2-chimerin (chn1), which controls the activity of Rac, an upstream regulator of the actin nucleator Arp2/3 (Lai et al., 2008; Leskow et al., 2006). However, how these factors are localized and/or activated during YSL actomyosin ring initiation and formation is still unclear.

Several mechanisms by which the YSL actomyosin ring pulls on the margin of the EVL to drive EVL epiboly movements have been proposed. Originally it was suggested that the actomyosin ring functions as a purse-string by constricting around its circumference, which, once the ring has crossed the equator of the yolk cell, would result in a pulling force exerted on the EVL margin to which the actomyosin ring is coupled (Cheng et al., 2004; Köppen et al., 2006). The existence of such cable-constriction motor activity of the YSL actomyosin ring has further been supported by laser-cutting experiments showing that the ring displays considerable circumferential tension, consistent with the notion of circumferential contraction (Behrndt et al., 2012). Interestingly, laser-cutting experiments also revealed significant tension along the width of the YSL actomyosin ring, suggesting that the ring also contracts along its width. Moreover, this contraction was found to generate a retrograde flow of actin and myosin from more vegetal portions of the YSL toward the EVL margin where the actomyosin ring is located. Based on the velocity profile of this actomyosin flow and theoretical considerations, it has further been proposed that the flow is resisted by friction with adjacent structures within the YSL, such as the yolk membrane or the yolk cytoplasm, and that such friction-resisted flow will give rise to a force pulling on the EVL margin. To test whether this flow-friction motor activity of the YSL actomyosin ring would also contribute to spreading of the EVL, Behrndt et al. (2012) generated cylindrically shaped embryos in which the cable-constriction motor activity was rendered inactive due to the absence of a spherical substrate on which the actomyosin ring can constrict. Surprisingly in these cylindrical embryos, EVL spreading remained unaffected, suggesting that

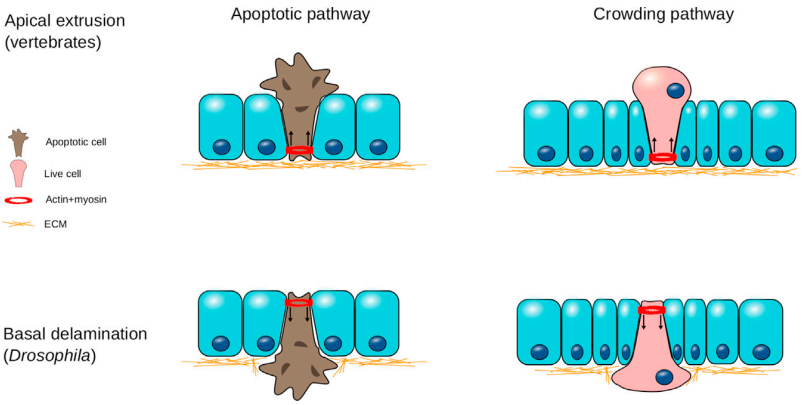

Figure 6. Epithelial Cell Extrusion
Cells can extrude either apically (upper panels) or basally (lower panels) depending on the subcellular localization of the contractile actomyosin ring (arrows delineate the direction of cell extrusion). Rho-mediated actin cable constriction can be triggered in response to cell damage (left panels, brown cells) or cellular crowding (right panels, pink cells).

the flow-friction motor activity of the actomyosin ring is sufficient to drive EVL epiboly movements.

The actomyosin network has to be mechanically linked to the EVL margin for the YSL actomyosin ring to transmit forces to EVL cells. In contrast to epithelial cells, where the mechanical coupling of the actomyosin cytoskeleton across cells is mainly mediated by E-cadherin-based AJs (Gates and Peifer, 2005; Halbleib and Nelson, 2006; Lecuit and Yap, 2015), force transmission between the YSL and EVL appears to be mediated via TJs, connecting the EVL margin to the adjacent YSL actomyosin ring (Köppen et al., 2006) (Figure 5). Although experiments showing that interfering with the actomyosin ring within the YSL affects EVL advancement (Behrndt et al., 2012) and EVL cell-shape changes (Köppen et al., 2006) support the notion of force transmission between YSL and EVL, the precise mechanisms by which TJs transmit these forces are not yet fully understood.

Cell Extrusion

Actomyosin ring constriction also plays an important role for cell extrusion within epithelial cell layers. Epithelial cell layers need to maintain their barrier function despite individual cells joining or leaving the epithelium. Cell extrusion is a unique process by which epithelia actively expulse individual cells without compromising their barrier function. A key feature of this process is the assembly of a contractile actomyosin ring-like structure surrounding the extruding cell (Rosenblatt et al., 2001). Constriction of this actomyosin ring-like structure has been shown to drive the extrusion of dying cells in response to apoptotic stimuli (Rosenblatt et al., 2001; Toyama et al., 2008), transformed cells (oncogene-expressing cells) (Hogan et al., 2009; Kajita et al., 2010; Leung and Brugge, 2012), and cells within crowded epithelial cell layers (Eisenhoffer et al., 2012; Marinari et al., 2012) (Figure 6).

For cell extrusion to occur, a multicellular actomyosin ring forms within the surrounding cells, which by constricting squeezes the cell out of the epithelial sheet and closes any possible gap that could have occurred during the extrusion process (Rosenblatt et al., 2001). Interestingly, extruding cells have also been found to constrict by themselves at their contact with the neighboring cells, thereby facilitating the extrusion process (Kuipers et al., 2014; Slattum and Rosenblatt, 2014).

The process of cell extrusion seems to be an evolutionarily highly conserved phenomenon playing a fundamental role in epithelial morphogenesis and homeostasis (Eisenhoffer et al., 2012; Kiehart et al., 2000; Madara, 1990; Marinari et al., 2012; Rosenblatt et al., 2001). In general, cells can be extruded either apically into the surrounding lumen or basally into the underlying tissue and/or extracellular matrix (Figure 6). In *Drosophila*, for instance, cells extrude predominantly basally, in a process known as cell delamination (Marinari et al., 2012; Meghana et al., 2011; Muliyil et al., 2011), whereas in vertebrates, epithelial cells are predominantly extruded apically. The direction in which cells are extruded can have major consequences for their fate. Apically extruded cells preferentially die by anoikis (Frisch and Francis, 1994) while cells extruding basally often survive and, in some instances, invade the matrix, proliferate, and even form tumors (Hogan et al., 2009).

For cells to be extruded, they are thought to produce and secrete the bioactive lipid sphingosine-1-phosphate (S1P), which triggers via the activation of $Ga_{12/13}$-coupled receptors actomyosin ring formation and contraction in surrounding cells (Eisenhoffer et al., 2012; Gu et al., 2011; Rosenblatt et al., 2001). This process involves activation of RhoA and its downstream effector ROCK in these cells, eventually leading to activation of myosin and ring contraction (Marshall et al., 2011; Slattum et al., 2009; Tamada et al., 2007).

During apical extrusion of epithelial cells, the actomyosin ring within the surrounding cells becomes thicker and constricts, thereby descending basally, and once it reaches the bottom of the monolayer it closes below the extruding cell (Figure 6). In addition, lamellipodial protrusions originating from surrounding cells and extending beneath the extruding cell are thought to help in apical extrusion (Tamada et al., 2007). During basal cell extrusion, the actomyosin ring forms at the level of the AJs at the cell apex and by constriction pushes the cell basally out of the epithelium (Figure 6). For constricting, the ring is thought to utilize a filament sliding mechanism similar to the situation in sarcomeres or cytokinetic rings (Mitchison and Cramer, 1996; Rosenblatt et al., 2001). Interestingly, when microtubule dynamics and/or S1P signaling are impaired, cells generally are extruded basally, suggesting that basal extrusion constitutes the default pathway, whereas apical extrusion requires additional signals and/or cytoskeletal elements.

Recently, extrusion of live cells has been shown to occur in response to cellular crowding in epithelia and to require the activation of mechanosensitive ion channels by S1P-mediated actomyosin contraction in surrounding cells (Eisenhoffer et al., 2012; Katoh and Fujita, 2012; Marinari et al., 2012). In contrast to the

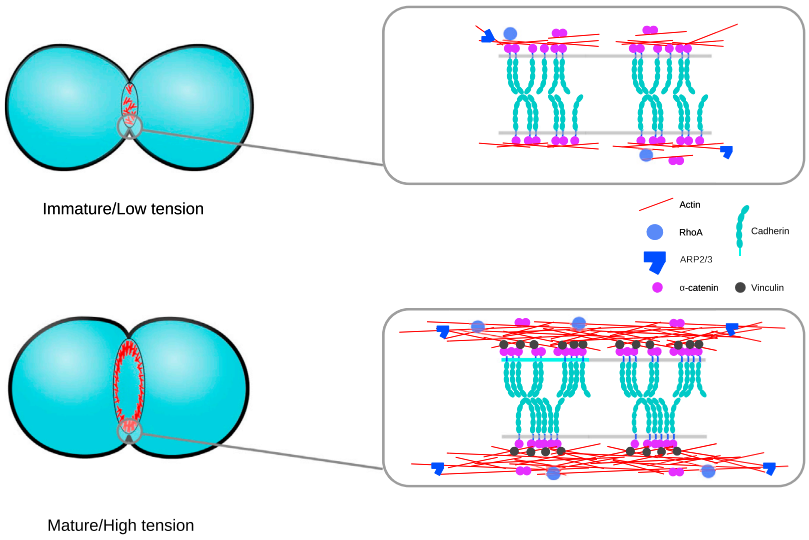

Figure 7. Cell-Cell Adhesion
Upon cell-cell contact initiation, apposing cell membranes form small *cis* clusters of cadherin molecules bound to actin, which then engage in *trans* interactions. In immature contacts with low cortical tension (upper panels) this organization persists and RhoA and actin activity only moderately increases. When cortical tension increases during contact maturation (lower panels), α-catenin unfolds and additional proteins, such as vinculin and Mena/VASP, are recruited to the adhesion clusters. Moreover, ARP2/3-mediated branched actin polymerization at the contact edge and concomitant depletion from the contact center lead to the characteristic actin ring-like appearance at the contact.

extrusion of live and apoptotic cells, extrusion of transformed cells does not necessarily involve the formation of an actomyosin ring in the surrounding cells but rather depends on the elongation of the extruding cell, which appears to be driven by pronounced reorganization of F-actin within the extruding cell and E-cadherin-mediated cell-cell adhesion to the surrounding cells (Hogan et al., 2009; Leung and Brugge, 2012).

Cell-Cell Adhesion

While the formation of actomyosin rings is typically associated with ring constriction and resultant changes in cell and tissue shape, actin rings can also be found during cell-cell contact formation, where their appearance plays an important role in stabilizing the forming contact.

In doublets of adhering cells, actin frequently localizes in a ring-like fashion at the edge of the cell-cell contact zone (Figure 7). This actin ring colocalizes with cadherin cell-cell adhesion molecules, which mechanically link the adhering cells at the contact. Importantly, actin rings are forming on both sides of the contact, giving rise to a double ring-like structure that is held together at the contact by cadherins. Such double actin ring-like structures have been observed at homotypic contacts of both murine cells (Engl et al., 2014) and zebrafish germ-layer progenitors (Maitre et al., 2012).

In epithelial tissues, the geometry of actin accumulation at the cell-cell contact zone changes, with actin preferentially accumulating at the apical side of contacting cells where the AJs are located (Kovacs et al., 2011; Tepass and Hartenstein, 1994). This junctional actin accumulation in epithelial cells leads to the formation of an actin ring-like structure at the cell apex, which by contracting can trigger apical cell constriction, leading, for instance, to tissue invagination. Similar to the situation in adhering cell doublets, the actin ring-like accumulations in neighboring epithelial cells are mechanically coupled to each other at the AJs.

A key feature of actin rings at cell-cell contacts is their colocalization with classical cadherin adhesion molecules. Cadherins are calcium-dependent transmembrane glycoproteins, which can engage in homotypic *trans* interactions across the contact, and *cis* interactions, modulating their subcellular distribution within the plasma membrane. The cytoplasmic tail of cadherins is known to stoichiometrically bind to β-catenin, which recruits the actin-binding protein α-catenin, required to anchor the cadherin adhesion complex to the actomyosin cortex of adhering cells (Drees et al., 2005). Various other regulatory proteins, including scaffolding proteins, signaling molecules, and cytoskeletal regulators (Niessen et al., 2011; Zaidel-Bar, 2013), can be recruited to the adhesion complex, allowing it to dynamically regulate the cytoskeleton during cell-cell contact formation and maturation.

Cadherin adhesion complexes can spontaneously cluster via *cis* interactions, even in the absence of cell-cell contact formation (Hong et al., 2013; Truong Quang et al., 2013; Wu et al., 2015). Cluster formation is promoted by cell-cell contact formation (Figure 7), and clusters are typically associated with highly stable, latrunculin-resistant actin pools (Cavey et al., 2008). During nascent contact formation, cadherin clusters are rearranged in an actin-dependent manner (Hong et al., 2013) into ring-like structures with actin bundles connecting adjacent cadherin clusters. Interestingly, in contrast to the actin pool colocalizing with the cadherin clusters, the connecting actin bundles are highly unstable (Nowotarski and Peifer, 2014).

Cell-cell contact initiation occurs when cadherins from apposing membranes engage in *trans* interactions (Figure 7). These interactions are quickly strengthened by *cis* and *trans* binding of additional cadherins, forming small clusters, which require actin for further stabilization (Harrison et al., 2011; Hong et al., 2010, 2011). Contact expansion is triggered by activation of the small GTPase Rac1 (Perez et al., 2008), which enhances membrane dynamics and stabilizes growing cadherin clusters by recruiting actin (Delva and Kowalczyk, 2009). Rac1 activation predominantly occurs at the contact edge (Yamada and Nelson, 2007), leaving the center of the expanding contact more quiescent. Actin is also nucleated at the nascent adhesion sites by actin nucleators, such as formins and Arp2/3, leading to rapid filament growth and branching, and promoting membrane protrusive activity (Carramusa et al., 2007; Verma et al., 2012).

Following Rac activation, RhoGAPs are activated by maturing cadherin clusters in the center of the growing contact,

inactivating Rac and diminishing actin dynamics there (Kitt and Nelson, 2011). This inactivation of Rac at the contact center is accompanied by cadherin clusters moving from the center toward the contact edge, where they form a stable ring-like distribution of equidistant nanoscopic clusters. A corresponding process is also known in epithelial tissues, where E-cadherin clusters move apically in response to actin reorganization (Kametani and Takeichi, 2007). Interestingly, the diameter of the actin-cadherin ring structure at the cell-cell contact depends critically on the activity of myosin (Engl et al., 2014). Myosin is thought to function in this process by triggering the recruitment of E-cadherin to the clusters at the contact edge via modulation of actin turnover and promoting E-cadherin cluster stability. Considering that actomyosin cortical tension between contacting cells would be highest at the contact edge where the cortices of the two contacting cells are linked together by cadherins, this would also explain why actin and cadherin accumulate there. Activation of RhoA at the contact edge by components associated with the adhesion complex, such as the RhoGEF Ect2 and ROCK, has been implicated in the maintenance of myosin-mediated tension at the contact edge and, thus, stabilization of the actin-cadherin ring (Priya et al., 2013, 2015; Ratheesh et al., 2012) (Figure 7). Furthermore, recruitment of the actin-binding protein vinculin to the adhesion cluster has been shown to contribute to actin-cadherin ring stabilization. Vinculin is recruited to the cadherin adhesion complex in a mechanosensitive manner by binding to α-catenin, which again changes its conformation upon stress, thereby revealing its vinculin-binding sites. This mechanosensitive stabilization of the actin-cadherin ring via recruitment of vinculin has been proposed to allow adherent cells to strengthen their cell-cell contacts upon mechanical stress, thereby ensuring tissue integrity in challenging mechanical conditions (Huveneers et al., 2012; Leerberg et al., 2014; Thomas et al., 2013). How vinculin stabilizes the actin-cadherin ring is not yet entirely clear, but vinculin promoting Mena/VASP-dependent actin assembly (Leerberg et al., 2014) and/or suppressing actin turnover and junctional remodeling (Chen et al., 2015; Hong et al., 2010; Lambert et al., 2007) have been proposed as potential effector processes.

Actin within the actin-cadherin ring at the contact edge is thought to be predominantly organized in non-branched bundles oriented parallel to the cell membrane (Buckley et al., 2014). This organization appears to be dependent on the activity of α-catenin, which has been shown to bind not only to actin but also to other actin-associated factors, such as actinin, Ajuba, paxillin, EPLIN, and ZO-1 (Abe and Takeichi, 2008; Itoh et al., 1997; Maiden, and Hardin, 2011; Nola et al., 2011). Dimeric cytoplasmic α-catenin can actively bundle actin (Rimm et al., 1995) and, at the same time, inhibit actin branching and severing by competing with the Arp2/3 complex and cofilin, respectively (Hansen et al., 2013). α-Catenin has been suggested to preferentially perform this function close to cadherin clusters where the local concentration of α-catenin is sufficiently high to dissociate from the adhesion complex and form dimers (Benjamin et al., 2010) (Figure 7). However, also when bound to E-cadherin, α-catenin can directly bind to pre-stressed actin filaments, thereby promoting actin bundling and adhesion complex clustering. Besides α-catenin, other actin modulators, such as the actin nucleator Arp2/3 and actin scaffolding protein anillin (Reyes et al., 2014), are thought to influence actin organization at the ring by promoting actin bundling and cell-cell junction integrity, respectively.

Conclusions

Based on their specific functions, actin rings can be grouped into two main classes: (1) constricting actomyosin rings that cleave cells, such as in cytokinesis, or close openings, such as in wound healing and cell extrusion; and (2) stabilizing actin rings that function as cytoskeletal scaffolds maintaining already established cytoskeletal anisotropies, such as in cell-cell adhesion. For these different types of actin rings to exert their specific functions, precise positioning of the actin filaments within the ring is fundamental. In constricting rings, actin filaments can either be highly aligned, such as in certain types of cytokinetic rings (Schroeder, 1968, 1972, 1973), or form a rather isotropic network, such as the actomyosin ring within the zebrafish yolk cell driving EVL epiboly movements (Behrndt et al., 2012). Interestingly, in both such cases ring formation is associated with cortical flow of actin filaments toward the place of ring assembly (Behrndt et al., 2012; Bray and White, 1988). This suggests that cortical flows can have very different effects on actin ring organization depending on the specific cellular context. Much like the situation in constricting actomyosin rings, stabilizing actin rings in, for example, cell-cell adhesion can display rather different actin network organization: while in mature epithelial cell-cell junctions a continuous E-cadherin band around the apical circumference is closely associated with a circumferential ring-like belt containing both actin and myosin (Martin, 2010; Yonemura et al., 1995), contacts between mesenchymal cells have been associated with actin rings devoid of myosin (Maitre et al., 2012). This difference in ring organization at different cell-cell contacts likely is due to different functions of the rings in epithelial versus mesenchymal cell-cell contact formation. Yet the basic principles underlying the relationship between actin ring organization and function have only begun to be unraveled, due to technical limitations of visualizing the actin network organization within rings (e.g., by electron or super-resolution fluorescence microscopy). In a recent study, the role of actin network organization and connectivity for actomyosin ring contraction was analyzed (Ennomani et al., 2016). As expected, it was found that in the absence of actin cross-linkers, ordered anti-parallel (sarcomere-like) bundles showed a higher level of contractility than disordered actin networks or actin bundles with mixed polarity. However, when actin cross-linkers, such as α-actinin, were added, disordered bundles became considerably more contractile, while the contractility of anti-parallel bundles and disordered networks was reduced (Ennomani et al., 2016). Consistent with this, in cytokinetic rings the amount of α-actinin is important for determining the kinetics of ring constriction (Mukhina et al., 2007). Collectively, these observations suggest that the network architecture of actomyosin rings alone does not allow conclusions to be drawn on the contractility of the rings, and that the presence/absence of specific actin cross-linkers plays a decisive role therein.

Intriguingly, the cytokinetic ring of dividing yeast cells can be transformed into a ring sliding on the curved surface of the yeast cell, rather than constricting it, when the ring-anchoring protein anillin is depleted (Mishra et al., 2012). This sliding activity closely resembles the behavior of the actomyosin ring pulling

the EVL over the yolk cell during zebrafish epiboly, pointing at the intriguing possibility that the actomyosin ring within the zebrafish yolk cell might actually be derived from a cytokinetic ring by changes in the expression of certain ring-anchoring and/or actin cross-linking proteins. More generally, considering that cytokinetic rings existed before the emergence of multicellularity, it is conceivable that the cytokinetic rings represent an ancient prototype of actin rings that has subsequently been adapted for different functions. Supporting this notion are reports demonstrating striking similarities between the molecular compositions of cytokinetic rings and apical actomyosin rings associated with AJs in epithelial cells (Ratheesh et al., 2012). Alternatively, different actin rings might have independently emerged multiple times in evolution by modifying the existent actin network for specific functions requiring a ring-like organization.

The different types of actin rings discussed in this review are far from exhausting the subject of ring-like actin structures found across different cell types. For instance, there are other more specialized structures, such as the immunological synapse in immune cells (Dustin, 2009; Huppa and Davis, 2003), the function and stability of which depends on the formation of an actin ring-like structure at the contact. Another surprising actin ring system has been recently described in *Ciona intestinalis*, where the elongation of notochord cells is triggered by an actomyosin ring squeezing these cells around their circumference, similar to the cytokinetic furrow during cell division (Sehring et al., 2014). There have been many more actin ring-like structures described in a variety of other species and organs, including fish retina (Lin-Jones et al., 2009; O'Connor and Burnside, 1981), amphibian nerves (Holtfreter, 1946), plant roots (Volkmann and Baluska, 1999), and fruit-fly ovaries (He et al., 2010), the specific function of which is often not entirely clear.

Various important questions remain as to the formation and function of actin ring-like structures. What distinguishes squeezing from gliding actomyosin rings, and are there specific ring architectures and/or compositions favoring either of these activities? One possibility is that rings composed of highly aligned actin filaments, such as some types of cytokinetic rings, would squeeze a cell when constricting, while a more isotropic meshwork-like actin organization would lead to ring gliding rather than squeezing. Also, it remains unclear to what extent ring assembly is driven by tension gradients within the actomyosin network and/or extracellular signals controlling actin network formation and contraction. Cortical flows were shown to contribute to actin ring formation in some cases (Salbreux et al., 2009), but de novo assembly of actin ring elements has also been reported (Wu et al., 2006; Yumura, 2001). Interestingly, ring-like actomyosin structures seem to have the capacity for self-assembly in permissive conditions (Miyazaki et al., 2015). This points to the intriguing possibility that actin rings might represent a generic form of actin organization in certain cellular geometries, which has been adapted by different cell types for their specific functions.

REFERENCES

Abe, K., and Takeichi, M. (2008). EPLIN mediates linkage of the cadherin catenin complex to F-actin and stabilizes the circumferential actin belt. Proc. Natl. Acad. Sci. USA *105*, 13–19.

Abreu-Blanco, M.T., Verboon, J.M., and Parkhurst, S.M. (2011). Cell wound repair in *Drosophila* occurs through three distinct phases of membrane and cytoskeletal remodeling. J. Cell Biol. *193*, 455–464.

Abreu-Blanco, M.T., Verboon, J.M., and Parkhurst, S.M. (2014). Coordination of Rho family GTPase activities to orchestrate cytoskeleton responses during cell wound repair. Curr. Biol. *24*, 144–155.

Amano, M., Ito, M., Kimura, K., Fukata, Y., Chihara, K., Nakano, T., Matsuura, Y., and Kaibuchi, K. (1996). Phosphorylation and activation of myosin by rho-associated kinase (Rho-kinase). J. Biol. Chem. *271*, 20246–20249.

Antunes, M., Pereira, T., Cordeiro, J.V., Almeida, L., and Jacinto, A. (2013). Coordinated waves of actomyosin flow and apical cell constriction immediately after wounding. J. Cell Biol. *202*, 365–379.

Behrndt, M., Salbreux, G., Campinho, P., Hauschild, R., Oswald, F., Roensch, J., Grill, S.W., and Heisenberg, C.-P. (2012). Forces driving epithelial spreading in zebrafish gastrulation. Science *338*, 257–260.

Bement, W.M., and von Dassow, G. (2014). Single cell pattern formation and transient cytoskeletal arrays. Curr. Opin. Cell Biol. *26*, 51–59.

Bement, W.M., Forscher, P., and Mooseker, M.S. (1993). A novel cytoskeletal structure involved in purse string wound closure and cell polarity maintenance. J. Cell Biol. *121*, 565–578.

Benink, H.A., and Bement, W.M. (2005). Concentric zones of active RhoA and Cdc42 around single cell wounds. J. Cell Biol. *168*, 429–439.

Benjamin, J.M., Kwiatkowski, A.V., Yang, C., Korobova, F., Pokutta, S., Svitkina, T., Weis, W.I., and Nelson, W.J. (2010). αE-catenin regulates actin dynamics independently of cadherin-mediated cell-cell adhesion. J. Cell Biol. *189*, 339–352.

Bertin, A., McMurray, M.A., Thai, L., Garcia, G., 3rd, Votin, V., Grob, P., Allyn, T., Thorner, J., and Nogales, E. (2010). Phosphatidylinositol-4,5-bisphosphate promotes budding yeast septin filament assembly and organization. J. Mol. Biol. *404*, 711–731.

Blanchoin, L., Boujemaa-Paterski, R., Sykes, C., and Plastino, J. (2014). Actin dynamics, architecture, and mechanics in cell motility. Physiol. Rev. *94*, 235–263.

Bray, D., and White, J.G. (1988). Cortical flow in animal cells. Science *239*, 883–888.

Brock, J., Midwinter, K., Lewis, J., and Martin, P. (1996). Healing of incisional wounds in the embryonic chick wing bud: characterization of the actin purse-string and demonstration of a requirement for Rho activation. J. Cell Biol. *135*, 1097–1107.

Buckley, C.D., Tan, J., Anderson, K.L., Hanein, D., Volkmann, N., Weis, W.I., Nelson, W.J., and Dunn, A.R. (2014). Cell adhesion. The minimal cadherin-catenin complex binds to actin filaments under force. Science *346*, 1254211.

Bugyi, B., and Carlier, M.F. (2010). Control of actin filament treadmilling in cell motility. Annu. Rev. Biophys. *39*, 449–470.

Burkel, B.M., Benink, H.A., Vaughan, E.M., von Dassow, G., and Bement, W.M. (2012). A rho GTPase signal treadmill backs a contractile array. Dev. Cell *23*, 384–396.

Burnside, B. (1971). Microtubules and microfilaments in newt neurulation. Dev. Biol. *26*, 416–441.

Carramusa, L., Ballestrem, C., Zilberman, Y., and Bershadsky, A.D. (2007). Mammalian diaphanous-related formin Dia1 controls the organization of E-cadherin-mediated cell-cell junctions. J. Cell Sci. *120*, 3870–3882.

Carvalho, A., Desai, A., and Oegema, K. (2009). Structural memory in the contractile ring makes the duration of cytokinesis independent of cell size. Cell *137*, 926–937.

Cavey, M., Rauzi, M., Lenne, P.-F., and Lecuit, T. (2008). A two-tiered mechanism for stabilization and immobilization of E-cadherin. Nature *453*, 751–756.

Cheng, J.C., Miller, A.L., and Webb, S.E. (2004). Organization and function of microfilaments during late epiboly in zebrafish embryos. Dev. Dyn. *231*, 313–323.

Chen, C.S., Hong, S., Indra, I., Sergeeva, A.P., Troyanovsky, R.B., Shapiro, L., Honig, B., and Troyanovsky, S.M. (2015). α-Catenin-mediated cadherin clustering couples cadherin and actin dynamics. J. Cell Biol. *210*, 647–661.

Clark, A.G., Miller, A.L., Vaughan, E., Yu, H.Y., Penkert, R., and Bement, W.M. (2009). Integration of single and multicellular wound responses. Curr. Biol. *19*, 1389–1395.

Conti, M.A., and Adelstein, R.S. (2008). Nonmuscle myosin II moves in new directions. J. Cell Sci. *121*, 11–18.

Cordeiro, J.V., and Jacinto, A. (2013). The role of transcription-independent damage signals in the initiation of epithelial wound healing. Nat. Rev. Mol. Cell Biol. *14*, 249–262.

Danjo, Y., and Gipson, I.K. (1998). Actin "purse string" filaments are anchored by E-cadherin-mediated adherens junctions at the leading edge of the epithelial wound, providing coordinated cell movement. J. Cell Sci. *111*, 3323–3332.

Delva, E., and Kowalczyk, A.P. (2009). Regulation of cadherin trafficking. Traffic *10*, 259–267.

Démoulin, D., Carlier, M.F., Bibette, J., and Baudry, J. (2014). Power transduction of actin filaments ratcheting in vitro against a load. Proc. Natl. Acad. Sci. USA *111*, 17845–17850.

Drees, F., Pokutta, S., Yamada, S., Nelson, W.J., and Weis, W.I. (2005). α-Catenin is a molecular switch that binds E-cadherin-β-catenin and regulates actin-filament assembly. Cell *123*, 903–915.

Dulyaninova, N.G., Malashkevich, V.N., Almo, S.C., and Bresnick, A.R. (2005). Regulation of myosin-IIA assembly and Mts1 binding by heavy chain phosphorylation. Biochemistry *44*, 6867–6876.

Dustin, M.L. (2009). Modular design of immunological synapses and kinapses. Cold Spring Harb. Perspect. Biol. *1*, a002873.

Egelhoff, T.T., Lee, R.J., and Spudich, J.A. (1993). Dictyostelium myosin heavy chain phosphorylation sites regulate myosin filament assembly and localization in vivo. Cell *75*, 363–371.

Eisenhoffer, G.T., Loftus, P.D., Yoshigi, M., Otsuna, H., Chien, C.-B., Morcos, P.A., and Rosenblatt, J. (2012). Crowding induces live cell extrusion to maintain homeostatic cell numbers in epithelia. Nature *484*, 546–549.

Engl, W., Arasi, B., Yap, L.L., Thiery, J.P., and Viasnoff, V. (2014). Actin dynamics modulate mechanosensitive immobilization of E-cadherin at adherens junctions. Nat. Cell Biol. *16*, 587–594.

Ennomani, H., Letort, G., Guérin, C., Martiel, J.L., Cao, W., Nédélec, F., De La Cruz, E.M., Théry, M., and Blanchoin, L. (2016). Architecture and connectivity govern actin network contractility. Curr. Biol. *26*, 616–626.

Feng, J., Ito, M., Ichikawa, K., Isaka, N., Nishikawa, M., Hartshorne, D.J., and Nakano, T. (1999). Inhibitory phosphorylation site for Rho-associated kinase on smooth muscle myosin phosphatase. J. Biol. Chem. *274*, 37385–37390.

Field, C.M., and Alberts, B.M. (1995). Anillin, a contractile ring protein that cycles from the nucleus to the cell cortex. J. Cell Biol. *131*, 165–178.

Firat-Karalar, E.N., and Welch, M.D. (2011). New mechanisms and functions of actin nucleation. Curr. Opin. Cell Biol. *23*, 4–13.

Fishkind, D.J., and Wang, Y.L. (1993). Orientation and three-dimensional organization of actin filaments in dividing cultured cells. J. Cell Biol. *123*, 837–848.

Franke, J.D., Montague, R.A., and Kiehart, D.P. (2005). Nonmuscle myosin II generates forces that transmit tension and drive contraction in multiple tissues during dorsal closure. Curr. Biol. *15*, 2208–2221.

Frisch, S.M., and Francis, H. (1994). Disruption of epithelial cell-matrix interactions induces apoptosis. J. Cell Biol. *124*, 619–626.

Gates, J., and Peifer, M. (2005). Can 1000 reviews be wrong? Actin, α-catenin, and adherens junctions. Cell *123*, 769–772.

Goldbach, P., Wong, R., Beise, N., Sarpal, R., Trimble, W.S., and Brill, J.A. (2010). Stabilization of the actomyosin ring enables spermatocyte cytokinesis in *Drosophila*. Mol. Biol. Cell *21*, 1482–1493.

Gu, Y., Forostyan, T., Sabbadini, R., and Rosenblatt, J. (2011). Epithelial cell extrusion requires the sphingosine-1-phosphate receptor 2 pathway. J. Cell Biol. *193*, 667–676.

Guillot, C., and Lecuit, T. (2013). Adhesion disengagement uncouples intrinsic and extrinsic forces to drive cytokinesis in epithelial tissues. Dev. Cell *24*, 227–241.

Halbleib, J.M., and Nelson, W.J. (2006). Cadherins in development: cell adhesion, sorting, and tissue morphogenesis. Genes Dev. *20*, 3199–3214.

Hansen, S.D., Kwiatkowski, A.V., Ouyang, C.Y., Liu, H., Pokutta, S., Watkins, S.C., Volkmann, N., Hanein, D., Weis, W.I., Mullins, R.D., et al. (2013). E-catenin actin-binding domain alters actin filament conformation and regulates binding of nucleation and disassembly factors. Mol. Biol. Cell *24*, 3710–3720.

Harrison, O.J., Jin, X., Hong, S., Bahna, F., Ahlsen, G., Brasch, J., Wu, Y., Vendome, J., Felsovalyi, K., Hampton, C.M., et al. (2011). The extracellular architecture of adherens junctions revealed by crystal structures of type I cadherins. Structure *19*, 244–256.

He, L., Wang, X., Tang, H.L., and Montell, D.J. (2010). Tissue elongation requires oscillating contractions of a basal actomyosin network. Nat. Cell Biol. *12*, 1133–1142.

Hickson, G.R., and O'Farrell, P.H. (2008). Rho-dependent control of anillin behavior during cytokinesis. J. Cell Biol. *180*, 285–294.

Hogan, C., Dupré-Crochet, S., Norman, M., Kajita, M., Zimmermann, C., Pelling, A.E., Piddini, E., Baena-López, L.A., Vincent, J.P., Itoh, Y., et al. (2009). Characterization of the interface between normal and transformed epithelial cells. Nat. Cell Biol. *11*, 460–467.

Holtfreter, J. (1946). Structure, motility and locomotion in isolated embryonic amphibian cells. J. Morphol. *79*, 27–62.

Hong, S., Troyanovsky, R.B., and Troyanovsky, S.M. (2010). Spontaneous assembly and active disassembly balance adherens junction homeostasis. Proc. Natl. Acad. Sci. USA *107*, 3528–3533.

Hong, S., Troyanovsky, R.B., and Troyanovsky, S.M. (2011). Cadherin exits the junction by switching its adhesive bond. J. Cell Biol. *192*, 1073–1083.

Hong, S., Troyanovsky, R.B., and Troyanovsky, S.M. (2013). Binding to F-actin guides cadherin cluster assembly, stability, and movement. J. Cell Biol. *201*, 131–143.

Huppa, J.B., and Davis, M.M. (2003). T-cell-antigen recognition and the immunological synapse. Nat. Rev. Immunol. *3*, 973–983.

Hutson, M.S., Tokutake, Y., Chang, M.S., Bloor, J.W., Venakides, S., Kiehart, D.P., and Edwards, G.S. (2003). Forces for morphogenesis investigated with laser microsurgery and quantitative modeling. Science *300*, 145–149.

Huveneers, S., Oldenburg, J., Spanjaard, E., van der Krogt, G., Grigoriev, I., Akhmanova, A., Rehmann, H., and de Rooij, J. (2012). Vinculin associates with endothelial VE-cadherin junctions to control force-dependent remodeling. J. Cell Biol. *196*, 641–652.

Itoh, M., Nagafuchi, A., Moroi, S., and Tsukita, S. (1997). Involvement of ZO-1 in cadherin-based cell adhesion through its direct binding to alpha catenin and actin filaments. J. Cell Biol. *138*, 181–192.

Jacinto, A., Wood, W., Balayo, T., Turmaine, M., Martinez-Arias, A., and Martin, P. (2000). Dynamic actin-based epithelial adhesion and cell matching during *Drosophila* dorsal closure. Curr. Biol. *10*, 1420–1426.

Jacinto, A., Martinez-Arias, A., and Martin, P. (2001). Mechanisms of epithelial fusion and repair. Nat. Cell Biol. *3*, E117–E123.

Jacinto, A., Wood, W., Woolner, S., Hiley, C., Turner, L., Wilson, C., Martinez-Arias, A., and Martin, P. (2002a). Dynamic analysis of actin cable function during *Drosophila* dorsal closure. Curr. Biol. *12*, 1245–1250.

Jacinto, A., Woolner, S., and Martin, P. (2002b). Dynamic analysis of dorsal closure in *Drosophila*: from genetics to cell biology. Dev. Cell *3*, 9–19.

Jankovics, F., and Brunner, D. (2006). Transiently reorganized microtubules are essential for zippering during dorsal closure in *Drosophila melanogaster*. Dev. Cell *11*, 375–385.

Kajita, M., Hogan, C., Harris, A.R., Dupre-Crochet, S., Itasaki, N., Kawakami, K., Charras, G., Tada, M., and Fujita, Y. (2010). Interaction with surrounding normal epithelial cells influences signalling pathways and behaviour of Src-transformed cells. J. Cell Sci. *123*, 171–180.

Kaltschmidt, J.A., Lawrence, N., Morel, V., Balayo, T., Fernández, B.G., Pelissier, A., Jacinto, A., and Martinez Arias, A. (2002). Planar polarity and actin dynamics in the epidermis of *Drosophila*. Nat. Cell Biol. *4*, 937–944.

Kamasaki, T., Osumi, M., and Mabuchi, I. (2007). Three-dimensional arrangement of F-actin in the contractile ring of fission yeast. J. Cell Biol. *178*, 765–771.

Kametani, Y., and Takeichi, M. (2007). Basal-to-apical cadherin flow at cell junctions. Nat. Cell Biol. *9*, 92–98.

Katoh, H., and Fujita, Y. (2012). Epithelial homeostasis: elimination by live cell extrusion. Curr. Biol. *22*, R453–R455.

Kiehart, D.P., Galbraith, C.G., Edwards, K.A., Rickoll, W.L., and Montague, R.A. (2000). Multiple forces contribute to cell sheet morphogenesis for dorsal closure in *Drosophila*. J. Cell Biol. *149*, 471–490.

Kimura, K., Ito, M., Amano, M., Chihara, K., Fukata, Y., Nakafuku, M., Yamamori, B., Feng, J., Nakano, T., Okawa, K., et al. (1996). Regulation of myosin phosphatase by rho and rho-associated kinase (Rho-Kinase). Science *273*, 245–248.

Kitt, K.N., and Nelson, J.W. (2011). Rapid suppression of activated Rac1 by cadherins and nectins during de novo cell-cell adhesion. PLoS One *6*, e17841.

Köppen, M., Fernández, B.G., Carvalho, L., Jacinto, A., and Heisenberg, C.-P. (2006). Coordinated cell-shape changes control epithelial movement in zebrafish and *Drosophila*. Development *133*, 2671–2681.

Kovacs, E.M., Verma, S., Ali, R.G., Ratheesh, A., Hamilton, N.A., Akhmanova, A., and Yap, A.S. (2011). N-WASP regulates the epithelial junctional actin cytoskeleton through a non-canonical post-nucleation pathway. Nat. Cell Biol. *13*, 934–943.

Kuipers, D., Mehonic, A., Kajita, M., Peter, L., Fujita, Y., Duke, T., Charras, G., and Gale, J.E. (2014). Epithelial repair is a two-stage process driven first by dying cells and then by their neighbours. J. Cell Sci. *127*, 1229–1241.

Küssel-Andermann, P., El-Amraoui, A., Safieddine, S., Nouaille, S., Perfettini, I., Lecuit, M., Cossart, P., Wolfrum, U., and Petit, C. (2000). Vezatin, a novel transmembrane protein, bridges myosin VIIA to the cadherin-catenins complex. EMBO J. *19*, 6020–6029.

Lai, S.-L., Chan, T.-H., Lin, M.-J., Huang, W.-P., Lou, S.-W., and Lee, S.-J. (2008). Diaphanous-related formin 2 and profilin I are required for gastrulation cell movements. PLoS One *3*, e3439.

Lambert, M., Thoumine, O., Brevier, J., Choquet, D., Riveline, D., and Mege, R.M. (2007). Nucleation and growth of cadherin adhesions. Exp. Cell Res. *313*, 4025–4040.

Laplante, C., and Nilson, L.A. (2011). Asymmetric distribution of Echinoid defines the epidermal leading edge during *Drosophila* dorsal closure. J. Cell Biol. *192*, 335–348.

Laplante, C., Berro, J., Karatekin, E., Hernandez-Leyva, A., Lee, R., and Pollard, T.D. (2015). Three myosins contribute uniquely to the assembly and constriction of the fission yeast cytokinetic contractile ring. Curr. Biol. *25*, 1955–1965.

Lecuit, T., and Yap, A.S. (2015). E-cadherin junctions as active mechanical integrators in tissue dynamics. Nat. Cell Biol. *17*, 533–539.

Leerberg, J.M., Gomez, G.A., Verma, S., Moussa, E.J., Wu, S.K., Priya, R., Hoffman, B.D., Grashoff, C., Schwartz, M.A., and Yap, A.S. (2014). Tension-sensitive actin assembly supports contractility at the epithelial zonula adherens. Curr. Biol. *24*, 1689–1699.

Lepage, S.E., and Bruce, A.E. (2010). Zebrafish epiboly: mechanics and mechanisms. Int. J. Dev. Biol. *54*, 1213–1228.

Leskow, F.C., Holloway, B.A., Wang, H., Mullins, M.C., and Kazanietz, M.G. (2006). The zebrafish homologue of mammalian chimerin Rac-GAPs is implicated in epiboly progression during development. Proc. Natl. Acad. Sci. USA *103*, 5373–5378.

Leung, C.T., and Brugge, J.S. (2012). Outgrowth of single oncogene-expressing cells from suppressive epithelial environments. Nature *482*, 410–413.

Lin, H.-P., Chen, H.-M., Wei, S.-Y., Chen, L.-Y., Chang, L.-H., Sun, Y.-J., Huang, S.-Y., and Hsu, J.-C. (2007). Cell adhesion molecule Echinoid associates with unconventional myosin VI/Jaguar motor to regulate cell morphology during dorsal closure in *Drosophila*. Dev. Biol. *311*, 423–433.

Lin-Jones, J., Sohlberg, L., Dosé, A., Breckler, J., Hillman, D.W., and Burnside, B. (2009). Identification and localization of myosin superfamily members in fish retina and retinal pigmented epithelium. J. Comp. Neurol. *513*, 209–223.

Mabuchi, I., Tsukita, S., Tsukita, S., and Sawai, T. (1988). Cleavage furrow isolated from newt eggs: contraction, organization of the actin filaments, and protein components of the furrow. Proc. Natl. Acad. Sci. USA *85*, 5966–5970.

Madara, J.L. (1990). Maintenance of the macromolecular barrier at cell extrusion sites in intestinal epithelium: physiological rearrangement of tight junctions. J. Membr. Biol. *116*, 177–184.

Maddugoda, M.P., Crampton, M.S., Shewan, A.M., and Yap, A.S. (2007). Myosin VI and vinculin cooperate during the morphogenesis of cadherin cell-cell contacts in mammalian epithelial cells. J. Cell Biol. *178*, 529–540.

Magie, C.R., Pinto-Santini, D., and Parkhurst, S.M. (2002). Rho1 interacts with p120ctn and alpha-catenin, and regulates cadherin-based adherens junction components in *Drosophila*. Development *129*, 3771–3782.

Maiden, S.L., and Hardin, J. (2011). The secret life of α-catenin: moonlighting in morphogenesis. J. Cell Biol. *195*, 543–552.

Maitre, J.-L., Berthoumieux, H., Krens, S.F.G., Salbreux, G., Julicher, F., Paluch, E., and Heisenberg, C.-P. (2012). Adhesion functions in cell sorting by mechanically coupling the cortices of adhering cells. Science *338*, 253–256.

Mandato, C.A., and Bement, W.M. (2001). Contraction and polymerization cooperate to assemble and close actomyosin rings around *Xenopus* oocyte wounds. J. Cell Biol. *154*, 785–797.

Mandato, C.A., and Bement, W.M. (2003). Actomyosin transports microtubules and microtubules control actomyosin recruitment during *Xenopus* oocyte wound healing. Curr. Biol. *13*, 1096–1105.

Marinari, E., Mehonic, A., Curran, S., Gale, J., Duke, T., and Baum, B. (2012). Live-cell delamination counterbalances epithelial growth to limit tissue overcrowding. Nature *484*, 542–545.

Marshall, T.W., Lloyd, I.E., Delalande, J.M., Näthke, I., and Rosenblatt, J. (2011). The tumor suppressor adenomatous polyposis coli controls the direction in which a cell extrudes from an epithelium. Mol. Biol. Cell *22*, 3962–3970.

Martin, A.C. (2010). Pulsation and stabilization: contractile forces that underlie morphogenesis. Dev. Biol. *341*, 114–125.

Martin, P., and Lewis, J. (1992). Actin cables and epidermal movement in embryonic wound healing. Nature *360*, 179–183.

Maupin, P., and Pollard, T.D. (1986). Arrangement of actin filaments and myosin-like filaments in the contractile ring and of actin-like filaments in the mitotic spindle of dividing HeLa cells. J. Ultrastruct. Mol. Struct. Res. *94*, 92–103.

Mavrakis, M., Azou-Gros, Y., Tsai, F.C., Alvarado, J., Bertin, A., Iv, F., Kress, A., Brasselet, S., Koenderink, G.H., and Lecuit, T. (2014). Septins promote F-actin ring formation by crosslinking actin filaments into curved bundles. Nat. Cell Biol. *16*, 322–334.

Meghana, C., Ramdas, N., Hameed, F.M., Rao, M., Shivashankar, G.V., and Narasimha, M. (2011). Integrin adhesion drives the emergent polarization of active cytoskeletal stresses to pattern cell delamination. Proc. Natl. Acad. Sci. USA *108*, 9107–9112.

Mendes Pinto, I., Rubinstein, B., Kurchavy, A., Unruh, J.R., and Li, R. (2012). Actin depolymerization drives actomyosin ring contraction during budding yeast cytokinesis. Dev. Cell *22*, 1247–1260.

Mishra, M., Huang, Y., Srivastava, P., Srinivasan, R., Sevugan, M., Shlomovitz, R., Gov, N., Rao, M., and Balasubramanian, M. (2012). Cylindrical cellular geometry ensures fidelity of division site placement in fission yeast. J. Cell Sci. *125*, 3850–3857.

Mitchison, T.J., and Cramer, L.P. (1996). Actin-based cell motility and cell locomotion. Cell *84*, 371–379.

Mitsui, T., Inagaki, M., and Ikebe, M. (1992). Purification and characterization of smooth muscle myosin-associated phosphatase from chicken gizzards. J. Biol. Chem. *267*, 16727–16735.

Miyazaki, M., Chiba, M., Eguchi, H., Ohki, T., and Ishiwata, S. (2015). Cell-sized spherical confinement induces the spontaneous formation of contractile actomyosin rings in vitro. Nat. Cell Biol. *17*, 480–489.

Mizuno, T., Tsutsui, K., and Nishida, Y. (2002). *Drosophila* myosin phosphatase and its role in dorsal closure. Development *129*, 1215–1223.

Mukhina, S., Wang, Y.-L., and Murata-Hori, M. (2007). Alpha-actinin is required for tightly regulated remodeling of the actin cortical network during cytokinesis. Dev. Cell *13*, 554–565.

Muliyil, S., Krishnakumar, P., and Narasimha, M. (2011). Spatial, temporal and molecular hierarchies in the link between death, delamination and dorsal closure. Development *138*, 3043–3054.

Munjal, A., and Lecuit, T. (2014). Actomyosin networks and tissue morphogenesis. Development *141*, 1789–1793.

Murányi, A., Derkach, D., Erdodi, F., Kiss, A., Ito, M., and Hartshorne, D.J. (2005). Phosphorylation of Thr695 and Thr850 on the myosin phosphatase target subunit: inhibitory effects and occurrence in A7r5 cells. FEBS Lett. *579*, 6611–6615.

Narasimha, M., and Brown, N.H. (2004). Novel functions for integrins in epithelial morphogenesis. Curr. Biol. *14*, 381–385.

Niederman, R., and Pollard, T.D. (1975). Human platelet myosin. II. In vitro assembly and structure of myosin filaments. J. Cell Biol. *67*, 72–92.

Niessen, C.M., Leckband, D., and Yap, A.S. (2011). Tissue organization by cadherin adhesion molecules: dynamic molecular and cellular mechanisms of morphogenetic regulation. Physiol. Rev. *91*, 691–731.

Nishimura, Y., and Yonemura, S. (2006). Centralspindlin regulates ECT2 and RhoA accumulation at the equatorial cortex during cytokinesis. J. Cell Sci. *119*, 104–114.

Nola, S., Daigaku, R., Smolarczyk, K., Carstens, M., Martin-Martin, B., Longmore, G., Bailly, M., and Braga, V.M. (2011). Ajuba is required for Rac activation and maintenance of E-cadherin adhesion. J. Cell Biol. *195*, 855–871.

Nowotarski, S.H., and Peifer, M. (2014). Cell biology: a tense but good day for actin at cell-cell junctions. Curr. Biol. *24*, R688–R690.

O'Connor, P., and Burnside, B. (1981). Actin-dependent cell elongation in teleost retinal rods: requirement for actin filament assembly. J. Cell Biol. *89*, 517–524.

Perez, T.D., Tamada, M., Sheetz, M.P., and Nelson, W.J. (2008). Immediate-early signaling induced by E-cadherin engagement and adhesion. J. Biol. Chem. *283*, 5014–5022.

Peskin, C.S., Odell, G.M., and Oster, G.F. (1993). Cellular motions and thermal fluctuations: the Brownian ratchet. Biophys. J. *65*, 316–324.

Piekny, A.J., and Glotzer, M. (2008). Anillin is a scaffold protein that links RhoA, actin, and myosin during cytokinesis. Curr. Biol. *18*, 30–36.

Pollard, T.D. (2007). Regulation of actin filament assembly by Arp2/3 complex and formins. Annu. Rev. Biophys. Biomol. Struct. *36*, 451–477.

Pollard, T.D., and Borisy, G.G. (2003). Cellular motility driven by assembly and disassembly of actin filaments. Cell *112*, 453–465.

Priya, R., Yap, A.S., and Gomez, G.A. (2013). E-cadherin supports steady-state Rho signaling at the epithelial zonula adherens. Differentiation *86*, 133–140.

Priya, R., Gomez, G.A., Budnar, S., Verma, S., Cox, H.L., Hamilton, N.A., and Yap, A.S. (2015). Feedback regulation through myosin II confers robustness on RhoA signalling at E-cadherin junctions. Nat. Cell Biol. *17*, 1282–1293.

Ratheesh, A., Gomez, G.A., Priya, R., Verma, S., Kovacs, E.M., Jiang, K., Brown, N.H., Akhmanova, A., Stehbens, S.J., and Yap, A.S. (2012). Centralspindlin and α-catenin regulate Rho signalling at the epithelial zonula adherens. Nat. Cell Biol. *14*, 818–828.

Reyes, C.C., Jin, M., Breznau, E.B., Espino, R., Delgado-Gonzalo, R., Goryachev, A.B., and Miller, A.L. (2014). Anillin regulates cell-cell junction integrity by organizing junctional accumulation of rho-GTP and actomyosin. Curr. Biol. *24*, 1263–1270.

Reymann, A.-C., Boujemaa-Paterski, R., Martiel, J.-L., Guérin, C., Cao, W., Chin, H.F., De La Cruz, E.M., Théry, M., and Blanchoin, L. (2012). Actin network architecture can determine myosin motor activity. Science *336*, 1310–1314.

Ricketson, D., Johnston, C.A., and Prehoda, K.E. (2010). Multiple tail domain interactions stabilize nonmuscle myosin II bipolar filaments. Proc. Natl. Acad. Sci. USA *107*, 20964–20969.

Rimm, D.L., Koslov, E.R., Kebriaei, P., Cianci, C.D., and Morrow, J.S. (1995). Alpha 1(E)-catenin is an actin-binding and -bundling protein mediating the attachment of F-actin to the membrane adhesion complex. Proc. Natl. Acad. Sci. USA *92*, 8813–8817.

Rodriguez-Diaz, A., Toyama, Y., Abravanel, D.L., Wiemann, J.M., Wells, A.R., Tulu, U.S., Edwards, G.S., and Kiehart, D.P. (2008). Actomyosin purse strings: renewable resources that make morphogenesis robust and resilient. HFSP J. *2*, 220–237.

Rosenblatt, J., Raff, M.C., and Cramer, L.P. (2001). An epithelial cell destined for apoptosis signals its neighbors to extrude it by an actin- and myosin-dependent mechanism. Curr. Biol. *11*, 1847–1857.

Russo, J.M., Florian, P., Shen, L., Graham, W.V., Tretiakova, M.S., Gitter, A.H., Mrsny, R.J., and Turner, J.R. (2005). Distinct temporal-spatial roles for rho kinase and myosin light chain kinase in epithelial purse-string wound closure. Gastroenterology *128*, 987–1001.

Saias, L., Swoger, J., D'Angelo, A., Hayes, P., Colombelli, J., Sharpe, J., Salbreux, G., and Solon, J. (2015). Decrease in cell volume generates contractile forces driving dorsal closure. Dev. Cell *33*, 611–621.

Salbreux, G., Prost, J., and Joanny, J.F. (2009). Hydrodynamics of cellular cortical flows and the formation of contractile rings. Phys. Rev. Lett. *103*, 058102.

Sanger, J.M., and Sanger, J.W. (1980). Banding and polarity of actin filaments in interphase and cleaving cells. J. Cell Biol. *86*, 568–575.

Scholey, J.M., Taylor, K.A., and Kendrick-Jones, J. (1980). Regulation of non-muscle myosin assembly by calmodulin-dependent light chain kinase. Nature *287*, 233–235.

Schroeder, T.E. (1968). Cytokinesis: filaments in the cleavage furrow. Exp. Cell Res. *53*, 272–276.

Schroeder, T.E. (1972). The contractile ring: II. Determining its brief existence, volumetric changes, and vital role in cleaving *Arbacia* eggs. J. Cell Biol. *53*, 419–434.

Schroeder, T.E. (1973). Actin in dividing cells: contractile ring filaments bind heavy meromyosin. Proc. Natl. Acad. Sci. USA *70*, 1688–1692.

Sehring, I.M., Dong, B., Denker, E., Bhattachan, P., Deng, W., Mathiesen, B.T., and Jiang, D. (2014). An equatorial contractile mechanism drives cell elongation but not cell division. PLoS Biol. *12*, e1001781.

Sept, D., and McCammon, J.A. (2001). Thermodynamics and kinetics of actin filament nucleation. Biophys. J. *81*, 667–674.

Sharif, B., and Maddox, A.S. (2012). Wound Healing: GTPases flux their muscles. Dev. Cell *23*, 236–238.

Shirazi, A., Iizuka, K., Fadden, P., Mosse, C., Somlyo, A.P., Somlyo, A.V., and Haystead, T.A. (1994). Purification and characterization of the mammalian myosin light chain phosphatase holoenzyme. The differential effects of the holoenzyme and its subunits on smooth muscle. J. Biol. Chem. *269*, 31598–31606.

Slattum, G.M., and Rosenblatt, J. (2014). Tumour cell invasion: an emerging role for basal epithelial cell extrusion. Nat. Rev. Cancer *14*, 495–501.

Slattum, G., McGee, K.M., and Rosenblatt, J. (2009). P115 RhoGEF and microtubules decide the direction apoptotic cells extrude from an epithelium. J. Cell Biol. *186*, 693–702.

Solon, J., Kaya-Copur, A., Colombelli, J., and Brunner, D. (2009). Pulsed forces timed by a ratchet-like mechanism drive directed tissue movement during dorsal closure. Cell *137*, 1331–1342.

Sonnemann, K.J., and Bement, W.M. (2011). Wound repair: toward understanding and integration of single-cell and multicellular wound responses. Annu. Rev. Cell Dev. Biol. *27*, 237–263.

Straight, A.F., Field, C.M., and Mitchison, T.J. (2005). Anillin binds nonmuscle myosin II and regulates the contractile ring. Mol. Biol. Cell *16*, 193–201.

Strutt, D.I., Weber, U., and Mlodzik, M. (1997). The role of RhoA in tissue polarity and Frizzled signalling. Nature *387*, 292–295.

Sun, L., Guan, R., Lee, I.J., Liu, Y., Chen, M., Wang, J., Wu, J.Q., and Chen, Z. (2015). Mechanistic insights into the anchorage of the contractile ring by anillin and Mid1. Dev. Cell *33*, 413–426.

Takeichi, M. (2014). Dynamic contacts: rearranging adherens junctions to drive epithelial remodelling. Nat. Rev. Mol. Cell Biol. *15*, 397–410.

Tamada, M., Perez, T.D., Nelson, W.J., and Sheetz, M.P. (2007). Two distinct modes of myosin assembly and dynamics during epithelial wound closure. J. Cell Biol. *176*, 27–33.

Tatsumoto, T., Xie, X., Blumenthal, R., Okamoto, I., and Miki, T. (1999). Human Ect2 is an exchange factor for Rho GTPases, phosphorylated in G2/M phases, and involved in cytokinesis. J. Cell Biol. *147*, 921–928.

Tepass, U., and Hartenstein, V. (1994). The development of cellular junctions in the *Drosophila* embryo. Dev. Biol. *161*, 563–596.

Thomas, W.A., Boscher, C., Chu, Y.S., Cuvelier, D., Martinez-Rico, C., Seddiki, R., Heysch, J., Ladoux, B., Thiery, J.P., Mege, R.M., et al. (2013). α-Catenin and vinculin cooperate to promote high E-cadherin-based adhesion strength. J. Biol. Chem. *288*, 4957–4969.

Toyama, Y., Peralta, X.G., Wells, A.R., Kiehart, D.P., and Edwards, G.S. (2008). Apoptotic force and tissue dynamics during *Drosophila* embryogenesis. Science *321*, 1683–1686.

Truong Quang, B.A., Mani, M., Markova, O., Lecuit, T., and Lenne, P.F. (2013). Principles of E-cadherin supramolecular organization in vivo. Curr. Biol. *23*, 2197–2207.

Turbedsky, K., Pollard, T.D., and Yeager, M. (2005). Assembly of acanthamoeba myosin-II minifilaments. Model of anti-parallel dimers based on EM and X-ray diffraction of 2D and 3D crystals. J. Mol. Biol. *345*, 363–373.

Tuxworth, R.I., Weber, I., Wessels, D., Addicks, G.C., Soll, D.R., Gerisch, G., and Titus, M.A. (2001). A role for myosin VII in dynamic cell adhesion. Curr. Biol. *11*, 318–329.

Vaughan, E.M., Miller, A.L., Yu, H.Y., and Bement, W.M. (2011). Control of local rho GTPase crosstalk by Abr. Curr. Biol. *21*, 270–277.

Vavylonis, D., Wu, J.Q., Hao, S., O'Shaughnessy, B., and Pollard, T.D. (2008). Assembly mechanism of the contractile ring for cytokinesis by fission yeast. Science *319*, 97–100.

Verma, S., Han, S.P., Michael, M., Gomez, G.A., Yang, Z., Teasdale, R.D., Ratheesh, A., Kovacs, E.M., Ali, R.G., and Yap, A.S. (2012). A WAVE2-Arp2/3 actin nucleator apparatus supports junctional tension at the epithelial zonula adherens. Mol. Biol. Cell *23*, 4601–4610.

Vicente-Manzanares, M., Ma, X., Adelstein, R.S., and Horwitz, A.R. (2009). Non-muscle myosin II takes centre stage in cell adhesion and migration. Nat. Rev. Mol. Cell Biol. *10*, 778–790.

Volkmann, D., and Baluska, F. (1999). Actin cytoskeleton in plants: from transport networks to signaling networks. Microsc. Res. Tech. *47*, 135–154.

Weeds, A.G., and Lowey, S. (1971). Substructure of the myosin molecule. II. The light chains of myosin. J. Mol. Biol. *61*, 701–725.

Wood, W., Jacinto, A., Grose, R., Woolner, S., Gale, J., Wilson, C., and Martin, P. (2002). Wound healing recapitulates morphogenesis in *Drosophila* embryos. Nat. Cell Biol. *4*, 907–912.

Wu, J.-Q., Sirotkin, V., Kovar, D.R., Lord, M., Beltzner, C.C., Kuhn, J.R., and Pollard, T.D. (2006). Assembly of the cytokinetic contractile ring from a broad band of nodes in fission yeast. J. Cell Biol. *174*, 391–402.

Wu, Y., Kanchanawong, P., and Zaidel-Bar, R. (2015). Actin-delimited adhesion-independent clustering of E-cadherin forms the nanoscale building blocks of adherens junctions. Dev. Cell *32*, 139–154.

Yamada, S., and Nelson, J.W. (2007). Localized zones of Rho and Rac activities drive initiation and expansion of epithelial cell-cell adhesion. J. Cell Biol. *178*, 517–527.

Yonemura, S., Itoh, M., Nagafuchi, A., and Tsukita, S. (1995). Cell-to-cell adherens junction formation and actin filament organization: similarities and differences between non-polarized fibroblasts and polarized epithelial cells. J. Cell Sci. *108*, 127–142.

Young, P.E., Richman, A.M., Ketchum, A.S., and Kiehart, D.P. (1993). Morphogenesis in *Drosophila* requires nonmuscle myosin heavy chain function. Genes Dev. *7*, 29–41.

Yüce, Ö., Piekny, A., and Glotzer, M. (2005). An ECT2-centralspindlin complex regulates the localization and function of RhoA. J. Cell Biol. *170*, 571–582.

Yumura, S. (2001). Myosin II dynamics and cortical flow during contractile ring formation in *Dictyostelium* cells. J. Cell Biol. *154*, 137–146.

Zaidel-Bar, R. (2013). Cadherin adhesome at a glance. J. Cell Sci. *126*, 373–378.

Zecchini, V., Brennan, K., and Martinez-Arias, A. (1999). An activity of Notch regulates JNK signalling and affects dorsal closure in *Drosophila*. Curr. Biol. *9*, 460–469.

Zumdieck, A., Kruse, K., Bringmann, H., Hyman, A.A., and Jülicher, F. (2007). Stress generation and filament turnover during actin ring constriction. PLoS One *2*, e696.

1.2.2 Cell-cell junctions in tissues

As mentioned above, actin ring structures are part of the driving forces of diverse developmental and physiological processes. In addition to the requirement for force-generating machineries, these structures need to be anchored at adhesion sites in order to properly execute their function during tissue morphogenesis[2,10]. In other words, the integration of the cytoskeleton at cell-cell junctions is crucial for the coordinated behavior of tissues[2,10]. Hence, in the next section we will first introduce different cell-cell junctions and then further emphasize the mechanosensitive behavior as well as their function in tissue morphogenesis.

1.2.2.1 Types of cell-cell junctions

Cells are coupled to each other via different kinds of junctions, such as Adherens junctions (AJs), Tight junctions (TJs) and Desmosomes (Figure 1A). While AJs and TJs mainly connect their transmembrane receptors to the actomyosin or microtubule cytoskeleton, desmosomes interact with the intermediate filament system of cells[12–16]. Besides the typical cell-cell adhesive junctions, the cell also has intercellular gates - gap junctions - allowing for the exchange of ions and small hydrophilic molecules between cells[12].

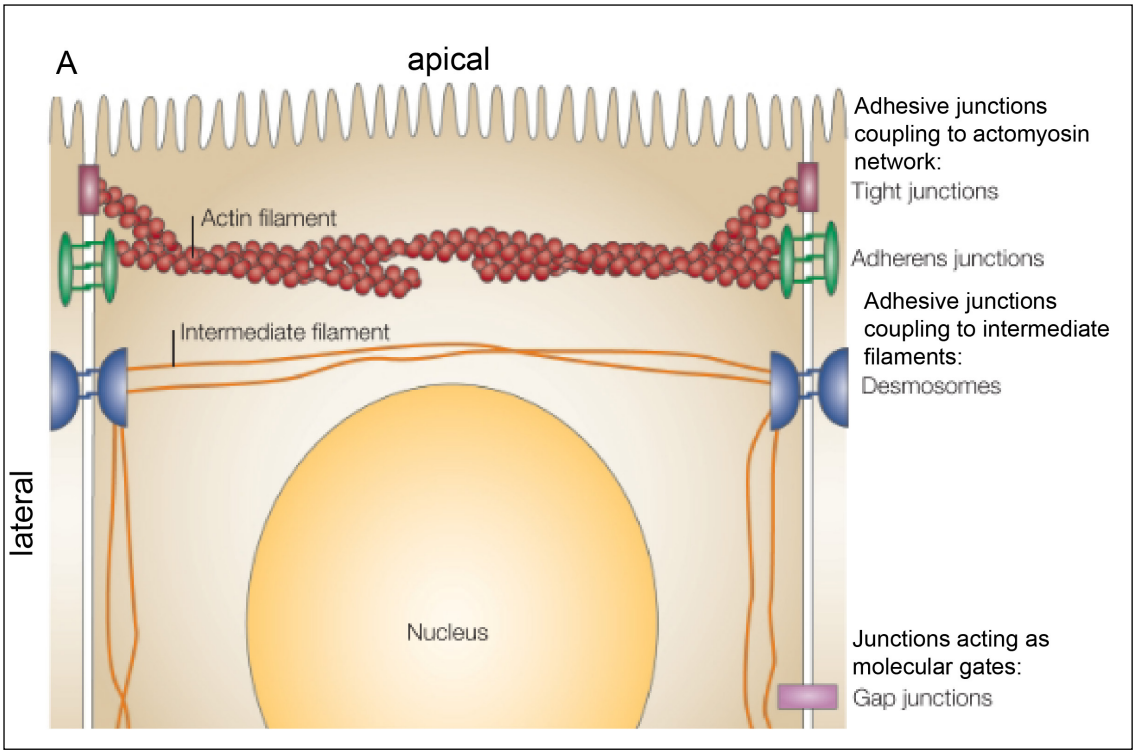

Figure 1. Intercellular junctions of a polarized epithelial cell.
(A) Adhesive cell-cell junctions such as TJs, AJs and desmosomes are coupled to the actomyosin, microtubule or intermediate filamentous network[12]. Gap junctions act as molecular gates[12]. Figure adapted from ref[12].

The main focus of this chapter, however, lies on the junctional types shown to be mainly involved in mediating proper cell-cell adhesion through their coupling to the actomyosin network as shown for AJs and TJs[12,15,16]. While AJs were known for a long time as the primary cell-cell junctional type to interact with the actomyosin cytoskeleton, within the last

decade more evidence was provided showing that TJs also connect to cytoskeletal networks such as the actomyosin and microtubule networks[12,16] and therefore might also serve in cell-cell communication and mechanosensation/-transduction. We will first discuss the rather well established mechanosensing process at AJs and then continue with a detailed description of TJs.

1.2.2.2 Mechanosensing at AJs

A plethora of studies have demonstrated that AJs are mechanosensitive: upon force application on AJs, a mechanosensitive cascade is triggered allowing the junctions to grow and to reinforce their adhesion strength[17–20] (Figure 2A). The strengthening of adhesions works on several levels in parallel, such as on the extra-cellular binding of E-cadherin ectodomains as well as on their intracellular coupling of E-cadherin receptors to the cytoskeleton (Figure 2A',A'')[21]. Both E-cadherin homophilic interactions, and α-catenin-F-Actin binding can behave as so-called 'catch bonds', meaning that upon applying mechanical force, the lifetime of their interactions increases[22]. This is in contrast to 'slip bonds', which are interactions between proteins that are lost upon higher force application and hence its binding lifetime is shortened upon mechanical load[22]. In addition to the importance of catch bonds during AJ mechanosensation, α-catenin is unfolded and exposes a cryptic site thereby enabling vinculin binding[23]. At homeostatic conditions vinculin is present in an auto-inhibitory mode and becomes unfolded itself upon mechanical load allowing for further recruitment of actin-polymerizing components such as Ena/Vasp[21]. Several other potentially mechanosensitive proteins have been implicated in the tension-dependent response at AJ, for instance, the actin nucleator Diaphanous, a formin, and the actin-binding protein EPLIN, have been shown to enhance actin polymerization or stabilization, respectively[24–26]. In summary, these mechanisms help in strengthening AJ-mediated cell-cell adhesion upon mechanical load[21].

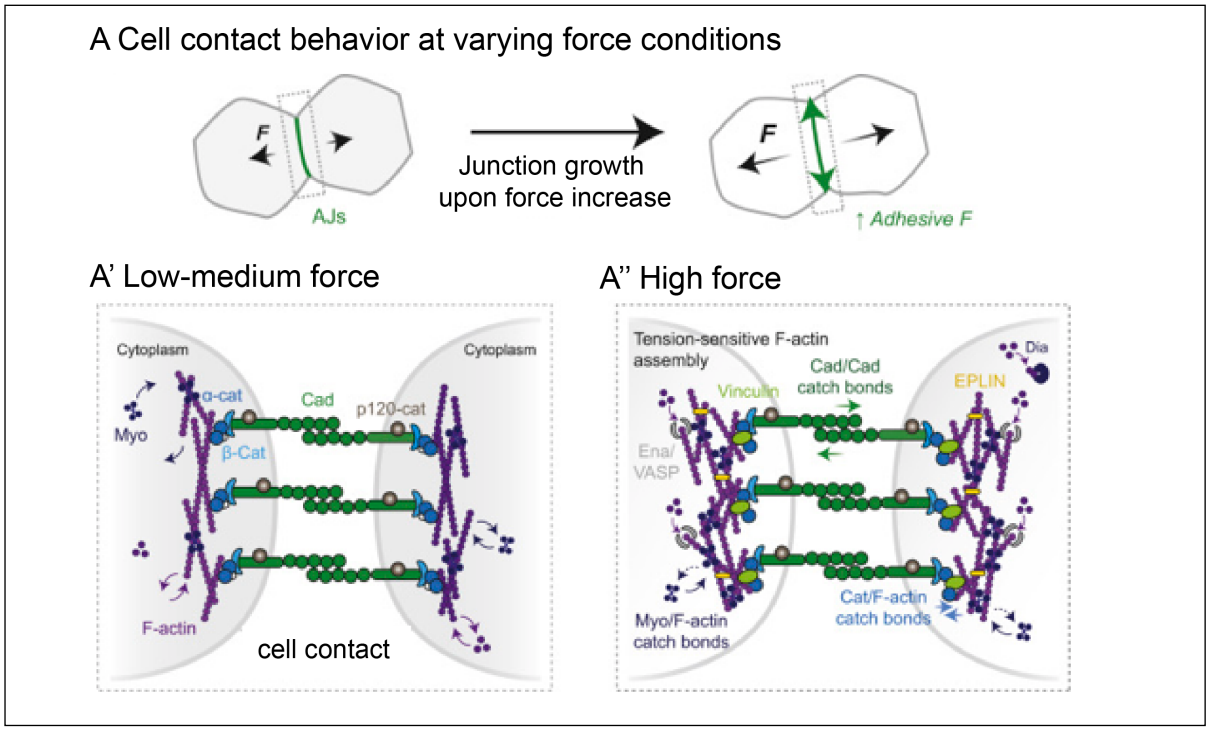

Figure 2. Mechanosensing response at AJs
Upon force application, E-cadherin mediated junctions grow (A) and reinforce their junctional and cytoskeletal connections through E-cadherin catch bonds, and α-catenin-F-Actin catch bonds as well as through the assembly of tension-sensitive F-actin structures (A', A'')[21]. Figure adapted from ref[21].

1.2.2.3 Function and structure of TJs

TJs serve to keep the epithelial barrier intact, help maintaining apicobasal polarity of epithelial cells and have been shown to affect the establishment of the perijunctional actomyosin ring[12,16]. In the course of this PhD project, we have established an assay for monitoring barrier leakage in zebrafish embryos (see Appendix, Figure 19), which has been successfully used in *Xenopus laevis* for high spatiotemporal imaging of barrier breaches[27]. However, in our current study we have mainly investigated the effect of TJs on actomyosin ring dynamics and will therefore keep a primary focus on this interplay in the following paragraphs.

Similar to the structure of AJs (discussed in chapters 1.2.1 and 1.2.2.2), TJs consist of (1) transmembrane proteins and (2) scaffolding proteins that connect transmembrane proteins to the cytoskeleton[16] (Figure 3A). The prevalent TJ transmembrane proteins are tetraspan proteins like Claudins and MARVEL domain containing proteins like Occludins. In addition to tetraspan receptors, single span transmembrane proteins such as Junctional Adhesion Molecules (JAMs) and trispan proteins such as blood vessel epicardial substance (BVES) belong to the TJ transmembrane protein family. Polarity complexes such as the CRB3 (crumbs homologue 3 protein) are involved in apical polarization and TJ regulation[28]. Cytoplasmic plague protein families consist of Zonula Occludens proteins such as ZO-1, ZO-2 and ZO-3 and Cingulins as well as Paracingulins (Cingulin-like 1)[16]. These scaffolding proteins mediate the binding of TJ transmembrane proteins to microtubules and to the actomyosin cytoskeleton[16].

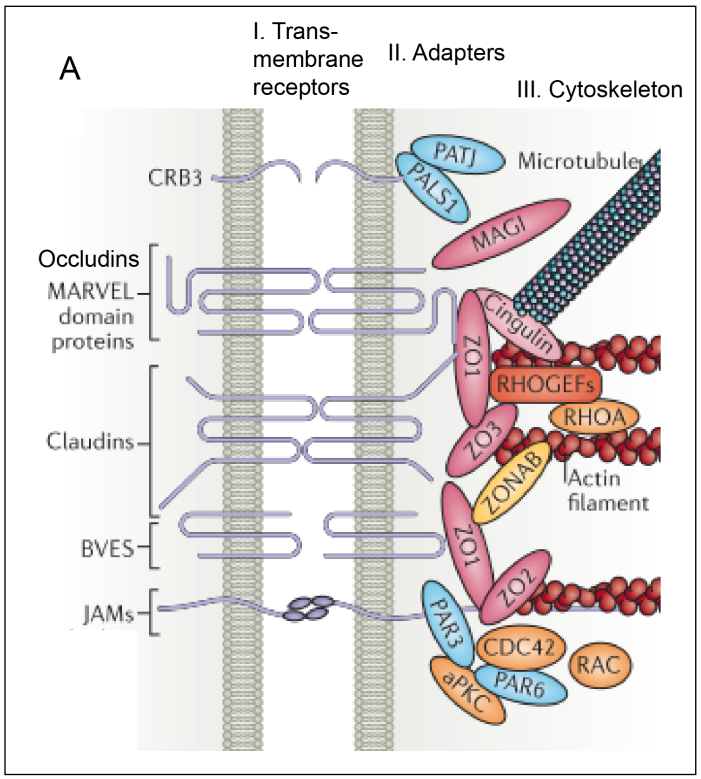

Figure 3. TJ structure
(A) TJ characteristic transmembrane proteins are MARVEL domain proteins, Claudins, BVES and JAMs[16]. CRB3 is a TJ associated protein important during apical differentiation[28]. Cytoplasmic adapters are ZO proteins and Cingulins that couple the transmembrane proteins to the cytoskeleton[16]. Figure modified from ref[16].

Since ZO-1 counts as one of the main regulators at the TJ cytoplasmic scaffold[16,29] and because we demonstrate in this PhD project that it plays a major role in the *mechanosensation of tight junctions*, we will focus on ZO-1 in the upcoming chapters. In order to shed more light on the interplay of TJs and the actomyosin network we will discuss (1) how the actomyosin network regulates TJ formation/maturation through Rho GTPase signaling and (2) how TJs, and especially ZO proteins, can affect actomyosin network functionality and thereby tissue morphogenesis.

1.2.2.4 Contribution of Rho GTPase signaling to TJ formation and maturation

During the initial phases of junction formation, Cdc42-mediated filopodial-like extensions of cells meet and assemble spot-like nectin- and E-Cadherin-based junctions[16]. These very early forms of junctions (primordial junctions) are not yet well separated in space as found in fully matured epithelial cells with TJs most apically and AJs more sub-apically localized[16]. In these primordial junctions, components of TJs and AJs reside in close proximity, which in part explains the observed interaction of TJ and AJ components such as ZO-1 and α-catenin during the initial junction formation phase[16,30,31]. During early junction formation, nectin, an AJ associated protein, mediates the recruitment of JAM-A (TJ transmembrane component) and ZO-1 via interaction of afadin to the newly forming junction, again demonstrating the close coordination of AJ and TJ formation[16,32]. Maturation and polarization of TJs and AJs involve regulation via small GTPases such as RhoA and Cdc42, and factors of the apical polarization machinery e.g. atypical Protein Kinase C (aPKC), Partitioning-defective protein 3 (Par3) and 6 (Par6)[16] (Figure 4A).

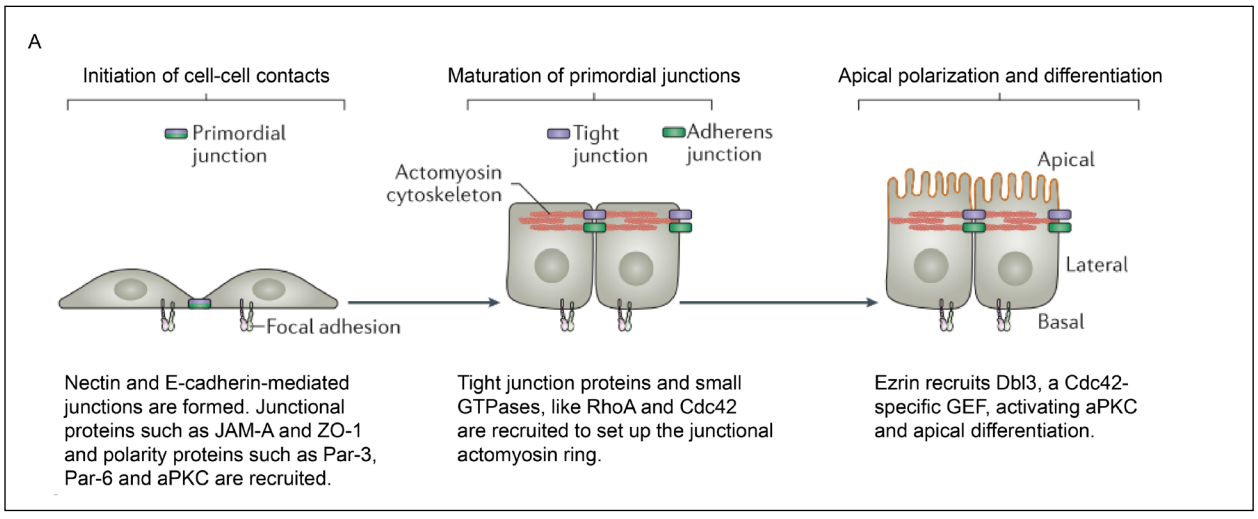

Figure 4. Epithelial junction formation and maturation

(A) During the initiation of junction formation, nectin and E-cadherin based connections form and several AJ and TJ components are recruited to the primordial junction[16]. Recruitment of small GTPases, such as RhoA and Cdc42, and TJ components is crucial in regulating junctional maturation[16]. The final stage of polarization involves apical differentiation through apical polarity proteins and small GTPases such as Cdc42[16]. Image modified from ref[16].

The following paragraph should give a glimpse, not a holistic view into the complexity of junction formation and maturation with several layers of regulation through small GTPases (Figure 4A).

During junction formation and maturation, an active RhoA zone is established at cell-cell junctions, which can be controlled via the spatiotemporal regulation of Rho GTPase activators/de-activators[33,34]. In principle, the regulation of Rho GTPases happens through cycling between active (GTP-bound) and inactive (GDP-bound) states mediated by its activators, RhoGEFs (Guanine nucleotide exchange factor) and its negative regulators, RhoGAPs (GTPase-activating proteins), respectively[35]. For instance, p114RhoGEF and ARHGEF11 are recruited to forming junctions by a complex of cingulin/PATJ (Crumbs polarity protein) or ZO-1, respectively, and help in spatially regulating active RhoA zones[33,36,37]. In the absence of p114RhoGEF, the RhoA zone at junctions does not form properly but instead spreads to non-junctional, basal regions, leading to delay in junctional maturation and abnormal epithelial morphogenesis in three-dimensional MDCK cysts[33]. Additionally to its GTPase function, p114RhoGEF assembles in a complex with myosin-2/Rock II and thereby likely helps in proper build-up of junctional tension[33,38]. In order to spatially restrict and attenuate the magnitude of active RhoA junctional zones, RhoGAPs, such as myosin-IXA and myosin-IXB are fundamental[39,40]. In the absence of myosin-IXA or myosin-IXB, Rho activity is increased, leading to hyperactivation of the actomyosin cytoskeleton, ZO-1 depletion from the leading edge and impairment of collective migration of epithelial cells[39,40]. Taken together, the above-mentioned cases support the view that the spatiotemporal regulation is critical for generating narrow RhoA activity zones leading to controlled junction assembly and integration.
In addition to RhoA, the small GTPase Cdc42 is also involved in tight junction formation and maturation[16]. At early stages of cell-cell junction formation, Cdc42-driven filopodial-like contacting points mediate contact establishment[16]; however, Cdc42 activation also needs to be spatiotemporally regulated, which is in part mediated by a Cdc42-specific GAP called SH3BP1[41]. Further, a Cdc42-specific positive regulator Tuba (Cdc42-GEF) helps in forming the apical junction via its interaction with ZO-1 and the recruitment of N-WASP, an actin-polymerizing factor[42]. When Cdc42 or its effector (N-WASP) are down regulated, junctional tension during initial stages is reduced[43] and/or junctional configuration and formation are affected[42,43]. Following these initial regulatory steps, another Cdc42-specific GAP gets involved, called RICH1, and mediates the acquisition of apicobasal polarity[44]. Further, Cdc42 recruits Par6 and aPKC, components of the Par polarity complex[16]. Through the antagonizing principles between the apical (Crumbs complex mediated) domain, the mobile Par complex at TJs and the lateral scribble complex, the different domains are kept separated and in place[45]. To mediate the final stages of apical membrane specification, another Cdc42-specific GEF, Dbl3, is recruited by Ezrin and besides Cdc42 signaling, it regulates the size of the apical domain and apical membrane differentiation[46,47] (Figure 4A).
Taken together, the spatiotemporal regulation of RhoA and Cdc42 activity zones are critically involved in proper TJ junction formation, configuration and apical membrane differentiation[16].

Interestingly, small GTPases regulate TJ formation, but there is also plenty of evidence that TJs regulate the actomyosin cytoskeleton via small GTPases and thereby act as signaling

centers[38]. Hence in the next subchapter we will focus on how ZO proteins affect actomyosin network organization and contractility through regulatory mediators such as Rho GTPases.

1.2.2.5 TJs' regulation of the actomyosin cytoskeleton

Early studies in mouse showed that ZO-1 knockout mutants are embryonic lethal due to defects in angiogenesis of endothelial tissues such as the yolk sac[48]. The exact mechanisms of how ZO-1 contributes to this phenotype in mammalian embryogenesis are not yet completely understood[48,49]. However, a study in human dermal microvascular endothelial cells (HDMEC) showed that ZO-1 recruits paracingulin and p114RhoGEF to the vascular endothelial cadherin (VE-cadherin) complex and thereby positively affects the actomyosin network and junctional tension[49]. This regulatory cascade triggered by ZO-1 then mediates proper cell migration, angiogenesis and barrier formation[49]. While in endothelial cells, ZO proteins seem to have a positive effect on the actomyosin organization and contractility, the results in epithelial cells are more controversial[50–53]. For instance, in *Xenopus laevis* gastrulation, TJ-associated proteins ZO-1 and GEF-H1, negatively regulate mechanical tension acting on AJs that connect the surface epithelium[50]. Different means of depleting (knockout or knockdown) ZO-1 and ZO-2 in MDCK cells show a misplaced and enlarged perijunctional actomyosin ring, resulting in elevated contractility and tension, mediated via pMLC kinase, Rho kinase 1 or ROCK activity[51,54,55]. This change in perijunctional ring organization then has a negative impact on tissue integrity and barrier function[51,54]. Similarly, in migratory mammary (MCF10A) cells, ZO-1 depletion results in increased cell-cell and cell-substrate forces[56]. The above-mentioned examples of epithelial cells rather suggests ZO proteins negatively influence cell-cell contractility and tension; however, data from mammary epithelial Eph4 cells show that the perijunctional myosin structure upon ZO-1/2 depletion is misplaced from the AJ belt and the RhoA activity zone is depleted[52]. This phenotype can be rescued by expressing a constitutively active RhoA version[52]. Taken together, this study shows that ZO-1/2 is critical in establishing a proper perijunctional myosin ring at the zonula adherens through RhoA activation[52]. Hence, these contradictory results suggest that in different environments (eg. depending on the tissue type) ZO-1/2 can exert different functions concerning actomyosin contractility and tension. However, independently of ZO-1/2's attenuating or strengthening function on the perijunctonal ring, in all mentioned cases, tissue integrity and morphogenesis are negatively affected pointing towards the importance of a finely tuned spatiotemporal regulation of the apical actomyosin ring in order to have fully functional TJs.

In the next chapter we will switch gears and delve into the topic of phase transitions and specifically phase separation in biology. After briefly mentioning some examples of phase-separated clusters in biological systems, we will talk about the physical principles behind liquid-liquid phase separation, formation, requirements/hallmarks and functionality of phase-separated condensates.

1.3 Phase transitions in biology

The term phase transition – a concept from the discipline of soft matter physics - describes the change of matter or a substance from one physical state to another; in the case of water it would be the transition from gaseous to aqueous phase (water vapor to water) or from aqueous to solid phase (water to ice)[57]. Phase separation also belongs to the field of phase transitions, which describes the de-mixing of two phases[57].

Recently, the concept of phase transition, and specifically phase separation, has been used in biological systems to describe the principles of membrane-less condensate formation within cells[58,59]. One of the first membrane-less structures, identified already in the 18th century, is the nucleolus[59] (Figure 5A). More examples for such membrane-less, and now described as phase-separated, condensates are ranging from nuclear bodies such as Cajal body, cleavage body, PML body to cytoplasmic localized structures such as germ granules, Balbiani and P bodies, stress and RNA transport granules to membrane localized clusters and synaptic densities[9] (Figure 5A).

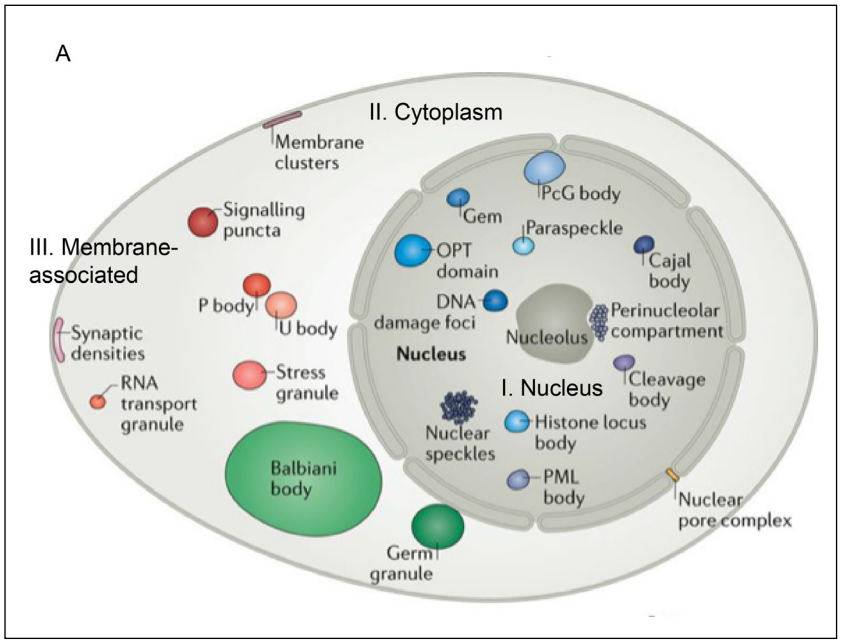

Figure 5. Membrane-less compartments within cells
(A) Several phase-separated condensates have been identified with localization in the (1) nucleus, such as the Nucleolus, cleavage body etc., in the (2) cytoplasm, like stress granules or (3) wetting membranes such as synaptic densities[9]. Figure modified from ref[9].

In cells, canonical membrane-bound compartments or organelles, are surrounded by physical barriers, lipid bilayers. Such a physical barrier allows for the separation of the cytosolic environment from environments specifically needed for energy production eg. in the mitochondrion or for protein degradation eg. in lysosomes[58,60,61]. While in the case of a membrane-enclosed organelle the lipid bilayer serves as such a barrier, membrane-less condensates lack any obvious physical barriers[9]. Importantly, the concept of phase separation has provided more insight into how membrane-less structures are formed and how they maintain their environment within the condensate[57,58].

1.3.1 Physical principles of liquid-liquid phase separation (LLPS)

Phase separation is the de-mixing of substance A from a substance B[58]. A frequently used example to easily explain the concept of phase separation is the de-mixing of oil and water phases for instance in a salad dressing: initially well mixed oil and aqueous phases will start

separating into few and big oil droplets in a surrounding aqueous (vinegar) phase[58] (Figure 6).

Figure 6. Phase separation of a salad dressing
After mixing the ingredients for a salad dressing (in this case vinegar and oil made of pumpkin seeds), the oil and aqueous phases will separate or de-mix from each other over time.

When describing the phase separation process from a physics perspective, one has to consider the second law of thermodynamics, which states that the entropy of an isolated system always increases[59,62]. Such increase in entropy means that a system is moving from an ordered to a less ordered state[59,62], which seems counterintuitive for a phase-separating system because it shows higher order and therefore lower entropy[59]. Hence, for phase separation to be a thermodynamically favored process, a specific situation has to be given, in which the free energy will still be decreased[59] (iBiology.org – Brangwynne on LLPS). An example for such a situation would be if the interaction energy between substance A and substance B (A-B) is much larger than the interaction energy of (A-A) and (B-B); then it would be energetically more favorable to keep substances A and B apart from each other (iBiology.org – Brangwynne on LLPS). In summary, this would be a regime, in which the contribution of interaction energy is larger than the contribution of the entropic force (iBiology.org – Brangwynne on LLPS). In this way, a system can undergo a thermodynamically-driven phase separation, because it can reduce its free energy, even though lowering its entropy[59,62,63] (iBiology.org – Brangwynne on LLPS).

1.3.2 Cell sorting - phase separation on a tissue scale

A very similar situation has been observed on larger, micrometer-sized scales as the process of *cell sorting*. Holtfreter and colleagues initially observed the sorting of germlayer cells isolated from amphibian embryos[64] (Figure 7). Later, Steinberg and colleagues proposed a liquid-like behavior for tissues[65,66]. Accordingly, mixed (heterotypic) cells could be descripted as Newtonian fluids, in which relative surface and interfacial tensions dictate the geometry and dynamics of the sorting behavior, in order to decrease the free energy of the system[67]. The above-mentioned studies suggest a resemblance of cell sorting processes with phase separating systems[59]. In order to describe intermolecular forces (found in liquids) in the context of cells and tissues, several theoretical models such as the 'differential adhesion hypothesis', 'differential surface contraction hypothesis' and 'differential interfacial tension hypothesis' were utilized in considering additional factors such as adhesion and contractility[67].

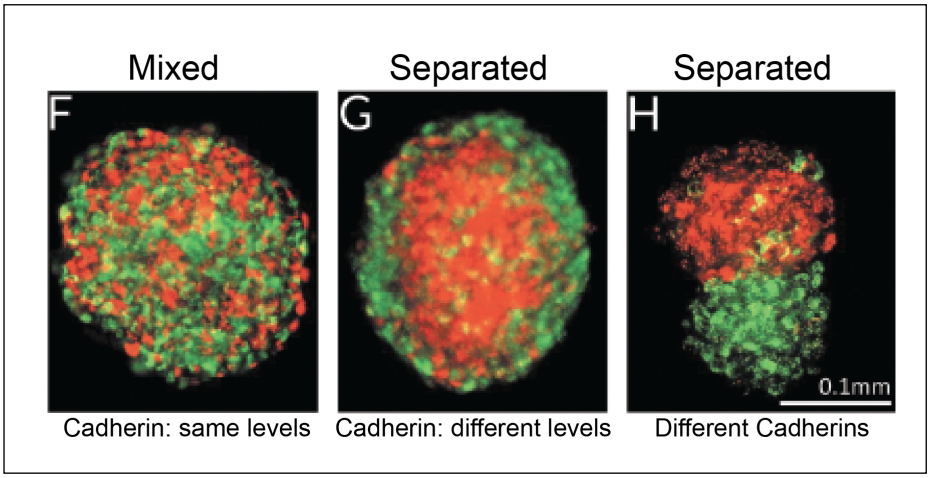

Figure 7. Cell sorting behavior of cells with different adhesion properties
Images of red and green labeled N5A cells expressing the same amount of cadherin and staying mixed (F) or red cell expressing much higher levels of cadherin compared to green cells and get separated (G), or red and green cells expressing different types of cadherins (H). Figure adapted from ref[59].

In summary, phase separation processes in biology have been observed over different scales: from a micron-sized scale of biomolecular condensates to a mesoscale of cell and tissue sorting behaviors.

1.3.3 Formation of phase-separated droplets

Phase separation is a thermodynamic process, in which the system tries to reduce its free energy[8,57]. Considering a condition with only one protein species and a solvent, the protein will undergo phase separation once a critical concentration is reached: a homogeneous protein solution will switch to a two-phase system with areas of higher concentration of the protein and areas of lower protein concentration[57] (Figure 8A). Interestingly, such de-mixing process is reversible, meaning that condensates will dissolve again and form a homogenous solution, when the concentration reaches below a critical concentration[57]. An example for such a phase separation system is stress granules[8,68]. These condensates contain translationally stalled messenger ribonucleoproteins and are triggered by environmental stress situations and are also reversible[8,68]. Interestingly, the threshold of a protein's critical concentration can be lowered for instance by increasing protein-protein affinities eg. via modulating posttranslational modifications through phosphorylation or changes in salt concentration or temperature[57].

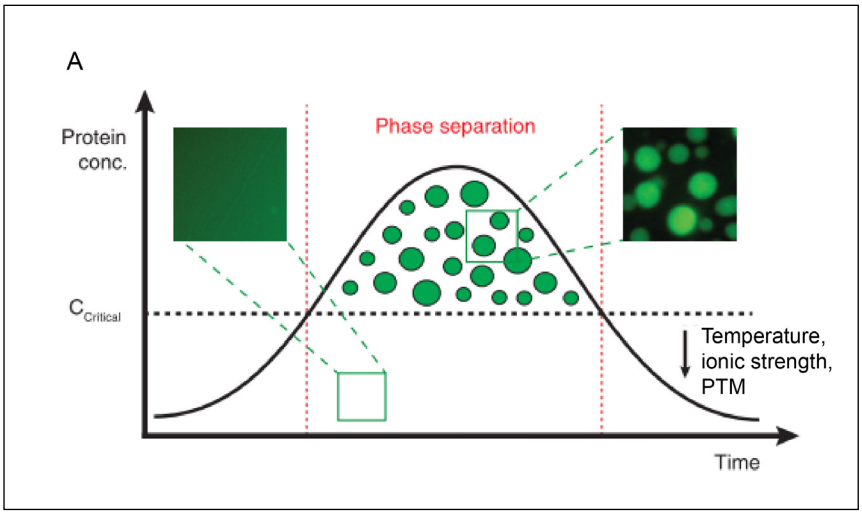

Figure 8. Phase separation process
(A) When reaching a critical concentration, the protein separates into highly concentrated droplets[57]. The threshold can be lowered through modifications of temperature, ionic strength and through posttranslational modification (PTM)[57]. Figure adapted from ref[57].

In LLPS, molecules/components are rapidly diffusing between the dense droplet phase and the lower concentrated surrounding phase and therefore such condensates stay highly dynamic[57,69]. To reach a de-mixed state, droplets either directly fuse or undergo a process called Ostwald ripening, in which case larger droplets grow in size at the expense of eventually disappearing smaller droplets[58]. In addition to coalescence, phase-separated entities have the ability to wet surfaces[8,57]. All the above mentioned properties are indicative of a liquid-like nature[57,69].

1.3.4 Multivalency of proteins undergoing LLPS

One key requirement for LLPS is the multivalent character of proteins[8,68,70,71]. Multivalency of proteins is mainly mediated by weak interactions either via repetitive domain-domain interactions[70,71] or via intrinsically disordered regions (IDR)[8,68]. One of the first examples for domain-domain interactions mediating phase separation comes from the signaling network of the immunological synapse: the SH3 domains of Grb2 bind to proline-rich motifs (PRMs) of Sos1 protein (Figure 9A)[70]. In a minimal *in vitro* reconstitution system, the phase separation capacity of SH3 and PRM with multiple repeats has been demonstrated (Figure 9B)[70]. In contrast to domain-domain interactions, IDR containing molecules show stretches of low sequence complexity and therefore higher-order protein folding is absent[8,68]. Instead of hydrophobic residues that mediate binding in domain-domain interacting systems, IDRs often contain aromatic amino acids (tyrosine and phenylalanine), as well as charged and polar amino acids (glutamine, proline, serine, glycine)[8].

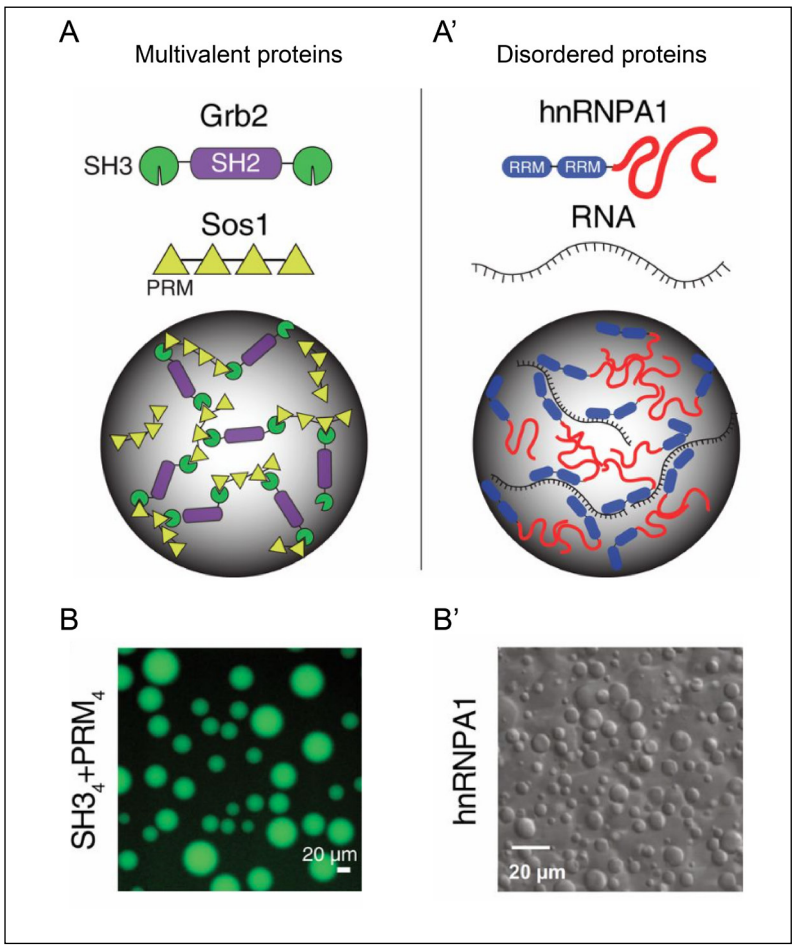

Figure 9. Multivalency-driven phase separation
(A,A') Phase separation can be mediated through weak interactions between domain-domain structures (eg. SH3 and PRM domains) or between intrinsically disordered protein stretches (eg. C-terminus of hnRNPA1 RNA-binding protein)[8].
(B,B') In vitro reconstitution of examples shown in (A). Figure adapted from ref[8].

Through the interspersed arrangement of such amino acids, a low-complexity protein sequence can be patterned in order to allow for charge-charge, dipole-dipole, cation-pi and pi-pi stacking interactions[63]. Interestingly, the exact arrangement and patterning of these amino acids and its charges have turned out to be important for efficient phase separation[72]. An example for disordered protein phase separation comes from stress granules. Stress granules consist of RNA and RNA-binding proteins (RBPs). For instance, the RBP hnRNP can bind to RNA via RNA recognition motifs (RRMs) within the N-terminus, while its C-terminus is composed of low-complexity domains or IDRs (Figure 9A'). The C-terminal low-complexity domain is sufficient for the RBP to undergo phase separation, but in the presence of RNA the RRM motifs enhance LLPS capacity[68] (Figure 9B').

1.3.5 Functionality of phase separation

The physical barrier and the specific environment of membrane-enclosed cellular compartments have proven to be critical for their function eg. energy production in mitochondria happens across the membrane, or the acidic environment within lysosomes is critical for its degradation function[58,60,61]. When shifting the focus to membrane-less intracellular condensates, three functional concepts have been proposed and more evidence for each class is provided continuously: condensates can act as *reaction crucibles*, or to *sequester* protein assemblies or as *organizational hubs*[8] (Figure 10A). In the following paragraph, we will discuss at least one example each and interestingly, we will also see that some condensates serve two different purposes at the same time, and therefore these classes are not mutually exclusive.

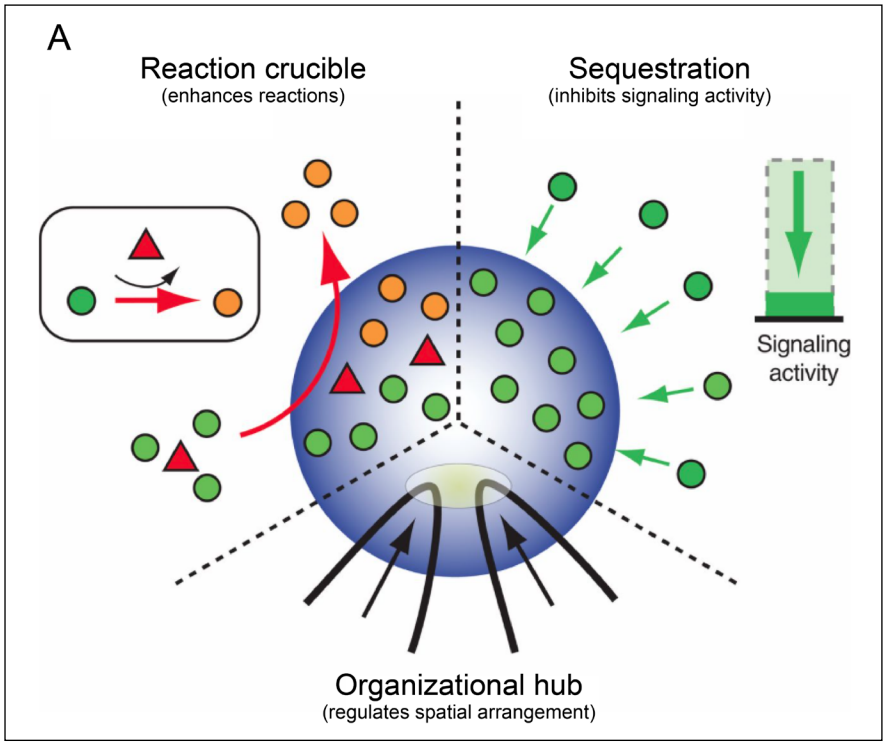

Figure 10. Functions of phase-separated condensates
(A) Intracellular phase-separated condensates can have different functions: they can be positive regulators of reactions as *reaction crucibles* or inhibit processes through *sequestration* or help with intracellular *spatial organization*[8]. Figure adapted from ref[8].

Reaction crucible

The formation of highly concentrated phases of proteins can help to facilitate chemical reactions[8]. For instance, a synthetic three-component system of multivalent signaling

proteins (nephrin, the adapter protein NCK and neural Wiskott–Aldrich syndrome protein, N-WASP), known for its importance in establishing the filtration barrier in the kidney, can undergo a phase transition *in vitro* from a mixed to a de-mixed state[70,73]. The phase separation is mediated via domain interactions of SH3-containing NCK and proline-rich motif (PRM)-containing N-WASP[70,73]. While NCK and N-WASP are sufficient for the phase transition per se, the phosphorylation state of nephrin can tune the threshold for initiating a phase transition[70]. Upon addition of Arp2/3, an actin filament branching factor, to the three-component system, actin filament polymerization is triggered within phase-separated droplets[70,73]. In summary, this synthetic multivalent system shows the functional coupling of phase-separated systems with the activation of actin filament assembly in a spatially localized manner[70,73]. In addition, such SH3/PRM-driven phase separation system has been shown to elicit downstream signaling cascades e.g. in T cell receptor (TCR) signaling[71]. In a reconstitution system, the protein LAT (linker for activation of T cells) mediates LLPS on a model membrane and triggers MAPK(ERK) signaling in T cells[71]. Many other intracellular membrane-less compartments have been suggested to work as reaction crucibles such as Cajal bodies, nucleoli and RNP bodies[8].

Sequestration

When a cell is exposed to environmental stresses, such as heat shock or nutrient deprivation, the cell reacts to these stimuli for instance by stalling the RNA translational machinery of certain RNAs[74]. This transient 'silencing' or sequestration of untranslating messenger ribonucleoproteins (mRNPs) happens within so-called stress granules[74]. One example is the sequestering of components of the TOR (target of rapamycin) pathway, known to regulate protein synthesis[8,75]. Upon osmotic stress, mTORC1 (mechanistic/mammalian target of rapamycin complex 1) gets recruited into stress granules, where its signaling function is inactivated[75]. This functional inhibition of signaling by a phase transition mechanism is mediated via a dual specificity tyrosine-phosphorylation-regulated kinase 3 (DYRK3), which keeps inactivated mTORC1 within stress granules[75]. Taken together, this mechanism might help the cell to regulate its growth cycle, and to shut down the growth signals in stress conditions with suboptimal nutrient, energy or oxygen availability[75].

Organizational hub

Besides serving as reaction or sequestration crucibles, intracellular assemblies can also help with spatial arrangement of non-membrane bound structures, such as the spindle apparatus[76]. BuGZ, a protein found in Xenopus (evolutionarily conserved) undergoes a phase transition process resulting in promotion of spindle assembly in vitro and in vivo[76]. BuGZ mainly consists of low complexity domains plus a microtubule-binding site and it has been proposed that it functions via concentrating initial building blocks of a spindle in a spatially restricted manner to allow for a transiently stable environment suitable to polymerize microtubules[76].

As briefly mentioned before, these conceptual classes are not strictly separated from each other[8]. There are many examples, where phase-separated entities belong to two or more of these classes at the same time[8] or they can change their function in a context-dependent manner[77,78]. For instance, the previously mentioned case of nephrin-NCK-N-WASP component system not only serves as a reaction crucible, but also works as an organizational hub by spatially regulating the initialization of the reaction[8,70,73]. Or in the

case of stress granules, usually such condensates sequester components from the cytoplasm which would otherwise regulate cell growth[8,75]. However, in case of some viral infections, stress granules get restructured and may be exploited for viral replication by concentrating and activating the translational machinery for viral replication; this is the opposite of the usual host's response of concentrating in-activated translational machinery[77,78].

After discussing the basic hallmarks of phase separation, we will now discuss phase transition behaviors of members of the Membrane-associated guanylate kinase (MAGUK) family to which ZO-1/2/3 belong as well.

1.3.6 Phase transition of MAGUK family members

MAGUKs are adapter or scaffolding proteins localized at various types of cell-cell junctions[79]. Members of this family, such as ZO proteins and the postsynaptic density protein (PSD-95), share a highly conserved PSG region: PDZ-SH3 (Src homology 3)-GUK (guanylate kinase)[79] (Figure 11A). In the following paragraphs, we will discuss their potential role as organizational hubs and/or as reaction crucibles in the synaptic density in neurons and in the assembly of cell-cell junctions.

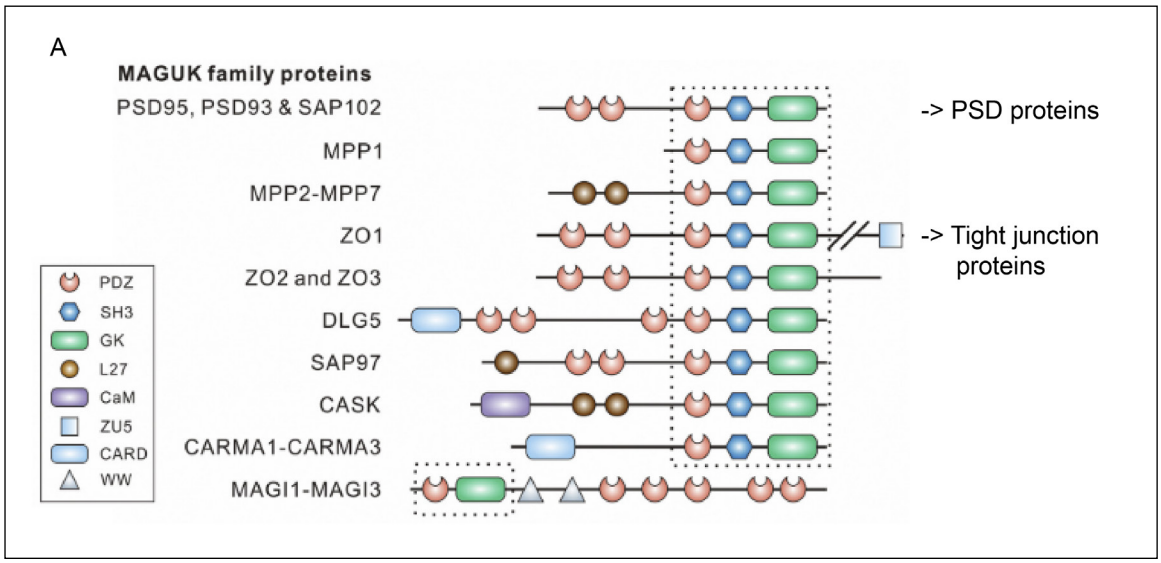

Figure 11. Domain structures of MAGUK family proteins
(A) Image depicts domain structures of different members of the MAGUK family sharing a conserved PSG region: PDZ-SH3-GUK[79]. Figure adapted from ref[79].

The synapse of neuronal cells consists of a presynaptic axonal terminus enriched with neurotransmitter-filled synaptic vesicles and a postsynaptic terminus, which harbors a protein-rich region, the so-called post synaptic density (PSD) (Figure 12A)[80]. Proper synaptic plasticity in the nervous system is given by a dynamic and rapid regulation of the PSD[80]. The MAGUK protein member PSD-95, together with another synaptic protein SynGAP, can undergo a phase transition process leading to formation of condensates in the post synaptic density[80] (Figure 12B). The phase transition-mediated clustering of the PSD proteins has been associated with proper plasticity of synapses[80]. Interestingly, in *in vitro* reconstitution experiments on lipid bilayers, PSD condensates consisting of four major PSD scaffolding proteins can serve in clustering receptors, such as NMDA glutamate receptors, and in actin filament bundling[81] (Figure 12A). When the SynGAP/PSD-95 complex is not phase-transition-

competent, its synaptic localization and activity-dependent dynamics are altered, resulting in hypersensitive synaptic responses[80]. Hence, efficient and dynamic clustering of receptors might explain the optimized plasticity responses of neuronal synapses, brought about by a phase transition mechanism of the synaptic proteins SynGAP and PSD-95[80,81].

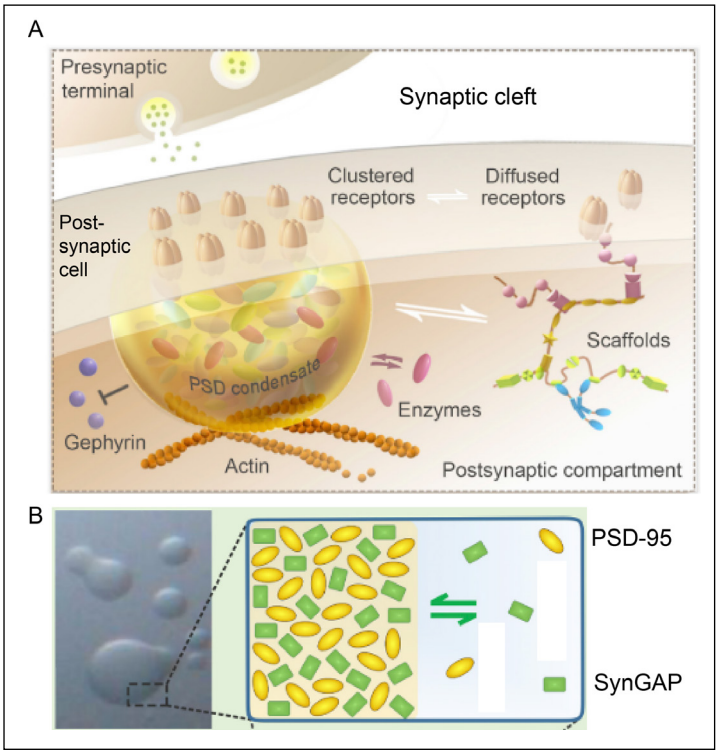

Figure 12. Function of phase-separated condensates during neuronal plasticity
(A) PSD proteins undergo a phase transition process, which helps in clustering PSD components and receptors, and induces actin filament assembly[81].
(B) Image depicts phase-separated droplets of synaptic proteins PSD-95 and SynGAP in an *in vitro* reconstitution assay[80]. Figure adapted from refs[80,81].

Interestingly, tight junction proteins ZO-1,2,3 also belong to the MAGUK family and Beutel et al. showed that ZO proteins can phase separate in *in vitro* reconstitution systems and in cell culture[82]. ZO-1's phase separation capacity is important for tight junction assembly by recruiting tight junction proteins to the initially formed droplets, as shown in MDCK cells and cysts[82]. ZO proteins contain multiple intra- and intermolecular interaction sites that contribute to their multivalency[82]. ZO-1 for instance harbors a PDZ2 domain that mediates homo- and hetero-dimerization[83], and the U6 domain (downstream of PSG domain)[82,84] and another region close to the C-terminus can fold backwards onto the PSG supramodule[85] (Figure 13A). ZO proteins, as members of the MAGUK family, share a conserved domain sequence of PDZ, SH3 and GUK, the PSG supramodule (Figure 11A). Crystal structure analysis suggests that the PSG module can form an intramolecular hairpin, via 'domain swapping'[79,86,87], thereby likely contributing to the multivalent character of ZO proteins. Strikingly, this PSG supramodule is sufficient for ZO protein phase separation[82] (Figure 13B). Interestingly though, the degree of phase separation is different in the full-length constructs compared to the PSG domains only (Figure 13B, compare droplet sizes; different saturation concentration[82]) [82]. In summary, these data show that while the PSG domain of ZO-1 is sufficient for inducing phase separation behavior *in vitro*, the presence of additional domains and intrinsically disordered structures increases phase separation capacity of ZO proteins[82] (Figure 13B). The observation that phase separation scales with the degree of multivalency is also consistent with previous studies[68,70,72].

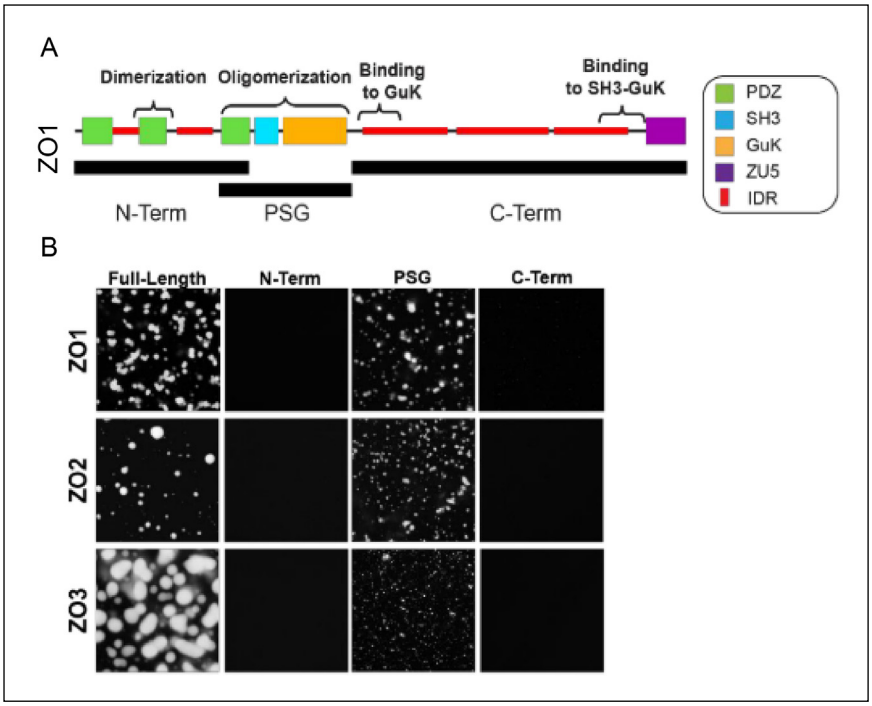

Figure 13. Phase separation of ZO proteins
(A) Image depicts intra- and intermolecular interaction sites of ZO-1 and truncation versions used in (B)[82].
(B) *In vitro* reconstitution assay of differently truncated ZO versions: N-terminus, PSG module or C-terminus only[82]. Figure modified from ref[82].

After discussing tissue morphogenesis and phase transitions in biology, we will now move to the topic of early zebrafish development in order to set up the grounds for the results section.

1.4 Zebrafish early development

After fertilization of the zebrafish egg the cytoplasm separates from the yolk in a process called cytoplasmic streaming[88]. Blastoderm cells then undergo several rounds of meroblastic cleavages[89] (Figure 14). During the following blastula period, surface epithelial layer cells, also called enveloping layer (EVL), start their differentiation program by expressing markers such as keratin[90]. At the 10th cell cycle (512-cell stage) the maternal-zygotic transition (MZT) is initiated[91], and at the same time, marginal blastomeres fuse with the yolk cell[89]. During this fusion process, the blastoderm cells release their content – nuclei and cytoplasm – into the yolk cell and the so-called yolk syncytial layer (YSL) is formed[92,93]. The YSL plays critical roles in patterning the early embryo: it secretes Nodal signals, which are required for later germlayer specification[92]. During the late blastula stage, the first morphogenetic movement, called epiboly, starts. Epiboly is the spreading of the blastoderm over the yolk cell to finally engulf it by the end of gastrulation[94]. At the onset of epiboly, the yolk takes on a typical dome-like shape through radially intercalating cells, leading to blastoderm thinning[95,96]. The process of dome formation is regulated through a force balance at the contact line between the blastoderm and the yolk cell[96]. Decreased EVL surface tension induces a force imbalance, which triggers blastoderm thinning and spreading[96]. Additionally, the central tissue of the blastoderm undergoes a fluidization process resulting in proper thinning of the central tissue, while this process is inhibited in marginal regions through non-canonical *Wnt* signaling[97]. The progression of epiboly stages is expressed by the percentage of how much the blastoderm has engulfed the yolk cell; hence, 30% epiboly for instance means that the blastoderm has covered 30% of the yolk cell[89]. At around 50% epiboly, the gastrulation period starts[89]. When the blastoderm reaches the yolk equator, the marginal tissues start

thickening and the germlayers separate – this process is called internalization and it is the second morphogenetic movement during early zebrafish development[89]. The germlayers separate, with mesendodermal cells moving to the inside (internalization) and then animal-wards and ectodermal tissues keep moving towards the vegetal pole[89,98]. During zebrafish gastrulation, a third morphogenetic movement, referred to as convergence and extension contributes to the shaping of embryo: cells intercalate along the mediolateral axis towards the dorsal side[89]. The end of gastrulation is reached, once the blastoderm has completely engulfed the yolk cell at 10 hours post fertilization (hpf) and at this point, the first head and tail structures become apparent[89]. All three morphogenetic movements are crucial for the embryo to reach its proper shape at the end of gastrulation[99]. The embryo then continues with somitogenesis and organogenesis in order to hatch at around 48 hpf and enter into early larval stages by 72 hpf[89].

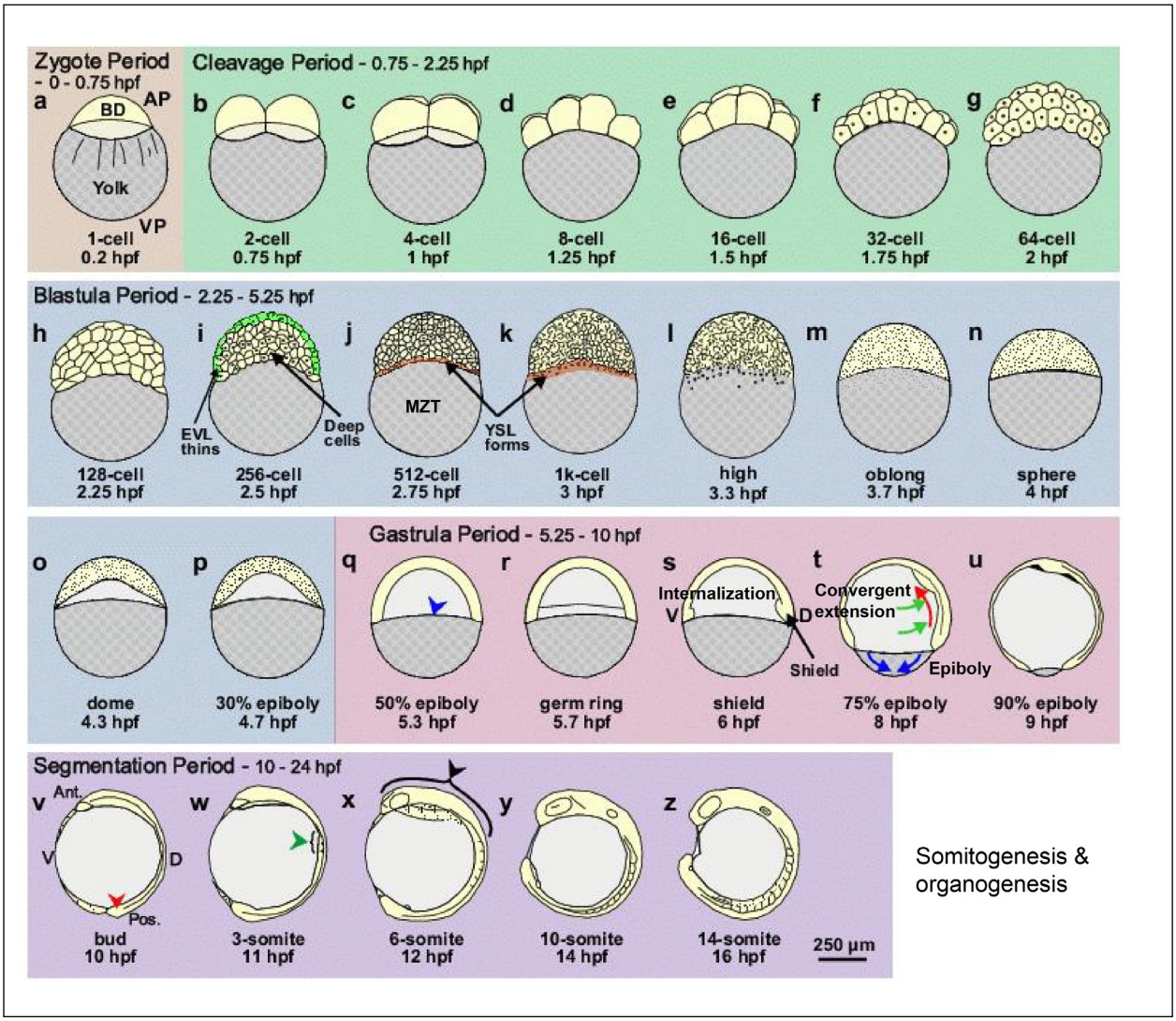

Figure 14. Zebrafish early development
Image depicts different stages of early zebrafish development starting with the zygote period (a), then progressing to the cleavage period (b-g) continuing to the blastula stages (h-p) and then to the gastrula stage (q-u), which ends at 10 hours post fertilization[100]. Figure adapted from ref[100].

The main focus of this PhD thesis lies on zebrafish epiboly; therefore, in the next section, we will mainly focus on details of epiboly movements and the regulation of its force-generating motor.

1.4.1.1 Zebrafish epiboly

In zebrafish epiboly, two different cell layers and one syncytial layer move together towards the vegetal pole: the YSL, the EVL and the deep cells[94,101] (Figure 15A). Epiboly movements are tightly coordinated; however, two layers involved – the EVL and the YSL - show rather autonomous movements: in E-cadherin mutants or morphants, the EVL and YSL manage to finish epiboly movements, while deep cells stop epibolizing[102,103]. Similarly, in the teleost *Fundulus heteroclitus*, the YSL can also spread in the absence of the overlying structures and thereby exhibits an autonomous character[104,105]. In zebrafish early development, the YSL and its actomyosin network therein is one of the driving forces of EVL epiboly [94,101,106]. Before going into detail about how cytoskeletal structures regulate epiboly movements, we will first take a look at the anatomy of the yolk cell during epiboly. At the onset of epiboly, the yolk cell can be divided into different regions: the already mentioned YSL, a syncytial layer containing yolk syncytial nuclei (YSN) covering the animal side of the yolk and the so-called yolk cytoplasmic layer (YCL), a thin cytoplasmic layer lacking YSN and covering the more vegetal portion of the yolk cell[92]. The YCL and YSL are continuous structures without any physical barrier[92]. At this point, the YSL itself consists of the internal YSL (iYSL), which later will undergo convergent extension and epiboly movements[92,94], and of the external YSL (eYSL) with its eYSN staying on the periphery and it will mainly exhibit epiboly movements at later stages[92,94] (Figure 15A).

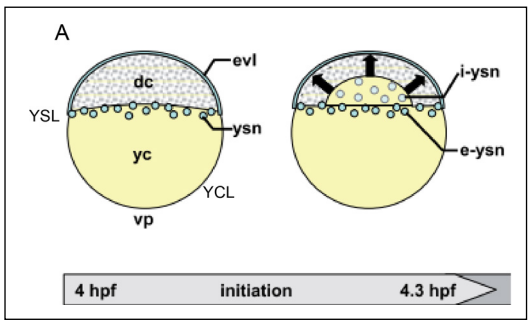

Figure 15. Initiation phase of zebrafish epiboly
(A) Image depicts the anatomy of the yolk cell (yc) during epiboly initiation phase. The YSL covers the animal pole of the yolk cell, and the YCL the vegetal half[94]. Deep cells (dc) sit in between the EVL and the yolk cell[94]. The internal yolk syncytial nuclei (iYSN) are located centrally and the external YSN (eYSN) on the periphery[94]. The eYSL, together with the eYSN, will mainly undergo epiboly movements, while the iYSN will show convergent extension and epiboly movements during the progression phase[94]. Vp: vegetal pole. Figure modified from ref[94].

Several early studies showed that actomyosin structures within the embryo are crucial for epiboly movements: whole embryo drug treatments (cytochalasin, blebbistatin) were used to inhibit actin polymerization or myosin contractility resulting in delay or complete stalling of epiboly movements[102,107]. While these studies gave first hints that actomyosin structures within the embryo in general are important for epiboly, it remained to be addressed if the yolk cell cortex and the YSL cortex specifically contribute to these tissue movements. Recently, several tissue specific and spatially refined methods offered new informative results on the contribution of the YSL actomyosin cortex for EVL movement: upon continuous ablation of the eYSL actomyosin cortex, EVL vegetalward movement slows down suggesting that the eYSL actomyosin cortex promotes EVL epiboly[106]. Additionally, since zebrafish embryos are amenable to manipulations this allows for injection of mRNA, dyes or morpholinos directly into the yolk cell, thereby affecting only the yolk cell and the YSL[102,108].

Reducing contractility specifically within the yolk cell by injecting a constitutively active (ca) version of Mypt-1 – a protein within the myosin phosphatase complex - has previously been shown to delay epiboly movements (*Behrndt M., PhD thesis*). This further confirms that the yolk cell and its YSL cortex specifically contribute to epiboly of the overlying tissues (*Behrndt M., PhD thesis*). More examples for YSL-specific epiboly contribution will be provided in the next subchapter (1.4.1.1.1). Initially, it has been proposed that the actomyosin ring contracts and constricts along its circumference and thereby pulls on the EVL above[94]. In addition to such circumferentially working 'cable-constriction' motor, a 'flow-friction' motor has been demonstrated to be sufficient in driving epithelial tissue spreading[106]. In this model, retrograde actomyosin flows generate an opposite-directed friction force that elicits a pulling and vegetal-directed force on EVL cells[106]. For a detailed view on how the YSL actomyosin ring contributes to EVL epiboly, the reader is referred to chapter 1.2.1. Since the YSL actomyosin ring is suggested to be the main driver of epiboly[94,101,106], we will now discuss how ring formation is regulated.

1.4.1.1.1 Formation and regulation of the YSL actomyosin ring

Known upstream regulating factors of actomyosin ring formation within the YSL are transcription factors, kinases and GPCR (G-protein coupled receptor) signaling pathways: *Tnika (TRAF2 and NCK interacting kinase a)* a Ste20-like kinase, and *MAPKAPK2*, a serine-threonine kinase, and *mxtx2* (*mix-type homeobox gene 2*) a homeobox transcription factor, and *Pou5f1/Oct4* a pluripotency transcription factor, and the GPCR subunit $G_{\alpha 12/13}$[94,102,109–114]. Upon YSL specific knock down of *Tnika* kinase or *mxtx2* transcription factor, the YSL actomyosin ring does not form properly and EVL movement is impaired[102,109,110] resulting in slower or stalled epiboly movements and in case of mxtx2 eventually in later constriction of the yolk cell[109]. Interestingly, in *Tnika* morphants, diminished actomyosin ring formation also correlates with aberrant EVL cell shapes indicating that the pulling from the actomyosin ring affects EVL cell shape[102]. However, it is not yet clear, whether *Tnika (also known as misshapen 1)* directly or indirectly affects actomyosin activity[102]. Also the downstream cascade of *mxtx2* still needs to be elucidated in order to understand how actomyosin is regulated through *mxtx2*; an upstream regulator of *mxtx2* is *eomesodermin*[110]. In MZ*spg* (*spiel ohne grenzen*) fish, the Pou Domain class 5 transcription factor 1 (*Pou5f1/Oct4*) is mutated resulting in a delay of all three epibolizing structures and in diminished actomyosin ring formation, atypical EVL shapes and microtubule yolk network[112,113]. The epiboly phenotypes in part result from aberrant E-cadherin trafficking in the EVL and deep cells[113]; therefore, it is not yet clear if *Pou5f1* has a direct effect on the actomyosin ring formation or a secondary effect through other processes failing in adjacent structures. Interestingly, a striking opposite effect on epiboly was observed in embryos mutated in the *betty boop* locus, a serine-threonine kinase gene, (*MAPKAPK2 - Mitogen Activated Protein Kinase Activated Protein Kinase 2*), in which case the blastoderm and yolk cell prematurely constricts, resulting in yolk cell lysis[111]. The yolk cell constriction was accompanied by abnormally high and ectopic calcium release within the YSL[111]. Given that calcium is known to regulate actomyosin contractility for instance through activating Myosin light-chain kinase[115], the premature constriction of the ring structure has been attributed to an over-activation of YSL actomyosin ring[111]. Taken together, these studies underline the importance of a finely tuned regulation of the YSL actomyosin structure that appears necessary to balance between too little contractility potentially resulting in a slower movement of tissues

versus too high contractility that will result in a premature constriction of the actomyosin structure and end in yolk cell lysis and death of the embryo.
Closer monitoring of the YSL reveals a maturation of the actomyosin ring: an initially 80 µm thick actomyosin band matures in a thinner (~ 20 µm) ring-like structure adjacent to the leading edge of EVL cells[106]. The adjacent yolk cell cortex is less dense in actin and myosin signal compared to the YSL cortex[94] (Figure 16A), probably due to retrograde actomyosin flows[106] locally depleting the cortical pool. YSL cortical tension along the circumference of the yolk cell increases over time[106], providing further evidence for ring maturation into a higher contractile structure. The formation and maturation of ring structures at junctions are usually mediated through actin and myosin regulators from the family of small GTPases and its effectors[35]. Indeed, *arhgef11*, a RhoGEF is involved in actomyosin ring formation and works downstream of GPCR signaling through the $G_{\alpha 12/13}$ subunit[114]. In addition, an effector protein of Rho GTPases, a formin called *Diaphanous* (*Diaph2)* has been implicated in zebrafish epiboly[116]*. Diaph2* morphant embryos display delayed epiboly in conjunction with diminished actomyosin ring formation[116]. Formin, which is a well-described actin nucleator, could in this context help to assemble the YSL actin ring. On the other hand, also a negative regulator of actin dynamics *Chimerin 1*, a Rac-specific GAP, is involved in epiboly movements[117]. Reduction of Chimerin1 levels lead to increased epiboly speed and an abnormally large cell mass at the vegetal pole[117]. Hence, *Chimerin 1* through its negative regulation of actin dynamics potentially keeps epiboly speed at a certain pace to ensure properly coordinated tissue movements[117].

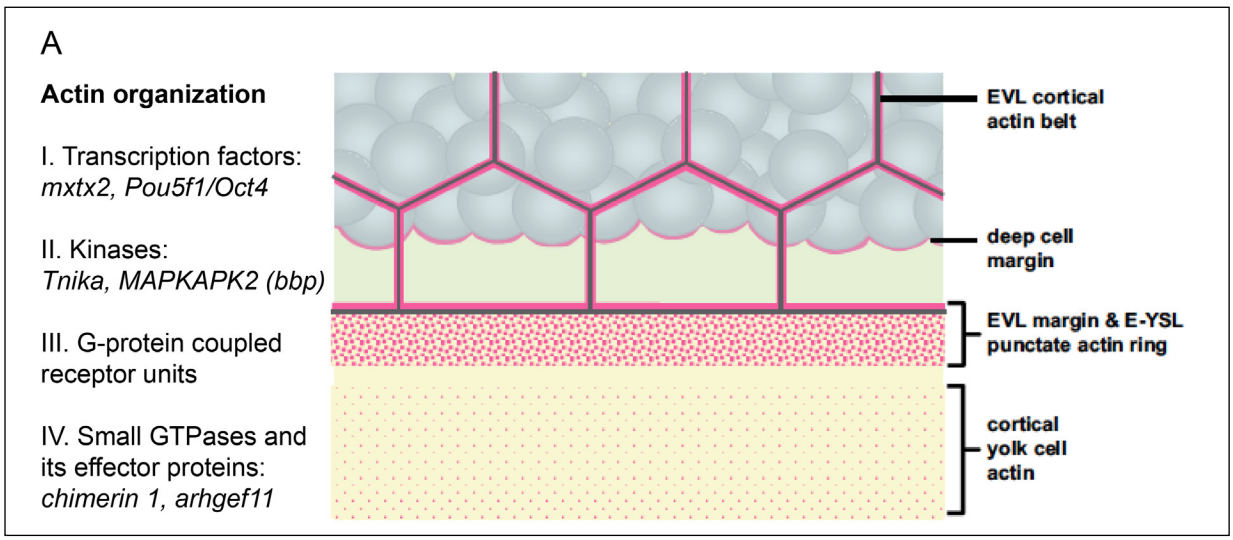

Figure 16. Actin organization at the EVL-YSL boundary
(A) Image depicts different actin structures at the EVL-YSL boundary[94]. EVL cells show a cortical actin belt[94]. The eYSL actin ring has higher density compared to the neighboring YCL actin cortex[94]. Different regulators of actin dynamics and organization are mentioned in sections on the left: I. transcription factors, II. kinases, III. G-protein coupled receptor units, IV. small GTPases and its effector proteins[94]. Figure adapted from ref[94].

Taken together, while above mentioned studies provide evidence supporting the view that the epiboly-driving force originates from the YSL actomyosin ring the exact spatiotemporal regulation of the YSL actomyosin ring still remains to be clearly demonstrated. Further, it was not yet clear how the actomyosin ring is coupled to the overlying EVL tissue and how junction formation and maturation would affect epiboly movements. In our study we tried to address both of these questions and the results are presented in the next section.

2 Results

The results section consists of the main project during this PhD thesis entitled '*Mechanosensation of tight junctions depends on ZO-1 phase separation and flow*' (chapter 2.1), and a second chapter (2.2) on the phase separation behavior of other ZO proteins and the recruitment of mechanoeffectors.

2.1 Mechanosensation of tight junctions depends on ZO-1 phase separation and flow[118]

Publication:

Schwayer C, Shamipour S, Pranjic-Ferscha K, Schauer A, Balda M, Tada M, Matter K and Heisenberg CP. Mechanosensation of tight junctions depends on ZO-1 phase separation and flow. *Cell* **179**, 937-952.e18 (2019)
DOI: https://doi.org/10.1016/j.cell.2019.10.006

Article

Cell

Mechanosensation of Tight Junctions Depends on ZO-1 Phase Separation and Flow

Graphical Abstract

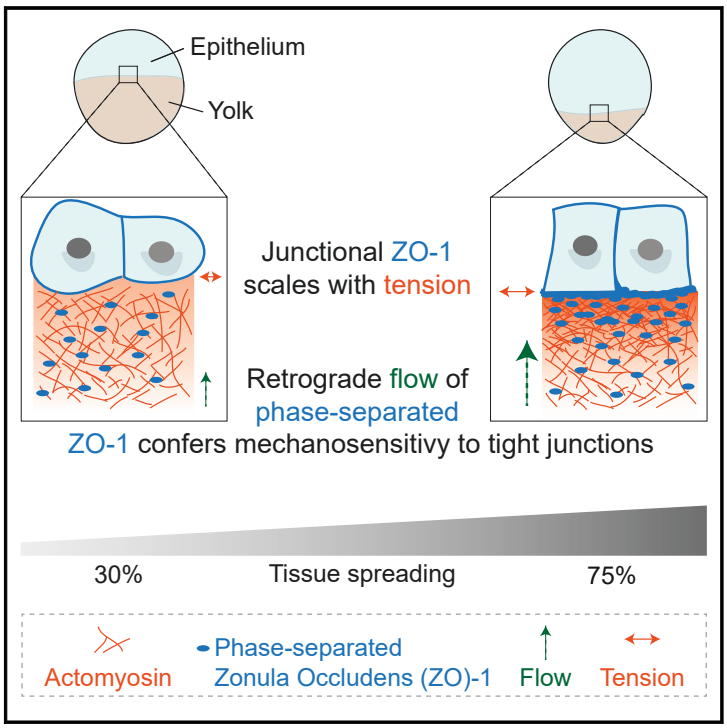

Highlights

- Non-junctional Zonula Occludens-1 (ZO-1) protein undergoes phase separation
- Actomyosin flow transports phase-separated ZO-1 toward tight junctions (TJs)
- Mechanosensitivity of TJs depends on flow and incorporation of phase-separated ZO-1
- TJ mechanosensitivity is required for epithelial tissue spreading in zebrafish

Authors

Cornelia Schwayer, Shayan Shamipour, Kornelija Pranjic-Ferscha, ..., Masazumi Tada, Karl Matter, Carl-Philipp Heisenberg

Correspondence

heisenberg@ist.ac.at

In Brief

Non-junctional ZO-1 protein clusters travel with actomyosin flows toward tight junctions, thereby confering mechanosensitivity to those junctions required for their function during zebrafish gastrulation.

Schwayer et al., 2019, Cell *179*, 937–952
October 31, 2019
https://doi.org/10.1016/j.cell.2019.10.006

CellPress

Article

Cell

Mechanosensation of Tight Junctions Depends on ZO-1 Phase Separation and Flow

Cornelia Schwayer,[1] Shayan Shamipour,[1] Kornelija Pranjic-Ferscha,[1] Alexandra Schauer,[1] Maria Balda,[3] Masazumi Tada,[2] Karl Matter,[3] and Carl-Philipp Heisenberg[1,4,*]

[1]Institute of Science and Technology Austria, Klosterneuburg, Austria
[2]Department of Cell and Developmental Biology, University College London, London, UK
[3]Institute of Ophthalmology, University College London, London, UK
[4]Lead Contact
*Correspondence: heisenberg@ist.ac.at
https://doi.org/10.1016/j.cell.2019.10.006

SUMMARY

Cell-cell junctions respond to mechanical forces by changing their organization and function. To gain insight into the mechanochemical basis underlying junction mechanosensitivity, we analyzed tight junction (TJ) formation between the enveloping cell layer (EVL) and the yolk syncytial layer (YSL) in the gastrulating zebrafish embryo. We found that the accumulation of Zonula Occludens-1 (ZO-1) at TJs closely scales with tension of the adjacent actomyosin network, revealing that these junctions are mechanosensitive. Actomyosin tension triggers ZO-1 junctional accumulation by driving retrograde actomyosin flow within the YSL, which transports non-junctional ZO-1 clusters toward the TJ. Non-junctional ZO-1 clusters form by phase separation, and direct actin binding of ZO-1 is required for stable incorporation of retrogradely flowing ZO-1 clusters into TJs. If the formation and/or junctional incorporation of ZO-1 clusters is impaired, then TJs lose their mechanosensitivity, and consequently, EVL-YSL movement is delayed. Thus, phase separation and flow of non-junctional ZO-1 confer mechanosensitivity to TJs.

INTRODUCTION

A key step in the emergence of multicellularity is the development of different junctional complexes mechanically connecting cells and allowing the transfer of biochemical and mechanical signals between cells. The molecular composition and dynamic regulation of different cell-cell junction types, such as adherens junctions (AJs), tight junctions (TJs), and desmosomes, have been studied extensively over the past decades (Franke, 2009; Godsel et al., 2004; Niessen, 2007; Van Itallie and Anderson, 2014). Likewise, detailed insight has been gained into the intracellular signaling cascades activated by the different junctional complexes and their function in tissue homeostasis (Johnson et al., 2014; Matter and Balda, 2003; Wheelock and Johnson, 2003; Zihni et al., 2016). There is also compelling evidence that changes in the molecular composition, size, and turnover of junctional complexes directly affect their mechanical integrity and signaling activity (Baum and Georgiou, 2011; Cunningham and Turner, 2012; Nekrasova and Green, 2013; Shen et al., 2008). In contrast, much less is known about how mechanical forces influence cell-cell junction formation and signaling.

Recent studies of AJs indicate that mechanical forces and actin dynamics at E-cadherin-mediated cell-cell contacts can promote E-cadherin clustering, leading to formation of larger and more stable junctional complexes (Cavey and Lecuit, 2009; Cavey et al., 2008; Engl et al., 2014; Ladoux et al., 2010). An important step in this mechanosensing process is the modulation of AJ anchoring to the cortical actomyosin network, with junctional tension changing the conformation of AJ components, such as α-catenin and vinculin, increasing their binding capacity to the actomyosin network (Gomez et al., 2011; Watabe-Uchida et al., 1998; Weiss et al., 1998; Yonemura et al., 2010). Tension-dependent changes in the composition and organization of AJs are thought to affect both their coupling strength and signaling activity (Gomez et al., 2011). Although recent studies suggest that certain components of other junction types, such as TJs, can, in principle, undergo conformational changes upon mechanical loading (Spadaro et al., 2017), it is not yet entirely clear how this molecular mechanosensitivity translates into changes in global junction organization and function.

TJs play an essential role in tissue homeostasis by limiting the passage of molecules and ions between cells and restricting the movement of molecules between the apical and basolateral domains, thereby maintaining apicobasal polarity of epithelial cells (Shin et al., 2006). Similar to AJs, TJs are composed of transmembrane proteins, such as Occludins and Claudins, and cytoplasmic scaffolding proteins connecting the transmembrane proteins to the cytoskeleton (e.g., Zonula Occludens [ZO] proteins and Cingulins; Zihni et al., 2016). TJs also function as intracellular signaling centers regulating the activity of small Rho GTPases, such as RhoA and Cdc42, thereby affecting actomyosin network organization and contraction at the junction (Zihni and Terry, 2015). Conversely, actomyosin regulators, such as RhoA, Cdc42, and Rac, have been shown to be important for TJ formation (Zihni et al., 2016); however, to what extent mechanical signals (for instance, by triggering conformational changes of TJ components; Spadaro et al., 2017) are involved in this process still needs to be established.

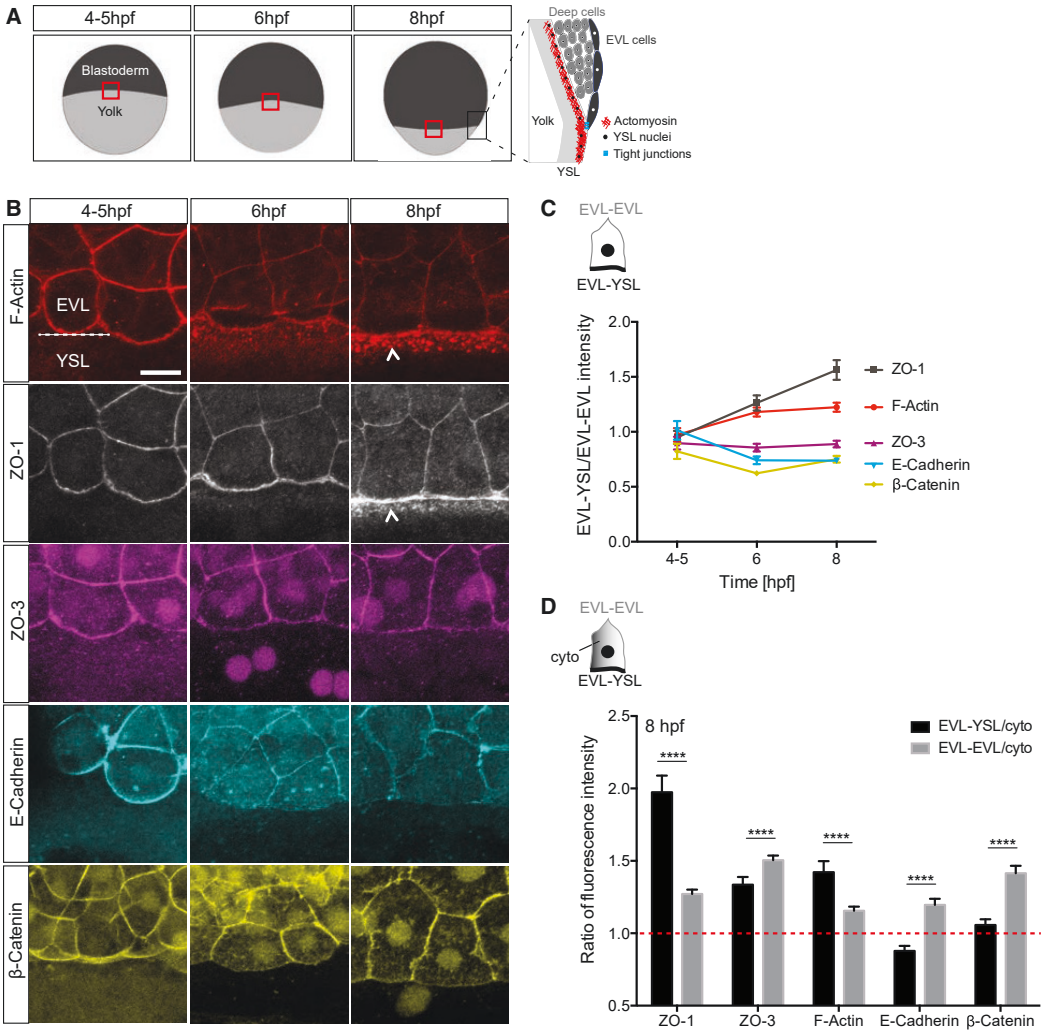

Figure 1. TJ Components Accumulate at the EVL-YSL Boundary

(A) Schematic representation of enveloping cell layer (EVL) spreading during consecutive stages of epiboly (4–5, 6, and 8 hpf). Yolk cell, light gray; blastoderm (EVL and deep cells), dark gray. The black rectangle demarcates the region of the enlarged sagittal view outlining the tissue structure at 8 hpf. The red rectangle demarcates regions of the EVL-YSL boundary shown in (B).

(B) Maximum intensity projections (MIPs) of F-actin, ZO-1, ZO-3, E-cadherin, and β-catenin localization at the EVL-YSL boundary at 4–5, 6, and 8 hpf. ZO-1, ZO-3, E-cadherin, and β-catenin were detected by immunohistochemistry, and F-actin by Phalloidin. White arrowheads point to increased accumulation at the EVL-YSL boundary. Scale bar, 20 μm.

(C) Plot of EVL-YSL junctional intensity normalized to EVL-EVL junctional intensity as a function of time during EVL epiboly (see also schematic above). Data are mean at 95% confidence. F-actin with N = 2, n = 15 at 4–5 hpf, n = 42 at 6 hpf, and n = 46 at 8 hpf. ZO-1 with N = 2, n = 15 at 4–5 hpf, n = 42 at 6 hpf, and n = 46 at 8 hpf. ZO-3 with N = 2, n = 26 at 4–5 hpf, n = 52 at 6 hpf, and n = 58 at 8 hpf. E-cadherin with N = 3, n = 29 at 4–5 hpf; with N = 2, n = 32 at 6 hpf; and with N = 3, n = 84 at 8 hpf. β-Catenin with N = 2, n = 54 at 4–5 hpf, n = 29 at 6 hpf, and n = 28 at 8 hpf.

(D) Plot of EVL-YSL junctional intensity (black) and EVL-EVL junctional intensity (gray) normalized to cytoplasmic intensity at 8 hpf. The red dashed line indicates a ratio of 1, demarcating the boundary between accumulation (>1) and depletion (<1). Data are mean at 95% confidence. N/n same as in (C), except for E-cadherin with N = 2, n = 40. Mann-Whitney test for F-Actin, ZO-3, and E-cadherin; unpaired t test for ZO-1 and β-catenin.

****$p < 0.0001$; n, number of cells.

See also Figure S1.

During zebrafish epiboly, the enveloping cell layer (EVL), a simple squamous epithelial monolayer covering the blastoderm at the animal pole of the yolk cell, spreads together with the underlying deep cells over the entire yolk cell (Figure 1A; Bruce, 2016; Lepage and Bruce, 2010). EVL spreading is driven by a large actomyosin ring-like structure positioned within the yolk syncytial layer (YSL) on the surface of the yolk cell and presumably coupled to the EVL leading edge by TJs (Figure 1A; Behrndt

et al., 2012; Cheng et al., 2004; Holloway et al., 2009; Köppen et al., 2006). The actomyosin ring drives EVL spreading by actively pulling on the EVL leading edge through two distinct motor activities: (1) a cable constriction motor, where the actomyosin band constricts around its circumference, generating pulling forces on the EVL margin when the band has crossed the yolk cell equator; and (2) a flow friction motor, where a gradient of actomyosin tension along the width of the actomyosin band gives rise to retrograde actomyosin flow (Behrndt et al., 2012). This actomyosin flow, when resisted by friction to adjacent structures within the YSL, generates a traction force pulling the EVL margin toward the vegetal pole (Behrndt et al., 2012). The pulling forces generated by the actomyosin band within the YSL are likely transmitted to the margin of the EVL by junctional complexes connecting the leading edge of the EVL to the YSL (Behrndt et al., 2012; Köppen et al., 2006). Whether and how junction formation at the EVL-YSL boundary relates to actomyosin ring formation and function within the YSL is still unknown.

Here we show that TJ rather than AJ components accumulate at the EVL-YSL boundary during the course of EVL epiboly and that this accumulation closely scales with the degree of actomyosin tension within the YSL. We further show that the accumulation of TJ components at the EVL-YSL boundary is mediated by tension-dependent retrograde actomyosin flow within the YSL, transporting non-junctional phase-separated ZO-1b clusters toward the boundary. Finally, we show that the junctional incorporation of those clusters depends on ZO-1b binding to actin and that the mechanosensitive response of TJs at the EVL-YSL junction is required for proper EVL spreading.

RESULTS

TJ Components Accumulate at the EVL-YSL Boundary

We have noted previously that both AJ and TJ components localize to the boundaries between EVL cells and at the leading edge of the EVL where it contacts the YSL (EVL-YSL boundary; Köppen et al., 2006). To investigate which junctions form at the EVL-YSL boundary during the course of EVL epiboly, we systematically analyzed how the localization of various AJ and TJ components changes. Interestingly, we found that the accumulation of components typically associated with AJs, such as E-cadherin, α-catenin, and β-catenin, decreased at the EVL-YSL boundary during epiboly (Figures 1A–1D and S1A–S1D). In contrast, the accumulation of various components typically associated with TJs either increased (ZO-1b and Cingulin-like 1) or remained unchanged (ZO-3, Claudin-D, and Occludin-A) at this boundary during epiboly (Figures 1A–1D and S1A–S1D). This suggests that, during the course of EVL epiboly, TJs become the predominant junction type connecting the EVL leading edge to the YSL.

ZO-1b and ZO-3 Are Required for Proper EVL Epiboly Movements by Regulating Actomyosin Flow and Tension within the YSL

To determine whether this accumulation of TJ components at the EVL-YSL boundary during epiboly is functionally relevant for EVL epiboly movements, we sought to interfere with the expression of those components and analyze the resultant changes in EVL epiboly movements. Given the known signaling function of TJs in regulating actin network organization and contraction (Zihni and Terry, 2015), we speculated that TJs might function in EVL epiboly movements by controlling actomyosin ring formation and flow within the YSL, shown previously to drive EVL epiboly movements (Behrndt et al., 2012). To test this possibility, we injected morpholinos (MOs) directed against the TJ components *zo-1b* and *zo-3*, implicated previously in TJ organization and signaling to the actomyosin cytoskeleton (Itoh et al., 2012; Otani et al., 2006; Tornavaca et al., 2015; Wittchen et al., 2003), directly into the YSL to specifically interfere with ZO-1b/3 expression at the EVL-YSL boundary (Figure 2A). YSL morphant embryos displayed clearly reduced EVL epiboly movements that could be partially rescued by co-injecting GFP-tagged *zo-1b* and *zo-3* mRNA (Figures 2A–2A''; Video S1). In contrast, injection of *zo-1b* and *zo-3* mismatch MOs or a standard negative control MO into the YSL did not elicit a recognizable epiboly phenotype (Figure S2A), supporting the specificity of the *zo-1b/3* MO effect. Slower EVL spreading was accompanied by diminished retrograde actomyosin flow and ring formation within the YSL (Figures 2C–2D'; Video S2), a phenotype that could be partially rescued by co-injecting GFP-tagged *zo-1b* and *zo-3* mRNA (Figures 2C–2D'; Video S2). Notably, the epiboly phenotype in *zo-1b/3* morphant embryos was not due to a general developmental delay because YSL morphant embryos formed the first somite, visualized by *papc* expression, at the same time as their control-injected siblings (Figures S2B and S2B'). Together, these observations suggest that TJ formation at the EVL-YSL boundary is required for EVL epiboly movements by regulating actomyosin flow and ring formation within the YSL.

To determine whether the obtained morphant phenotypes are specific, we generated maternal-zygotic (MZ) mutants for the TJ components ZO-1b and ZO-3 using the CRISPR/Cas9 technique (Figure S2C). We found that, in MZ*zo-1b* and MZ*zo-3* single mutants, EVL spreading appeared to be largely unaffected (Figure S2D). In contrast, MZ*zo-1b/3* double mutants displayed an epiboly phenotype closely resembling the phenotypes observed in embryos where ZO-1b and ZO-3 expression was knocked down either uniformly or locally within the YSL using MOs (Figures 2A–2B'' and S2G''). This phenotypic similarity between mutant and morphant embryos suggests that the obtained *zo-1b/3* morphant phenotypes are specific and, thus, that the *zo-1b* and *zo-3* MOs can be used to analyze the function of those proteins in EVL-YSL epiboly. Additionally, when *zo-1b/3* was ubiquitously knocked down or knocked out (MZ*zo-1b/3* mutants), the majority of morphant or mutant embryos were found to form the first somite on time (Figures S2E and S2E'), suggesting that, similar to the situation in YSL morphant embryos, the observed epiboly phenotype is not due to a general delay in the development of mutant or morphant embryos. Notably, TJs were reduced but not completely absent at the EVL-YSL boundary in *zo-1b/3* YSL morphants (Figures S2F and S2F') and mutants (Figures S2G and G'), likely because of incomplete knockdown in morphant embryos and functional redundancy and/or compensatory upregulation in expression of the remaining *zo* genes (*zo-1a*, *zo-2a*, and *zo-2b*) in mutant embryos (Figure S2H).

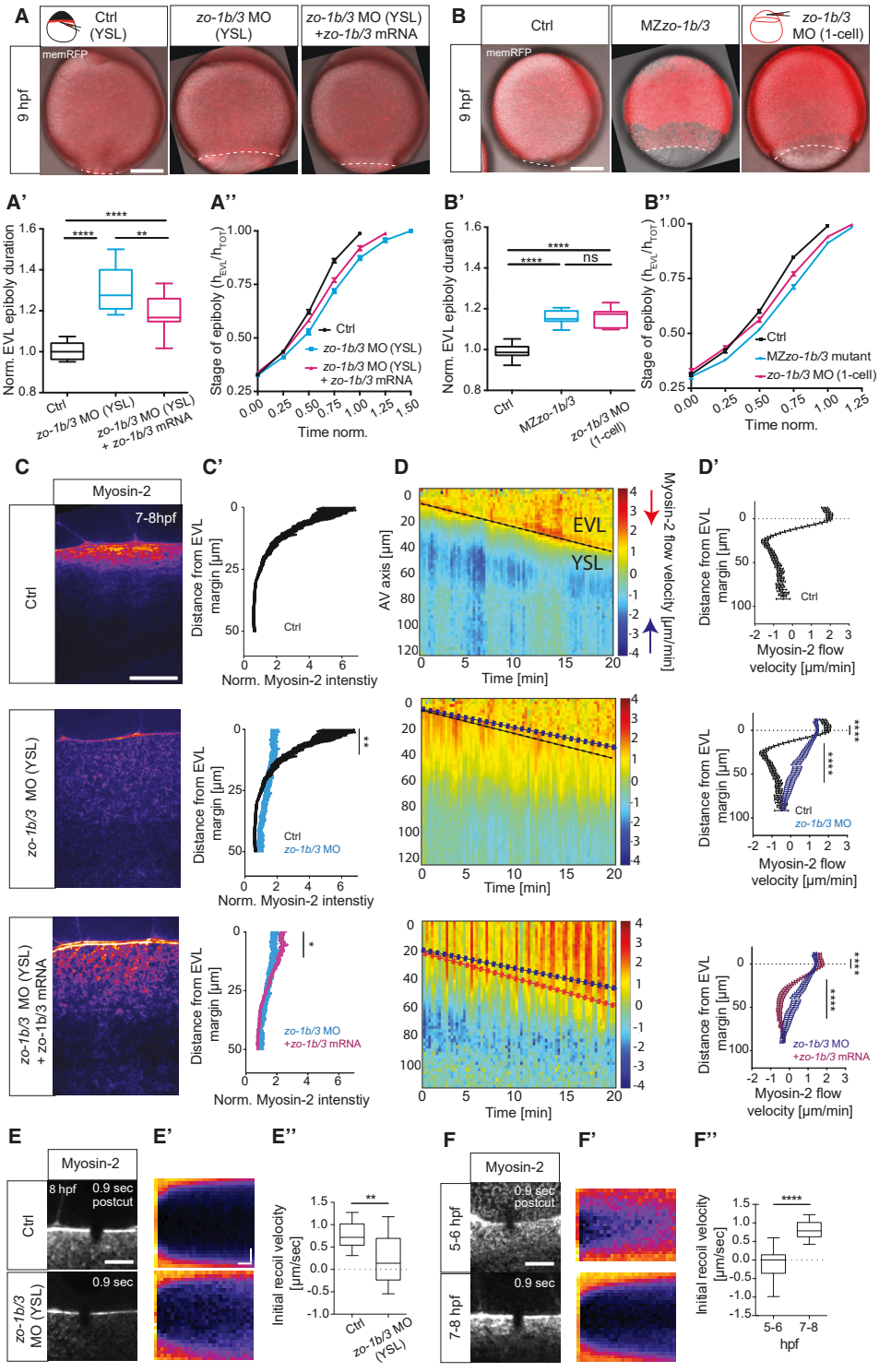

(legend on next page)

It has been shown previously that gradients of actomyosin contractility can trigger actin flows (Lecuit et al., 2011; Mayer et al., 2010; Munro et al., 2004). Hence, we asked whether TJ components control actomyosin flow within the YSL by modulating tension at the EVL-YSL boundary. To address this possibility, we measured tension at the EVL-YSL boundary oriented along the circumference of the yolk cell in wild-type and *zo-1b/3* YSL morphant embryos using UV laser ablation. We found that junctional tension was strongly reduced in *zo-1b/3* YSL morphants compared with wild-type embryos at late stages of epiboly (8 hours post fertilization [hpf]; Figures 2E–2E'', S2I, and S2I'). Together, these data indicate that normal TJ formation is required for proper buildup of tension at the EVL-YSL boundary and, consequently, for actomyosin flow within the YSL needed for proper EVL epiboly movements.

Actomyosin Contractility Controls ZO-1 Recruitment to the EVL-YSL Boundary

Our junctional tension measurements at the EVL-YSL boundary in wild-type embryos also revealed that tension was considerably higher at late (8 hpf) compared with early-mid (6 hpf) stages of epiboly (Figures 2F–2F'', S2J, and S2J'), consistent with our previous observation that actomyosin network tension within the YSL increases during the course of epiboly (Behrndt et al., 2012). Interestingly, this increase in junctional tension coincides with TJ component accumulation at the EVL-YSL boundary (Figures 1A–1D and S1A–S1D), pointing to the intriguing possibility that TJs might be mechanosensitive. To determine whether and how increased junctional tension at the EVL-YSL boundary relates to TJ formation at this interface, we sought to modulate actomyosin contractility within the YSL and determine the resultant effects on TJ formation at the EVL-YSL boundary. To modulate actomyosin contractility specifically within the YSL, we performed YSL injections of mRNAs encoding constitutively active (ca) versions of either myosin phosphatase (caMypt) (Jayashankar et al., 2013; Smutny et al., 2017) or RhoA (caRhoA) (Takesono et al., 2012), shown previously to decrease or increase actomyosin contractility, respectively. Strikingly, we found that, in embryos with reduced actomyosin contractility and retrograde flow rates within the YSL (Figures S3A–S3B' and 2C–2D', control [Ctrl]), accumulation of ZO-1b at the EVL-YSL boundary was clearly reduced (Figures 3A–3A''). Conversely, ZO-1b at the EVL-YSL boundary showed premature and strong accumulation in embryos with increased actomyosin contractility and retrograde flow rates within the YSL (Figures 3B–3B'' and S3C–S3D'). AJ components, in contrast, did not display any recognizable changes in response to altered actomyosin tension at the EVL-YSL junction (Figures S3E and S3E'). Collectively, these findings indicate that actomyosin network contractility and retrograde flow within the YSL triggers TJ component accumulation

Figure 2. ZO-1b and 3 Are Required for Proper EVL Epiboly Movements and Actomyosin Flows and Tension within the YSL

(A and B) MIPs of bright-field/fluorescence images of embryos injected directly into the YSL at 3.3 hpf with phenol red and *H2A*-mcherry mRNA as control (Ctrl), *zo-1b* and *zo-3* MOs, and *zo-1b/3* MOs together with GFP-tagged *zo-1b* and *zo-3* mRNA (mutated for the MO recognition site) at 9 hpf (A) and wild-type control embryos (Ctrl) and MZ*zo-1b/3* mutant and 1-cell *zo-1b/3* morphant embryos at 9 hpf (B). The plasma membrane is marked by membrane-RFP (red fluorescent protein) to outline cells. The EVL-YSL boundary is marked by a white dashed line to demarcate the extent of EVL epiboly under the different conditions. Schemes of different injection methods show injection into the YSL (A) to obtain YSL-specific knockdown and into the 1-cell stage embryo (B) to gain ubiquitous knockdown. Scale bar, 200 μm.

(A' and B') Plot of the total time required for EVL to complete epiboly for the conditions shown in (A) and (B) and normalized to the average time needed by Ctrl embryos. (A') YSL-Ctrl with N = 3, n = 11; YSL-morphant with N = 3, n = 12; YSL morphant rescue with N = 3, n = 11. (B') Wild-type (WT) Ctrl with N = 4, n = 11; 1-cell stage injected Ctrl for morphant with N = 3, n = 11; mutant with N = 4, n = 13; 1-cell morphant with N = 3, n = 8. Data are shown as box-and-whisker plots (whiskers, Tukey); one-way ANOVA with Tukey's multiple comparisons test.

(A'' and B'') Plot of EVL tissue spreading, expressed as height of EVL (h_{EVL}) normalized to total embryo height (h_{TOT}) as a function of time normalized to the average time needed by Ctrl embryos for the conditions shown in (A) and (B). N/n as in (A') and (B'). Data are mean ±SEM.

(C) MIPs of Myosin-2 localization at the EVL-YSL boundary in Tg(*actb1:myl12.1-eGFP*) or Tg(*actb1:myl12.1-mcherry*) YSL-Ctrl (phenol red injected), *zo-1b/3* YSL-morphant, and *zo-1b/3* YSL-morphant embryos rescued by co-injection of GFP-tagged *zo-1b* and *zo-3* (mutated for the MO recognition site) mRNAs at 7–8 hpf. Scale bar, 20 μm.

(C') Plot of Myosin-2 intensity as a function of distance from the EVL margin in YSL-Ctrl, *zo-1b/3* YSL-morphant, and rescued *zo-1b/3* YSL-morphant embryos at 7–8 hpf. Fluorescence intensity was normalized to the EVL cortical signal. Data are mean ± SEM; unpaired t test; YSL-Ctrl with N = 4, n = 8 and *zo-1b/3* YSL-morphant with N = 5, n = 8; rescued *zo-1b/3* YSL-morphant with N = 6, n = 13.

(D) Kymograph of Myosin-2 flow velocities along the animal-vegetal (AV) axis of the embryo as a function of time during epiboly in an exemplary YSL-Ctrl, *zo-1b/3* YSL-morphant and rescued *zo-1b/3* YSL-morphant embryo at 7–8 hpf. The kymograph ranges from negative values (blue and blue arrow) indicating retrograde flows toward the EVL margin to positive values (red and red arrow) indicating anterograde flows toward the vegetal pole. Dashed lines mark the slope of EVL movement (black, YSL-Ctrl; blue, *zo-1b/3* YSL-morphant; pink, rescued *zo-1b/3* YSL-morphant embryos). The EVL is located above the dashed line and the YSL below.

(D') Plot of Myosin-2 mean flow velocities along the AV axis, averaged over 5–30 min in YSL-Ctrl, *zo-1b/3* YSL-morphant, and rescued *zo-1b/3* YSL-morphant embryos between 7 and 8 hpf. Data are mean ± SEM. EVL peak velocities were averaged over 10 μm; unpaired t test. YSL peak velocities were averaged over 45 μm (15–60 μm from the EVL margin); Mann-Whitney test; N/n same as in (C').

(E and F) MIPs of the EVL-YSL boundary in Myosin-2-expressing Tg(*actb1:myl12.1-eGFP*) YSL-Ctrl and *zo-1b/3* YSL-morphant embryos at 7–8 hpf (E) and Tg(*actb1:myl12.1-eGFP*)-expressing WT embryos at 6 and 8 hpf (F) after UV laser cutting (fourth post-cut frame) along a 5-μm line oriented perpendicular to the boundary. Scale bar, 10 μm.

(E' and F') Exemplary kymographs of EVL-YSL junctional opening in response to UV laser cutting as a function of time for the conditions shown in (E) and (F). Horizontal scale bar, 1.2 s; vertical scale bar, 1 μm.

(E'' and F'') Plot of initial recoil velocities of EVL-YSL junctions after UV laser cutting for the conditions shown in (E) and (F). Data are shown as box-and-whisker plots (whiskers, Tukey); unpaired t test; YSL-Ctrl and *zo-1b/3* YSL-morphant with each N = 2, n = 12; WT embryos at 6 hpf and 8 hpf with each N = 3, n = 17. ****p < 0.0001, ***p < 0.001, **p < 0.01, *p < 0.05; n, number of embryos.

See also Figure S2 and Videos S1 and S2.

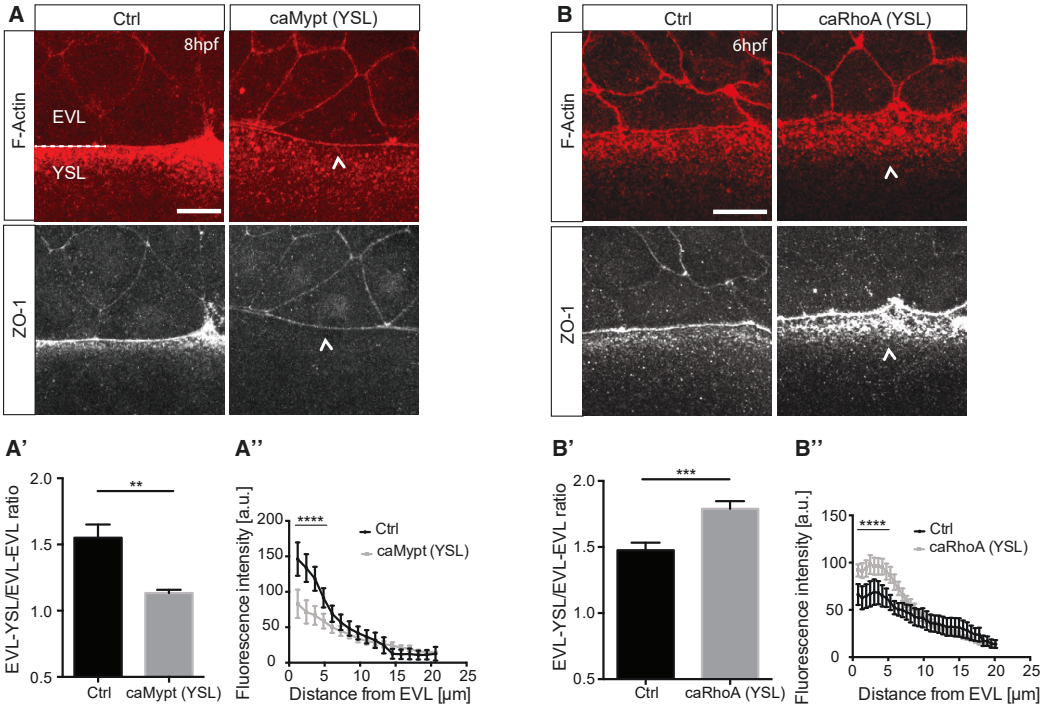

Figure 3. Actomyosin Contractility Affects ZO-1 Recruitment to the EVL-YSL Boundary

(A and B) MIPs of F-actin and ZO-1 localization at the EVL-YSL junction in embryos that were either injected into the YSL at 3.3 hpf with *H2A-mcherry* mRNA as control (Ctrl) and *caMypt* plus *H2A-mcherry* mRNA, shown at 8 hpf (A), or injected into marginal blastomeres/YSL at the 128-cell stage with *H2B*-EGFP mRNA (Ctrl) and *caRhoA* plus *H2B-GFP* mRNA, shown at 6 hpf (B). ZO-1 was detected by immunohistochemistry, F-actin by Phalloidin. White arrowheads point to a decrease (A) or increase (B) in signal at the EVL-YSL boundary. Scale bars, 20 μm.

(A' and B') Plot of EVL-YSL/EVL-EVL junctional ZO-1 intensity ratio for the conditions described in (A) and (B). (A') Ctrl with N = 2, n = 44; *caMypt* with N = 2, n = 39. (B') Ctrl with N = 2, n = 28; *caRhoA* with N = 2, n = 52. Mann-Whitney test.

(A'' and B'') Plot of non-junctional ZO-1 fluorescence intensity as a function of distance from the EVL margin for the conditions shown in (A) and (B). (A'') Ctrl with N = 2, n = 6; *caMypt* with N = 2, n = 7. (B'') Ctrl with N = 2, n = 6; *caRhoA* with N = 2, n = 9. Unpaired t test (A'') and Mann-Whitney test (B'') were used for non-junctional ZO-1 pool comparisons within the first 5 μm from the EVL margin, respectively.

Data are mean ± SEM. ****p < 0.0001, ***p < 0.001, **p < 0.01; n, number of cells in (A') and (B') and embryos in (A'') and (B'').

See also Figure S3.

at the EVL-YSL boundary, suggesting that TJs at this boundary are mechanosensitive.

Non-junctional Clusters of ZO-1b within the YSL Form by Phase Separation, Undergo Retrograde Flow, and Are Incorporated into TJs at the EVL-YSL Boundary

To understand how actomyosin network tension translates into accumulation of TJ components at the EVL-YSL boundary, we performed high-resolution time-lapse imaging of ZO-1b accumulation at the EVL-YSL boundary at 7 hpf. Remarkably, in addition to junctional ZO-1b, we detected non-junctional clusters of ZO-1b within the YSL close to the EVL-YSL boundary that traversed at a similar velocity as the actomyosin network toward this boundary (Figures 4A–4B''; Video S3). ZO-1b clusters arriving at the EVL-YSL boundary were then incorporated into the junction, locally increasing the amount of ZO-1b at the junction (Figures 4C and 4C'). Closer analysis of these non-junctional ZO-1b clusters showed that ZO-1b close to the EVL-YSL boundary displayed a tendency to fuse into larger clusters (Figures 4D–4D''; Video S4). Given that fusion of protein clusters or "droplets" has been associated previously with protein phase separation (Brangwynne et al., 2009; Li et al., 2012), this points to the intriguing possibility that non-junctional ZO-1b clusters within the YSL might form by phase separation. To form phase-separated droplets, multivalent interactions on an intra- or inter-molecular level are necessary (Banani et al., 2017; Kato et al., 2012; Li et al., 2012). Indeed, ZO-1 can undergo multivalent interactions with other ZO proteins, such as ZO-2 and ZO-3, as well as other TJ scaffolding proteins, such as Cingulins (Fanning et al., 1998; Utepbergenov et al., 2006). There is also evidence of intra-molecular interaction sites for ZO-1 and other members of the MAGUK (membrane-associated guanylate kinase) protein family (Fanning et al., 2007; Lye et al., 2010; Spadaro et al., 2017; Ye et al., 2018). This suggests that ZO-1b might be capable of undergoing phase separation and that this property might contribute to its previously demonstrated scaffolding function in recruiting other proteins to TJs (Bauer et al., 2010; Fanning and Anderson, 2009; Matter and Balda, 2003).

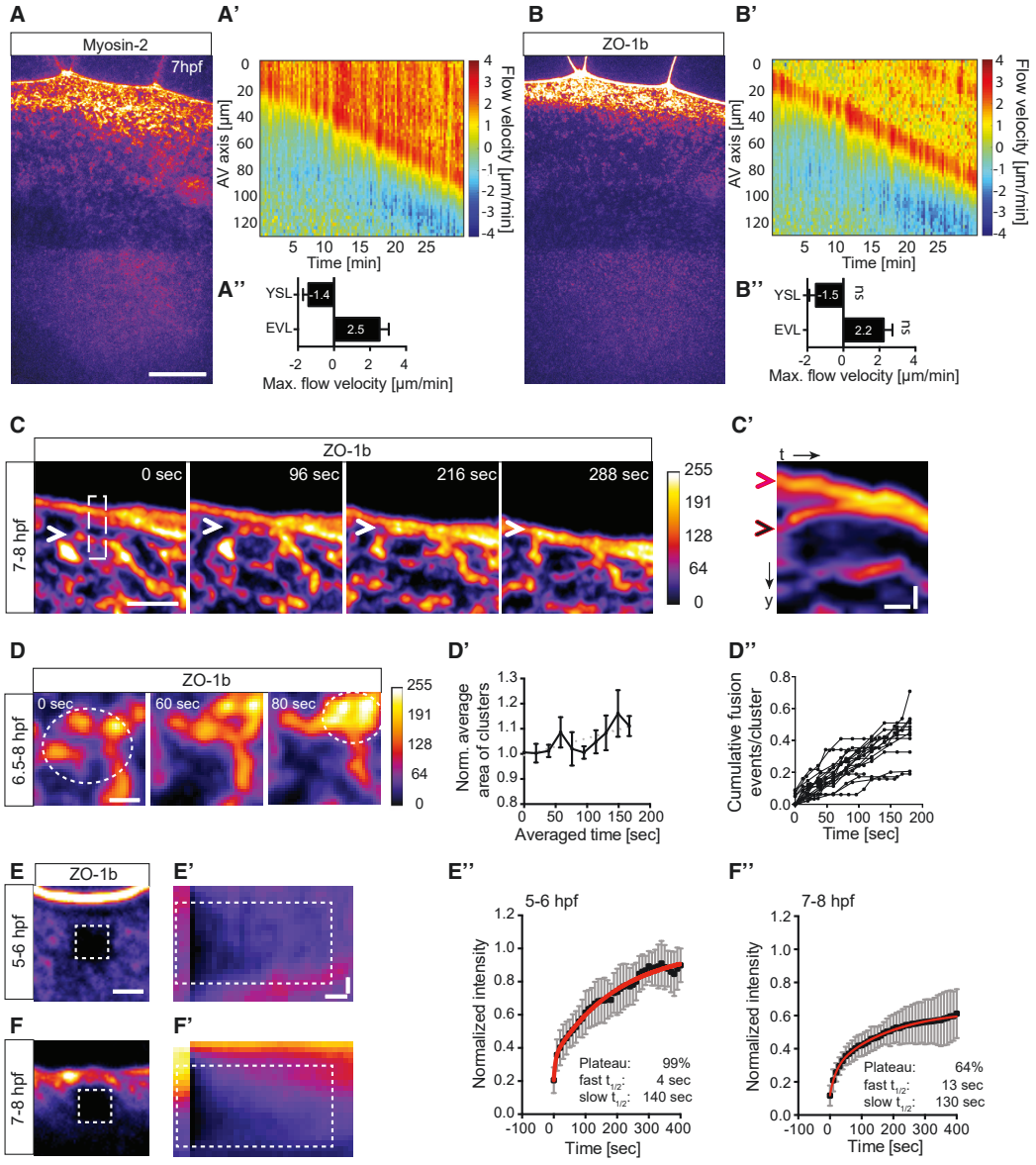

Figure 4. Non-junctional Clusters of ZO-1b within the YSL Undergo Retrograde Flows and Are Incorporated into TJs at the EVL-YSL Boundary

(A and B) MIPs of Myosin-2 (A) or ZO-1b (B) localization at the EVL-YSL boundary in Tg(*actb1:myl12.1-mcherry*; *actb2:mNeonGreen-zo-1b*) embryos at 7–8 hpf. Scale bar, 20 µm.

(A' and B') Exemplary kymographs of Myosin-2 (A') and ZO-1b (B') flow velocities along the AV axis of the YSL as a function of time during epiboly. The kymographs range from negative (retrograde flows toward the EVL-YSL boundary, blue) to positive (anterograde flows away from the EVL-YSL boundary, red) values.

(A'' and B'') Maximum Myosin-2 (A'') and ZO-1b (B'') flow velocities, indicating peak retrograde flow rates within the YSL (negative value) and maximum epiboly movement velocity of the EVL-YSL boundary (positive value). Data are mean ± SD. N = 4, n = 7; Mann-Whitney test.

(C) Consecutive MIP high-resolution (Airy Scan) images of non-junctional ZO-1b being incorporated at the EVL-YSL boundary (white arrowhead) in a Tg(*act2:mNEONgreen-zo-1b*) embryo at 7–8 hpf. Horizontal scale bar, 48 s; vertical scale bar, 2 µm. A calibration bar shows look up table (LUT) for gray value range.

(C') Kymograph of the boxed region in (C), showing non-junctional ZO-1b cluster (black arrowhead) incorporation at the EVL-YSL boundary (pink arrowhead). Horizontal scale bar, 40 s; vertical scale bar, 1 µm.

(legend continued on next page)

To test whether ZO-1b within the YSL has further properties indicative of a phase separation process, we sought to analyze ZO-1b turnover in clusters adjacent to the EVL margin using fluorescence recovery after photobleaching (FRAP). Based on previous observations that proteins undergoing liquid-liquid phase separation stay highly dynamic within phase-separated droplets (Brangwynne et al., 2009; Hyman et al., 2014), we hypothesized that, if ZO-1b undergoes phase separation within the YSL, then the turnover of the ZO-1b non-junctional pool should be rather fast. Consistent with ZO-1b potentially undergoing phase separation, we found that, at early to mid-gastrulation stages (5–6 hpf), non-junctional ZO-1b showed fast turnover on a scale of seconds ($t_{1/2}$ fast = 4 s), and almost all of it was mobile (99% mobile fraction) (Figures 4E–4E''). Interestingly, non-junctional ZO-1b also exhibited turnover on a scale of minutes ($t_{1/2}$ slow = 140 s), indicative of the presence of a second, slower ZO-1b species (Figures 4E–4E''). Surprisingly, however, at later gastrulation stages (7–8 hpf), the turnover time of non-junctional ZO-1b during the fast phase ($t_{1/2}$ fast) increased (4–13 s), and its mobile fraction decreased from 99% to 64% (Figures 4F–4F''). This suggests that clusters of non-junctional ZO-1b within the YSL, initially displaying properties of liquid-liquid phase-separated condensates, might undergo a maturation process leading to their immobilization. Interestingly, analyzing turnover of ZO-1b directly at the EVL-YSL junction at early (5–6 hpf) and later stages of gastrulation (8 hpf) revealed an even smaller fraction (~40%) of mobile ZO-1b at both of these stages (Figures S4A–S4B''), suggesting that junctional incorporation of ZO-1b might further promote its immobilization.

To further test whether non-junctional ZO-1b clusters indeed form by phase separation, we analyzed its dependency on concentration, a typical feature of a thermodynamically driven phase separation processes. To determine how the concentration of ZO-1b expressed within the YSL relates to cluster formation of ZO-1b, we analyzed the size and fusion rate of those clusters as a function of ZO-1b concentration within the YSL. We found that both the size and fusion rate of non-junctional clusters of ZO-1b linearly scaled with the concentration of ZO-1b expressed within the YSL (Figures 5A–5A''' and S5A), demonstrating that cluster formation is dependent on ZO-1b concentration, as expected for a phase separation mechanism.

Different domains of ZO-1b have been associated previously with ZO proteins binding to each other (Fanning et al., 1998, 2007; Utepbergenov et al., 2006) and the actin cytoskeleton (Fanning et al., 1998, 2002). To determine whether those multivalent interactions are important for ZO-1b cluster formation and presumed phase separation behavior, we generated deletion constructs lacking certain regions of ZO-1b and asked how this affects ZO-1b cluster formation. First we tested a C-terminally truncated version of ZO-1b (ZO-1bΔC) (Figure 5B), which has been found recently in cell culture assays to be defective in undergoing phase separation, likely because of changes in intra-molecular interactions of the truncated protein (Beutel et al., 2019). Substituting full-length ZO-1b with ZO-1bΔC by expressing ZO-1bΔC in MZ*zo-1b/3* mutant embryos revealed that ZO-1bΔC exclusively localized to TJs between EVL cells and at the EVL-YSL boundary and was unable to form non-junctional clusters within the YSL (Figure 5C). This is consistent with the notion that non-junctional ZO-1b clusters within the YSL might form by phase separation.

Because the C terminus of ZO-1b also harbors an actin binding region (ABR) (Fanning et al., 2002; Figure 5B), and non-junctional ZO-1b appears to partially co-localize with the cortical actomyosin network within the YSL (Figures S5B and S5B'), we further hypothesized that the failure of ZO-1bΔC to undergo phase separation and form non-junctional clusters within the YSL might also be caused by its inability to directly bind to actin. To test this possibility, we generated a version of ZO-1b specifically lacking its ABR (ZO-1bΔABR) and substituted full-length ZO-1b with ZO-1bΔABR in MZ*zo-1b/3* mutant embryos. Unexpectedly, we found that, in ZO-1bΔABR-expressing MZ*zo-1b/3* mutant embryos, non-junctional clusters still formed and underwent fusion, similar to full-length ZO-1b (Figures 5D–5D''). However, analysis of cluster size and shape in ZO-1bΔABR-expressing embryos revealed that these clusters took more circular droplet-like shapes compared with the elongated rod-like shapes typically observed when expressing full-length ZO-1b (Figures 5D''' and D''''). This points to the intriguing possibility that ZO-1b directly binding to actin, rather than being required for ZO-1b to undergo phase separation and to form non-junctional clusters within the YSL, might restrict the ability of ZO-1b to form more circular droplet-like clusters within the YSL.

(D) Consecutive MIP high-resolution images of non-junctional ZO-1b clusters undergoing fusion close to the EVL-YSL boundary in a Tg(*actb2:mNeonGreen-zo-1b*) embryo at 6.5–8 hpf. A white dashed circle shows the region of fusing non-junctional clusters. Scale bar, 500 nm. A calibration bar shows LUT for gray value range.

(D') Plot of average ZO-1b non-junctional cluster size normalized to initial average size within the YSL as a function of time between 5.7–8 hpf. Cluster size was averaged over acquisition times of 20 ± 5.5 s. Data are mean ± SEM. N = 5, n = 9.

(D'') Plot of cumulative fusion events per ZO-1b cluster as a function of time in Tg(*actb2:mNeonGreen-zo-1b*) embryos at 6–8 hpf. Each line represents fusion events averaged per embryo. N = 5, n = 15.

(E and F) Sum intensity projection image (sum of all slices) of ZO-1b signal in Tg(*actb2:mNeonGreen-zo-1b*) embryos within the YSL (2–5 μm from the EVL margin) after bleaching in FRAP experiments at early to mid- (5–6 hpf; E) and late epiboly stage (7–8 hpf; F). (E) N = 4, n = 13; (F) N = 4, n = 12. A white dashed box outlines the bleached region. Scale bar, 5 μm.

(E' and F') Exemplary kymograph of the bleached region for the conditions described in (E) and (F). A white dashed box outlines the region used for intensity measurements. Horizontal scale bar, 40 s; vertical scale bar, 1 μm.

(E'' and F'') Plot of GFP-ZO-1b fluorescence recovery as a function of time for the conditions described in (E) and (F). Data are mean ± SD. Solid line shows a double exponential fit (E'',F'').

ns, not significant; n, number of embryos.

See also Figure S4 and Videos S3 and S4.

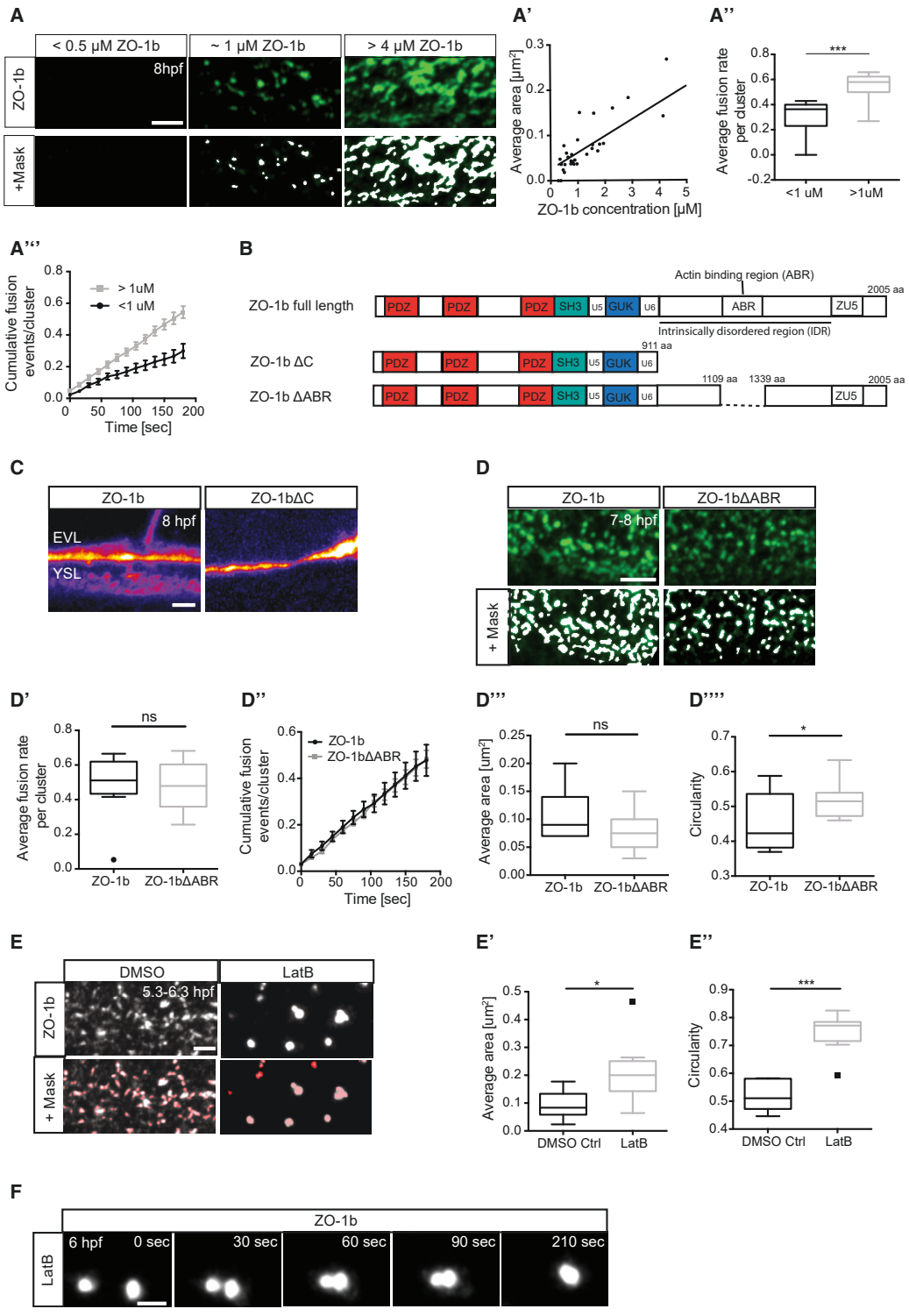

(legend on next page)

To determine whether an intact actomyosin network is required for ZO-1b phase separation and cluster formation, we disassembled the actomyosin network within the YSL by exposing embryos to Latrunculin B, blocking actin polymerization. Strikingly, disassembly of the actomyosin network led to formation of much larger and more circular droplet-like clusters of non-junctional ZO-1b within the YSL compared with those found in DMSO-exposed control embryos (Figures 5E–5E''). Moreover, these clusters underwent fusion within the YSL despite the notable absence of actomyosin network structures between those clusters (Figures 5F, S5C, and S5C'; Video S5), suggesting that these clusters can fuse independent of actomyosin network contraction. Collectively, these findings indicate that ZO-1b forms non-junctional clusters within the YSL by phase separation and that ZO-1b binding to actin gives ZO-1b clusters within the YSL their characteristic elongated rod-like shape.

TJ Mechanosensitivity Is Mediated by Retrograde Actomyosin Flows within the YSL Transporting Non-junctional Phase-Separated ZO-1b Clusters toward the Junction

Next we investigated whether ZO-1b phase separation is required for TJ mechanosensitivity at the EVL-YSL boundary. To this end, we substituted full-length ZO-1b with ZO-1bΔC, incapable of forming phase-separated non-junctional clusters within the YSL (Figure 5C), by expressing ZO-1bΔC in MZ*zo-1b/3* mutant embryos. To monitor TJ mechanosensitivity, we increased YSL actomyosin tension by expressing caRhoA within the YSL and analyzed how this affects junctional accumulation of ZO-1bΔC. We found that junctional ZO-1bΔC levels remained unchanged in response to caRhoA-mediated increased actomyosin tension and flow within the YSL (Figures 6A–6B', ctrl), suggesting that the ability of ZO-1b to form non-junctional phase-separated clusters within the YSL is critical for TJ mechanosensitivity. Importantly, the failure of ZO-1bΔC to respond to increased actomyosin tension within the YSL is unlikely to be due to ZO-1bΔC being degraded or non-functional because the total expression level of these two ZO-1 versions were comparable (Figures S6A and S6A').

To further determine whether ZO-1b directly binding to actin is needed for TJ mechanosensitivity, we substituted full-length ZO-1b with ZO-1bΔABR, lacking its actin-binding region within the C terminus, by expressing ZO-1bΔABR in MZ*zo-1b/3* mutant embryos. Interestingly, we found that non-junctional ZO-1bΔABR clusters displayed retrograde flow within the YSL, similar to clusters formed by full-length ZO-1b (Figures S5D–S5D''), suggesting that direct binding of ZO-1b to actin is not required for it to undergo actomyosin contraction-dependent retrograde flow within the YSL. However, accumulation of non-junctional ZO-1bΔABR clusters close to the EVL-YSL boundary (Figures S5E and S5E') and stable incorporation of ZO-1bΔABR clusters into TJs at this boundary were severely reduced. Retrogradely flowing ZO-1bΔABR clusters, instead of being incorporated into TJs

Figure 5. Non-junctional ZO-1b Undergoes Phase Separation within the YSL

(A) MIP high-resolution images of non-junctional GFP-ZO-1b clusters within the YSL of MZ*zo-1b/3* mutants injected at 1-cell stage with different concentrations of *GFP-zo-1b* mRNAs at 7–8 hpf. First row, GFP signal only; second row, GFP signal overlaid with the white signal obtained by cluster masking (STAR Methods). ZO-1b concentrations (micromolar) were determined via quantitative fluorescence microscopy. Calibration curves (Figure S5A) were acquired with the same imaging settings. The intensity for the image of 1 μM ZO-1b concentration was enhanced to better display the small and less intense clusters. Scale bar, 2 μm.

(A') Plot of the average area of ZO-1b clusters as a function of ZO-1b concentration. N = 3, n = 33.

(A'') Plot of the average fusion rate per ZO-1b cluster for different ZO-1b concentrations within the YSL. Average fusion rate was determined as the total fusion number divided by the average cluster number in a time window of 3 min. Data are shown as box-and-whisker plots (whiskers, Tukey); Mann Whitney test; N = 3, n = 32.

(A''') Plot of cumulative fusion events per ZO-1b cluster as a function of time. Curves show the different ZO-1b concentrations. Data are shown as mean ± SEM. For N/n, see (A'').

(B) Schematic representation of the domain structure of the full-length ZO-1b construct; the ZO-1bΔC construct lacking its mainly intrinsically disordered C terminus, including an actin binding region (ABR); and the ZO-1bΔABR construct only lacking the ABR within the intrinsically disordered region (IDR).

(C) MIP high-resolution images of MZ*zo-1b/3* mutant embryos injected at 1-cell stage with either *GFP-zo-1b* (Ctrl) or *GFP-zo-1bΔC* mRNAs at 8 hpf. Scale bar, 2 μm.

(D and E) MIP high-resolution images of non-junctional ZO-1b clusters within the YSL of MZ*zo-1b/3* mutants injected at 1-cell stage with either *GFP-zo-1b* or *GFP-zo-1bΔABR* mRNA at 7–8 hpf (D) and MIP high-resolution images of Tg(*actb2:mNeonGreen-zo-1b*) embryos treated for 1 h with either DMSO control (Ctrl) or 1 μg/mL Latrunculin B prior to imaging at 5.3–6.3 hpf (E). First row, GFP signal only; second row, GFP signal (green in D and white in E) overlaid with a white (D) or red (E) signal obtained by cluster masking (STAR Methods). Scale bars, 2 μm.

(D') Plot of the average fusion rate per ZO-1b and ZO-1bΔABR cluster within the YSL. Average fusion rate was determined as the total fusion number divided by the average cluster number in a time window of 3 min. Data are shown as box-and-whisker plots (whiskers, Tukey); Mann-Whitney test; ZO-1b with N = 4, n = 8; ZO-1bΔABR with N = 4, n = 12.

(D'') Plot of cumulative fusion events per cluster as a function of time for ZO-1b and ZO-1bΔABR. Data are shown as mean ± SEM. For N/n, see (D').

(D''' and E') Plot of the average ZO-1b cluster area per embryo for the conditions described in (D) and (E). Data are shown as box-and-whisker plots (whiskers, Tukey). Average Area of (D''') with unpaired t test. GFP-ZO-1b with N = 6, n = 9; GFP-ZO-1bΔABR with N = 5, n = 14. Average area of (E') with unpaired t test. DMSO Ctrl with N = 4, n = 8; LatB with N = 4, n = 9.

(D'''' and E'') Plot of average ZO-1b cluster circularity per embryo for the conditions described in (D) and (E). The circularity of individual clusters above a 0.15 μm^2 area were averaged per embryo and further analyzed (STAR Methods). Data are shown as box-and-whisker plots (whiskers, Tukey). A circularity value of 1 reflects a perfect circle, whereas values close to 0 indicate more elongated shapes. Circularity of (D'''') with unpaired t test. GFP-ZO-1b with N = 6, n = 9; GFP-ZO-1bΔABR with N = 5, n = 12. Circularity of (E'') with Mann-Whitney test. DMSO Ctrl with N = 4, n = 6; LatB with N = 4, n = 9.

(F) Consecutive MIP high-resolution (Airy Scan) images of ZO-1b clusters undergoing fusion within the YSL of Tg(*actb2:mNeonGreen-zo-1b*) embryos treated for 1 h with 1 μg/mL Latrunculin B prior to imaging at 5.3–6.3 hpf. Scale bar, 1 μm.

***p = 0.001; *p < 0.05; n, number of embryos.

See also Figure S5 and Video S5.

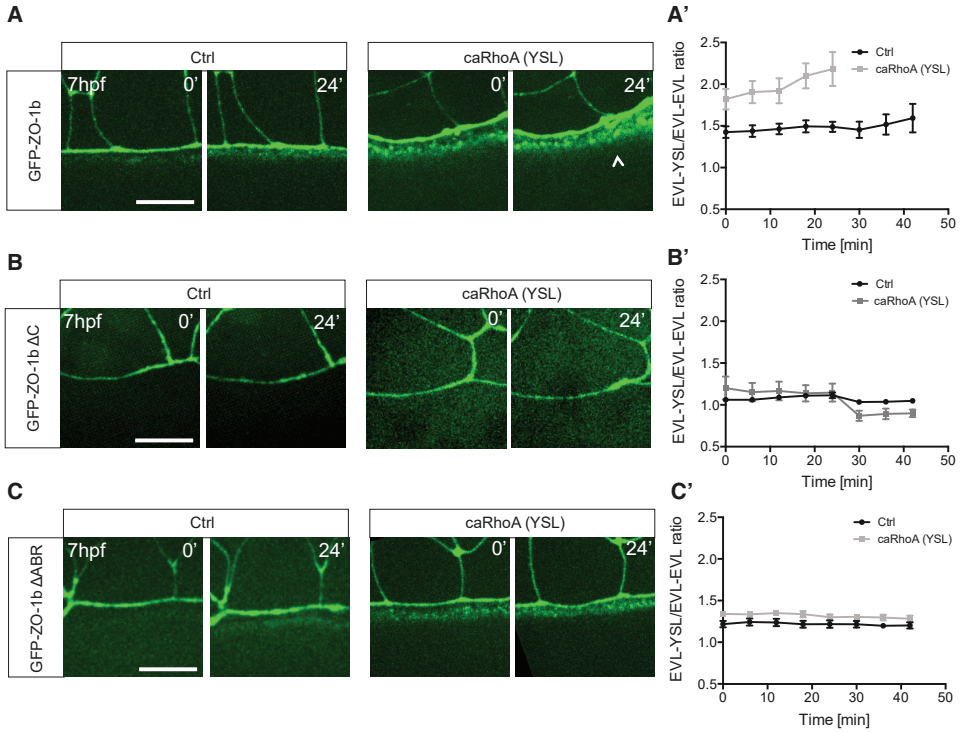

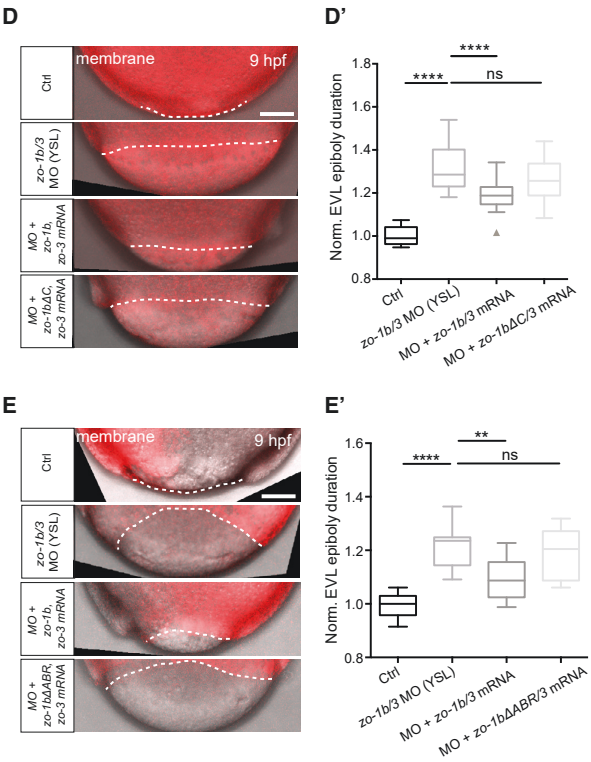

(legend on next page)

when arriving at the EVL-YSL boundary (Figures S6B and S6B'; Video S6), frequently "bypassed" this boundary or detached from the junctional pool (Figures S6C–S6C''). Analysis of the subcellular distribution of ZO-1bΔABR clusters within the YSL further revealed that these clusters were not confined to the surface of the YSL, where the actomyosin cortex is located and most of the full-length ZO-1b clusters were found (Figures S6C–S6C''), but were more broadly distributed throughout the YSL (Figure S6C''). This led to some of the ZO-1bΔABR clusters flowing below the TJ complex at the EVL-YSL boundary, bypassing this boundary and not being stably incorporated into the TJ (Figures S6C–S6C''). To test whether this reduced junctional incorporation of ZO-1bΔABR interferes with TJ mechanosensitivity, we increased YSL actomyosin tension by expressing caRhoA and analyzed how this affects junctional accumulation of ZO-1bΔABR. Interestingly, we found that the increase in junctional levels of ZO-1bΔABR in response to increased actomyosin tension and flow within the YSL was much less pronounced than that observed for full-length ZO-1b (Figures 6C and 6C'). This suggests that direct binding of ZO-1b to the actomyosin cortex confines non-junctional ZO-1b clusters to the YSL surface, where they can be most effectively incorporated into the TJ at the EVL-YSL interface.

Importantly, although substituting full-length ZO-1b with forms that either cannot form phase-separated clusters (ZO-1bΔC) or cannot directly bind actin (ZO-1bΔABR) abolished the effect of increased actomyosin tension on junctional accumulation of ZO-1b, both forms of ZO-1b still showed substantial base-level junctional accumulation at the EVL-YSL boundary. This suggests that the formation, retrograde flow, and junctional incorporation of ZO-1b clusters are needed for tuning the amount of junctional ZO-1b at the EVL-YSL boundary with the tension of the associated YSL actomyosin cytoskeleton but not for the general accumulation of junctional ZO-1b at this boundary.

TJ Mechanosensitivity Is Required for EVL Spreading

Finally, we tested whether TJ mechanosensitivity is required for normal EVL epiboly movements. To this end, we attempted to rescue the epiboly phenotype of *zo-1b/3* YSL morphant embryos by injecting mRNA for either the full-length and, thus, mechanosensitive ZO-1b or the mechano-insensitive ZO-1bΔC and ZO-1bΔABR versions. Strikingly, we found that, although the full-length version of ZO-1b in combination with ZO-3 could partially rescue the delay in epiboly progression and actomyosin ring formation in the morphant (Figures 6D–6E', 2C, and 2C'), expression of ZO-1bΔC or ZO-1bΔABR together with ZO-3 at the same stoichiometric ratios as their full-length counterparts failed to rescue these phenotypes (Figures 6D–6E', S6D, and S6D'). This suggests that the C terminus and, specifically, the ABR therein is important for ZO-1b function in EVL-YSL epiboly movement, and, given that these parts of ZO-1b are also required for ZO-1b mechanosensitivity, that ZO-1b mechanosensitivity is important for EVL-YSL epiboly progression.

DISCUSSION

Our study provides direct evidence that TJ mechanosensitivity is achieved by contractility-driven cortical actomyosin flow transporting phase-separated non-junctional ZO-1b clusters toward the junction. Recent biochemical evidence from *in vitro* reconstitution and cell culture experiments suggests that ZO proteins, like other members of the MAGUK family (Zeng et al., 2016), can undergo phase separation (Beutel et al., 2019). Our data support these observations by showing that ZO-1b can undergo phase separation within the YSL. Importantly, the ability of ZO-1b to undergo phase separation seems to be required to form non-junctional clusters within the YSL, given that versions of ZO-1b incapable of undergoing phase separation, such as ZO-1bΔC (Beutel et al., 2019), failed to form those clusters. Whether other TJ proteins also undergo phase separation and/or localize to ZO-1b non-junctional clusters is not yet entirely clear. So far, our data suggest that TJ adhesion receptors, such as Occludins and Claudins, are exclusively localizing to TJ but do not form non-junctional clusters (Figures S6E, S6F, and S1A–S1D). In contrast, the cytoskeletal adaptor protein Cingulin-like 1/Paracingulin, shown previously to also localize to TJs (Citi et al., 2012; Guillemot et al., 2014), colocalizes with both junctional and non-junctional ZO-1b (Figures S6G and S6G'). This points to the possibility that TJ adaptor proteins, but not adhesion receptors, can form non-junctional phase-separated clusters within the YSL. Our findings also suggest that ZO-1b can form phase-separated clusters even when it

Figure 6. The Mechanosensitive Response of ZO-1b Is Dependent on Its C Terminus

(A, B, and C) MIPs of GFP-tagged ZO-1b (A), GFP-tagged ZO-1bΔC (B), and GFP-tagged ZO-1b-ΔABR (C) localization at the EVL-YSL boundary in MZ*zo-1b/3* embryos injected with *H2A*-mCherry mRNA (Ctrl; A with N = 5, n = 23; B with N = 4, n = 43; C with N = 3, n = 17) and embryos injected with *caRhoA* mRNA specifically within the YSL (A with N = 3, n = 19; B with N = 3, n = 13; C with N = 3, n = 27) at the onset of imaging (7 hpf) and 24 min later. GFP-tagged ZO-1b, ZO-1bΔC, and ZO-1bΔABR are visualized by expression of their respective fusion constructs. A white arrowhead points to increased accumulation at the EVL-YSL boundary. Scale bars, 10 μm.

(A', B', and C') Plot of EVL-YSL junctional intensity normalized to EVL-EVL junctional intensity as a function of time during EVL epiboly in the conditions described in (A), (B), and (C). Data are mean ± SEM.

(D and E) MIPs of bright-field/fluorescence images of embryos injected directly into the YSL at 3.3 hpf with phenol red and *H2A-mcherry* mRNA as control (Ctrl in D with N = 8, n = 27; Ctrl in E with N = 3, n = 10), *zo-1b/3* MO (D with N = 8, n = 28; E with N = 3, n = 12) alone, *zo-1b/3* MO together with *GFP-zo-3* and GFP-*zo-1b* mRNA (D with N = 8, n = 27; E with N = 3, n = 8), and *zo-1b/3* MO together with *GFP-zo-3* and GFP-*zo-1b*ΔC mRNA (D with N = 8, n = 26) or *zo-1b/3* MO together with *GFP-zo-3* and GFP-*zo-1b*ΔABR mRNA (E with N = 3, n = 8) at 9 hpf. The plasma membrane is marked by membrane-RFP to outline cells. The EVL-YSL boundary is marked by a white dashed line to demarcate the extent of EVL epiboly under the different conditions. Scale bar, 100 μm.

(D' and E') Plot of the total time required for EVL to complete epiboly for the conditions shown in (D) and (E) and normalized to the average time needed by Ctrl embryos. Data are shown as box-and-whisker plots (whiskers, Tukey); one-way ANOVA. For full-length rescue (D and D'), data shown in Figure 2A' were included. ****$p < 0.0001$; **$p < 0.01$; n, number of cells (A'–C') or embryos (D and E).

See also Figures S5 and S6 and Video S6.

lacks its ABR, suggesting that directly binding to actin is not a prerequisite for ZO-1b to undergo phase separation. However, actin binding seems to be important for ZO-1b clusters to take their characteristic elongated rod-like shapes, an effect most likely to be due to those clusters adhering and spreading on the filamentous actin network. Further, the presence of a functional actomyosin network appears to restrict the maximum size of ZO-1b clusters, consistent with previous studies showing that the mesh size of elastic polymers can tune the phase separation capacity (Style et al., 2018).

Besides influencing the shape of ZO-1b clusters, ZO-1b directly binding to actin also appears to be critical for ZO-1b mechanosensation, given that ZO-1bΔABR failed to respond to changes in actomyosin tension. This loss of mechanosensitivity is likely due to ZO-1bΔABR clusters being less effectively incorporated into TJs, an effect presumably caused by ZO-1bΔABR clusters being less confined to the surface of the YSL and, therefore, flowing below the TJs without being integrated. Additionally, ZO-1bΔABR showed reduced junctional stability, with clusters frequently dissociating from the EVL-YSL junction. Interestingly, ZO-1 lacking its ABR has been found previously to display reduced junctional immobilization (Yu et al., 2010), supporting the view that actin binding promotes stable junctional incorporation of ZO-1. Furthermore, our observation that the retrograde flow of ZO-1bΔABR clusters within the YSL was largely unaffected suggests that ZO-1b directly binding to actin is predominantly required for localizing non-junctional ZO-1b clusters to the YSL surface and not transporting it toward the EVL-YSL boundary. How the retrograde flow of non-junctional ZO-1b clusters within the YSL is achieved is not yet entirely clear, but it is conceivable that advection of the YSL cytoplasm caused by the flow of the actomyosin network might be involved.

TJ mechanosensitivity is likely to be important for both junctional signaling and mechanics at the EVL-YSL boundary. Foremost, it might be required for triggering the formation and maturation of the contractile actomyosin band within the YSL by establishing a positive feedback loop, where actomyosin contractility and flow promotes TJ formation (Zihni et al., 2016), and TJs promote actomyosin contractility and flow. Our observation that TJ and actomyosin ring formation at the EVL-YSL boundary are interdependent processes clearly supports this notion. Interestingly, we only detected retrograde actomyosin and TJ protein flows toward the EVL-YSL junction on the side of the YSL but not at the leading edge of EVL forming the other side of the contact. Although this might be due to technical limitations in imaging, such flows in EVL cells that are much smaller than the yolk cell, it is also conceivable that TJ mechanosensitivity is restricted to the side of the YSL. How such potential asymmetric mechanosensitive regulation of TJs at the EVL-YSL boundary affects the biochemical and mechanical function of this junction is not yet clear, but binding of adhesion receptors over the contact might trigger non-autonomous effects, eventually equilibrating the amount of TJ components on both sides of the EVL-YSL boundary.

TJ mechanosensitivity might also be required for TJs mechanically linking the EVL margin to the YSL by balancing the coupling strength of TJs to the mechanical force applied to this junction by the contractile actomyosin network within the YSL. Such function has been demonstrated for AJs, where junctional tension leads to conformational changes of α-catenin and vinculin, which again increases the actin-binding capability of these AJ components to the adjacent actomyosin cortex (Gomez et al., 2011). Although the role of TJ in regulating cell-cell coupling strength remains largely unknown, recent studies showing that the TJ component ZO-1 modulates tension at cell-cell junctions (Hatte et al., 2018; Tornavaca et al., 2015) and can be stretched by tension (Spadaro et al., 2017) suggest that ZO proteins are involved in force transduction and reception at cell-cell contacts (Hashimoto et al., 2019). Our observation that TJs appear to be the predominant junction type at the EVL-YSL boundary and that there is force transduction from the actomyosin band within the YSL to the leading edge of the EVL (Behrndt et al., 2012) point to the possibility that TJ have a force-transducing function. Whether and how forces are being transmitted by TJs and how mechanosensitive junction growth affects such a potential function remains to be investigated.

Interestingly, previous studies have suggested that the C terminus of ZO-1 can fold back on its N-terminal part in an auto-inhibitory fashion and that this auto-inhibition can be released by ZO-1 binding to and being stretched by the contractile actomyosin network, allowing it to bind to other junctional proteins (Spadaro et al., 2017). This might explain why versions of ZO-1b lacking either the ABR or entire C terminus are unable to rescue the epiboly phenotype of *zo-1b/3* YSL morphant embryos; their failure to directly bind to the actin cytoskeleton might not only diminish their localization to the YSL surface and, thus, their effective incorporation into TJs at the EVL-YSL boundary but might also interfere with tension-induced conformational changes of ZO-1b required for its biological activity. Future experiments aimed at a systematic structure-function analysis of different ZO proteins will be needed to determine which regions, in addition to the ABR within the C terminus, binding directly or indirectly to the actin cytoskeleton, are needed to confer mechanosensitivity to those proteins. It will also be interesting to investigate how phase separation at the membrane is initiated, whether clusters form spontaneously through random fluctuations or through pre-existing structures leading to heterogeneous nucleation events (Hyman et al., 2014) or whether there is any additional fine-tuning of critical concentration levels or phase separation capacity via post-translational modifications (Alberti, 2017; Monahan et al., 2017) of ZO proteins.

There is increasing evidence of mechanochemical feedback loops forming the basis of various developmental processes (Goehring and Grill, 2013; Hannezo and Heisenberg, 2019). A key feature of those feedback loops is the interdependency of mechanical and chemical signals whose concerted actions drive key cellular processes, such as cell polarization and migration. Although the biochemical basis of force generation and transmission is increasingly well understood (Lecuit et al., 2011), comparably little is known about how mechanical forces feed back on biochemical processes. Our findings of mechanical forces promoting the growth of TJs through generation of actomyosin flow not only unravels that TJs, similar to AJs, are mechanosensitive but also more broadly point to a still underestimated role of TJs in controlling tissue mechanics within the developing organism.

STAR★METHODS

Detailed methods are provided in the online version of this paper and include the following:

- KEY RESOURCES TABLE
- LEAD CONTACT AND MATERIALS AVAILABILITY
- EXPERIMENTAL MODEL AND SUBJECT DETAILS
- METHOD DETAILS
  - CRISPR/Cas9 mutant generation
  - Cloning of expression constructs
  - Transgenic zebrafish line generation
  - mRNA and Morpholino injections
  - Sample preparation for live imaging
  - Imaging setups for live and fixed imaging
  - Analysis of EVL progression
  - Whole mount *in situ* hybridization
  - UV laser ablation
  - Imaging of cortical flows within the YSL
  - ZO-1b cluster size and circularity analysis
  - ZO-1b cluster fusion analysis
  - Quantitative imaging of ZO-1b
  - ZO-1b junctional integration efficiency
  - Tracking analysis of non-junctional clusters
  - Immunostaining
  - Junctional and YSL cortical quantifications
  - Quantification of total intensities
  - qRT-PCR (quantitative Real-Time PCR)
  - Colocalization analysis
  - Fluorescence Recovery After Photobleaching
  - Latrunculin B treatment
- QUANTIFICATION AND STATISTICAL ANALYSIS
- DATA AND CODE AVAILABILITY

SUPPLEMENTAL INFORMATION

Supplemental Information can be found online at https://doi.org/10.1016/j.cell.2019.10.006.

ACKNOWLEDGMENTS

We thank Ashley Bruce for the Claudin-D construct; Alf Honigmann for sharing unpublished data and providing GFP; the Heisenberg group for fruitful discussions; the bioimaging and zebrafish facilities of IST Austria for continuous support; and Robert Hauschild, Christoph Sommer, and Lenka Matejovicova for help with image analysis. We are also particularly grateful to the late Suzanne Eaton for discussions regarding the initial idea of phase separation in the context of TJ formation. This project was supported by funding from the European Union (European Research Council advanced grant 742573 to C.-P.H.) and the Biotechnology and Biological Sciences Research Council (BBSRC; BB/N014855/1 to M.B., M.T., and K.M.).

AUTHOR CONTRIBUTIONS

C.S. and C.-P.H. designed the research. C.S. performed the experiments and analyzed the experimental data. S.S., K.P.-F., and A.S. contributed to the experimental work and data analysis. M.B., M.T., and K.M. provided reagents and conceptual input. C.S., C.-P.H., M.B., M.T., and K.M. wrote the manuscript.

DECLARATION OF INTERESTS

The authors declare no competing interests.

Received: March 11, 2019
Revised: August 19, 2019
Accepted: October 7, 2019
Published: October 31, 2019

REFERENCES

Alberti, S. (2017). Phase separation in biology. Curr. Biol. *27*, R1097–R1102.

Arboleda-Estudillo, Y., Krieg, M., Stühmer, J., Licata, N.A., Muller, D.J., and Heisenberg, C.-P. (2010). Movement directionality in collective migration of germ layer progenitors. Curr. Biol. *20*, 161–169.

Banani, S.F., Lee, H.O., Hyman, A.A., and Rosen, M.K. (2017). Biomolecular condensates: organizers of cellular biochemistry. Nat. Rev. Mol. Cell Biol. *18*, 285–298.

Bauer, H., Zweimueller-Mayer, J., Steinbacher, P., Lametschwandtner, A., and Bauer, H.C. (2010). The dual role of zonula occludens (ZO) proteins. J. Biomed. Biotechnol. *2010*, 402593.

Baum, B., and Georgiou, M. (2011). Dynamics of adherens junctions in epithelial establishment, maintenance, and remodeling. J. Cell Biol. *192*, 907–917.

Behrndt, M., Salbreux, G., Campinho, P., Hauschild, R., Oswald, F., Roensch, J., Grill, S.W., and Heisenberg, C.-P. (2012). Forces driving epithelial spreading in zebrafish gastrulation. Science *338*, 257–260.

Benais-Pont, G., Punn, A., Flores-Maldonado, C., Eckert, J., Raposo, G., Fleming, T.P., Cereijido, M., Balda, M.S., and Matter, K. (2003). Identification of a tight junction-associated guanine nucleotide exchange factor that activates Rho and regulates paracellular permeability. J. Cell Biol. *160*, 729–740.

Beutel, O., Maraspini, R., Pombo-García, K., Martin-Lemaitre, C., and Honigmann, A. (2019). Phase Separation of Zonula Occludens Proteins Drives Formation of Tight Junctions. Cell *179*. Published on October 31, 2019. https://doi.org/10.1016/j.cell.2019.10.011.

Bolte, S., and Cordelières, F.P. (2006). A guided tour into subcellular colocalization analysis in light microscopy. J. Microsc. *224*, 213–232.

Brangwynne, C.P., Eckmann, C.R., Courson, D.S., Rybarska, A., Hoege, C., Gharakhani, J., Jülicher, F., and Hyman, A.A. (2009). Germline P granules are liquid droplets that localize by controlled dissolution/condensation. Science *324*, 1729–1732.

Bruce, A.E.E. (2016). Zebrafish epiboly: Spreading thin over the yolk. Dev. Dyn. *245*, 244–258.

Cavey, M., and Lecuit, T. (2009). Molecular bases of cell–cell junctions stability and dynamics. Cold Spring Harb. Perspect. Biol. *1*, a002998.

Cavey, M., Rauzi, M., Lenne, P.-F., and Lecuit, T. (2008). A two-tiered mechanism for stabilization and immobilization of E-cadherin. Nature *453*, 751–756.

Cheng, J.C., Miller, A.L., and Webb, S.E. (2004). Organization and function of microfilaments during late epiboly in zebrafish embryos. Dev. Dyn. *231*, 313–323.

Citi, S., Pulimeno, P., and Paschoud, S. (2012). Cingulin, paracingulin, and PLEKHA7: signaling and cytoskeletal adaptors at the apical junctional complex. Ann. N Y Acad. Sci. *1257*, 125–132.

Compagnon, J., Barone, V., Rajshekar, S., Kottmeier, R., Pranjic-Ferscha, K., Behrndt, M., and Heisenberg, C.-P. (2014). The notochord breaks bilateral symmetry by controlling cell shapes in the zebrafish laterality organ. Dev. Cell *31*, 774–783.

Cunningham, K.E., and Turner, J.R. (2012). Myosin light chain kinase: pulling the strings of epithelial tight junction function. Ann. N Y Acad. Sci. *1258*, 34–42.

El-Brolosy, M.A., Kontarakis, Z., Rossi, A., Kuenne, C., Günther, S., Fukuda, N., Kikhi, K., Boezio, G.L.M., Takacs, C.M., Lai, S.-L., et al. (2019). Genetic compensation triggered by mutant mRNA degradation. Nature *568*, 193–197.

Engl, W., Arasi, B., Yap, L.L., Thiery, J.P., and Viasnoff, V. (2014). Actin dynamics modulate mechanosensitive immobilization of E-cadherin at adherens junctions. Nat. Cell Biol. *16*, 587–594.

Fanning, A.S., and Anderson, J.M. (2009). Zonula occludens-1 and -2 are cytosolic scaffolds that regulate the assembly of cellular junctions. Ann. N Y Acad. Sci. *1165*, 113–120.

Fanning, A.S., Jameson, B.J., Jesaitis, L.A., and Anderson, J.M. (1998). The tight junction protein ZO-1 establishes a link between the transmembrane protein occludin and the actin cytoskeleton. J. Biol. Chem. *273*, 29745–29753.

Fanning, A.S., Ma, T.Y., and Anderson, J.M. (2002). Isolation and functional characterization of the actin binding region in the tight junction protein ZO-1. FASEB J. *16*, 1835–1837.

Fanning, A.S., Little, B.P., Rahner, C., Utepbergenov, D., Walther, Z., and Anderson, J.M. (2007). The unique-5 and -6 motifs of ZO-1 regulate tight junction strand localization and scaffolding properties. Mol. Biol. Cell *18*, 721–731.

Franke, W.W. (2009). Discovering the molecular components of intercellular junctions–a historical view. Cold Spring Harb. Perspect. Biol. *1*, a003061.

Gagnon, J.A., Valen, E., Thyme, S.B., Huang, P., Akhmetova, L., Pauli, A., Montague, T.G., Zimmerman, S., Richter, C., and Schier, A.F. (2014). Efficient mutagenesis by Cas9 protein-mediated oligonucleotide insertion and large-scale assessment of single-guide RNAs. PLoS ONE *9*, e98186.

Godsel, L.M., Getsios, S., Huen, A.C., and Green, K.J. (2004). The molecular composition and function of desmosomes. Handb. Exp. Pharmacol. *165*, 137–193.

Goehring, N.W., and Grill, S.W. (2013). Cell polarity: mechanochemical patterning. Trends Cell Biol. *23*, 72–80.

Gomez, G.A., McLachlan, R.W., and Yap, A.S. (2011). Productive tension: force-sensing and homeostasis of cell-cell junctions. Trends Cell Biol. *21*, 499–505.

Guillemot, L., Guerrera, D., Spadaro, D., Tapia, R., Jond, L., and Citi, S. (2014). MgcRacGAP interacts with cingulin and paracingulin to regulate Rac1 activation and development of the tight junction barrier during epithelial junction assembly. Mol. Biol. Cell *25*, 1995–2005.

Hannezo, E., and Heisenberg, C.-P. (2019). Mechanochemical Feedback Loops in Development and Disease. Cell *178*, 12–25.

Hashimoto, Y., Kinoshita, N., Greco, T.M., Federspiel, J.D., Jean Beltran, P.M., Ueno, N., and Cristea, I.M. (2019). Mechanical Force Induces Phosphorylation-Mediated Signaling that Underlies Tissue Response and Robustness in Xenopus Embryos. Cell Syst. *8*, 226–241.e7.

Hatte, G., Prigent, C., and Tassan, J.-P. (2018). Tight junctions negatively regulate mechanical forces applied to adherens junctions in vertebrate epithelial tissue. J. Cell Sci. *131*, jcs208736.

Holloway, B.A., Gomez de la Torre Canny, S., Ye, Y., Slusarski, D.C., Freisinger, C.M., Dosch, R., Chou, M.M., Wagner, D.S., and Mullins, M.C. (2009). A novel role for MAPKAPK2 in morphogenesis during zebrafish development. PLoS Genet. *5*, e1000413.

Hyman, A.A., Weber, C.A., and Jülicher, F. (2014). Liquid-liquid phase separation in biology. Annu. Rev. Cell Dev. Biol. *30*, 39–58.

Iioka, H., Ueno, N., and Kinoshita, N. (2004). Essential role of MARCKS in cortical actin dynamics during gastrulation movements. J. Cell Biol. *164*, 169–174.

Itoh, M., Tsukita, S., Yamazaki, Y., and Sugimoto, H. (2012). Rho GTP exchange factor ARHGEF11 regulates the integrity of epithelial junctions by connecting ZO-1 and RhoA-myosin II signaling. Proc. Natl. Acad. Sci. USA *109*, 9905–9910.

Jayashankar, V., Nguyen, M.J., Carr, B.W., Zheng, D.C., Rosales, J.B., Rosales, J.B., and Weiser, D.C. (2013). Protein phosphatase 1 β paralogs encode the zebrafish myosin phosphatase catalytic subunit. PLoS ONE *8*, e75766.

Johnson, J.L., Najor, N.A., and Green, K.J. (2014). Desmosomes: regulators of cellular signaling and adhesion in epidermal health and disease. Cold Spring Harb. Perspect. Med. *4*, a015297.

Kato, M., Han, T.W., Xie, S., Shi, K., Du, X., Wu, L.C., Mirzaei, H., Goldsmith, E.J., Longgood, J., Pei, J., et al. (2012). Cell-free formation of RNA granules: low complexity sequence domains form dynamic fibers within hydrogels. Cell *149*, 753–767.

Keller, P.J., Schmidt, A.D., Wittbrodt, J., and Stelzer, E.H.K. (2008). Reconstruction of zebrafish early embryonic development by scanned light sheet microscopy. Science *322*, 1065–1069.

Kimmel, R.A., and Meyer, D. (2010). Molecular regulation of pancreas development in zebrafish. Methods Cell Biol. *100*, 261–280.

Kimmel, C.B., Ballard, W.W., Kimmel, S.R., Ullmann, B., and Schilling, T.F. (1995). Stages of embryonic development of the zebrafish. Dev. Dyn. *203*, 253–310.

Köppen, M., Fernández, B.G., Carvalho, L., Jacinto, A., and Heisenberg, C.-P. (2006). Coordinated cell-shape changes control epithelial movement in zebrafish and *Drosophila*. Development *133*, 2671–2681.

Kwan, K.M., Fujimoto, E., Grabher, C., Mangum, B.D., Hardy, M.E., Campbell, D.S., Parant, J.M., Yost, H.J., Kanki, J.P., and Chien, C.B. (2007). The Tol2kit: A multisite gateway-based construction kit for Tol2 transposon transgenesis constructs. Dev. Dyn. *236*, 3088–3099.

Labun, K., Montague, T.G., Gagnon, J.A., Thyme, S.B., and Valen, E. (2016). CHOPCHOP v2: a web tool for the next generation of CRISPR genome engineering. Nucleic Acids Res. *44* (W1), W272-6.

Ladoux, B., Anon, E., Lambert, M., Rabodzey, A., Hersen, P., Buguin, A., Silberzan, P., and Mège, R.-M. (2010). Strength dependence of cadherin-mediated adhesions. Biophys. J. *98*, 534–542.

Lecuit, T., Lenne, P.-F., and Munro, E. (2011). Force generation, transmission, and integration during cell and tissue morphogenesis. Annu. Rev. Cell Dev. Biol. *27*, 157–184.

Lepage, S.E., and Bruce, A.E.E. (2010). Zebrafish epiboly: mechanics and mechanisms. Int. J. Dev. Biol. *54*, 1213–1228.

Li, Q., Lau, A., Morris, T.J., Guo, L., Fordyce, C.B., and Stanley, E.F. (2004). A syntaxin 1, Galpha(o), and N-type calcium channel complex at a presynaptic nerve terminal: analysis by quantitative immunocolocalization. J. Neurosci. *24*, 4070–4081.

Li, P., Banjade, S., Cheng, H.-C., Kim, S., Chen, B., Guo, L., Llaguno, M., Hollingsworth, J.V., King, D.S., Banani, S.F., et al. (2012). Phase transitions in the assembly of multivalent signalling proteins. Nature *483*, 336–340.

Lye, M.F., Fanning, A.S., Su, Y., Anderson, J.M., and Lavie, A. (2010). Insights into regulated ligand binding sites from the structure of ZO-1 Src homology 3-guanylate kinase module. J. Biol. Chem. *285*, 13907–13917.

Maître, J.-L., Berthoumieux, H., Krens, S.F.G., Salbreux, G., Jülicher, F., Paluch, E., and Heisenberg, C.-P. (2012). Adhesion functions in cell sorting by mechanically coupling the cortices of adhering cells. Science *338*, 253–256.

Matter, K., and Balda, M.S. (2003). Signalling to and from tight junctions. Nat. Rev. Mol. Cell Biol. *4*, 225–236.

Mayer, M., Depken, M., Bois, J.S., Jülicher, F., and Grill, S.W. (2010). Anisotropies in cortical tension reveal the physical basis of polarizing cortical flows. Nature *467*, 617–621.

Meeker, N.D., Hutchinson, S.A., Ho, L., and Trede, N.S. (2007). Method for isolation of PCR-ready genomic DNA from zebrafish tissues. Biotechniques *43*, 610, 612, 614.

Miesfeld, J.B., Gestri, G., Clark, B.S., Flinn, M.A., Poole, R.J., Bader, J.R., Besharse, J.C., Wilson, S.W., and Link, B.A. (2015). Yap and Taz regulate retinal pigment epithelial cell fate. Development *142*, 3021–3032.

Monahan, Z., Ryan, V.H., Janke, A.M., Burke, K.A., Rhoads, S.N., Zerze, G.H., O'Meally, R., Dignon, G.L., Conicella, A.E., Zheng, W., et al. (2017). Phosphorylation of the FUS low-complexity domain disrupts phase separation, aggregation, and toxicity. EMBO J. *36*, 2951–2967.

Montague, T.G., Cruz, J.M., Gagnon, J.A., Church, G.M., and Valen, E. (2014). CHOPCHOP: a CRISPR/Cas9 and TALEN web tool for genome editing. Nucleic Acids Res. *42*, W401-7.

Montero, J.-A., Carvalho, L., Wilsch-Bräuninger, M., Kilian, B., Mustafa, C., and Heisenberg, C.-P. (2005). Shield formation at the onset of zebrafish gastrulation. Development *132*, 1187–1198.

Munro, E., Nance, J., and Priess, J.R. (2004). Cortical flows powered by asymmetrical contraction transport PAR proteins to establish and maintain anterior-posterior polarity in the early C. elegans embryo. Dev. Cell *7*, 413–424.

Nekrasova, O., and Green, K.J. (2013). Desmosome assembly and dynamics. Trends Cell Biol. *23*, 537–546.

Niessen, C.M. (2007). Tight junctions/adherens junctions: basic structure and function. J. Invest. Dermatol. *127*, 2525–2532.

Otani, T., Ichii, T., Aono, S., and Takeichi, M. (2006). Cdc42 GEF Tuba regulates the junctional configuration of simple epithelial cells. J. Cell Biol. *175*, 135–146.

Preibisch, S., Saalfeld, S., and Tomancak, P. (2009). Globally optimal stitching of tiled 3D microscopic image acquisitions. Bioinformatics *25*, 1463–1465.

Schindelin, J., Arganda-Carreras, I., Frise, E., Kaynig, V., Longair, M., Pietzsch, T., Preibisch, S., Rueden, C., Saalfeld, S., Schmid, B., et al. (2012). Fiji: an open-source platform for biological-image analysis. Nat. Methods *9*, 676–682.

Shaner, N.C., Lambert, G.G., Chammas, A., Ni, Y., Cranfill, P.J., Baird, M.A., Sell, B.R., Allen, J.R., Day, R.N., Israelsson, M., et al. (2013). A bright monomeric green fluorescent protein derived from Branchiostoma lanceolatum. Nat. Methods *10*, 407–409.

Shen, L., Weber, C.R., and Turner, J.R. (2008). The tight junction protein complex undergoes rapid and continuous molecular remodeling at steady state. J. Cell Biol. *181*, 683–695.

Shin, K., Fogg, V.C., and Margolis, B. (2006). Tight junctions and cell polarity. Annu. Rev. Cell Dev. Biol. *22*, 207–235.

Smutny, M., Ákos, Z., Grigolon, S., Shamipour, S., Ruprecht, V., Čapek, D., Behrndt, M., Papusheva, E., Tada, M., Hof, B., et al. (2017). Friction forces position the neural anlage. Nat. Cell Biol. *19*, 306–317.

Sommer, C., Straehle, C., Köthe, U., and Hamprecht, F.A. (2011). Ilastik: Interactive learning and segmentation toolkit. In IEEE International Symposium on Biomedical Imaging: From Nano to Macro (IEEE), pp. 230–233.

Spadaro, D., Le, S., Laroche, T., Mean, I., Jond, L., Yan, J., and Citi, S. (2017). Tension-Dependent Stretching Activates ZO-1 to Control the Junctional Localization of Its Interactors. Curr. Biol. *27*, 3783–3795.e8.

Style, R.W., Sai, T., Fanelli, N., Ijavi, M., Smith-Mannschott, K., Xu, Q., Wilen, L.A., and Dufresne, E.R. (2018). Liquid-Liquid Phase Separation in an Elastic Network. Phys. Rev. X *8*, 011028.

Takesono, A., Moger, J., Farooq, S., Cartwright, E., Dawid, I.B., Wilson, S.W., and Kudoh, T. (2012). Solute carrier family 3 member 2 (Slc3a2) controls yolk syncytial layer (YSL) formation by regulating microtubule networks in the zebrafish embryo. Proc. Natl. Acad. Sci. USA *109*, 3371–3376.

Talbot, J.C., and Amacher, S.L. (2014). A streamlined CRISPR pipeline to reliably generate zebrafish frameshifting alleles. Zebrafish *11*, 583–585.

Thielicke, W., and Stamhuis, E.J. (2014). PIVlab – Towards User-friendly, Affordable and Accurate Digital Particle Image Velocimetry in MATLAB. J. Open Res. Softw. *2*, e30.

Tornavaca, O., Chia, M., Dufton, N., Almagro, L.O., Conway, D.E., Randi, A.M., Schwartz, M.A., Matter, K., and Balda, M.S. (2015). ZO-1 controls endothelial adherens junctions, cell-cell tension, angiogenesis, and barrier formation. J. Cell Biol. *208*, 821–838.

Utepbergenov, D.I., Fanning, A.S., and Anderson, J.M. (2006). Dimerization of the scaffolding protein ZO-1 through the second PDZ domain. J. Biol. Chem. *281*, 24671–24677.

Van Itallie, C.M., and Anderson, J.M. (2014). Architecture of tight junctions and principles of molecular composition. Semin. Cell Dev. Biol. *36*, 157–165.

Villefranc, J.A., Amigo, J., and Lawson, N.D. (2007). Gateway compatible vectors for analysis of gene function in the zebrafish. Dev. Dyn. *236*, 3077–3087.

Watabe-Uchida, M., Uchida, N., Imamura, Y., Nagafuchi, A., Fujimoto, K., Uemura, T., Vermeulen, S., van Roy, F., Adamson, E.D., and Takeichi, M. (1998). alpha-Catenin-vinculin interaction functions to organize the apical junctional complex in epithelial cells. J. Cell Biol. *142*, 847–857.

Weiss, E.E., Kroemker, M., Rüdiger, A.H., Jockusch, B.M., and Rüdiger, M. (1998). Vinculin is part of the cadherin-catenin junctional complex: complex formation between alpha-catenin and vinculin. J. Cell Biol. *141*, 755–764.

Westerfield, M. (2007). The zebrafish book: a guide for the laboratory use of zebrafish (Danio rerio) (University of Oregon Press).

Wheelock, M.J., and Johnson, K.R. (2003). Cadherin-mediated cellular signaling. Curr. Opin. Cell Biol. *15*, 509–514.

Wittchen, E.S., Haskins, J., and Stevenson, B.R. (2003). NZO-3 expression causes global changes to actin cytoskeleton in Madin-Darby canine kidney cells: linking a tight junction protein to Rho GTPases. Mol. Biol. Cell *14*, 1757–1768.

Ye, F., Zeng, M., and Zhang, M. (2018). Mechanisms of MAGUK-mediated cellular junctional complex organization. Curr. Opin. Struct. Biol. *48*, 6–15.

Yonemura, S., Wada, Y., Watanabe, T., Nagafuchi, A., and Shibata, M. (2010). alpha-Catenin as a tension transducer that induces adherens junction development. Nat. Cell Biol. *12*, 533–542.

Yu, D., Marchiando, A.M., Weber, C.R., Raleigh, D.R., Wang, Y., Shen, L., and Turner, J.R. (2010). MLCK-dependent exchange and actin binding region-dependent anchoring of ZO-1 regulate tight junction barrier function. Proc. Natl. Acad. Sci. USA *107*, 8237–8241.

Zeng, M., Shang, Y., Araki, Y., Guo, T., Huganir, R.L., and Zhang, M. (2016). Phase Transition in Postsynaptic Densities Underlies Formation of Synaptic Complexes and Synaptic Plasticity. Cell *166*, 1163–1175.e12.

Zihni, C., and Terry, S.J. (2015). RhoGTPase signalling at epithelial tight junctions: Bridging the GAP between polarity and cancer. Int. J. Biochem. Cell Biol. *64*, 120–125.

Zihni, C., Mills, C., Matter, K., and Balda, M.S. (2016). Tight junctions: from simple barriers to multifunctional molecular gates. Nat. Rev. Mol. Cell Biol. *17*, 564–580.

STAR★METHODS

KEY RESOURCES TABLE

REAGENT or RESOURCE	SOURCE	IDENTIFIER
Antibodies		
Anti-ZO-1 mouse Monoclonal Antibody (ZO1-1A12)	Thermo Fisher Scientific	Cat# 33-9100; RRID:AB_2533147
Anti-ZO-3 rabbit Antibody	Benais-Pont et al., 2003	N/A
Anti-E-Cadherin (zebrafish) rabbit Antibody	Maître et al., 2012	N/A
Anti-alpha-Catenin antibody produced in rabbit	Sigma-Aldrich	Cat# C2081; RRID:AB_476830
Monoclonal Anti-beta-Catenin antibody produced in mouse	Sigma-Aldrich	Cat# C7207; RRID:AB_476865
Alexa Fluor 488 goat anti-mouse IgG (H+L)	Thermo Fisher Scientific	Cat# A-11001; RRID:AB_2534069
Alexa Fluor 488 goat anti-rabbit IgG (H+L)	Thermo Fisher Scientific	Cat# A-11008; RRID: AB_143165
Alexa Fluor 594 Goat Anti-Mouse IgG (H+L)	Thermo Fisher Scientific	Cat# A-11005; RRID:AB_2534073
Alexa Fluor 546 goat anti-rabbit IgG (H+L)	Thermo Fisher Scientific	Cat# A-11010; RRID:AB_2534077
Alexa Fluor 647 goat anti-mouse IgG (H+L)	Thermo Fisher Scientific	Cat# A-21235; RRID:AB_2535804
Alexa Fluor 647 goat anti-rabbit IgG (H+L)	Thermo Fisher Scientific	Cat# A-21244; RRID:AB_2535812
Chemicals, Peptides, and Recombinant Proteins		
GFP protein	Gift from Alf Honigmann (MPI-CBG Dresden)	N/A
Latrunculin B	EMD Millipore	Cat# 428020-1MG
DMSO	Sigma	Cat# D8418-100ML; CAS: 67-68-5
Experimental Models: Organisms/Strains		
Zebrafish: TL wild-type	MPI-CBG Dresden	N/A
Zebrafish: AB wild-type	MPI-CBG Dresden	N/A
Zebrafish: Tuebingen wild-type	MPI-CBG Dresden	N/A
Zebrafish: MZ*zo-1b*	this study	N/A
Zebrafish: MZ*zo-3*	this study	N/A
Zebrafish: MZ*zo-1b/3*	this study	N/A
Zebrafish: Tg(*actb2:mNeonGreen-zo-1b*)	this study	N/A
Zebrafish: MZ*zo-1b/3*; Tg(*actb2:mNeonGreen-zo-1b*)	this study	N/A
Zebrafish: MZ*zo-1b/3*; Tg(*actb2:mNeonGreen-zo-1bΔABR*)	this study	N/A
Zebrafish: Tg(*actb1:Utr-mCherry*)	Behrndt et al., 2012	N/A
Zebrafish: Tg(*actb1:myl12.1-GFP*)	Behrndt et al., 2012; Maître et al., 2012	RRID: ZFIN_ ZDB-TGCONSTRCT-130108-2
Zebrafish: Tg(*actb1:myl12.1-mcherry*)	Behrndt et al., 2012; Maître et al., 2012	N/A
Zebrafish: Tg(*actb1:myl12.1-mcherry; actb2:mNeonGreen-zo-1b*)	this study	N/A
Zebrafish: Tg(*actb2:mNeonGreen-zo-1b; actb1:Utrophin-mcherry*)	this study	N/A
Tg(*actb2:Lyn-TdTomato*)	Compagnon et al., 2014	ZFIN ID: ZDB-TGCONSTRCT-130516-1
Recombinant DNA		
pCS2-*GFP-zo-1b* (zebrafish version)	This study	N/A
pCS2-*mcherry-zo-1b* (zebrafish version)	This study	N/A

(*Continued on next page*)

Continued

REAGENT or RESOURCE	SOURCE	IDENTIFIER
pCS2-*GFP-zo-3* (zebrafish version)	This study	N/A
pCS2-*GFP-zo-3_4mismatch* (zebrafish version)	This study	N/A
pCS2-*mcherry-zo-3* (zebrafish version)	This study	N/A
pCS2-*mcherry-cingulin-like 1* (zebrafish version)	This study	N/A
pCS2-*Occludin-A-mNEONgreen* (zebrafish version)	This study	N/A
pCS2-*GFP-Claudin D* (zebrafish version)	Gift from Ashley Bruce (University of Toronto)	N/A
pCS2-*GFP-zo-1b-ΔC* (zebrafish version)	This study	N/A
pCS2-*GFP-zo-1b-ΔABR* (zebrafish version)	This study	N/A
pTol2-*actb2:mNEONgreen-zo-1b* (zebrafish version)	This study	N/A
pTol2-*actb2:mNeonGreen-zo-1bΔABR* (zebrafish version)	This study	N/A
pCS2-*membrane-RFP*	Iioka et al., 2004	N/A
pCS2-*membrane-GFP*	Kimmel and Meyer 2010	N/A
pCS2-*lifeact-RFP*	Behrndt et al., 2012	N/A
pCS2-*H2A-mCherry*	Arboleda-Estudillo et al., 2010	N/A
pCS2-*H2B-GFP*	Keller et al., 2008	N/A
Software and Algorithms		
Fiji	Schindelin et al., 2012	https://fiji.sc/
Imaris	Bitplane	https://imaris.oxinst.com/packages
Excel	Microsoft	https://products.office.com/en-us/?rtc=1
GraphPad Prism	GraphPad Software	https://www.graphpad.com/scientific-software/prism/
PIVlab	Thielicke and Stamhuis 2014	https://pivlab.blogspot.com/
MATLAB	MATLAB Software	https://www.mathworks.com/products/matlab.html
Ilastik	Sommer et al., 2011	https://www.ilastik.org/
R; Cumulative Link Models for Ordinal Regression (R Package ordinal)	The R Project for Statistical Computing	https://cran.r-project.org/web/packages/ordinal/index.html

LEAD CONTACT AND MATERIALS AVAILABILITY

Further information and requests for resources, reagents, data, and code should be addressed to the Lead Contact, Carl-Philipp Heisenberg (heisenberg@ist.ac.at). All reagents generated in this study are available from the Lead Contact without restriction.

EXPERIMENTAL MODEL AND SUBJECT DETAILS

Zebrafish (Danio rerio) maintenance and embryo collection were carried out as described (Westerfield, 2007). Embryos were raised at 25-31°C in E3 medium or Danieaus' buffer and staged as described (Kimmel et al., 1995). Embryos from TL or AB strains were used as wild-type control embryos. Fish were bred in the zebrafish facility at IST Austria according to local regulations, and all procedures were approved by the Ethic Committee of IST Austria regulating animal care and usage.

METHOD DETAILS

CRISPR/Cas9 mutant generation

For target site determination of CRISPR/Cas9 mutants of *zo-1b (also known as tjp-1b, ZFIN ID: ZDB-GENE-070925-1)* and *zo-3* (also known as *tjp-3, ZFIN ID: ZDB-GENE-030828-10*) genes, the CHOPCHOP tool was used (https://chopchop.cbu.uib.no) (Labun et al., 2016; Montague et al., 2014). The following target sites were chosen: targeting exon number 13 (3rd PDZ domain) in *zo-1b* and '**g**(A)

GCAAATGGGGACGCGGCAGTGG' targeting exon number 3 (1st PDZ domain) in *zo-3*. To increase the mutagenesis efficiency, the first (A) in the *zo-3* target site was mutated to a **g** (Gagnon et al., 2014). To generate gRNA, a cloning-free method described in Talbot and Amacher (2014) was used. Briefly, sgDNA templates were generated via PCR with the following general oligos: gRNA Primer 1: 5′ - GCGTAATACGACTCACTATAG - 3′, gRNA primer 2: 5′ - AAAGCACCGACTCGGTGCCAC - 3′ and sgDNA_rv: 5' - AAAAGCACC GACTCGGTGCCACTTTTTCAAGTTGATAACGGACTAGCCTTATTTTAACTTGCTATTTCTAGCTCTAAAAC - 3′ and gene specific oligos: *zo-1b* oligo: 5' - GCGTAATACGACTCACTATAGTGGGCTTGAGGCTCGCTGGGTTTTAGAGCTAGAAATAGCAAG - 3′ and *zo-3* oligo: 5' - GCGTAATACGACTCACTATA**g**GCAAATGGGGACGCGGCAGGTTTTAGAGCTAGAAATAGCAAG - 3′. Ambion MAXIscript T7 kit was used to transcribe sgRNA *in vitro*. sgRNA was co-injected with cas9 mRNA (transcribed from Addgene plasmid pCS2-Cas9 #47322 (Gagnon et al., 2014) and a STOP cassette (GTCATGGCGTTTAAACCTTAATTAAGCTGTTGTAG flanked by 20nt homology arms). To determine indel frequencies, genomic DNA was prepared via HotSHOT protocol (Meeker et al., 2007) and the following primer pairs were used for identification of positive insertions of the STOP cassette: PCR of entire locus of *zo-1b* (5′ - TGA AGG TGT TGA GAG AGA GCA G - 3′ and 5′ - CGTTTTTAGGACGTCTCTCACC - 3′), *zo-3* (5′ - TTC TGT CTT TCA CAG GAT TCC A - 3′ and 5′ - CAT AAC AAT CTG ATC TCG CGT C - 3′); PCR of STOP cassette insertion site (5′ - CATGGCGTTTAAACCT TAATTAAGCTGTTG - 3′ in combination with gene-specific reverse primer; gene-specific forward primer in combination with 5′ - CAACAGCTTAATTAAGGTTTAAACGCCATG - 3′).

Finally, the following mutations in *zo-1b* and *zo-3* mutants were identified:

zo-1b mutant (#7, #14): 462 aa before STOP codon (*)
…APVPSVTHDDSILRPSMKLVKFKKGESVGLRHDV*
zo-3 mutant (#13, #20): 44 aa before STOP codon (*)
MEEMTIWEQHTVTLSKDSKVGFGFAVSGGLDKPNPANGDAGHGV*

Frequently, we observed smaller egg sizes in the case of MZ*zo-1b* single mutants and sometimes also in the MZ*zo-1b/3* double mutants. For quantification of EVL epiboly movement in those mutants, we thus only used wild-type eggs with similar sizes as controls.

While we were able to rescue the *zo-1b/3* morphant phenotype by co-injection of *zo-1b* and *zo-3* mRNA, attempts to rescue the MZ*zo-1b/3* mutant phenotype by *zo-1b* and *zo-3* mRNA injection frequently resulted in gain-of-function phenotypes, recognizable by ectopic constriction of the yolk cell by the circumferential actomyosin ring within the YSL. This difference in the efficiency of rescuing the morphant compared to the mutant phenotype might be due to difficulties in achieving the right level of expression in the mutant but not the morphant required for a successful rescue. This could be due to the upregulation of other *zo* genes in mutants (Figure S2H) but not morphants as a result of potential nonsense-mediated decay (El-Brolosy et al., 2019).

Cloning of expression constructs

Wild-type TL or Tuebingen embryos were collected at 4 hpf or 8 hpf, dechorionated and total RNA was extracted from 10-15 embryos per sample using Trizol (Invitrogen). cDNA library was generated with the Superscript III reverse transcription kit according to manufacturer's instructions. Coding region of zebrafish ZO-1b (splice variant: ENSDART00000112588.5), ZO-3 (splice variant: ENSDART00000012336.10) and Cingulin-like 1 (splice variant: ENSDART00000129769.4) were cloned with following primers: *zo-1b* (5′ - GGGG ACA AGT TTG TAC AAA AAA GCA GGC TTC ATG TCT GCC CGG GCT GC - 3′ and 5′ - GGG GAC CAC TTT GTA CAA GAA AGC TGG GTC TCA GAA GTG GTC GAT CAG CAC - 3′), *zo-3* (5′ - GGGG ACA AGT TTG TAC AAA AAA GCA GGC TTC ATG GAG GAG ATG ACG ATA TGG G - 3′ and 5′ - GGG GAC CAC TTT GTA CAA GAA AGC TGG GTC TTA CAG CTC TGT AGC AGG TCC - 3′) and *cingulin-like 1 (*5′ - GGGG ACA AGT TTG TAC AAA AAA GCA GGC TTA ATG GAG TCG TAC AGA GT TGG T - 3′ and 5′ - GGG GAC CAC TTT GTA CAA GAA AGC TGG GTA TCA CAT TGA GAA ACT GGA GAT - 3′). Occludin-A was cloned from 5604348 (IMAGE ID) cDNA clone ordered from Source BioScience with following primers: *oclnA* (5′ - GGGG ACA AGT TTG TAC AAA AAA GCA GGC TTC ATG TCG TCG AAG CAC ATC GG - 3′ and 5′ - GGG GAC CAC TTT GTA CAA GAA AGC TGG GTC GGA TCT GCG GTC GTA ATC GC - 3′).

PCR products were used to generate entry vectors via recombining with pDONR(P1-P2) (Lawson#208) and the entry clone was further recombined with pCS-N-term-EGFP (Lawson #223) or pCS-N-term-mCherry (Lawson #362) destination vector (*zo-1b*, *zo-3*, *cingulin-like1*) or p3E mNeonGreen, pCS2-Dest (Lawson #444) for C-terminal tagging (*occludin-A*).

For morphant rescue experiments, a slightly shorter transcript of *zo-1b* was expressed (splice variant: ENSDART00000112588.5) that is not targeted by the MO. For *zo-3* morphant rescue, four mutations were introduced into the MO recognition site of *zo-3* (pCS2-*GFP-zo-3_4mismatch*): 5' - GAa GAG ATG ACc ATt TGG GAa CAG CAC ACG −3′.

To obtain the different *zo-1b* deletion constructs, the following primers were used to generate different truncated constructs: GFP-ZO-1b-ΔC (5′ - **TGA** GAC CCA GCT TTC TTG TAC AAA G - 3′ and 5′ - AAT GAC TGG CGG GTC CTC TCG C - 3′), GFP-ZO-1b-ΔABR (5′ - AGC GCT GGA GTA AAC CGC TTC - 3′ and 5′ - AGG TTT GGG GTG CCG CGG - 3′).

The desired truncations were amplified with PCR, followed by DpnI digest to remove template DNA (methylated DNA). T4 Polynucleotide kinase kit (NEB) was used for 5′ phosphorylation of DNA for subsequent ligation with T4 ligase kit (NEB). Transformation was performed in One Shot TOP10 Chemically Competent *E. coli* (Thermo Fisher Scientific).

Transgenic zebrafish line generation

The Tol2/Gateway technology was used to generate transgenic fish lines (Kwan et al., 2007; Villefranc et al., 2007). For imaging of ZO-1b and ZO-1b-ΔABR flows and FRAP experiments, transgenic lines ubiquitously expressing mNeonGreen-tagged ZO-1b and ZO-1bΔABR were generated. The following primers with gateway arms were used to amplify the coding region of *zo-1b* (ENSDART00000112588.5) from a cDNA library of wild-type TL embryos at 8 hpf or from *zo-1b-ΔABR* template plasmid:

5' - GGGGACAGCTTTCTTGTACAAAGTGGCTATGTCTGCCCGGGCTGCCTCTAAT - 3′ 5′ - GGGGACAACTTTGTATAATAAA GTTGCTCAGAAGTGGTCGATCAGCACAGAC - 3′. PCR products were used to generate entry vectors via recombing with pDONRP2r-P3 (Lawson#211) and entry clones were further recombined with pDestTol2pA2 (Chien #394), p5E-β-actin promoter (Chien#229), pME mNeonGreen (Shaner et al., 2013) (mNeonGreen licensed by Allelebiotech) and p3E-polyA (Chien#302). Transposase mRNA (Invitrogen) along with the Tol2 construct were co-injected into wild-type embryos (TL strain) to generate Tg(*actb2:mNeonGreen-zo-1b*) transgenic line. To generate the transgenic lines MZ*zo-1b/3*;Tg(*actb2:mNeonGreen-zo-1b*) and MZ*zo-1b/3*; Tg(*actb2:mNeonGreen-zo-1bΔABR*), the respective constructs were co-injected with transposase mRNA into MZ*zo-1b/3* mutant embryos.

Tg(*actb1:myl12.1-mcherry;actb2:mNeonGreen-zo-1b*) and Tg(*actb2:mNeonGreen-zo-1b; actb1:Utrophin-mcherry*) transgenic lines were generated by crossing Tg(*actb2:mNeonGreen-zo-1b*) with pre-existing Tg(*actb1:myl12.1-mcherry*) or Tg(*actb1:Utrophin-mcherry*) lines, respectively.

Other transgenic lines used were Tg(*actb1:myl12.1-eGFP*) and Tg(*actb1:myl12.1-mcherry*) (Behrndt et al., 2012; Maître et al., 2012) to follow cortical actomyosin flow rates and perform laser cuts, and Tg(*actb2:Lyn-TdTomato*) (Compagnon et al., 2014) to label cell membranes for tracking EVL margin progression.

mRNA and Morpholino injections

mRNA transcription was performed using the SP6 mMessage mMachine Kit (Ambion). Glass capillaries (30-0020, Harvard Apparatus) were pulled using a needle puller (P-97, Sutter Instruments) and mounted on a microinjection system (PV820, World Precision Instruments). Injections at 1-cell stage were performed as described (Westerfield, 2007). YSL injections were performed at high stage (3.3 hpf). *H2A-mcherry* (30pg) mRNA and/or 0.2% Phenol red was co-injected as control. For labeling cell membranes and cortical actin, 50 pg *membrane-RFP* (Iioka et al., 2004), 50 pg of *membrane-GFP* (Kimmel and Meyer, 2010), and 40 pg *lifeact-RFP* (Behrndt et al., 2012), and for labeling nuclei to mark the injection site, 2-100 pg *H2A-mCherry* (Arboleda-Estudillo et al., 2010) and 2-25 pg *H2B-GFP* (Keller et al., 2008) were injected. For caMypt overexpression experiments, 100 pg *H2A-mcherry* (Ctrl) and 75 pg *caMypt* plus 25 pg *H2A*-mcherry mRNA were injected into the YSL at 3.3 hpf. For caRhoA overexpression experiments, embryos were injected into marginal blastomeres at 128-cell stage with 2.3-2.5 pg *H2B-EGFP* or *H2A-mcherry* (control) and 0.3-0.5 pg *caRhoA* plus 2 pg *H2B-GFP* or *H2A*-mcherry mRNA. Injection into marginal blastomeres at 128-cell stage was done to achieve locally restricted caRhoA overexpression within the YSL, since uniformly overexpressing caRhoA within the YSL resulted in premature constriction of the actomyosin band and, consequently, embryo lysis. For rescue experiments of *zo-1b/3* YSL-morphant phenotypes, 25 pg GFP-tagged *zo-1b* or 15 pg *zo-1bΔC* or 22 pg GFP-*zo-1b*ΔABR together with 5 pg *zo-3* (mutated in the MO recognition sites) mRNA were co-injected. For expressing different ZO-1b concentrations within the YSL (Figure 5A), *GFP-zo-1b* mRNA was injected in a range of 50 pg to 150 pg. For imaging different ZO-1b constructs at stoichiometric levels in the *MZzo-1b/3* mutant background, 50 pg *GFP-zo-1b* or 30 pg *GFP-zo-1bΔC* or 44 pg *GFP-zo-1bΔABR* mRNA were injected. To image Cingulin-like 1, Claudin-D and Occludin-A, 15- 50 pg mRNA encoding for their respective GFP- or mNeonGreen-fusion constructs were injected at the 1-cell stage. For the colocalization experiments, 30 pg of GFP-tagged *Claudin-D* plus 70 pg mcherry-tagged *zo-1b* mRNA and 30-50 pg mNeonGreen-tagged *Occludin-A* plus 70 pg mcherry-tagged *zo-1b* mRNA and 50 pg GFP-tagged *zo-1b* plus 50 pg mcherry-tagged *Cingulin-like 1* mRNA were injected at the 1-cell stage.

The following Morpholino (MO) sequences were used to generate translation initiation MO: *zo-1b* (ENSDART00000173656.2 - longest variant): 5′ - GTCCGCCAAAGACAGACAAGAGCAT −3′; *zo-3* (ENSDART00000012336.10 - longest variant, ENSDART00000147070.3, ENSDART00000139911.2): 5′ - GCTCCCATATCGTCATCTCCTCCAT - 3′. Titration curves with different *zo-1b/3* MO concentrations and different amounts of *zo-1b/3* mRNAs were performed to find a dose of MOs, which induces phenotypes that can be rescued. This dose (1.5 ng *zo-1b* MO and 0.5 ng *zo-3* MO) was then injected into MZ*zo-1b/3* mutants at 1-cell stage to exclude that additional (potentially unspecific) phenotypes are induced. The above mentioned MO dose was used for all experiments. As further controls, 5-base mismatch control MOs (1.5 ng *zo-1b* 5-base mismatch MO 5′ - GTgCGgCAAAGAgAcACAAcA GCAT - 3; 0.5 ng *zo-3* 5-base mismatch MO 5′ - GgTCgCATATCcTCATCTCgTCgAT - 3′) and a standard negative control MO (2ng human beta-globin MO 5′ - 'CCTCTTACCTCAGTTACAATTTATA' - 3′, Gene Tools) were used.

Sample preparation for live imaging

Embryos were dechorionated and mounted in 0.3%–0.5% low melting point (LMP) agarose (Invitrogen) for live imaging on glass bottom dishes (MatTek). Fixed samples were mounted in 0.5%–1% LMP agarose and put into prepared agarose molds (2%) for upright imaging. Live embryos were imaged at 28.5°C ± 1°C.

Imaging setups for live and fixed imaging

For live imaging, Leica SP5 inverted microscope equipped with a 20x/0.7 CS objective (HC PL APO, 11506513 WD = 0.59 mm, D = 0.17 mm) was used. For imaging fixed samples, Leica SP5 inverted microscope equipped with a 40x objective (HCX PL APO 40x/1.25-0.75 OIL CS - 11506251, WD = 0.1 mm, D = 0.17 mm) or Leica SP5 upright equipped with a 25x/0.95 W dipping lense (HCX IRAPO L, 11506323, WD = 2.5 mm) were used.

Analysis of EVL progression

To determine EVL progression throughout development, the height of EVL (h_{EVL}) was normalized to the total embryo height (h_{TOT}), and then normalized to the average time needed by control embryos and plotted as a function of time. In general, the interval time was set by the acquisition time (10 min); in case of different acquisition times, the EVL progression was interpolated to gain intervals of 10 min. Data of Figures 6D–6E' were randomized before quantification of total EVL epiboly duration.

Whole mount *in situ* hybridization

Embryos at 10.5 hpf were fixed in 4% PFA and then dehydrated and stored for at least 1 day in 100% Methanol at −20°C. Following rehydration in 1xPBS, *in situ* hybridization was performed as previously described (Montero et al., 2005). Antisense RNA probe for *papc* was synthesized from partial cDNA sequence via mMESSAGE mMACHINE T7 Transcription Kit (ThermoFisher AM1344) and DIG-RNA labeling mix (Sigma, 11 277 073 910). A stereomicroscope (Olympus SZX 12) equipped with QImaging Micropublisher 5.0 camera was used to take images of whole mount embryos.

UV laser ablation

Inverted Zeiss microscope (Axio Observer Z1) equipped with a 355 nm UV-A laser and a 63x/1.2 W objective (Korr UV-VIS-IR, 421787-9970) was used to assess junctional tension (Behrndt et al., 2012). Junctional cuts were performed on Tg(*actb1:myl12.1-eGFP*) (Maître et al., 2012) embryos by cutting at 10 equidistant sites along a 5 μm line perpendicular to the junction with 25 UV pulses at 1 kHz. Time for junctional laser ablation was 300-350 msec and for subsequent imaging 300 msec. For determining recoil velocities, first the movement of the junction was corrected (via stackreg function in ImageJ), and a line was drawn along the junction, including the position of ablation to generate a kymograph. The kymograph was then used to extract the opening distance after junctional ablation. A linear fit was performed on the first 4 post-cut distances when plotting distance (in μm) versus time (in s) (see Figures S2I–S2J'). Cases where a wound response after UV cutting was detected were excluded from the quantification.

Imaging of cortical flows within the YSL

For imaging cortical flows of Myosin-2, Tg(*actb1:myl12.1-eGFP*) (Maître et al., 2012) embryos were used, and for simultaneously monitoring ZO-1b and Myosin-2 flows, Tg(*actb1:myl12.1-mcherry*; *actb2:mNEONgreen-zo-1b*) embryos were used. For imaging flows of ZO-1b and ZO-1bΔABR in the MZ*zo-1b/3* mutant background, MZ*zo-1b/3*;Tg(*actb2:mNeonGreen-zo-1b*) and MZ*zo-1b/3*; Tg(*actb2:mNeonGreen-zo-1bΔABR*) were used. High-resolution confocal imaging was performed on a spinning disk setup (Axio Observer Z1, Zeiss) equipped with 100x/1.4 Oil/DIC (Plan APOCHROMAT, 420792-9900). Z stacks of 5-10 μm (0.5 μm in z) were acquired by recording multiple positions along the animal-vegetal (AV) axis of the YSL within the same embryo at a maximum acquisition time of 15 s. Afterwards, the different positions were stitched via ImageJ plugin (Preibisch et al., 2009). Particle image velocimetry (PIV) analysis on maximum intensity projections was performed by using PIVlab in MATLAB after applying a CLAHE filter (Contrast Limited Adaptive Histogram Equalization) to enhance the local contrast of the images. In order to gain mean flow profiles along the AV axis, the linear EVL movement was corrected in order to keep the EVL margin fixed at position 0. From these plots, the peak EVL and YSL flow velocities were extracted to determine whether flow rates had changed in the different conditions. Movies lasted for 5-30 min.

ZO-1b cluster size and circularity analysis

For high spatiotemporal resolution imaging of non-junctional ZO-1b clusters within the YSL, an Axio Observer Z1 inverted microscope (Zeiss, LSM880) equipped with Plan-Apochromat 63x / NA 1.4 Oil was used. For determining the average cluster area, a maximum intensity projection (MIP) was performed and the movement of the junction was corrected (via stackreg function in ImageJ). Images were further processed using Ilastik (Sommer et al., 2011) to train the program for properly detecting signal intensities versus background signal. After cluster segmentation, the average cluster area size over time was determined. To determine circularity, clusters with an area size of more than 0.15 μm^2 were analyzed, because clusters much smaller than this threshold tended to converge to a perfect circle. Circularity was determined via using the plugin 'Circularity' in Fiji, which calculates circularity as

$$Circularity = 4\pi * \frac{area}{perimeter^2}. \quad \text{(Equation 1)}$$

A circularity value of 1 reflects a perfect circle, while values close to 0 indicate more elongated shapes.

ZO-1b cluster fusion analysis

For analyzing the cluster fusion rate, the FiJi plugin TrackMate, and specifically the 'FindMaxima' detector, was used to identify and track bright clusters on MIP images. From the tracking information, the cluster fusion events per time point were then extracted using a custom-made Python script. Average fusion rate was determined as the total fusion number divided by the average cluster number in a time window of 3 min.

Quantitative imaging of ZO-1b

Axio Observer Z1 inverted microscope (Zeiss, LSM880) equipped with Plan-Apochromat 63x / NA 1.4 Oil in Airy Scan mode was used for obtaining GFP calibration curves to determine ZO-1b concentrations. Before each experiment, the Argon laser power was measured with a power meter to normalize to potential fluctuations. For obtaining GFP calibration curves, Matek dishes were coated in 1% BSA for 2h at RT and washed several times before addition of a GFP solution with known concentration. GFP protein solutions were diluted in 1xPBS. Three images per GFP dilution were acquired and averaged. Finally, fluorescence intensity of GFP protein dilutions were plotted against protein concentration (Figure S5A) and the resulting equation of the linear relationship was used to convert fluorescence intensity to ZO-1b protein concentration in μM.

ZO-1b junctional integration efficiency

Non-junctional clusters of ZO-1b were manually tracked in maximum intensity projection images (MIP) using FIJI after EVL-YSL junctional movement correction (via stackreg function in ImageJ). The junctional integration efficiency was calculated as described in Figure S6B.

Tracking analysis of non-junctional clusters

For 3D tracking of non-junctional clusters of ZO-1b and ZO-1bΔABR (Figures S6C–S6C''), the EVL movement was corrected in order to keep the EVL margin fixed at position 0 via the plugin 'correct 3D drift' in FIJI. Then, Imaris tracking 'spots' tool was used. Tracks in yz planes were extracted and a custom-made MATLAB script was used to plot single tracks in yz axes. The percentages of tracks that bypassed the junction in z (lilac box) and tracks that detached from the junction (pink box) were calculated and indicated within the boxes.

Immunostaining

Immunostaining was performed as described (Köppen et al., 2006). Briefly, embryos were fixed in 4% PFA overnight at 4°C. For ZO-1 and ZO-3 immunohistochemistry, fixed embryos were washed in 0.1% Triton X-100 (in PBS) and dechorionated. After another washing step embryos were permeabilized in 0.5% Triton X-100 for 1h, and blocking was performed in blocking solution (10% normal goat serum, 1% DMSO, 0.3% Triton in PBS) for 3-5h at room temperature (RT). Embryos were incubated with primary antibodies in blocking solution overnight at 4°C. Primary antibodies used were mouse anti-ZO-1 (Invitrogen) at 1:50, and rabbit anti-ZO-3 (Benais-Pont et al., 2003) (generated by Karl Matter) at 1:300. After washing the embryos in 0.1% Triton in PBS, they were incubated for 3-4h in secondary antibody solutions at RT or at 4°C overnight and washed again before imaging.

For E-Cadherin, α- and β-Catenin staining, embryos were dehydrated after fixation and stored in 100% Methanol at −20°C overnight. After rehydration, embryos were washed in PBS and incubated in 0.5% Triton X-100 for 1h and blocking was performed in blocking solution (0.5% Tween-20, 0.5% Triton X-100, 1% DMSO, 1% BSA in PBS) for 3-5 h at RT. Embryos were incubated with primary antibodies (rabbit anti - zebrafish E-Cadherin 1:200; Maître et al., 2012; rabbit α-Catenin 1:1000, Sigma; mouse anti-β-Catenin, 1:500, Sigma) in blocking solution at 4°C overnight. Embryos were washed 4x 20 min in blocking buffer and then incubated with secondary antibodies in blocking solution for 3-5 h at RT. Secondary antibodies used were goat anti-mouse/rabbit conjugated to Alexa Fluor 488/594/647 (Molecular probes). To label F-Actin, Phalloidin conjugated to Alexa Fluor 488/Rhodamine/647 was added to the secondary antibody solutions. Finally, embryos were washed 4x 20 min in 0.5% Tween in PBS.

Junctional and YSL cortical quantifications

For quantification of junctional intensities of immunostained embryos, z stack planes were summed via SUM projection (in ImageJ), and of GFP-tagged and mNeonGreen-tagged protein expression constructs (Cingulin-like 1, Claudin-D, Occludin-A, ZO-1b, ZO-1b-ΔC and ZO-1b-ΔABR), maximum intensity projection was performed. A 1 μm segmented line was then drawn along EVL-YSL and EVL-EVL junctions to measure mean fluorescence intensity. For cytoplasmic signal intensities a window of around 5x5 μm was analyzed. For quantification of non-junctional intensities of YSL cortical signals, a mask of the YSL region was generated, and average intensity values along the distance to the EVL were extracted after background subtraction.

Quantification of total intensities

GFP-tagged constructs at stoichiometric ratios (50 pg of full-length GFP-*zo-1b* and 30 pg of truncated GFP-*zo-1bΔC* mRNA) were injected into MZ*zo-1b/3* embryos and z stack planes were summed via SUM projection (in ImageJ) over a 10 μm thickness. A 70 μm x 70 μm window was selected and total intensity was normalized to the used laser power.

qRT-PCR (quantitative Real-Time PCR)

Wild-type TL and MZ*zo-1b/3* embryos were collected at 6 hpf, dechorionated, and total RNA was extracted from 10-15 embryos per sample using Trizol (Invitrogen). To ensure complete removal of any contaminating genomic DNA, DNA-free DNA Removal Kit (Thermo Fisher Scientific) was used. cDNA library was generated with the Superscript III reverse transcription kit according to manufacturer's instructions. Equal amounts of mRNA were used from different samples for the actual qRT-PCR experiment. Experiments were repeated 3x independently in triplicates. Absolute QPCR SYBR Green Mixes (Thermo Scientific) and Bio-Rad C1000 Thermal Cycler was used for qRT-PCR reaction. As negative control, cDNA library generation was performed without adding the reverse transcriptase. As positive control and for later normalization, the housekeeping gene *elongation factor 1α* (Miesfeld et al., 2015) was used. To determine the linear range, different concentrations of cDNA concentrations were tested to finally use a 1:10 cDNA dilution. The following primers were used at a final concentration of 105 nM: *zo-1b* (5′ - CAACAACATCAACGCCATTC - 3′ and 5′ - CCACAA CTGTGTGTCCCTCA - 3′), *zo-3* (5′ - ACCTGGAGGAACCCTTAGGA - 3′ and 5′ - TGTAGGGAGGTTCAGGGCTA - 3′), *zo-1a* (5′ - CC AGCTACAACCGTTTTGTG - 3′ and 5′ - TTGGGAGTCATTAGGGAGGA - 3′), *zo-2a* (5′ - CATCATACCCAGCAAGAGCA - 3′ and 5′ - CT CCAGAAATCGCCTCTGTC - 3′) and *zo-2b* (5′ - GATTACCGCAGCCAGGACTA - 3′ and 5′ - GTCCCTCCGGTACCCACT - 3′).

Colocalization analysis

Images for colocalization analysis of ZO-1b and Myosin-2 were acquired on a Zeiss LSM880 inverted microscope (Airyscan mode, Plan-Apochromat 63x / NA 1.4 Oil) using Tg(*actb1:myl12.1-mcherry*; *actb2:mNeonGreen-zo-1b*) embryos at 6-8 hpf and colocalization of Cingulin-like 1 and ZO-1b images were acquired by injecting mcherry and GFP-tagged versions into wild-type embryos at 8 hpf. After determining the point spread function and the chromatic shift between channels (via imaging TetraSpeck Microspheres with the size of 100 nm), the mcherry channel was corrected for chromatic shift using DoM 'Detection of Molecules' plugin in ImageJ, and images were analyzed by using 'Coloc2′ plugin in ImageJ. As a quantitative measure for colocalization analysis of ZO-1b and Myosin-2, Li's Intensity Correlation Quotient (Li's ICQ) was determined, best suited for the rather complex and heterogeneous distribution of channel intensities in our samples (also see scatter-plot in Figure S5B') (Bolte and Cordelières, 2006; Li et al., 2004). Li's ICQ value ranges from 0.5 showing colocalization to −0.5 showing exclusion with values close to 0 indicate random localization. As a quantitative measure for colocalization between Cingulin-like 1 and ZO-1b, Pearson's R value was determined by using 'Coloc2′ plugin in ImageJ, which was best suited for the observed linear relationship between the two protein species (also see scatter-plot in Figure S6G') (Bolte and Cordelières, 2006).

Fluorescence Recovery After Photobleaching

Data acquisition

Fluorescence Recovery After Photobleaching (FRAP) experiments were performed on a Spinning Disk System (Andor, iXon 897, backthinned EMCCD) assembled on an Axio Observer Z1 microscope (Zeiss) equipped with a 40x/1.2 W objective (C-APOCHROMAT, Korr UV-VIS-IR). Three pre-bleach frames were acquired for estimating the level of bleaching followed by bleaching a 5x5 μm window with a 488 nm laser. For bleaching, a dwell time of 20-60μs and 5-30x repeats at laser powers of 9%–15% was used. Several junctions within the field of view were bleached, but only one junction per cell. Due to the continuous movement of the EVL-YSL junction, a 10μm z stack was imaged with an acquisition time of 10 s.

Data analysis

For FRAP analysis at the EVL-YSL boundary, sum intensity projection was performed on z stacks of the EVL-YSL junction. The ImageJ plugin 'stackreg with rigid body transformation' was used to correct for movement of the junction and to keep the FRAP window at a constant position. Then, a 1 μm thick line was drawn along the junction and the signal along the thickness of the line was averaged via the 'KymoResliceWide' function. Finally, a 5 μm thick line was used to measure the intensities before and after bleaching on the generated kymograph (see white dashed box in Figures S4A–S4B').

Background (BG) subtraction was performed by measuring signal outside of the junctional region of the pre-bleach frame (I_{BG}) to obtain the background corrected intensity at the EVL-YSL junction ($I_{J\text{-}BGcorr}$) and at the reference EVL-EVL junctions ($I_{Ref\text{-}BGcorr}$).

$$I_{J\text{-}BGcorr}(t) = I_J(t) - I_{BG} \quad \text{(Equation 2)}$$

$$I_{Ref\text{-}BGcorr}(t) = I_{Ref}(t) - I_{BG} \quad \text{(Equation 3)}$$

Next, to obtain the intensity corrected for bleaching ($I_{J\text{-}BLcorr}$), the intensity of junctional signal was divided by a reference signal (average of two EVL-EVL junctions):

$$I_{J\text{-}BLcorr}(t) = I_{J\text{-}BGcorr}(t) / I_{Ref\text{-}BGcorr}(t) \quad \text{(Equation 4)}$$

The bleach corrected intensity was then normalized to the mean pre-bleach intensity (average of three pre-bleach frames, N = 3):

$$I_{J\text{-}norm}(t) = \frac{1}{N} \sum_{N} I_{J\text{-}BLcorr}(t) \quad \text{(Equation 5)}$$

For the analysis of non-junctional FRAPs, initial data analysis was carried out as described for junctional FRAPs. A 5 μm thick line was drawn along the non-junctional pool and the signal along the thickness of the line was averaged via the 'KymoResliceWide' function. Finally, a 5μm thick line was used to measure the intensities before and after bleaching on the generated kymograph (see white dashed box in Figures 4E–4F'). Background subtraction was carried out as described for junctional FRAPs (Equations 2 and 3). Then, the background corrected intensities of the non-junctional signal ($I_{nJ\ -BGcorr}(t)$) and the reference signal ($I_{Ref\ -BGcorr}(t)$) were normalized to three pre-bleach frames.

$$I_{nJ\text{-}norm}(t) = \frac{1}{N}\sum_{N} I_{nJ\text{-}BGcorr}(t) \quad \text{(Equation 6)}$$

$$I_{Ref\text{-}norm}(t) = \frac{1}{N}\sum_{N} I_{Ref\text{-}BGcorr}(t) \quad \text{(Equation 7)}$$

Finally, the change in signal of the reference region (unbleached non-junctional region) was deducted from the non-junctional intensity measurements to account for retrograde flow that would otherwise also contribute to signal recovery within the bleached window:

$$I_{nJ\text{-}norm};\, corr(t) = I_{nJ\text{-}norm}(t) - [I_{Ref\text{-}norm}(t) - 1] \quad \text{(Equation 8)}$$

Latrunculin B treatment

Dechorionated embryos were mounted in 0.5% low melting point agarose containing 1 μg/ml Latrunculin B or DMSO as control at the onset of epiboly (4.3 hpf). Danieau's medium containing 1 μg/ml Latrunculin B (EMD Millipore) or DMSO (Sigma) was then added. After a 1h incubation period, embryos were imaged with Axio Observer Z1 inverted microscope (Zeiss, LSM880) equipped with Plan-Apochromat 63x / NA 1.4 Oil in Airy Scan mode at 5.3 till 6.3 hpf.

QUANTIFICATION AND STATISTICAL ANALYSIS

Graphpad Prism 6 was used for statistical analysis. All data were tested for normal distribution with 'D'Agostino & Pearson omnibus normality test'. In case data passed normality test (alpha = 0.05), then a parametric test, such as unpaired t test or ordinary one-way ANOVA (in the case of multiple comparisons) was used. In case the data did not pass the normality test, a non-parametric test was used (Mann-Whitney test or Kruskal-Wallis test for multiple comparisons). To correct for multiple comparisons either Tukey's multiple comparisons test (for ordinary one-way ANOVA) or Dunn's multiple comarisons test (for Kruskal-Wallis test) was used. The individual statistical tests used for experiments are mentioned in the according figure legends. In general, N were considered as independent experiments and n were determined either as number of embryos or number of cells, which is specified in the individual figure legends.

DATA AND CODE AVAILABILITY

All data and code supporting the current study are available from the corresponding author upon request.

Cell

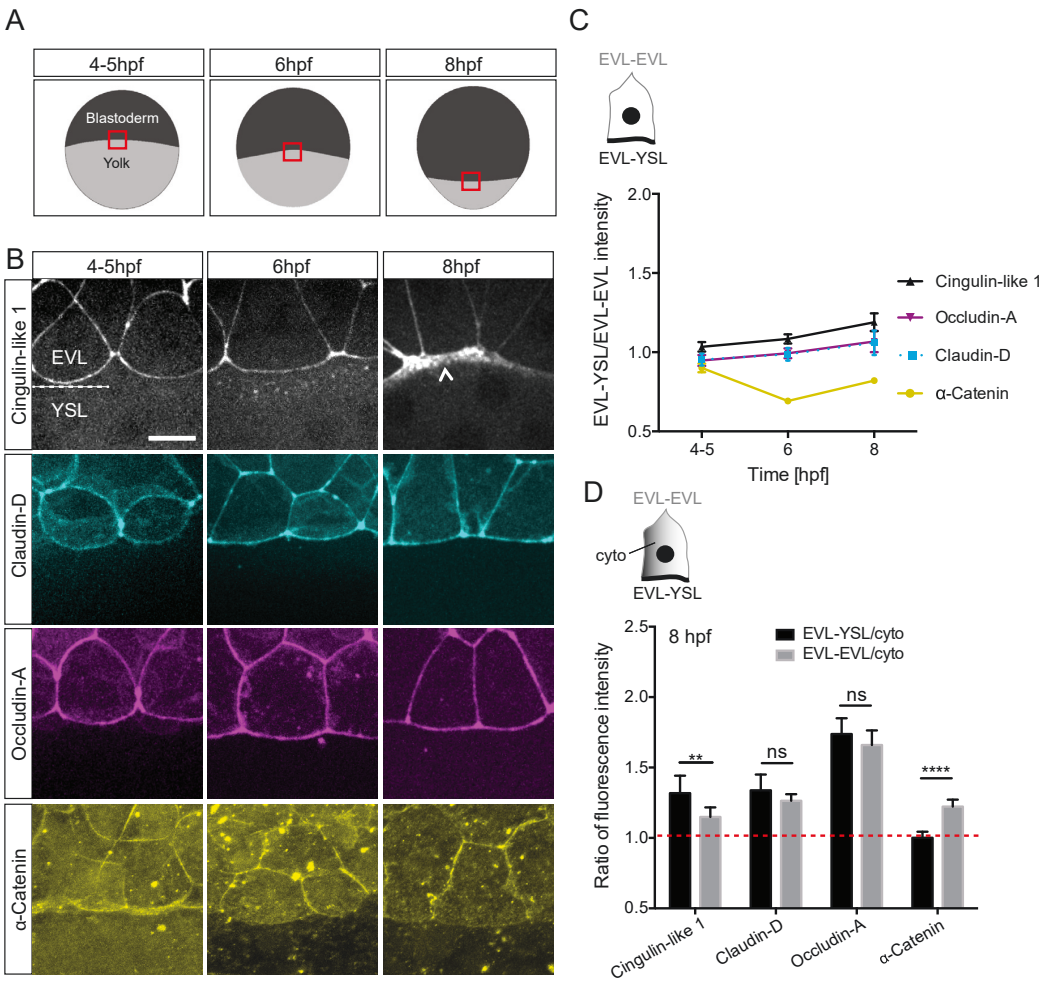

Figure S1. TJ and AJ Component Localization at the EVL-YSL Boundary, Related to Figure 1

(A) Schematic representation of EVL spreading during consecutive stages of epiboly (4-5, 6 and 8 hpf). Yolk cell, light gray; blastoderm (EVL and deep cells), dark gray. Red rectangle demarcates regions of the EVL-YSL boundary shown in (B).

(B) Maximum intensity projections (MIPs) of GFP-Cingulin-like 1, GFP-Claudin-D, Occludin-A-mNeonGreen and α-Catenin localization at the EVL-YSL boundary at 4-5, 6 and 8 hpf. α-Catenin is visualized by immunohistochemistry, Cingulin-like 1 and Claudin-D and Occludin-A by expression of their respective GFP- or mNEONgreen-fusion constructs, respectively, in wild-type embryos. White arrowheads point to increased accumulation at the EVL-YSL boundary. Scale bar, 20 μm.

(C) Plot of EVL-YSL junctional intensity normalized to EVL-EVL junctional intensity as a function of time during EVL epiboly (see also schematic above). Data are mean at 95% confidence. Cingulin-like 1 with N = 2, n = 33 at 4-5 hpf, n = 37 at 6 hpf and n = 31 at 8 hpf. Claudin-D with N = 2, n = 40 at 4-5 hpf, n = 50 at 6 hpf, n = 29 at 8 hpf. Occludin-A with N = 2, n = 27 at 4-5 hpf; N = 2, n = 54 at 6 hpf; N = 3, n = 43 at 8 hpf. α-Catenin with N = 2, n = 45 at 4-5 hpf, n = 29 at 6 hpf, n = 28 at 8 hpf.

(D) Plot of EVL-YSL junctional intensity (black) and EVL-EVL junctional intensity (gray) normalized to cytoplasmic intensity at 8 hpf. Red dashed line indicates ratio of 1 demarcating the boundary between accumulation (> 1) and depletion (< 1). Data are mean at 95% confidence. Cingulin-like 1 with N = 2, n = 30. Claudin-D with N = 2, n = 29 cells. Occludin-A with N = 3, n = 43. α-Catenin with N = 2, n = 28. Cingulin-like 1, Claudin-D and Occludin-A with Mann-Whitney test. α-Catenin with Unpaired t test.

****p < 0.0001; **p < 0.01; ns, not significant; n, number of cells.

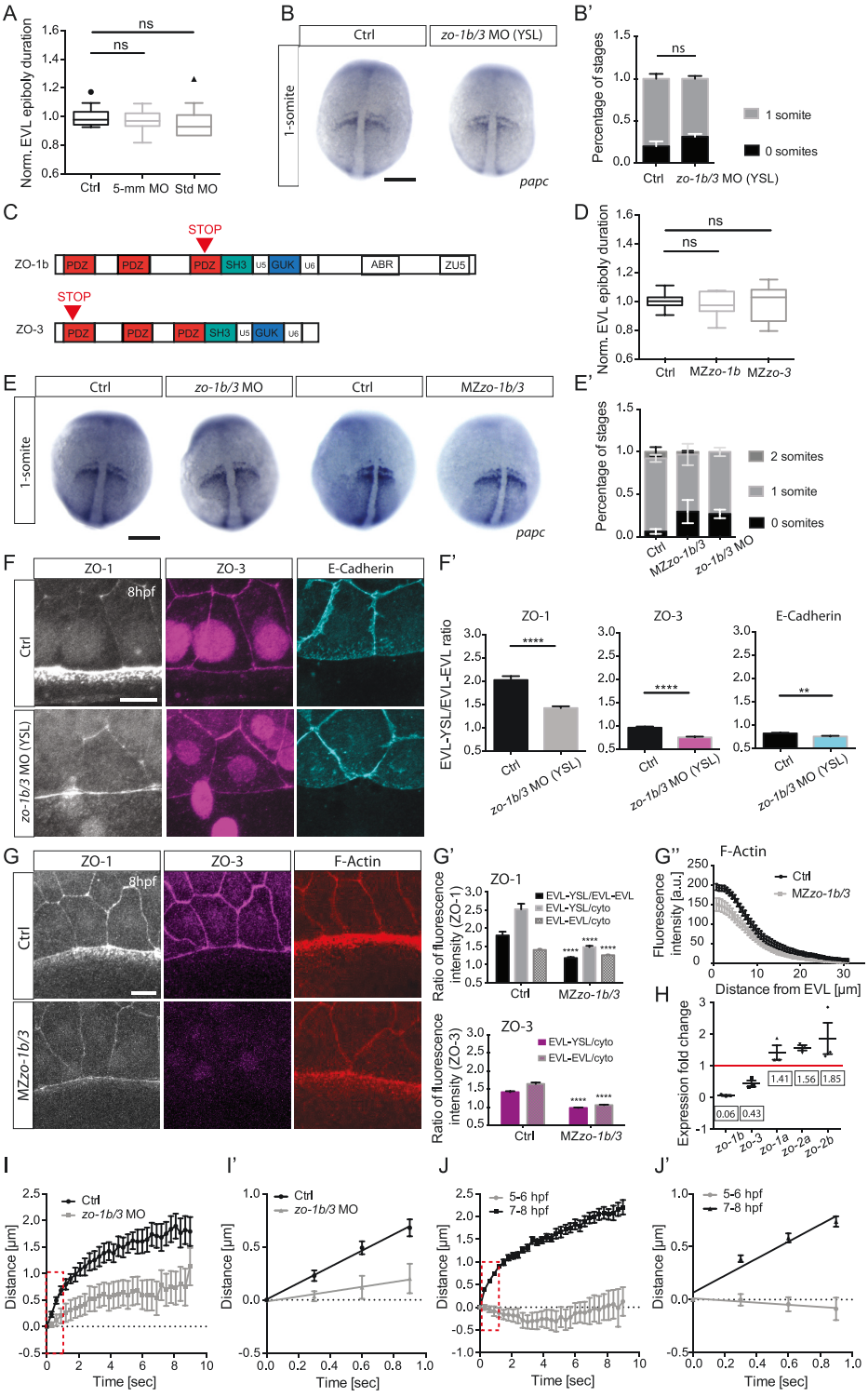

(legend on next page)

Figure S2. *zo-1b/3* Mutant and Morphant Analysis, Related to Figure 2

(A) Plot of total time required for EVL to complete epiboly normalized to the average time needed by control (Ctrl) embryos injected with either phenol-red (Ctrl), *zo-1b/3* 5-base mismatch Ctrl MO (*5mm*-MO) or standard negative Ctrl MO (Std MO) into the YSL. Data are mean ± s.e.m. Kruskal-Wallis test with Dunn's multiple comparisons test. Ctrl with N = 4, n = 14; *zo-1b/3* MO with N = 3, n = 12; standard control MO with N = 3, n = 11.

(B) Dorsal view of YSL-injected Ctrl (phenol-red, YSL-Ctrl) and *zo-1b/3* morphant (YSL-morphant) embryos at 1-somite stage (10.5 hpf) labeled by *in situ* hybridization for *papc* outlining the forming somites. Scale bar, 200 μm.

(B') Bar plot of stage distribution (categorized in 0 and 1 somite stages as revealed by *papc in situ* hybridization) for the conditions described in (B). Data are mean ± s.e.m. 80% of Ctrl-YSL embryos and 69% of *zo-1b/3* YSL-morphants showed 1 somite at 10.5 hpf. Mann-Whitney test. YSL-Ctrl with N = 3, n = 36; YSL-morphant with N = 3, n = 45.

(C) Mutation sites in MZ*zo-1b* and MZ*zo-3* mutants. Red triangles indicate the insertion sites of the STOP codon.

(D) Plot of EVL tissue spreading, expressed as height of EVL (h_{EVL}) normalized to total embryo height (h_{TOT}), as a function of time normalized to average time needed by Ctrl embryos shown for wild-type (wt) Ctrl, and MZ*zo-1b* and MZ*zo-3* single mutants. Data are mean ± s.e.m. One-way ANOVA with Tukey's multiple comparisons test. Wt (Ctrl) with N = 4, n = 27; MZ*zo-1b* with N = 3, n = 16; and MZ*zo-3* with N = 3, n = 18.

(E) Dorsal view of Ctrl (phenol-red, Ctrl) and *zo-1b/3* morphant embryos injected at the 1-cell stage, and of wt and MZ*zo-1b/3* mutant embryos labeled at 10.5 hpf by *in situ* hybridization for *papc* outlining the forming somites. Scale bar, 200 μm.

(E') Plot of stage distribution (categorized in 0, 1 and 2-somite stages as revealed by *papc in situ* hybridization) for the condition described in (E). 86% of Ctrl, 67% of MZ*zo-1b/3* embryos and 73% of *zo-1b/3* morphants showed 1 somite at 10.5 hpf. Data are mean ± s.e.m. Cumulative link mixed model was used to determine p values in R. Ctrl versus MZ*zo-1b/3* mutants with p = 0.0002 and Ctrl versus *zo-1b/3* morphants with p = 0.04. Ctrl with N = 2, n = 26; morphant with N = 3, n = 43; wt Ctrl with N = 4, n = 72 and mutant with N = 5, n = 77.

(F) Maximum intensity projections (MIPs) of ZO-1 (left column), ZO-3 (middle column) and E-cadherin (right column) localization at the EVL-YSL boundary in YSL-Ctrl (upper row) and *zo-1b/3* YSL-morphant (lower row) embryos at 8 hpf. ZO-1, ZO-3 and E-Cadherin were detected by immunohistochemistry. Scale bar, 20μm.

(F') Plot of EVL-YSL junctional intensity normalized to EVL-EVL junctional intensity at 8 hpf for the conditions described in (F). Data are mean ± s.e.m. Statistical test for ZO-1 intensity with Mann-Whitney test, ZO-3 intensity with unpaired t test and E-Cadherin intensity with unpaired t test; ZO-1: N = 2, YSL-Ctrl with n = 30 and *zo-1b/3* YSL-morphant with n = 40; ZO-3: N = 2, YSL-Ctrl with n = 42 and *zo-1b/3* YSL-morphant with n = 59. E-Cadherin: N = 3, Ctrl with n = 51 and *zo-1b/3* YSL-morphant with n = 54.

(G) MIPs of ZO-1, ZO-3 and F-actin localization at the EVL-YSL boundary in wt and MZ*zo-1b/3* mutant embryos at 8 hpf. ZO-1 and ZO-3 were detected by immunohistochemistry, and F-actin by Phalloidin. ZO-1 antibody likely detects both zebrafish ZO-1a and ZO-1b, suggesting that the remaining signal in the MZ*zo-1b/3* mutant reflects ZO-1a protein expression.

(G') Plot of EVL-YSL junctional intensity normalized to EVL-EVL junctional intensity, and EVL-YSL junctional intensity together with EVL-EVL junctional intensity normalized to cytoplasmic intensity at 8 hpf for the conditions shown in (G). Data are mean ± s.e.m. Statistical test for ZO-1: EVL-YSL/EVL-EVL with Mann-Whitney test, and EVL-YSL/cyto and EVL-EVL/cyto with unpaired t test; ZO-3: EVL-YSL/cyto and EVL-EVL/cyto with unpaired t test. N = 2, wt with n = 31 and MZ*zo-1b/3* mutant with n = 33.

(G'') Plot of F-Actin fluorescence intensity within the YSL as a function of distance from EVL margin for the conditions described in (D). F-actin was detected by Phalloidin. Data are mean ± SEM. [a.u.], arbitrary units. N = 2, wt with n = 7 and MZ*zo-1b/3* mutant with n = 7.

(H) Compensatory expression changes of *zo* genes in MZ*zo-1b/3* mutant embryos normalized to the expression level of a housekeeping gene (*elongation factor 1α*). Fold change reflects the relative change of expression levels in MZ*zo-1b/3* mutant compared to wt embryos in qRT-PCR. Data are mean ± SEM. Red solid line indicates 1-fold change in expression, demarcating the boundary between increase (> 1) and decrease (< 1) of expression levels of the five different *zo* genes (N = 3).

(I and J) Plot of junctional opening (distance in μm) of the EVL-YSL boundary marked by Myosin-2-GFP after UV laser cutting at late (8 hpf) stage of EVL epiboly in YSL-Ctrl and *zo-1b/3* YSL-morphant (I) embryos and in wt embryos (J) at mid (6 hpf) and late (8 hpf) stages of EVL epiboly as a function of time after cutting. Data are mean ± SEM. Red dashed boxes indicate regions for calculation of initial recoil velocity shown in (I',J').

(I' and J') Plot of the first four time-points from (I,J) with linear fit to extract initial recoil velocity shown in Figures 2E'' and 2F''). Data are mean ± SEM. N,n see (Figures 2E–2F).

****p < 0.0001; **p < 0.01; ns, not significant; n, number of embryos (A, B', D, E', and G'') and cells (F' and G').

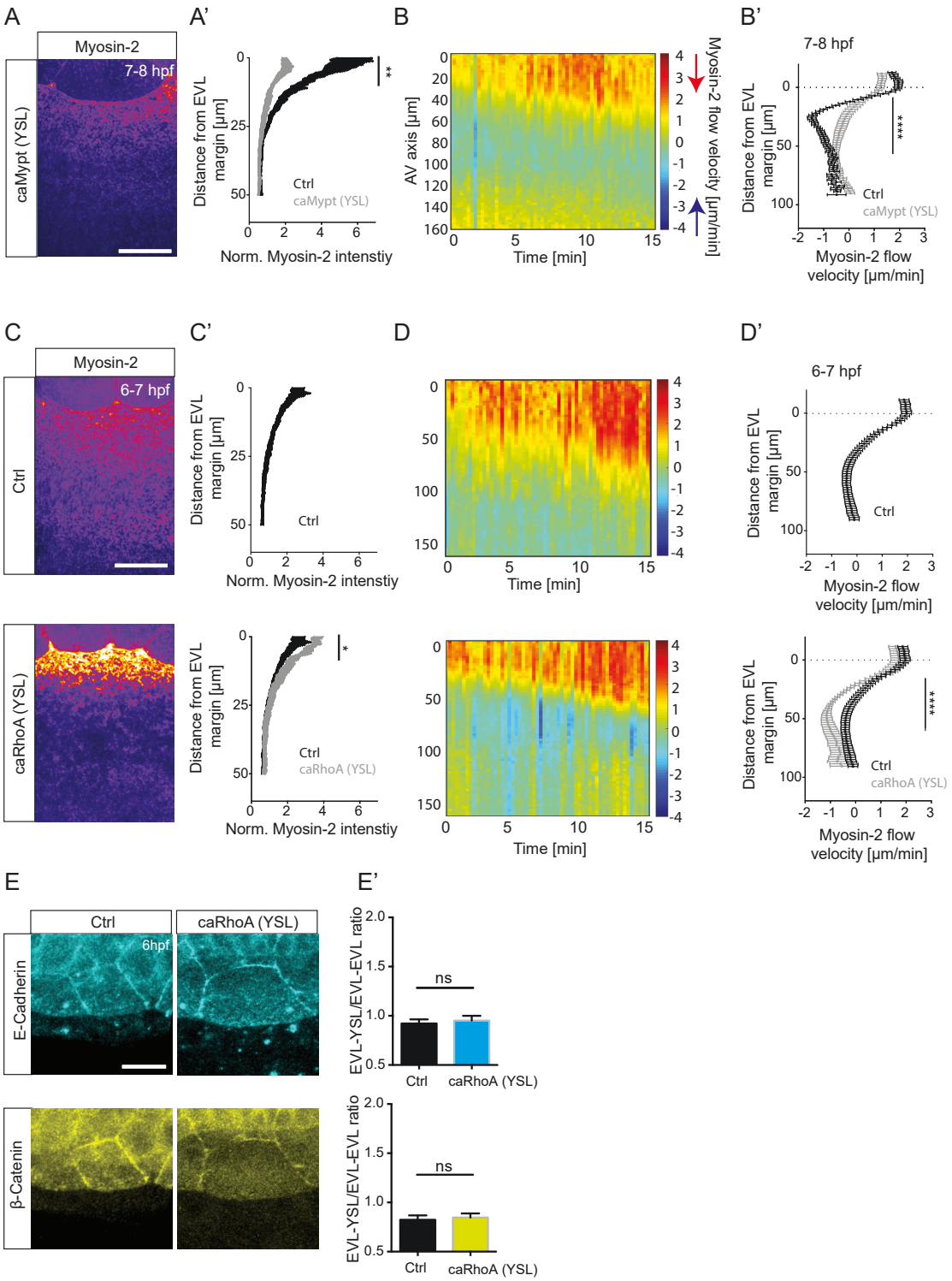

(legend on next page)

Figure S3. Effects of Actomyosin Contractility on Its Flow Rate and AJ Protein Recruitment to the EVL-YSL Boundary, Related to Figure 3

(A and C) MIPs of Myosin-2 localization at the EVL-YSL boundary in Tg(*actb1:myl12.1-eGFP*) embryos that were either injected into the YSL at 3.3 hpf with *caMypt* mRNA plus *H2A-mcherry* mRNA shown at 8 hpf (A), or injected into marginal blastomeres/YSL at 128-cell stage with *H2A*-mcherry mRNA (Ctrl) and *caRhoA* mRNA plus *H2A-mcherry* mRNA shown at 6-7 hpf (C). Scale bar, 20 μm.

(A' and C') Plot of Myosin-2 intensity as a function of distance from EVL margin in *caMypt* (A'), control (Ctrl) and *caRhoA* (C') mRNA YSL-injected embryos at 7-8 hpf and 6-7 hpf, respectively. Fluorescence intensity was normalized to EVL cortical signal. Data are mean ± SEM. Mann-Whitney test. For N/n of YSL-Ctrl see Figure 2C'. *caMypt* mRNA YSL-injected embryos with N = 3, n = 5 (A'); Ctrl with N = 2, n = 6 and *caRhoA* mRNA YSL-injected embryos with N = 3, n = 5 (C').

(B and D) Kymograph of Myosin-2 flow velocities along the animal-vegetal (AV) axis of the embryo as a function of time during epiboly in an exemplary *caMypt* mRNA YSL-injected embryo at 7-8 hpf (B), Ctrl and *caRhoA* mRNA YSL-injected embryo 6-7 hpf (D). Kymograph ranges from negative values (in blue), indicating retrograde flows toward the EVL margin, to positive values (in red), indicating anterograde flows toward the vegetal pole.

(B' and D') Plot of Myosin-2 mean flow velocities along AV axis averaged over 5-30 min in *caMypt* mRNA YSL-injected embryos (B'), Ctrl (phenol-red) and *caRhoA* mRNA (D') YSL-injected embryos between 7-8 hpf and 6-7 hpf, respectively. YSL peak velocities were determined 15-60 μm from EVL margin. Data are mean ± SEM. Statistical test for *caMypt*, Mann-Whitney test, and for *caRhoA*, Unpaired t test. N/n same as in (A',C').

(E) Maximum intensity projections (MIPs) of E-Cadherin and β-Catenin localization at the EVL-YSL boundary in uninjected Ctrl embryos and embryos injected into the YSL with *caRhoA* plus *H2B-EGFP* mRNA at 6 hpf. E-Cadherin and β-Catenin were detected by immunohistochemistry. Scale bar, 20μm.

(E') Plots of E-cadherin and β-Catenin intensities at the EVL-YSL boundary normalized to EVL-EVL junctional intensity for the conditions described in (E). Data are mean ± SEM. Mann-Whitney test, ns, not significant; E-cadherin and β-Catenin with N = 2, Ctrl with n = 31 and *caRhoA* mRNA YSL-injected embryos with n = 27. ****$p < 0.0001$, **$p < 0.01$, *$p < 0.05$; n, number of embryos (A' and C') and cells (E').

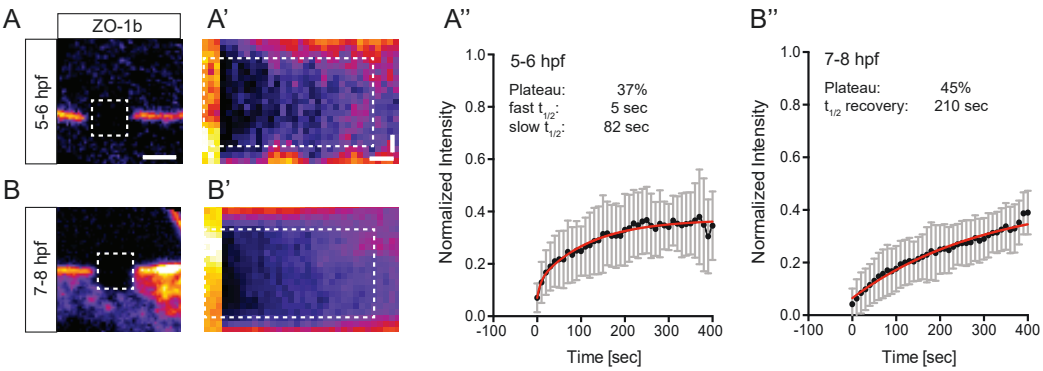

Figure S4. Junctional ZO-1b Dynamics, Related to Figure 4

(A and B) Sum intensity projection image (sum of all slices) of GFP-ZO-1b signal in Tg(*actb2:mNeonGreen-zo-1b*) embryos or in embryos injected with GFP-*zo-1b* mRNA, displaying the EVL-YSL boundary (A with N = 3, n = 9 and B with N = 2, n = 10) after bleaching in FRAP experiments at early-mid (5-6 hpf; A) and late epiboly stage (7-8 hpf; B). White dashed box outlines bleached region. Scale bar, 5 μm.

(A' and B') Exemplary kymograph of bleached region for the conditions described in (A,B). White dashed box outlines region used for intensity measurements. Horizontal scale bar, 40 s; vertical scale bar, 1 μm.

(A'' and B'') Plot of GFP-ZO-1b fluorescence recovery as a function of time for the conditions described in (A,B). Data are mean ± SD. Intensity values were normalized to the pre-bleach intensities and to reference junctional signals to correct for bleaching (more details see STAR Methods). Solid line shows a double exponential fit (A'') and single exponential fit (B''). Double exponential fit was used at early-mid stage (5-6 hpf) due to the presence of two species (fast and slow species) of ZO-1b. Single exponential fit was used at late (8 hpf) stage, because only ~1% of fast species was detectable.

n, number of cells.

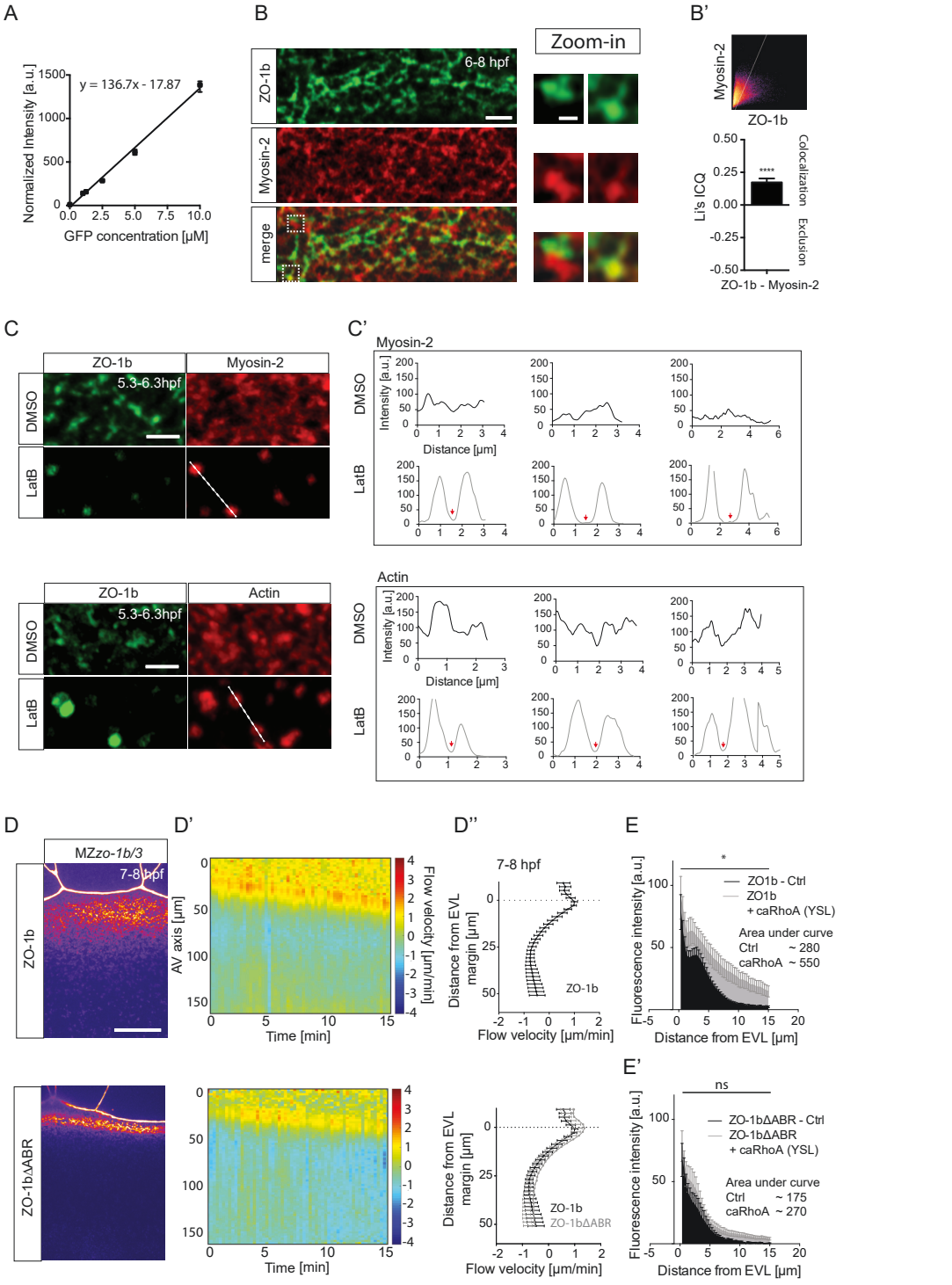

(legend on next page)

Figure S5. Interaction between ZO-1b and the Actomyosin Network within the YSL, Related to Figure 5

(A) Calibration curve of fluorescence intensity normalized to laser power as a function of GFP protein concentration. Data are shown as box-and-whisker plots (whiskers: min to max). a.u., arbitrary units. 0 μM (PBS) with N = 3; 1 μM with N = 1; 1.25 μM with N = 2; 2.5 μM with N = 2; 5 μM with N = 2; 10 μM with N = 3.

(B) Single plane fluorescence images of ZO-1b, Myosin-2 and an overlay of ZO-1b and Myosin-2 to visualize ZO-1b/Myosin-2 protein co-localization within the YSL of Tg(*actb1:myl12.1-mcherry*; *actb2:mNeonGreen-zo-1b*) embryo at 6-8 hpf. White boxes demarcate zoom-in region of examples of either mutual exclusive localization or co-localization of ZO-1b and Myosin-2. Scale bar, 2 μm (left panel) and 0.5 μm (right panel).

(B') Scatterplot of ZO-1b and Myosin-2 showing a wide signal spread indicative of partial colocalization (for more details see STAR Methods). Bar plot of Li's Intensity Correlation Quotient (ICQ) for colocalization quantification of ZO-1b and Myosin-2 between 6-8 hpf. Data are mean ± SD. Li's ICQ value ranges from 0.5 showing colocalization to −0.5 showing exclusion and values close to 0 indicate random localization. N = 4, n = 17.

(C) Maximum intensity projections (MIPs) of ZO-1b, Myosin-2 and Actin signals within the YSL of Tg(*actb1:myl12.1-mcherry*; *actb2:mNeonGreen-zo-1b*) *and Tg(actb2:mNeonGreen-zo-1b;actb2:Utrophin-mcherry)* embryos exposed for 1h to DMSO control (Ctrl) and 1 μg/ml Latrunculin B followed by imaging from 5.3 to 6.3hpf. White dashed line shows exemplary line for plot in (C'). Scale bar, 2 μm.

(C') Line plots of Myosin-2 and Actin network intensity distribution within the YSL of 3 exemplary embryos each treated with DMSO or Latrunculin B (LatB). Note the strong decrease in signal between different Myosin-2 or Actin clusters upon LatB treatment (indicated with red arrow heads).

(D) MIPs of ZO-1b and ZO-1b-ΔABR at the EVL-YSL boundary in *Tg(actb2:mNeonGreen-zo-1b) and Tg(actb2:mNeonGreen-zo-1b*ΔABR*)* transgenic MZ*zo-1b/3* mutant embryos at 7-8 hpf. Scale bar, 20 μm.

(D') Kymograph of flow velocities of ZO-1b and ZO-1b-ΔABR along the animal-vegetal (AV) axis of the embryo as a function of time during epiboly in exemplary embryos at 7-8 hpf. Kymograph ranges from negative values (in blue), indicating retrograde flows toward the EVL margin, to positive values (in red), indicating anterograde flows toward the vegetal pole.

(D'') Plot of mean flow velocities along AV axis averaged over 5-30 min for the conditions described in (D) between 7 and 8 hpf. Data are mean ± SEM. ZO-1b with N = 3, n = 4, ZO-1b-ΔABR with N = 3, n = 8.

(E and E') Plot of non-junctional fluorescence intensity of full-length ZO-1b (E) and ZO-1b-ΔABR (E') as a function of distance from the EVL margin in MZ*zo-1b/3* mutant embryos injected with GFP-*zo-1b* and GFP-*zo-1b-*Δ*ABR* mRNA in Ctrl conditions or after injection of *caRhoA* mRNA into the YSL. Data are mean ± SEM. Statistical test with Mann-Whitney test. Full-length ZO-1b: Ctrl with N = 6, n = 7 and *caRhoA* mRNA YSL-injected with N = 4, n = 7. ZO-1b-ΔABR: Ctrl with N = 3, n = 5 and *caRhoA* mRNA YSL-injected with N = 4, n = 7.

*p < 0.05; ns, not significant; n, number of embryos.

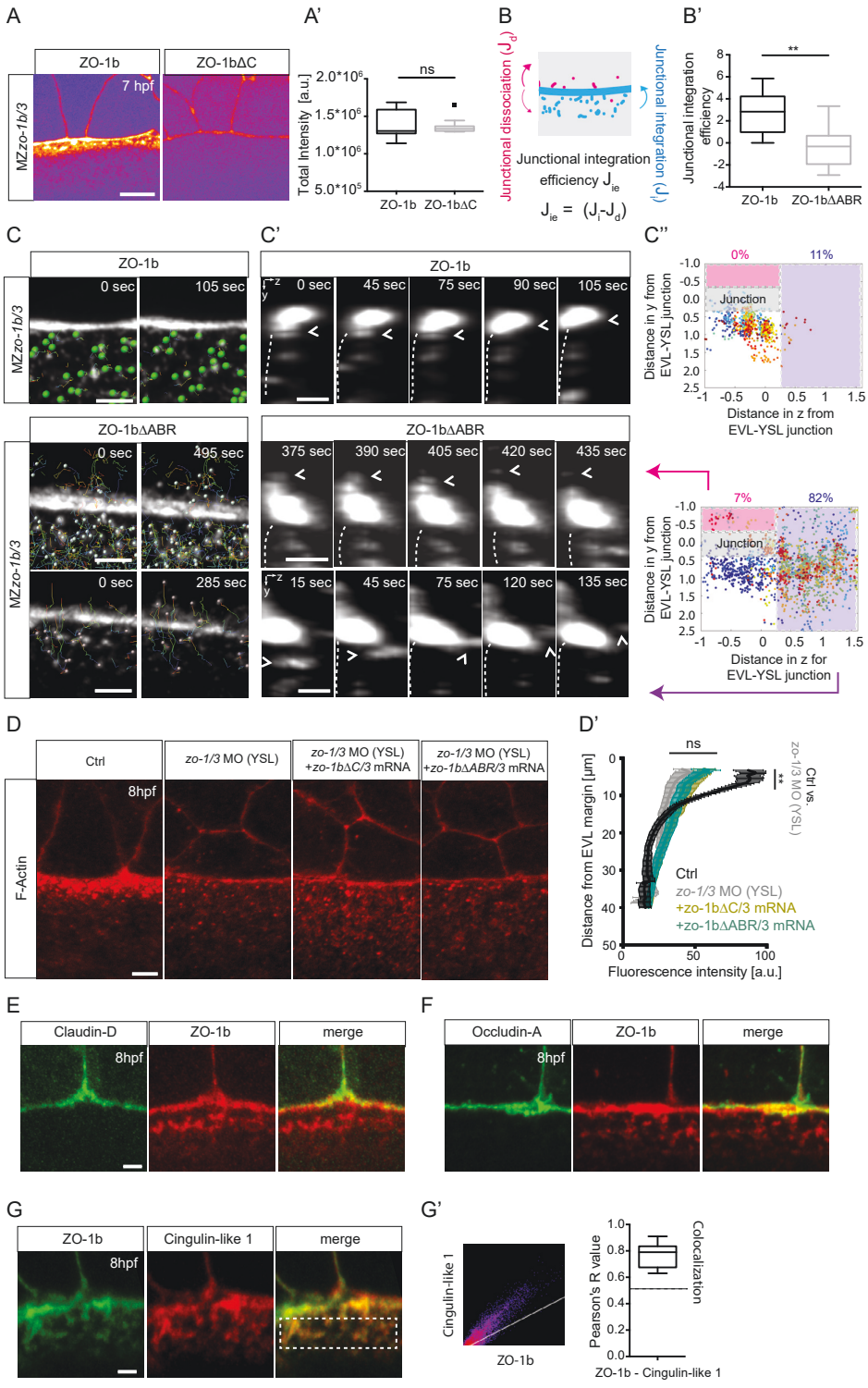

(legend on next page)

Figure S6. Characterization of Mechano-insensitive ZO-1b Constructs and Localization of TJ Proteins, Related to Figure 6

(A) Sum intensity projections (SUM) of GFP-ZO-1b and GFP-ZO-1bΔC localization in MZ*zo-1b/3* mutant embryos at the EVL-YSL boundary at 8 hpf. Scale bar 20 μm.

(A') Total intensity measurement normalized to laser power for the conditions described in (A). Data are shown as box-and-whisker plots (Whiskers: Tukey). Mann Whitney test. ZO-1b with N = 2, n = 20; ZO-1bΔC with N = 2, n = 21.

(B) Sketch of how junctional integration efficiency (J_{ie}) was calculated: number of clusters merging and integrating with the EVL-YSL junction (J_i) subtracted by the number of clusters dissociating from the junction (J_d) and leaving toward the internal or external YSL.

(B') Plot of junctional ZO-1b cluster integration efficiency in MZ*zo-1b/3* mutant embryos injected with either GFP-*zo-1b* mRNA or GFP-*zo-1bΔABR mRNA* normalized to a 3 min time window. Data are shown as box-and-whisker plots (whiskers: Tukey).

(C) Snapshots of 3D tracking of ZO-1b and ZO-1bΔABR non-junctional clusters in MZ*zo-1b/3* mutant embryos injected with either GFP-*zo-1b* mRNA or GFP-*zo-1bΔABR mRNA* at the first and last time points at 7-8 hpf. The EVL movement was corrected in order to keep the EVL-YSL junction fixed in y at position 0 (see STAR Methods). Scale bar, 2 μm.

(C') Single plane of yz of ZO-1b and ZO-1bΔABR cluster tracking with clusters typically being incorporated into the TJ for ZO-1b, and flowing below the TJ into the internal YSL or detaching from the junctional pool for ZO-1bΔABR (indicated by white arrow heads). White dashed line indicates apical side of YSL facing the outside. Scale bar, 1 μm (1st and 3rd row) and 2 μm (2nd row).

(C'') Tracks of non-junctional clusters for the conditions described in (C). Region shaded in gray outlines the EVL-YSL junction in yz direction; region shaded in pink outlines the internal YSL positioned animally from the EVL-YSL junction, where usually almost no cluster detachment is observed for ZO-1b, while for ZO-1bΔABR a substantial fraction (7%) of clusters detach (pink region); region shaded in lilac shows clusters positioned further away from apical YSL surface, where many more ZO-1bΔABR than ZO-1b clusters were found (82% versus 11%). ZO-1b with N = 2, n = 3; ZO-1bΔABR with N = 3, n = 3.

(D) MIPs of F-Actin (Phalloidin) of YSL-control (Ctrl; phenol red injected), *zo-1b/3* YSL-morphant and *zo-1b/3* YSL-morphant embryos co-injected with GFP-tagged *zo-1b*ΔC and *zo-3* (mutated for MO recognition site) as well as GFP-tagged *zo-1b*ΔABR and *zo-3* (mutated for MO recognition site) mRNAs at 8 hpf. Scale bar, 10 μm.

(D') Plot of F-Actin intensity as a function of distance from EVL margin for the conditions described in (D). Data are mean ± SEM. YSL-Ctrl with N = 2, n = 6, *zo-1b/3* YSL-morphant with N = 2, n = 4, *zo-1b/3* YSL-morphant embryos co-injected with a combination of *zo-3* (mutated for MO recognition site) and either GFP-tagged *zo-1b*ΔC mRNA with N = 2, n = 6 or GFP-tagged *zo-1b*ΔABR mRNA with N = 2, n = 6. Statistical testing with Mann-Whitney test. Ctrl versus *zo-1b/3* YSL-morphant with **p, Ctrl or *zo-1b/3* YSL-morphant versus *zo-1b/3* YSL-morphant plus zo-3/*zo-1b*ΔC mRNA with *p and ns, respectively; Ctrl or *zo-1b/3* YSL-morphant versus *zo-1b/3* YSL-morphant plus zo-3/*zo-1b*ΔABR mRNA with **p and ns, respectively.

(E) MIPs of GFP-tagged Claudin-D and mcherry-tagged ZO-1b localization at the EVL-YSL boundary at 8 hpf; visualized by expression of their respective fusion constructs in wild-type (wt) embryos. Scale bar, 2μm.

(F) MIPs of mNeonGreen-tagged Occludin-A and mcherry-tagged ZO-1b localization at the EVL-YSL boundary at 8 hpf; visualized by expression of their respective fusion constructs in wt embryos. Scale bar, 2μm.

(G) MIPs of GFP-tagged ZO-1b and mcherry-tagged Cingulin-like 1 co-localization at the EVL-YSL boundary at 8 hpf; visualized by expression of their respective fusion constructs in wt embryos. Scale bar, 2μm.

(G') Colocalization analysis (Pearson's R value) of GFP-tagged ZO-1b and mcherry-tagged Cingulin-like 1 in wild-type (wt) embryos at 8 hpf. Data are shown as box-and-whisker plots (whiskers: Tukey). Pearson's R value = 0.8, indicating strong colocalization between the two proteins. N = 3, n = 9.

**p < 0.01, *p < 0.05. ns, not significant; n, number of embryos.

2.2 *Phase separation behavior of other ZO proteins and recruitment of mechanoeffectors*

Interestingly, when we investigated the localization of ZO-3 within the YSL, either endogenous levels (Figure 1[118], chapter 2.1) or GFP-tagged ZO-3 at stoichiometric ratio compared to ZO-1b in the MZ*zo-1b/3* background (Figure 17B), we could not detect any obvious non-junctional pool. Consistent with previous cases, in which the lack of non-junctional pool results in the absence of a mechanosensitive response at the EVL-YSL boundary (ZO-1bΔC in Figure 6[118], chapter 2.1), ZO-3 did not show an obvious increase in EVL-YSL accumulation upon caRhoA overexpression (Figure 17B,B'). To investigate whether ZO-3 in principle can undergo phase separation within the YSL, but might be present at too low endogenous levels, we dramatically overexpressed ZO-3. Interestingly, upon expressing high levels of GFP-tagged ZO-3, a clear non-junctional pool became apparent (Figure 17C,C'). This suggests that ZO-3 can be present in a phase-separated state within the YSL, but the endogenous expression levels are below the critical concentration threshold necessary to form non-junctional clusters.

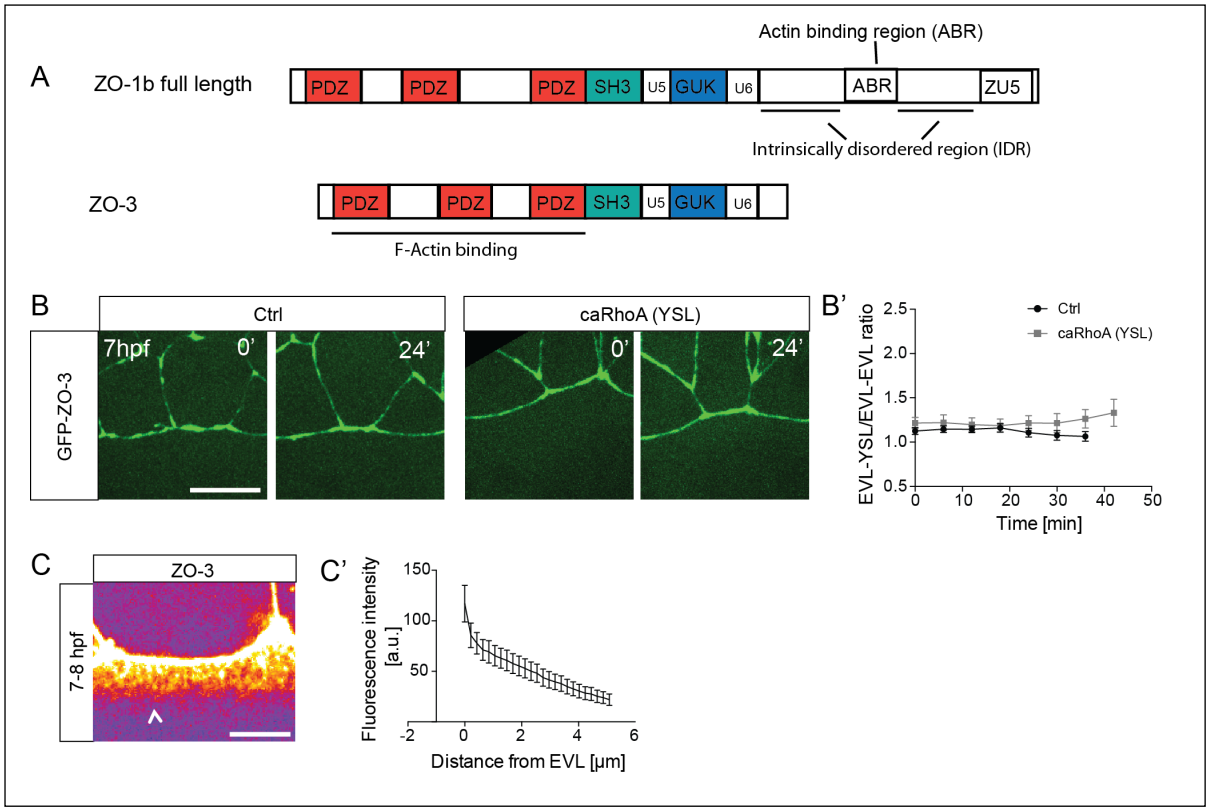

Figure 17. Mechanosensitive behavior of ZO-3

(A) Schematic representation of the domain structure of ZO-1b and ZO-3 proteins. ZO-3 has a much shorter intrinsically disordered C-terminus compared to ZO-1b. The F-actin binding region lies within the N-terminus of ZO-3[119–121].

(B) Maximum intensity projections (MIPs) of GFP-tagged ZO-3 (40 pg) localization at the EVL-YSL boundary in MZ*zo-1b/3* embryos injected with *H2A-mcherry* mRNA (Ctrl) and embryos injected with *caRhoA* mRNA plus *H2A-mcherry* mRNA at the onset of imaging (7hpf) and 24 min later. Scale bar, 10 µm.

(B') Plot of EVL-YSL junctional intensity normalized to EVL-EVL junctional intensity as a function of time during EVL epiboly in the condition described in (B). Data are mean ± SEM. Ctrl with N=3, n=14 cells; caRhoA with N=3, n=12 cells.

(C) MIP of highly expressing ZO-3 in wild-type embryos injected with 200 pg GFP-tagged *zo-3* mRNA. Scale bar, 10 µm.
(C') Plot of non-junctional ZO-3 protein fluorescence intensity as a function of distance from the EVL margin. Data are mean ± SEM. N=2, n=9 embryos. N are number of independent experiments.

In our study we could show that ZO-1b is a mechanosensitive protein, therefore we wanted to identify more candidates in this mechanosensitive cascade. When checking one of the main mechanoeffectors known from AJ mechanosensing[21], Vinculin, we strikingly found that Vinculin gets enriched at all junctions over time (Figure 18A,A'') and with preferential recruitment at the EVL-YSL junction (Figure 18A'). The localization pattern of Vinculin therefore resembles the dynamic behavior of ZO-1b during epiboly (Figure 1[118], chapter 2.1). While these results show a correlation between ZO-1b and Vinculin localization at the EVL-YSL junction, it remains to be tested, whether Vinculin indeed gets recruited indirectly or directly through ZO-1b and hence is indeed involved in the TJ mechanosensation process, or whether its localization is independent of ZO-1b regulation.

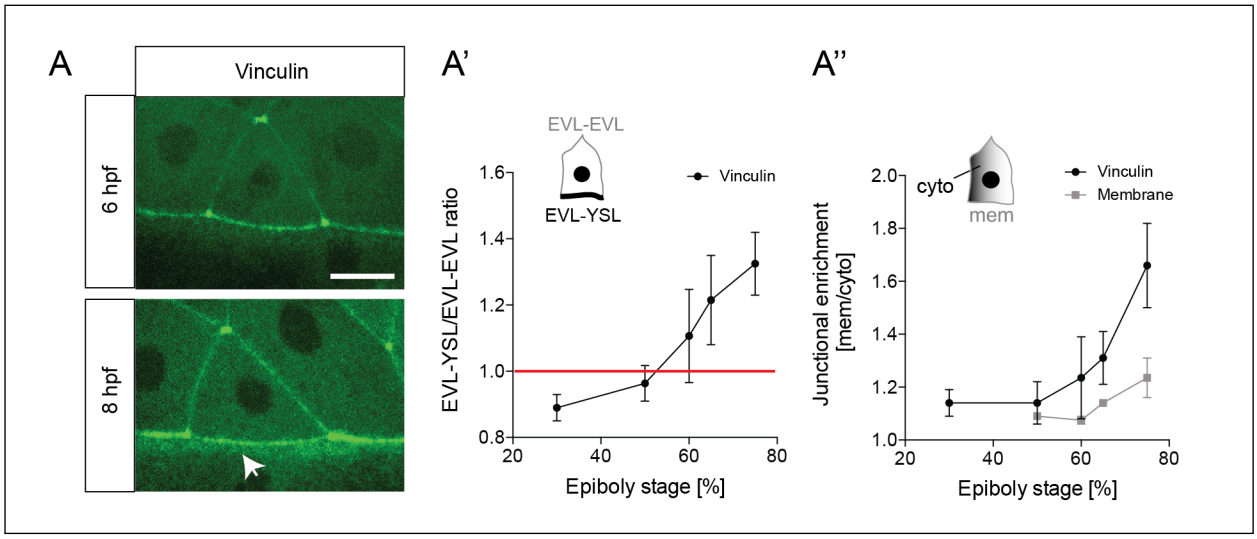

Figure 18. Mechanoeffector recruitment
(A) Maximum intensity projections (MIPs) of EGFP-Vinculin A (100 pg – construct cloned by Hitoshi Morita, former Postdoc in the Heisenberg group) at the EVL-YSL boundary at 6 and 8 hpf. Vinculin is visualized by expression of the respective EGFP-fusion construct in wild-type embryos. White arrowhead points to increased accumulation at the EVL-YSL boundary. Scale bar, 20 µm.
(A') Plot of EVL-YSL junctional intensity normalized to EVL-EVL junctional intensity as a function of time during EVL epiboly (see also schematic above). Red dashed line indicates ratio of 1 demarcating the boundary between accumulation (>1) and depletion (<1). Data are mean ± SEM. N=3, n> 9 cells each.
(A'') Plot of junctional enrichment over time. Junctional enrichment is measured by the ratio of membrane/junctional signal of EVL cells and the cytoplasmic EVL intensity. Data are mean ± SEM. Vinculin with N=2, n> 9 cells; membrane (50 pg Ras-GFP) with N=2, n> 8 cells.

3 Discussion and future directions

In our study, we could decipher the mechanism of how TJ mechanosensation contributes to epithelial tissues spreading. In this chapter we will summarize and further discuss some more aspects and interesting future questions concerning phase separation, mechanosensitivity of ZO-1 and details of ZO-dependent ring formation. Finally, in the last subchapter we will cover potential implications of such mechanosensation or polarization mechanism for other physiological and developmental processes.

3.1 Functionality of phase separation during zebrafish tissue spreading

Epithelial spreading during zebrafish epiboly is in part driven by retrograde actomyosin flows[106]. Here, we provide evidence that the EVL-YSL junction is a mechanosensitive structure, and therefore can respond to tension changes imposed by the adjacent actomyosin network (Figure 3[118], chapter 2.1), which is important for normal epithelial spreading (Figure 6[118], chapter 2.1). Mechanosensation is mediated via actomyosin-driven flows transporting phase-separated ZO-1b clusters towards the junction possibly through advection (Figure 4[118], chapter 2.1). Specifically, ZO-1b needs to reach a critical concentration in order to condense into small clusters (Figure 5[118], chapter 2.1), which are flow-responsive. Upon inhibition of ZO-1's phase separation capacity (ZO-1bΔC construct[82,118]), it fails to reach the proper spatial organization into droplets and cannot be transported in a tension-dependent manner towards the EVL-YSL junction (Figure 5,6[118], chapter 2.1). Hence, ZO-1bΔC is mechano-insensitive and EVL tissue spreading is not rescued when ZO-1bΔC is injected in the morphant (Figure 6[118], chapter 2.1). In summary, we could demonstrate that the phase separation capacity of ZO-1b coupled with the actomyosin-driven transportation of these phase-separated condensates can provide the grounds for a mesoscale mechanosensitive process.

Besides the main function of successfully transporting phase-separated clusters, ZO-1b clusters might also serve to generate 'reaction centers', by acting as scaffolds and recruiting other junctional proteins into pre-assembly sites adjacent to the junction. Indeed, we show that not only ZO-1b displays a non-junctional accumulation within the YSL but also another scaffolding protein, cingulin-like 1 (Figure 1 and S6[118], chapter 2.1) co-localizes with ZO-1b clusters. Surprisingly, we did not find evidence for a similar behavior of TJ transmembrane proteins, such as tetraspan proteins Claudins and Occludins (Figure 1 and S6[118], chapter 2.1). However, at this point we cannot exclude that other genes from the Occludin, Claudin (more than 20 annotated *claudin* genes in zebrafish[122]; zfin.org) or the JAM family could also flow together with ZO-1 and localize adjacent to the junction in order to serve as pre-assembly sites for junctions. Evidence supporting this idea of junction initialization through scaffolding other TJ proteins comes from an *in vitro* reconstitution assay, where ZO-1 condensates can recruit several client proteins such as Cingulin, ZO proteins but also receptors such as Claudin-1 and Occludin[82]. Taken together, in our system of zebrafish epiboly, the main function of phase separation is to enable the transport of ZO-1b towards the junction but it might also play a role in recruiting other TJ proteins towards junctional pre-assembly sites.

3.2 Regulation of the phase separation process in zebrafish epiboly

In our study, we found that ZO-1b is phase separated into clusters and crucial for the mechanosensation at tight junction. However, some open questions remain as to how phase separation is regulated in a spatiotemporal manner. In principle, phase separation can be regulated via concentration (through expression levels)[57,58], degree of multivalency[68,70,72,82], posttranslational modifications by other proteins[8,57,70,82] and via other active processes[123,124].

Interestingly, in the course of our study, endogenous protein expression and localization of different ZO proteins revealed a prominent non-junctional pool and progressive junctional accumulation of ZO-1 during epiboly (Figure 1[118], chapter 2.1); in contrast, ZO-3 EVL-YSL junctional signal remained unchanged during tissue spreading with the absence of a clear non-junctional pool (Figure 1[118], chapter 2.1). The result of ZO-3 not undergoing phase separation within the YSL is surprising, considering successful phase separation of ZO-3 in the *in vitro* reconstitution assay (Figure 13C)[82]. We hypothesized that the critical concentration necessary for ZO-3 phase separation might have not be reached within the YSL. Indeed, upon dramatic overexpression of ZO-3, a non-junctional pool became apparent (Figure 17C,C'). The absence of a non-junctional ZO-3 pool, either at endogenous levels (Figure 1[118], chapter 2.1) or at the same stoichiometric ratio as ZO-1b (in the MZ*zo1b/3* mutant background; Figure 17B,B'), likely underlines the different concentration thresholds of ZO proteins that are necessary for their phase separation. The observed difference in concentration thresholds might stem from the reduced multivalency of ZO-3 compared to ZO-1b due to a much shorter intrinsically disordered C-terminus (Figure 17A). This is consistent with previous data showing that the phase separation capacity scales with the degree of multivalency[68,70,72,82]. In summary, ZO-3 is in principle capable of undergoing phase separation within the YSL but at the given low endogenous expression level, the critical concentration threshold to trigger phase separation is likely not reached. This could also explain the observed absence in mechanosensitive behavior (Figure 17B,B'). In the future it will be interesting to address such differences more rigorously by modulating the multivalency of ZO-1 and ZO-3 proteins. For instance, exchanging C-terminal structures of ZO-1 with ZO-3 and vice versa or adding stretches of variable multivalency[70,72] will be critical to further test the scaling behavior of the phase separation capacity with the multivalency of ZO proteins.

Another way to regulate phase separation is via posttranslational modifications and specifically via de-/phosphorylation[8,57]. For ZO-1 and other MAGUK member interactions, phosphorylation has been demonstrated to likely weaken its phase separation[82] and clustering capacity[125], respectively. Interestingly, during early embryonic zebrafish stages, several protein kinases and phosphatases previously implicated in posttranslational modification of ZO proteins[82] are expressed eg. components of the Casein kinase 2 (CK2; zfin.org) and protein phosphatase 1 (PP1; zfin.org)[126]. Hence, CK2 and PP1 would be interesting next candidates that could be tested for their involvement in the process and to shed light onto the spatiotemporal regulation of ZO-1's phase separation capacity in zebrafish epiboly.

As phase separation is a thermodynamic process[8,57,58], active and energy consuming processes are in principle not required. However, there is evidence for spatial regulation and modulation of material properties in the presence of active processes[123,124]. For instance in the nucleolus, a subset of nucleolar factors undergo LLPS, but their proper localization within the nucleolus is regulated by the presence of active rRNA transcription[123]. Further,

material properties can be dictated by ATP supply, as demonstrated for the nucleolus, where its viscosity stays in a more fluid regime in the presence of ATP[124]. In the context of ZO-1, Beutel et al. show using an *in vitro* reconstitution assay that ZO-1 phase separates without any requirement for active processes[82]. In vivo this is not straightforward to address; however, we could test whether one active mechanism, the contraction of the actomyosin network, is necessary for ZO-1 phase separation. Interestingly, we found that in the absence of an intact actomyosin network, ZO-1 still phase separates, which led us to the conclusion that active contractility of the network is not necessary (Figure 5 and S5[118], chapter 2.1). However, we do not exclude at this point that there might be any other regulation of ZO-1 clustering through the actomyosin network. Especially, because it is conceivable that the actomyosin flows help enrich the ZO-1 non-junctional pool. The Latrunculin B experiments further show that the average size of ZO-1b clusters increases in the absence of a viscoelastic network (Figure 5[118], chapter 2.1), suggesting a role for the actomyosin network in keeping ZO-1b droplets at a certain smaller size and in a different distribution within the YSL. In summary, our results together with the in vitro data by Beutel et al.[82], support the notion that ZO-1b seems to have the inherent capacity to undergo phase separation, but its behavior is likely modulated by other active mechanisms. In summary, there are several layers of potential regulation of phase-separated proteins and assemblies, which will be interesting to be explored further to provide more insight into the interplay of thermodynamic and active processes involved.

3.3 Regulation of ZO-1 mechanosensation on a molecular scale

In our study, we have described a mesoscale mechanosensation process mediated by the cortical flow of cytoskeletal and junctional structures over several tens of micrometers[118] (chapter 2.1) due to the rather big size of the yolk cell. However, on a molecular scale, the mechanosensing process of ZO-1 is not yet entirely understood. A recent study shows that ZO-1 can be stretched and unfolded when put under mechanical load via magnetic tweezers[85]. The forces needed to unfold the C-terminal intrinsically disordered region of ZO-1 are around 2-4 pN[85], which is similar to forces needed to unfold other mechanosensitive proteins such as alpha-catenin[127]. ZO-1, in an unfolded state, has been shown to localize to TJs during homeostasis in mammary epithelial Eph4 cells[85]. However, methods used to visualize the stretched configuration were rather static with utilizing proximity ligation assays and structured illumination microscopy after fixing the tissue[85]. Therefore, the use of FRET tension sensors will be an integral part in addressing the dynamics of ZO-1's mechanosensitive nature in more detail. In short, the current model suggested for ZO-1's molecular mechanosensitivity is the following: ZO-1 gets unfolded and released from its auto-inhibitory state, to then expose the PSG (PDZ3-SH3-GUK) domain for binding transcription factors like ZONAB/DbpA and TJ transmembrane proteins such as Occludin[85]. Therefore, the ability of tension-dependent stretching of ZO-1 might be important for modulating junctional binding and recruitment of other TJ-associated proteins[85].

Interestingly, in our study we found additional mechanoeffectors localizing to the EVL-YSL junction, such as Vinculin (Figure 18A-A''). It is conceivable that Vinculin could be recruited through direct ZO-1 binding, since in mouse cardiac myocytes, Vinculin has been demonstrated to directly bind ZO-1 at gap junctions[128]. Vinculin binds ZO-1 within the PSG domain[128], which is exactly the domain that gets exposed upon force application, implying the following hypothesis: Upon higher tissue tension, ZO-1 gets unfolded and the PSG

domain becomes available for binding partners such as Occludin and Vinculin resulting in (1) enhanced binding to TJ transmembrane proteins and (2) in actomyosin cytoskeleton reinforcement through Vinculin recruitment (similar to Vinculin's mechanoeffector function at AJ[21]). However, this hypothesis still needs to be tested and it will be further interesting to identify more players involved in the tight junction mechanosensation process at the EVL-YSL boundary. Additionally, using FRET tension sensors to detect stretched or folded versions of ZO-1b at the junction and/or in the non-junctional pool will provide further insight into differences in the recruitment of junctional proteins (eg. Occludin, Claudins only detected at the EVL-YSL junction, but not present in the non-junctional pool).

3.4 ZO-1b/3 dependent regulation of the YSL actomyosin ring

In our study, we have identified a double positive feedback loop between ZO proteins and the contractile actomyosin network: (1) ZO-1b and ZO-3 mediate proper ring formation and maturation and on the other hand (2) actomyosin-driven retrograde flow positively affects ZO-1b recruitment. While the positive regulation mentioned in (2) has been extensively studied during this PhD project, there are remaining open questions in case of point (1): What is the nature of biochemical players between ZO-1b/3 proteins and their regulation of actomyosin flows? It is conceivable that this regulatory step could be conserved between other physiological processes of tissue morphogenesis or homeostasis, or during tissue closing processes eg. wound healing. In endothelial cells, ZO-1 indirectly recruits p114RhoGEF towards cell-cell junctions and thereby regulates the perijunctional actomyosin ring establishment through RhoA signaling (chapter 1.2.2.5)[49]. Interestingly, in scratch wound assays, ZO-1 positively affects the migration speed of the endothelial tissue through RhoA signaling[49]. Similarly, when comparing the cytoskeletal dynamics of wound closure and zebrafish epiboly, a lot of parallels can be drawn between the two processes. During single-cell or multicellular wound closure in *Xenopus laevis* oocytes/embryos for instance, actomyosin flows towards the margin and contributes to ring formation[129,130]. At the wound itself RhoA and Cdc42 zones mediate actomyosin contractility and polymerization, respectively[131] (chapter 1.2.1). Hence, this raises the hypothesis that also in the case of YSL actomyosin ring formation/maturation, small GTPases might be the regulatory link between ZO proteins and actomyosin contractility. Indeed, in zebrafish epiboly small GTPases and their regulators (GEFs and GAPs) have already been implicated in YSL actomyosin ring formation. For instance, formin[116] and a Rac-specific GAP[117] are both involved in regulating the actomyosin structure and epiboly movements therein (chapter 1.4.1.1.1). This indicates that similar to wound healing and other physiological processes, activity zones of small GTPases might help in spatially organizing cytoskeletal structures within the YSL actomyosin ring. As previously mentioned, the arrangement of actomyosin structures within the YSL also resembles the different zones in wound healing to a certain degree, with flowing cytoskeleton towards the margin and with a contractile and constricting ring adjacent to the leading edge (chapter 1.2.1). However, to gain more insight into the possible presence of active zones of small GTPases in the YSL, biosensors of RhoA, Cdc42 and Rac could be utilized. Further, a screen of GEFs and GAPs would help to identify candidates and to decipher more rigorously the role of small GTPases and its regulators during actomyosin ring morphogenesis in the YSL.

3.5 Implications of mechanosensation via flow and phase separation in other processes

The mechanosensitive ZO-1 behavior presented in our study might have implications in other mesoscale polarization processes, such as the immunological synapse, C. elegans zygote polarization and wound healing, which we will briefly discuss in this last subchapter. During T-cell activation the immunological synapse gets polarized by a similar process compared to TJ mechanosensation: actomyosin flows from the outer circumference of the synapse towards the center of the synapse and brings with it phase-separated receptor signaling clusters[132–135]. In an *in vitro* reconstitution system, a multicomponent complex around a T-cell receptor signaling complex, LAT-Nck-WASP (discussed in chapter 1.3.5), undergoes multivalency-driven phase separation[136]. Interesting parallels can be drawn between the mechanosensing behavior of the EVL-YSL junction and the immunological synapse: while in zebrafish, the phase separation capacity of ZO-1b is critical for its effective flow towards the tight junction (Figure 5,6[118], chapter 2.1), also in the immunological synapse the receptor signaling clusters have been shown to be present in phase-separated condensates[136]. This suggests that in different systems, phase separation might mediate efficient transport of various protein clusters. Hence, it is conceivable that phase separation per se is a mechanism to render protein assemblies responsive to transport via mesoscale cytoskeletal flows. Indeed, such dependence on clustering for effective flow has been demonstrated in the polarization of the C. elegans zygote[137]. Before the first cell division of the C. elegans zygote, a mesoscale polarization process, in part driven by cortical actomyosin flows, helps in segregating polarity proteins to the respective poles (anterior and posterior)[138,139]. Intriguingly, in this system, the polarity protein Par-3 undergoes oligomerization, which renders the protein responsive to actomyosin flows within a temporally refined window[137]. Par-3 then flows to the anterior pole in a complex with Par-6 and aPKC[137]. The sudden change in clustering state and the reversibility of the oligomerization at later stages hint at a phase separation process of polarity proteins. Although it has been suggested that polarity proteins, such as Par-3 might be able to undergo phase separation[140], clear biological evidence is still missing. Hence, it will be interesting to find out whether the polarization of C. elegans oocyte is mediated by a similar mechanism of actomyosin-driven transport of phase-separated clusters, as we could demonstrate in the case of TJ mechanosensation ([118], chapter 2.1). Lastly, in the case of wound healing, the closure is in part mediated by actomyosin flows towards the open site[129,130]. Therefore, it is conceivable that similar to zebrafish epiboly, ZO proteins could be transported towards the wound site in order to keep polarity but also to provide new anchoring and assembly points for actomyosin structures. This view is at least in part supported by the observation that ZO-1 localizes to the wound edge in monolayers of MDCK cells[141] and even increases its localization over time in wounds of intestinal epithelial cell line Caco-2[142]. However, high spatiotemporal resolution imaging will be necessary to detect the potential flow of phase-separated junctional clusters. Furthermore, knockdown studies of ZO-1 in endothelial cells[49], or knockdown of other TJ components in human keratinocytes[143] or of septate junction components in Drosophila[144] all show significant defects in wound-closure dynamics. Taken together, wound dynamics and zebrafish epiboly share a lot of features such as cytoskeletal flows and the contribution of TJ components for efficient tissue spreading/closure. Therefore, it will be interesting to investigate whether

similar processes through the flow of phase-separated junctional scaffolds contribute to the successful closure of wounds.

In summary, all of the above-mentioned processes share the feature of a mesoscale polarization mediated by active transport of phase-separated droplets[118,136] or oligomerized protein clusters[137]. It is conceivable that in all those systems phase separation/protein clustering per se is crucial in rendering the proteins responsive to flows, as clearly demonstrated in the case of oligomerized Par-3 transport[137] and in tight junction mechanosensation[118]. Importantly, phase separation provides several advantages to a system such as (1) rapid change of the spatial organization of a system, (2) reversibility, which might be important in transient processes, and (3) no requirement for additional input of energy to trigger phase separation, because it is a thermodynamically-driven process[8,57,58]. Finally, phase separation or protein clustering coupled to the active transport by the actomyosin cytoskeleton might be a common strategy to induce mesoscale polarization processes.

References

1. Hadjantonakis, K. & Solnica-Krezel, L. Developmental biology 50 years-investigating the emergence of shape. *Developmental Biology* **341**, 2–4 (2010).
2. Heisenberg, C. P. & Bellaïche, Y. Forces in tissue morphogenesis and patterning. *Cell* **153**, 948 (2013).
3. Lecuit, T. & Mahadevan, L. Morphogenesis one century after on growth and form. *Dev.* **144**, 4197–4198 (2017).
4. Thompson, D. On growth and form (Edition 1). *On growth and form.* 793 (1917). doi:10.2307/2019330
5. Leptin, M. Gastrulation movements: The logic and the nuts and bolts. *Dev. Cell* **8**, 305–320 (2005).
6. Suzuki, M., Morita, H. & Ueno, N. Molecular mechanisms of cell shape changes that contribute to vertebrate neural tube closure. *Dev. Growth Differ.* **54**, 266–276 (2012).
7. Solnica-Krezel, L. Conserved patterns of cell movements during vertebrate gastrulation. *Current Biology* **15**, (2005).
8. Shin, Y. & Brangwynne, C. P. Liquid phase condensation in cell physiology and disease. *Science (80-.).* **357**, (2017).
9. Banani, S. F., Lee, H. O., Hyman, A. A. & Rosen, M. K. Biomolecular condensates: Organizers of cellular biochemistry. *Nature Reviews Molecular Cell Biology* **18**, 285–298 (2017).
10. Lecuit, T., Lenne, P.-F. & Munro, E. Force Generation, Transmission, and Integration during Cell and Tissue Morphogenesis. *Annu. Rev. Cell Dev. Biol.* **27**, 157–184 (2011).
11. Schwayer, C., Sikora, M., Slováková, J., Kardos, R. & Heisenberg, C. P. Actin Rings of Power. *Dev. Cell* **37**, 493–506 (2016).
12. Matter, K. & Balda, M. S. Signalling to and from tight junctions. *Nature Reviews Molecular Cell Biology* **4**, 225–236 (2003).
13. Godsel, L. M., Getsios, S., Huen, A. C. & Green, K. J. The Molecular Composition and Function of Desmosomes. in 137–193 (2004). doi:10.1007/978-3-540-68170-0_6
14. Shin, K., Fogg, V. C. & Margolis, B. Tight Junctions and Cell Polarity. *Annu. Rev. Cell Dev. Biol.* **22**, 207–235 (2006).
15. Niessen, C. M. Tight junctions/adherens junctions: Basic structure and function. *Journal of Investigative Dermatology* **127**, 2525–2532 (2007).
16. Zihni, C., Mills, C., Matter, K. & Balda, M. S. Tight junctions: From simple barriers to multifunctional molecular gates. *Nat. Rev. Mol. Cell Biol.* **17**, 564–580 (2016).
17. Le Duc, Q. *et al.* Vinculin potentiates E-cadherin mechanosensing and is recruited to actin-anchored sites within adherens junctions in a myosin II-dependent manner. *J. Cell Biol.* **189**, 1107–1115 (2010).
18. Liu, Z. *et al.* Mechanical tugging force regulates the size of cell-cell junctions. *Proc. Natl. Acad. Sci. U. S. A.* **107**, 9944–9949 (2010).
19. Thomas, W. A. *et al.* α-Catenin and vinculin cooperate to promote high E-cadherin-based adhesion strength. *J. Biol. Chem.* **288**, 4957–4969 (2013).
20. Maître, J. L. *et al.* Adhesion functions in cell sorting by mechanically coupling the cortices of adhering cells. *Science (80-.).* **338**, 253–256 (2012).
21. Pinheiro, D. & Bellaïche, Y. Mechanical Force-Driven Adherens Junction Remodeling and Epithelial Dynamics. *Developmental Cell* **47**, 3–19 (2018).

22. Thomas, W. Catch Bonds in Adhesion. *Annu. Rev. Biomed. Eng.* **10**, 39–57 (2008).
23. Leckband, D. E. & de Rooij, J. Cadherin Adhesion and Mechanotransduction. *Annu. Rev. Cell Dev. Biol.* **30**, 291–315 (2014).
24. Abe, K. & Takeichi, M. EPLIN mediates linkage of the cadherin-catenin complex to F-actin and stabilizes the circumferential actin belt. *Proc. Natl. Acad. Sci. U. S. A.* **105**, 13–19 (2008).
25. Courtemanche, N., Lee, J. Y., Pollard, T. D. & Greene, E. C. Tension modulates actin filament polymerization mediated by formin and profilin. *Proc. Natl. Acad. Sci. U. S. A.* **110**, 9752–9757 (2013).
26. Jégou, A., Carlier, M. F. & Romet-Lemonne, G. Formin mDia1 senses and generates mechanical forces on actin filaments. *Nat. Commun.* **4**, (2013).
27. Stephenson, R. E. *et al.* Rho Flares Repair Local Tight Junction Leaks. *Dev. Cell* **48**, 445-459.e5 (2019).
28. Lemmers, C. *et al.* CRB3 Binds Directly to Par6 and Regulates the Morphogenesis of the Tight Junctions in Mammalian Epithelial Cells. *Mol. Biol. Cell* **15**, 1324–1333 (2004).
29. Fanning, A. S., Jameson, B. J., Jesaitis, L. A. & Anderson, J. M. The tight junction protein ZO-1 establishes a link between the transmembrane protein occludin and the actin cytoskeleton. *J. Biol. Chem.* **273**, 29745–29753 (1998).
30. Rajasekaran, A. K., Hojo, M., Huima, T. & Rodriguez-Boulan, E. Catenins and zonula occludens-1 form a complex during early stages in the assembly of tight junctions. *J. Cell Biol.* **132**, 451–463 (1996).
31. Maiers, J. L., Peng, X., Fanning, A. S. & DeMali, K. A. ZO-1 recruitment to α-catenin -a novel mechanism for coupling the assembly of tight junctions to adherens junctions. *J. Cell Sci.* **126**, 3904–3915 (2013).
32. Fukuhara, A. *et al.* Involvement of nectin in the localization of junctional adhesion molecule at tight junctions. *Oncogene* **21**, 7642–7655 (2002).
33. Terry, S. J. *et al.* Spatially restricted activation of RhoA signalling at epithelial junctions by p114RhoGEF drives junction formation and morphogenesis. *Nat. Cell Biol.* **13**, 159–166 (2011).
34. Yamada, S. & Nelson, W. J. Localized zones of Rho and Rac activities drive initiation and expansion of epithelial cell-cell adhesion. *J. Cell Biol.* **178**, 517–527 (2007).
35. Arnold, T. R., Stephenson, R. E. & Miller, A. L. Rho GTPases and actomyosin: Partners in regulating epithelial cell-cell junction structure and function. *Exp. Cell Res.* **358**, 20–30 (2017).
36. Itoh, M., Tsukita, S., Yamazaki, Y. & Sugimoto, H. Rho GTP exchange factor ARHGEF11 regulates the integrity of epithelial junctions by connecting ZO-1 and RhoA-Myosin II signaling. *Proc. Natl. Acad. Sci. U. S. A.* **109**, 9905–9910 (2012).
37. Nakajima, H. & Tanoue, T. Lulu2 regulates the circumferential actomyosin tensile system in epithelial cells through p114rhoGEF. *J. Cell Biol.* **195**, 245–261 (2011).
38. Zihni, C. & Terry, S. J. RhoGTPase signalling at epithelial tight junctions: Bridging the GAP between polarity and cancer. *International Journal of Biochemistry and Cell Biology* **64**, 120–125 (2015).
39. Chandhoke, S. K. & Mooseker, M. S. A role for myosin IXb, a motor-RhoGAP chimera, in epithelial wound healing and tight junction regulation. *Mol. Biol. Cell* **23**, 2468–2480 (2012).
40. Omelchenko, T. & Hall, A. Myosin-IXA regulates collective epithelial cell migration by

targeting RhoGAP activity to cell-cell junctions. *Curr. Biol.* **22**, 278–288 (2012).
41. Elbediwy, A. *et al.* Epithelial junction formation requires confinement of Cdc42 activity by a novel SH3BP1 complex. *J. Cell Biol.* **198**, 677–693 (2012).
42. Otani, T., Ichii, T., Aono, S. & Takeichi, M. Cdc42 GEF Tuba regulates the junctional configuration of simple epithelial cells. *J. Cell Biol.* **175**, 135–146 (2006).
43. Oda, Y., Otani, T., Ikenouchi, J. & Furuse, M. Tricellulin regulates junctional tension of epithelial cells at tricellular contacts through Cdc42. *J. Cell Sci.* **127**, 4201–4212 (2014).
44. Wells, C. D. *et al.* A Rich1/Amot Complex Regulates the Cdc42 GTPase and Apical-Polarity Proteins in Epithelial Cells. *Cell* **125**, 535–548 (2006).
45. Pieczynski, J. & Margolis, B. Protein complexes that control renal epithelial polarity. *Am. J. Physiol. - Ren. Physiol.* **300**, (2011).
46. Zihni, C. *et al.* Dbl3 drives Cdc42 signaling at the apical margin to regulate junction position and apical differentiation. *J. Cell Biol.* **204**, 111–127 (2014).
47. Zihni, C., Balda, M. S. & Matter, K. Signalling at tight junctions during epithelial differentiation and microbial pathogenesis. *J. Cell Sci.* **127**, 3401–3413 (2014).
48. Katsuno, T. *et al.* Deficiency of zonula occludens-1 causes embryonic lethal phenotype associated with defected yolk sac angiogenesis and apoptosis of embryonic cells. *Mol. Biol. Cell* **19**, 2465–2475 (2008).
49. Tornavaca, O. *et al.* ZO-1 controls endothelial adherens junctions, cell-cell tension, angiogenesis, and barrier formation. *J. Cell Biol.* **208**, 821–838 (2015).
50. Hatte, G., Prigent, C. & Tassan, J. P. Tight junctions negatively regulate mechanical forces applied to adherens junctions in vertebrate epithelial tissue. *J. Cell Sci.* **131**, (2018).
51. Fanning, A. S., Van Itallie, C. M. & Anderson, J. M. Zonula occludens-1 and -2 regulate apical cell structure and the zonula adherens cytoskeleton in polarized epithelia. *Mol. Biol. Cell* **23**, 577–590 (2012).
52. Yamazaki, Y. *et al.* ZO-1- and ZO-2-dependent integration of myosin-2 to epithelial zonula adherens. *Mol. Biol. Cell* **19**, 3801–3811 (2008).
53. Van Itallie, C. M., Fanning, A. S., Bridges, A. & Anderson, J. M. ZO-1 stabilizes the tight junction solute barrier through coupling to the perijunctional cytoskeleton. *Mol. Biol. Cell* **20**, 3930–3940 (2009).
54. Choi, W. *et al.* Remodeling the zonula adherens in response to tension and the role of afadin in this response. *J. Cell Biol.* **213**, 243–260 (2016).
55. Cartagena-Rivera, A. X., Van Itallie, C. M., Anderson, J. M. & Chadwick, R. S. Apical surface supracellular mechanical properties in polarized epithelium using noninvasive acoustic force spectroscopy. *Nat. Commun.* **8**, (2017).
56. Bazellières, E. *et al.* Control of cell-cell forces and collective cell dynamics by the intercellular adhesome. *Nat. Cell Biol.* **17**, 409–420 (2015).
57. Alberti, S. Phase separation in biology. *Current Biology* **27**, R1097–R1102 (2017).
58. Hyman, A. A., Weber, C. A. & Jülicher, F. Liquid-Liquid Phase Separation in Biology. *Annu. Rev. Cell Dev. Biol.* **30**, 39–58 (2014).
59. Falahati, H. & Haji-Akbari, A. Thermodynamically driven assemblies and liquid-liquid phase separations in biology. *Soft Matter* **15**, 1135–1154 (2019).
60. Luzio, J. P., Pryor, P. R. & Bright, N. A. Lysosomes: Fusion and function. *Nature Reviews Molecular Cell Biology* **8**, 622–632 (2007).
61. Friedman, J. R. & Nunnari, J. Mitochondrial form and function. *Nature* **505**, 335–343

(2014).
62. Gould, H., Tobochnik, J. & Colonna-Romano, L. Entropy-driven phase transitions. *Comput. Phys.* **11**, 157–163 (1997).
63. Brangwynne, C. P., Tompa, P. & Pappu, R. V. Polymer physics of intracellular phase transitions. *Nat. Phys.* **11**, 899–904 (2015).
64. Townes, P. L. & Holtfreter, J. Directed movements and selective adhesion of embryonic amphibian cells. *J. Exp. Zool.* **128**, 53–120 (1955).
65. STEINBERG, M. S. On the mechanism of tissue reconstruction by dissociated cells. I. Population kinetics, differential adhesiveness. and the absence of directed migration. *Proc. Natl. Acad. Sci. U. S. A.* **48**, 1577–1582 (1962).
66. Steinberg, M. S. ON THE MECHANISM OF TISSUE RECONSTRUCTION BY DISSOCIATED CELLS, III. FREE ENERGY RELATIONS AND THE REORGANIZATION OF FUSED, HETERONOMIC TISSUE FRAGMENTS. *Proc. Natl. Acad. Sci.* **48**, 1769–1776 (1962).
67. Krens, S. F. G. & Heisenberg, C. P. *Cell Sorting in Development*. *Current Topics in Developmental Biology* **95**, (2011).
68. Molliex, A. *et al.* Phase Separation by Low Complexity Domains Promotes Stress Granule Assembly and Drives Pathological Fibrillization. *Cell* **163**, 123–133 (2015).
69. Brangwynne, C. P. *et al.* Germline P granules are liquid droplets that localize by controlled dissolution/condensation. *Science (80-.).* **324**, 1729–1732 (2009).
70. Li, P. *et al.* Phase transitions in the assembly of multivalent signalling proteins. *Nature* **483**, 336–340 (2012).
71. Su, X. *et al.* Phase separation of signaling molecules promotes T cell receptor signal transduction. *Science (80-.).* **352**, 595–599 (2016).
72. Pak, C. W. *et al.* Sequence Determinants of Intracellular Phase Separation by Complex Coacervation of a Disordered Protein. *Mol. Cell* **63**, 72–85 (2016).
73. Banjade, S. & Rosen, M. K. Phase transitions of multivalent proteins can promote clustering of membrane receptors. *Elife* **3**, (2014).
74. Protter, D. S. W. & Parker, R. Principles and Properties of Stress Granules. *Trends Cell Biol.* **26**, 668–679 (2016).
75. Wippich, F. *et al.* Dual specificity kinase DYRK3 couples stress granule condensation/ dissolution to mTORC1 signaling. *Cell* **152**, 791–805 (2013).
76. Jiang, H. *et al.* Phase Transition of Spindle-Associated Protein Regulate Spindle Apparatus Assembly. *Cell* **163**, 108–122 (2015).
77. Katsafanas, G. C. & Moss, B. Colocalization of Transcription and Translation within Cytoplasmic Poxvirus Factories Coordinates Viral Expression and Subjugates Host Functions. *Cell Host Microbe* **2**, 221–228 (2007).
78. White, J. P. & Lloyd, R. E. Regulation of stress granules in virus systems. *Trends in Microbiology* **20**, 175–183 (2012).
79. Ye, F., Zeng, M. & Zhang, M. Mechanisms of MAGUK-mediated cellular junctional complex organization. *Current Opinion in Structural Biology* **48**, 6–15 (2018).
80. Zeng, M. *et al.* Phase Transition in Postsynaptic Densities Underlies Formation of Synaptic Complexes and Synaptic Plasticity. *Cell* **166**, 1163-1175.e12 (2016).
81. Zeng, M. *et al.* Reconstituted Postsynaptic Density as a Molecular Platform for Understanding Synapse Formation and Plasticity. *Cell* **174**, 1172-1187.e16 (2018).
82. Beutel, O., Maraspini, R., Pombo-Garcia, K., Martin-Lemaitre, C. & Honigmann, A. Phase Separation of Zonula Occludens Proteins Drives Formation of Tight Junctions. *SSRN Electron. J.* 923–936 (2019). doi:10.2139/ssrn.3362257

83. Utepbergenov, D. I., Fanning, A. S. & Anderson, J. M. Dimerization of the scaffolding protein ZO-1 through the second PDZ domain. *J. Biol. Chem.* **281**, 24671–24677 (2006).
84. Fanning, A. S. *et al.* The Unique-5 and-6 Motifs of ZO-1 Regulate Tight Junction Strand Localization and Scaffolding Properties □ D. *Mol. Biol. Cell* **18**, 721–731 (2007).
85. Spadaro, D. *et al.* Tension-Dependent Stretching Activates ZO-1 to Control the Junctional Localization of Its Interactors. *Curr. Biol.* **27**, 3783-3795.e8 (2017).
86. McGee, A. W. *et al.* Structure of the SH3-guanylate kinase module from PSD-95 suggests a mechanism for regulated assembly of MAGUK scaffolding proteins. *Mol. Cell* **8**, 1291–1301 (2001).
87. Tavares, G. A., Panepucci, E. H. & Brunger, A. T. Structural characterization of the intramolecular interaction between the SH3 and guanylate kinase domains of PSD-95. *Mol. Cell* **8**, 1313–1325 (2001).
88. Shamipour, S. *et al.* Bulk Actin Dynamics Drive Phase Segregation in Zebrafish Oocytes. *Cell* **177**, 1463-1479.e18 (2019).
89. Kimmel, C. B., Ballard, W. W., Kimmel, S. R., Ullmann, B. & Schilling, T. F. Stages of embryonic development of the zebrafish. *Dev. Dyn.* **203**, 253–310 (1995).
90. Fukazawa, C. *et al.* Poky/chuk/ikk1 is required for differentiation of the zebrafish embryonic epidermis. *Dev. Biol.* (2010). doi:10.1016/j.ydbio.2010.07.037
91. Kane, D. A. & Kimmel, C. B. The zebrafish midblastula transition. *Development* **119**, 447–456 (1993).
92. Carvalho, L. & Heisenberg, C. P. The yolk syncytial layer in early zebrafish development. *Trends in Cell Biology* **20**, 586–592 (2010).
93. Kimmel, C. B. & Law, R. D. Cell lineage of zebrafish blastomeres. II. Formation of the yolk syncytial layer. *Dev. Biol.* **108**, 86–93 (1985).
94. Lepage, S. E. & Bruce, A. E. E. Zebrafish epiboly: Mechanics and mechanisms. *Int. J. Dev. Biol.* **54**, 1213–1228 (2010).
95. Warga, R. M. & Kimmel, C. B. Cell movements during epiboly and gastrulation in zebrafish. *Development* **108**, 569–580 (1990).
96. Morita, H. *et al.* The Physical Basis of Coordinated Tissue Spreading in Zebrafish Gastrulation. *Dev. Cell* **40**, 354-366.e4 (2017).
97. Petridou, N. I., Grigolon, S., Salbreux, G., Hannezo, E. & Heisenberg, C. P. Fluidization-mediated tissue spreading by mitotic cell rounding and non-canonical Wnt signalling. *Nat. Cell Biol.* **21**, 169–178 (2019).
98. Montero, J. A. *et al.* Shield formation at the onset of zebrafish gastrulation. *Development* **132**, 1187–1198 (2005).
99. Jessen, J. R. & Solnica-Krezel, L. Morphogenetic cell movements shaping the zebrafish gastrula. *Advances in Developmental Biology* **14**, 131–165 (2005).
100. Webb, S. E. & Miller, A. L. Ca2+ signalling and early embryonic patterning during zebrafish development. *Clin. Exp. Pharmacol. Physiol.* **34**, 897–904 (2007).
101. Bruce, A. E. E. Zebrafish Epiboly: Spreading Thin Over the Yolk. doi:10.1002/dvdy
102. Köppen, M., García Fernández, B., Carvalho, L., Jacinto, A. & Heisenberg, C. P. Coordinated cell-shape changes control epithelial movement in zebrafish and Drosophila. *Development* **133**, 2671–2681 (2006).
103. Kane, D. A. *et al.* The zebrafish epiboly mutants. *Development* **123**, 47–55 (1996).
104. Trinkaus, J. P. Mechanism of Fundulus epiboly - a current view. *Integr. Comp. Biol.* **24**, 673–688 (1984).

105. Trinkaus, J. P. A study of the mechanism of epiboly in the egg of Fundulus heteroclitus. *J. Exp. Zool.* **118**, 269–319 (1951).
106. Behrndt, M. *et al.* Forces driving epithelial spreading in zebrafish gastrulation. *Science (80-.).* **338**, 257–260 (2012).
107. Cheng, J. C., Miller, A. L. & Webb, S. E. Organization and function of microfilaments during late epiboly in zebrafish embryos. *Dev. Dyn.* **231**, 313–323 (2004).
108. Chen, S. R. & Kimelman, D. The role of the yolk syncytial layer in germ layer patterning in zebrafish. *Development* **127**, 4681–4689 (2000).
109. Wilkins, S. J. *et al.* Mtx2 directs zebrafish morphogenetic movements during epiboly by regulating microfilament formation. *Dev. Biol.* **314**, 12–22 (2008).
110. Bruce, A. E. E., Howley, C., Fox, M. D. & Ho, R. K. T-box gene eomesodermin and the homeobox-containing mix/bix gene mtx2 regulate epiboly movements in the zebrafish. *Dev. Dyn.* **233**, 105–114 (2005).
111. Holloway, B. A. *et al.* A novel role for MAPKAPK2 in morphogenesis during zebrafish development. *PLoS Genet.* **5**, (2009).
112. Lachnit, M., Kur, E. & Driever, W. Alterations of the cytoskeleton in all three embryonic lineages contribute to the epiboly defect of Pou5f1/Oct4 deficient MZspg zebrafish embryos. *Dev. Biol.* **315**, 1–17 (2008).
113. Song, S. *et al.* Pou5f1-Dependent EGF Expression Controls E-Cadherin Endocytosis, Cell Adhesion, and Zebrafish Epiboly Movements. *Dev. Cell* **24**, 486–501 (2013).
114. Lin, F. *et al.* Gα 12/i3 regulate epiboly by inhibiting E-cadherin activity and modulating the actin cytoskeleton. *J. Cell Biol.* **184**, 909–921 (2009).
115. Clapham, D. E. *Calcium signaling*. *Calcium Signaling, Second Edition* (2007). doi:10.1201/9781420038231
116. Lai, S. L. *et al.* Diaphanous-related formin 2 and profilin I are required for gastrulation cell movements. *PLoS One* **3**, (2008).
117. Leskow, F. C., Holloway, B. A., Wang, H. Bin, Mullins, M. C. & Kazanietz, M. G. The zebrafish homologue of mammalian chimerin Rac-GAPs is implicated in epiboly progression during development. *Proc. Natl. Acad. Sci. U. S. A.* **103**, 5373–5378 (2006).
118. Schwayer, C. *et al.* Mechanosensation of Tight Junctions Depends on ZO-1 Phase Separation and Flow. *Cell* **179**, 937-952.e18 (2019).
119. Wittchen, E. S., Haskins, J. & Stevenson, B. R. Protein interactions at the tight junction. Actin has multiple binding partners, and ZO-1 forms independent complexes with ZO-2 and ZO-3. *J. Biol. Chem.* **274**, 35179–35185 (1999).
120. Wittchen, E. S., Haskins, J. & Stevenson, B. R. Exogenous expression of the amino-terminal half of the tight junction protein ZO-3 perturbs junctional complex assembly. *J. Cell Biol.* **151**, 825–836 (2000).
121. Bauer, H., Zweimueller-Mayer, J., Steinbacher, P., Lametschwandtner, A. & Bauer, H. C. The dual role of zonula occludens (ZO) proteins. *Journal of Biomedicine and Biotechnology* **2010**, (2010).
122. Siddiqui, M., Sheikh, H., Tran, C. & Bruce, A. E. E. The tight junction component Claudin E is required for zebrafish epiboly. *Dev. Dyn.* **239**, 715–722 (2010).
123. Falahati, H. & Wieschaus, E. Independent active and thermodynamic processes govern the nucleolus assembly in vivo. *Proc. Natl. Acad. Sci. U. S. A.* **114**, 1335–1340 (2017).
124. Brangwynne, C. P., Mitchison, T. J. & Hyman, A. A. Active liquid-like behavior of

nucleoli determines their size and shape in Xenopus laevis oocytes. *Proc. Natl. Acad. Sci. U. S. A.* **108**, 4334–4339 (2011).
125. Araki, Y., Zeng, M., Zhang, M. & Huganir, R. L. Rapid Dispersion of SynGAP from Synaptic Spines Triggers AMPA Receptor Insertion and Spine Enlargement during LTP. *Neuron* **85**, 173–189 (2015).
126. Jayashankar, V. *et al.* Protein phosphatase 1 β paralogs encode the zebrafish myosin phosphatase catalytic subunit. *PLoS One* **8**, (2013).
127. Yao, M. *et al.* Force-dependent conformational switch of α -catenin controls vinculin binding. *Nat. Commun.* **5**, (2014).
128. Zemljic-Harpf, A. E. *et al.* Vinculin directly binds zonula occludens-1 and is essential for stabilizing connexin-43-containing gap junctions in cardiac myocytes. *J. Cell Sci.* **127**, 1104–1116 (2014).
129. Mandato, C. A. & Bement, W. M. Contraction and polymerization cooperate to assemble and close actomyosin rings around Xenopus oocyte wounds. *J. Cell Biol.* **154**, 785–797 (2001).
130. Rodriguez, O. C. *et al.* Conserved microtubule-actin interactions in cell movement and morphogenesis. *Nature Cell Biology* **5**, 599–609 (2003).
131. Benink, H. A. & Bement, W. M. Concentric zones of active RhoA and Cdc42 around single cell wounds. *J. Cell Biol.* **168**, 429–439 (2005).
132. DeMond, A. L., Mossman, K. D., Starr, T., Dustin, M. L. & Groves, J. T. T cell receptor microcluster transport through molecular mazes reveals mechanism of translocation. *Biophys. J.* **94**, 3286–3292 (2008).
133. Murugesan, S. *et al.* Formin-generated actomyosin arcs propel t cell receptor microcluster movement at the immune synapse. *Journal of Cell Biology* **215**, 383–399 (2016).
134. Kaizuka, Y., Douglass, A. D., Varma, R., Dustin, M. L. & Vale, R. D. Mechanisms for segregating T cell receptor and adhesion molecules during immunological synapse formation in Jurkat T cells. *Proc. Natl. Acad. Sci. U. S. A.* **104**, 20296–20301 (2007).
135. Yi, J., Wu, X. S., Crites, T. & Hammer, J. A. Actin retrograde flow and actomyosin II arc contraction drive receptor cluster dynamics at the immunological synapse in Jurkat T cells. *Mol. Biol. Cell* **23**, 834–852 (2012).
136. Ditlev, J. A. *et al.* A composition-dependent molecular clutch between T cell signaling condensates and actin. *Elife* **8**, 1–44 (2019).
137. Dickinson, D. J., Schwager, F., Pintard, L., Gotta, M. & Goldstein, B. A Single-Cell Biochemistry Approach Reveals PAR Complex Dynamics during Cell Polarization. *Dev. Cell* **42**, 416-434.e11 (2017).
138. Goldstein, B. & Macara, I. G. The PAR Proteins: Fundamental Players in Animal Cell Polarization. *Dev. Cell* **13**, 609–622 (2007).
139. Munro, E., Nance, J. & Priess, J. R. Cortical flows powered by asymmetrical contraction transport PAR proteins to establish and maintain anterior-posterior polarity in the early C. elegans embryo. *Dev. Cell* **7**, 413–424 (2004).
140. Dine, E., Gil, A. A., Uribe, G., Brangwynne, C. P. & Toettcher, J. E. Protein Phase Separation Provides Long-Term Memory of Transient Spatial Stimuli. *Cell Syst.* **6**, 655-663.e5 (2018).
141. Brugués, A. *et al.* Forces driving epithelial wound healing. *Nat. Phys.* **10**, 683–690 (2014).
142. Bement, W. M., Forscher, P. & Mooseker, M. S. A novel cytoskeletal structure

involved in purse string wound closure and cell polarity maintenance. *J. Cell Biol.* **121**, 565–578 (1993).
143. Volksdorf, T. *et al.* Tight Junction Proteins Claudin-1 and Occludin Are Important for Cutaneous Wound Healing. *Am. J. Pathol.* **187**, 1301–1312 (2017).
144. Carvalho, L. *et al.* Occluding junctions as novel regulators of tissue mechanics during wound repair. *J. Cell Biol.* **217**, 4267–4283 (2018).
145. Zalik, S. E., Lewandowski, E., Kam, Z. & Geiger, B. Cell adhesion and the actin cytoskeleton of the enveloping layer in the zebrafish embryo during epiboly. *Biochem. Cell Biol.* **77**, 527–542 (1999).
Behrndt, M. (2014) 'Forces Driving Epithelial Spreading in Zebrafish Epiboly' PhD thesis, IST Austria

References for 'Actin Rings of Power' see in chapter 1.2.1.

References for 'Mechanosensation of tight junctions depends on ZO-1 phase separation and flow' see in chapter 2.1

A. Appendix

a. Establishment of a permeability assay for zebrafish embryos

In order to test TJ barrier sealing function, we established a permeability assay for zebrafish embryos, first described in *Xenopus laevis* and called ZnUMBA for 'Zinc-based Ultrasensitive Microscopic Barrier Assay'[27]. The principle behind the ZnUMBA assay is that Zn^{2+} ions are provided to the medium and FluoZin, a Zinc sensitive indicator is injected into the interstitial fluid (Figure 19A). Only upon TJ barrier breach, Zn^{2+} ions get in contact with Fluozin, which results in a rapid increase in its fluorescence by more than 50-fold (Figure 19A'). Therefore, this assay allows not only for detection of leakiness in a tissue, but also for monitoring rather local and transient barrier breaches[27]. To establish this assay for zebrafish embryos, we first determined concentrations of reagents suitable for developing zebrafish embryos (FluoZin and $ZnCl_2$; data not shown). Then, we tested for functionality of the assay as follows: as a negative control, wild-type embryos incubated in Danieaus medium were used, which are thought to start epithelial differentiation during early developmental stages[90] and as positive controls wild-type embryos embedded in Calcium-free medium with the addition of 10 mM EGTA were used. EGTA treatment disassembles cell-cell junctions[27] and when used at high levels can also result in cell dissociation[145]. Indeed, we only monitored a dramatic increase of FluoZin signal in the case of EGTA treated embryos but no obvious and/or long-lasting leakiness of the tissue during normal development (Figure 19B,B'). However, at this point we cannot exclude the possibility of transient and local barrier breaches occurring in the tissue during zebrafish early development as shown in the case of *Xenopus laevis*[27]. Importantly though, we could demonstrate that the ZnUMBA assay can also be utilized to detect barrier breaches in zebrafish embryos.

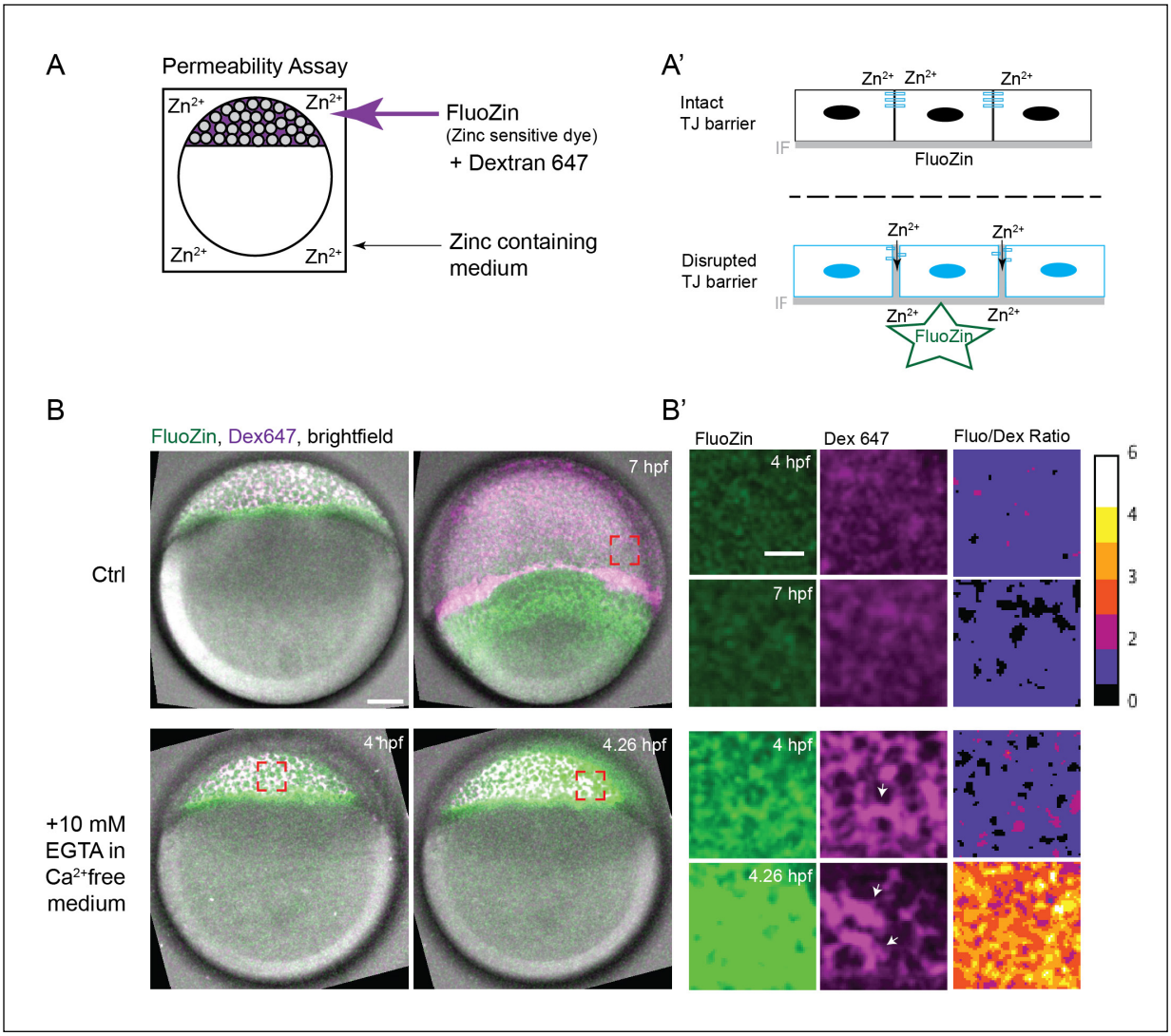

Figure 19: ZnUMBA assay for zebrafish embryos

(A) Outline of ZnUMBA experimental setup. Embryos are embedded in agarose and medium containing 750 µM $ZnCl_2$. FluoZin, a Zinc selective indicator, at a concentration of 100 µM is injected into the interstitial fluid along with Dextran 647 for normalization purposes.

(A') Scheme of an intact and disrupted TJ barrier: When the TJ barrier is intact interstitial fluid containing FluoZin is properly separated from Zn^{2+} ions present in the outside environment. Upon TJ barrier breach eg. through EGTA treatment, the junctions become 'leaky' resulting in a more than 50-fold fluorescence increase of FluoZin reacting with Zn^{2+} ions.

(B) Maximum intensity projection (MIPs) of bright-field/fluorescence signal of FluoZin (in green) and Dextran 647 (in magenta) of wild-type embryos (negative Ctrl - 1st row) at 4 and 7 hpf and embryos incubated in agarose and Calcium-free isotonic Ringer's medium and 10 mM EGTA (positive Ctrl - 2nd row) at 4 and 4.26 hpf. Red dashed box indicates zoom-in region of images in (B'). Scale bar, 100 µm.

(B') MIPs of FluoZin (in green; first colum), Dextran 647 (in magenta; 2nd column) and the ratio of FluoZin signal and Dextran signal of the zoom-in region shown in (B). Calibration bar on the right shows the FluoZin-Dextran ratio in color code. Scale bar, 30 µm. N > 3. N is the number of independent experiments.